Kathrin Glantschnig

First principles calculation of optical spectra

DISSERTATION

zur Erlangung des akademischen Grades einer
Doktorin der Naturwissenschaften
eingereicht an der

Naturwissenschaftlichen Fakultät der
Karl-Franzens-Universität Graz

Erstbegutachterin: Univ.-Prof. Dr. Dr. hc. Claudia Draxl
Theoretische Festkörperphysik
Institut für Physik
Humboldt-Universität zu Berlin

Zweitbegutachter: Ao. Univ.-Prof. Dr. Ulrich Hohenester
Theoretische Festkörperphysik
Institut für Physik
Karl-Franzens-Universität Graz

Juli 2014

Contents

1 Introduction

Detailed knowledge about the optical properties of elemental metals is not only of scientific interest, it is crucial for the understanding of complex materials. It even serves as starting point for the design of new materials and is therefore highly relevant for industrial applications. Density functional theory (DFT) [1,2] provides a framework which is capable of describing ground-state properties like equilibrium volumes, elastic constants, and phonon frequencies from first principles with high accuracy. The calculation of optical spectra, however, involves excited states. Over the years it turned out that the use of ground-state quantities in the description of excited states gives reasonable results for a large variety of materials, among them simple metals, but it naturally fails for others. The Kohn-Sham band structure does not need to provide a good description of the energy bands, since many-body effects have to be considered for this purpose.

Time-dependent DFT (TDDFT) [3, 4] is an, in principle, exact formalism for neutral excitations, including many-body corrections in a time-dependent exchange-correlation (xc) potential. The simplest possible approach for the dielectric response is the random-phase approximation (RPA) where electron-hole correlations are neglected, i.e., the xc kernel is set to zero. Since for zero momentum transfer local-field effects do not play an important role in the optical range, even the independent-particle approximation (IPA) can be adopted. This is done here for the majority of materials under investigation. The use of the IPA based on the Kohn-Sham band structure is regarded to be reasonable for elemental metals.

The aim of this work is twofold: first, to investigate the optical excitations in a variety of metals together with an in-depth analysis of their origin; second, to provide benchmark data obtained within the framework of TDDFT. Only if all possible sources of inaccuracy present in the calculation are eliminated, one is able to judge about the performance of the adopted method. For this purpose, highly-accurate *ab initio* calculations are necessary to prevent errors introduced from the solution of the Kohn-Sham equations. In this work, the

ground-state calculations were carried out within the framework of DFT adopting the APW+lo method [5] as implemented in the WIEN2k code [6] and in the **exciting** code [7], respectively. The optical spectra obtained within the IPA or RPA are compared to available experimental data, among them recent electron energy-loss spectroscopy (EELS) [8] and reflection EELS (REELS) [9, 10] measurements.

To investigate the origin of spectral features an analysis in terms of oscillator strengths is performed. The oscillator strengths are visualized for selected planes in the Brillouin zone, highlighting regions with the strongest contributions to a specific spectral feature. This analysis is supported by band structure plots including information about predominant band characters.

In the first part of this work, the theoretical framework underlying the calculation of optical properties is presented. It starts with an overview of the basic concepts of DFT given in Chapter 2, including the theorem of Hohenberg and Kohn [1], the Kohn-Sham equations [2], approximations for the description of xc effects, and the interpretation of Kohn-Sham energies. The time-dependent generalization of DFT (TDDFT), is presented in Chapter 3. Starting with the theorem of Runge and Gross [3], the time-dependent Kohn-Sham equations are derived and the density response is discussed to linear order in the perturbation. The approximations for the xc kernel, used in the present work, are given. In Chapter 4, the formulas for the longitudinal dielectric response are derived with the help of the self-consistent field method and the formalism used in the calculation of the optical spectra within TDDFT is provided. The aim of Chapter 5 is to summarize the basic ideas of the linearized augmented plane wave (LAPW) method to perform electronic-structure calculations, while in Chapter 6, the inclusion of scalar-relativistic effects and spin-orbit (SO) coupling in the LAPW method is described.

The second part of this work is dedicated to the presentation of the results. It starts with an overview of computational details in Chapter 7. Chapter 8 deals with the optical and electron loss spectra of palladium. For zero momentum transfer, the origin of the most prominent spectral features of Pd is investigated. The evolution of the electron energy-loss function of palladium is studied for increasing momentum transfer in (100), (110), and (111) direction.

Chapter 9 starts with the investigation of bulk aluminum at ambient conditions and under pressure. Thereafter, the behavior of Al(001) thin films is studied. The impact of increasing film thickness, particularly in view of the effects of surface bands on the dielectric function is examined. Again, analysis in terms of oscillator strengths provide deeper insight.

Chapter 10 concentrates on the influence of SO coupling on the optical spectra of gold, platinum, lead, and tungsten. In case of gold, the effects of a non-relativistic and scalar-relativistic treatment on the electronic structure and

optical spectra are examined.

A compilation of optical spectra for 12 elemental metals is given in Chapter 11. These are silver, copper, nickel, iron, molybdenum, tantalum, vanadium, cobalt, titanium, zinc, bismuth, and tellurium. The spectral features are compared to available experimental data and their origin is analyzed in order to identify possible sources of discrepancy between theory and experiment. This way we learn to which extent the IPA based on the Kohn-Sham band structure yields reasonable results and indicate possible drawbacks of the adopted approach. The overall outcome is summarized and an outlook is given in Chapter 12.

Part I

Theory

2 Density functional theory

Density functional theory (DFT) is the most powerful and widely used tool in computational materials science. Its origin can be traced back to the 1920's. At that time, Thomas and Fermi came up with a description of many-electron systems using the electron density $n(\mathbf{r})$ instead of the many-body wave function $\Psi(r_1, r_2, ..., r_n)$ as basic quantity. The Thomas-Fermi method, as presented in 1927 [11, 12], served to predict qualitative trends but failed in the description of important phenomena like bonding. The work by Hohenberg, Kohn, and Sham of the 1960's marked the starting point in the development of modern DFT [13].

In this Chapter, the basic ideas of static DFT are summarized. At first, the basic lemma of Hohenberg and Kohn [1] is presented, followed by the derivation of the Kohn-Sham equations [2]. Then, the most important approximations for the exchange-correlation (xc) potential are given including their applications and limitations. Finally, the applicability of DFT for the description of excited states is discussed. We follow closely the original works by Hohenberg and Kohn [1], as well as by Kohn and Sham [2]. In addition, Refs. [13–15] were used.

2.1 Lemma of Hohenberg and Kohn

By considering a system of N interacting electrons moving under the influence of an external potential $v(\mathbf{r})$, Hohenberg and Kohn [1] were able to show that the ground-state density $n(\mathbf{r})$ of such a bound system of interacting electrons determines the external potential $v(\mathbf{r})$ uniquely. The term uniquely in this context means that two external potentials corresponding to the same ground-state density $n(\mathbf{r})$ differ by a trivial additive constant C only. The proof of this lemma is restricted to non-degenerate ground states, but Kohn succeded to show the validity of this lemma also for the more general case of degenerate ground states [16].

An important consequence of this basic lemma of DFT for the treatment of many-body systems is, that the knowledge of the ground-state electron density $n(\mathbf{r})$ is sufficient to determine the external potential acting on the system. Now, this external potential $v(\mathbf{r})$ is used in the construction of the full Hamiltonian of the system. As a result, all properties which can be derived from H are fixed by the ground-state electron density $n(\mathbf{r})$ [1, 13–15].

2.2 Hohenberg-Kohn variational principle

Using conventional wave-function methods, the ground-state energy is obtained either by adopting the Rayleigh-Ritz variational principle or by solving the Schrödinger equation. Within the framework of DFT, Hohenberg and Kohn [1] developed a minimal principle for the energy as functional of the density. It states that it is possible to obtain the ground-state energy by varying trial densities $\tilde{n}(\mathbf{r})$ instead of trial wave functions $\tilde{\Psi}(\mathbf{r})$ [1, 13, 15].

The energy functional $E_{v(\mathbf{r})}[n(\mathbf{r})]$, with $v(\mathbf{r})$ being the external potential and $n(\mathbf{r})$ denoting a certain density, is defined through [1]

$$E_{v(\mathbf{r})}[n(\mathbf{r})] \equiv \int v(\mathbf{r})n(\mathbf{r})d\mathbf{r} + F[n(\mathbf{r})], \tag{2.1}$$

with

$$F[n(\mathbf{r})] \equiv \langle \Psi[n(\mathbf{r})]|T+U|\Psi[n(\mathbf{r})]\rangle \tag{2.2}$$

being also a functional of the density. T and U are the kinetic- and interaction-energy operators, respectively. Using the true ground-state electron density, $E_{v(\mathbf{r})}[n(\mathbf{r})]$, defined in (2.1), equals the ground-state energy. This was proven by Hohenberg and Kohn [1] in 1964 as well as by Levy [17] and Lieb [18]. The latter adopted an alternative approach known as the constrained search method, which will be presented below, following closely the formalism as given in Refs. [13] and [15].

The basic idea is to divide the minimization procedure into two steps. Firstly, the trial density $\tilde{n}(\mathbf{r})$ is fixed and the minimization is performed within the set of trial wave functions corresponding to $\tilde{n}(\mathbf{r})$. Consequently, the constrained energy minimum is defined via [13, 15]

$$\begin{aligned} E_{v(\mathbf{r})}[\tilde{n}(\mathbf{r})] &= \min_{\alpha} \langle \tilde{\Psi}^{\alpha}_{\tilde{n}(\mathbf{r})}|H|\tilde{\Psi}^{\alpha}_{\tilde{n}(\mathbf{r})}\rangle \\ &= \int v(\mathbf{r})\tilde{n}(\mathbf{r})d\mathbf{r} + F[\tilde{n}(\mathbf{r})], \end{aligned} \tag{2.3}$$

where

$$F[\tilde{n}(\mathbf{r})] = \min_{\alpha} \langle \tilde{\Psi}^{\alpha}_{\tilde{n}(\mathbf{r})}|T+U|\tilde{\Psi}^{\alpha}_{\tilde{n}(\mathbf{r})}\rangle, \tag{2.4}$$

and the trial wave functions are labelled by $\tilde{\Psi}^{\alpha}_{\tilde{n}(\mathbf{r})}$. As a result, one obtains the lowest possible energy for the chosen density $\tilde{n}(\mathbf{r})$. Secondly, the minimization of $E_{v(\mathbf{r})}[\tilde{n}(\mathbf{r})]$, defined in Eq. (2.3), is performed over all $\tilde{n}(\mathbf{r})$ by [13]

$$\begin{aligned} E &= \min_{\tilde{n}(\mathbf{r})} E_{v(\mathbf{r})}[\tilde{n}(\mathbf{r})] \\ &= \min_{\tilde{n}(\mathbf{r})} \left\{ \int v(\mathbf{r})\tilde{n}(\mathbf{r}) d\mathbf{r} + F[\tilde{n}(\mathbf{r})] \right\}. \end{aligned} \tag{2.5}$$

The minimum in (2.5) is reached for a non-degenerate ground state if $\tilde{n}(\mathbf{r})$ equals the ground-state density. In case of a degenerate ground state $\tilde{n}(\mathbf{r})$ must be equal to one of the ground-state densities [1, 13, 15]. This formalism allows for the determination of the ground-state energy. It does not include, however, any prescriptions concerning the solution of the corresponding minimization problem.

2.3 Kohn-Sham equations

The aim of this Section is to show how to derive a set of single-particle equations which allow for a straight-forward calculation of the ground-state energy of an interacting many-body system. This is done following closely the original work by Kohn and Sham [2] as well as Refs. [13, 15].

The exact solution of a many-body problem within DFT goes hand in hand with the knowledge of a proper expression for the functional $F[n(\mathbf{r})]$. Hohenberg and Kohn suggested to rewrite this functional as [1]

$$F[n(\mathbf{r})] = \frac{1}{2} \int \int \frac{n(\mathbf{r}) n(\mathbf{r}')}{\mid \mathbf{r} - \mathbf{r}' \mid} d\mathbf{r} d\mathbf{r}' + G[n(\mathbf{r})], \tag{2.6}$$

where the first term represents the Coulomb interaction energy and $G[n(\mathbf{r})]$ is a functional of the density $n(\mathbf{r})$. Then, Kohn and Sham introduced the decomposition [2]

$$G[n(\mathbf{r})] = T_s[n(\mathbf{r})] + E_{xc}[n(\mathbf{r})], \tag{2.7}$$

where $T_s[n(\mathbf{r})]$ represents the kinetic energy functional of the non-interacting and $E_{xc}[n(\mathbf{r})]$ the xc energy functional of the interacting electron system corresponding to a density $n(\mathbf{r})$. As pointed out in Ref. [15] there exists, however, no proof that it is reasonable to approximate $T[n(\mathbf{r})]$ by $T_s[n(\mathbf{r})]$. Nevertheless, one can get rid of this problem by absorbing the difference between the kinetic energy of the interacting and non-interacting system into the xc energy functional.

With the help of (2.6) and (2.7), (2.1) yields a modified expression for the energy functional given by

$$E_{v(\mathbf{r})}[n(\mathbf{r})] = \int v(\mathbf{r})n(\mathbf{r})d\mathbf{r} + \frac{1}{2}\int\int \frac{n(\mathbf{r})n(\mathbf{r}')}{\mid \mathbf{r}-\mathbf{r}' \mid} d\mathbf{r}d\mathbf{r}' + T_s[n(\mathbf{r})] + E_{xc}[n(\mathbf{r})]. \tag{2.8}$$

According to the Hohenberg-Kohn variational principle, $E_{v(\mathbf{r})}[n(\mathbf{r})]$ evaluated for some arbitrary electron density will give an energy value greater than the ground-state energy. In order to find the minimum value of (2.8), the Euler-Lagrange formalism is adopted. Using the stationary condition for $E_{v(\mathbf{r})}[n(\mathbf{r})]$ under the constraint of particle number conservation, i.e.,

$$\int n(\mathbf{r})d\mathbf{r} = N, \tag{2.9}$$

one obtains the Euler-Lagrange equation [2, 13, 15]

$$\int \delta n(\mathbf{r}) \left\{ v(\mathbf{r}) + \int \frac{n(\mathbf{r}')}{\mid \mathbf{r}-\mathbf{r}' \mid} d\mathbf{r}' + \frac{\delta T_s[n(\mathbf{r})]}{\delta n(\mathbf{r})} + \frac{\delta E_{xc}[n(\mathbf{r})]}{\delta n(\mathbf{r})} - \epsilon \right\} d\mathbf{r} \;\; = \;\; 0. \tag{2.10}$$

Here, ϵ denotes the Lagrange multiplier. Eq. (2.10) can be rewritten by introducing an effective potential via

$$v_{eff}(\mathbf{r}) = v(\mathbf{r}) + \int \frac{n(\mathbf{r}')}{\mid \mathbf{r}-\mathbf{r}' \mid} d\mathbf{r}' + v_{xc}(\mathbf{r}), \tag{2.11}$$

with

$$v_{xc}(\mathbf{r}) = \frac{\delta E_{xc}[n(\mathbf{r})]}{\delta n(\mathbf{r})} \tag{2.12}$$

representing the xc potential. Eq. (2.10) now reads

$$\int \delta n(\mathbf{r}) \left\{ \frac{\delta T_s[n(\mathbf{r})]}{\delta n(\mathbf{r})} + v_{eff}(\mathbf{r}) - \epsilon \right\} d\mathbf{r} = 0. \tag{2.13}$$

This expression is similar to that for non-interacting electrons moving in an effective potential. Consequently, one arrives at a set of Schrödinger-like single-particle equations given by

$$\left[-\frac{1}{2}\nabla^2 + v_{eff}(\mathbf{r}) \right] \psi_i(\mathbf{r}) = \epsilon_i \psi_i(\mathbf{r}), \;\; i = 1, ..., N, \tag{2.14}$$

which has to be solved self-consistently. In a first step, a starting density is chosen and the external potential is determined. Then, the set of equations

is solved, giving as result the Kohn-Sham orbitals $\psi_i(\mathbf{r})$ together with the corresponding eigenvalues ϵ_i. Now, the new electron density $n(\mathbf{r})$ is constructed with the help of

$$n(\mathbf{r}) = \sum_{i=1}^{N} \mid \psi_i(\mathbf{r}) \mid^2 . \tag{2.15}$$

(2.14) together with (2.11) and (2.15) represent the Kohn-Sham equations [2]. After self-consistency is reached, i.e., the densities of two subsequent cycles differ by a value smaller than a certain threshold, the ground-state energy is finally obtained via

$$E = \sum_{i=1}^{N} \epsilon_i + E_{xc}[n(\mathbf{r})] - \int v_{xc}(\mathbf{r}) n(\mathbf{r}) d\mathbf{r} - \frac{1}{2} \int \int \frac{n(\mathbf{r}) n(\mathbf{r}')}{\mid \mathbf{r} - \mathbf{r}' \mid} d\mathbf{r} d\mathbf{r}'. \tag{2.16}$$

As pointed out by Kohn [13], all many-body effects are in principle included in the xc energy functional $E_{xc}[n(\mathbf{r})]$ and potential $v_{xc}(\mathbf{r})$. The accuracy of the formalism, therefore, crucially depends on the quality of approximations found for $E_{xc}[n(\mathbf{r})]$, which should be at the same time as simple as possible and sufficiently accurate. Therefore, the next sections are dedicated to the xc potential and its most widely used approximations.

2.4 Exact expression for E_{xc}

An accurate description of many-body systems involves a proper treatment of xc effects. It is possible to derive an exact expression for the xc energy functional by adopting the concept of an average xc hole. The ideas behind will be summarized below, following the formalism outlined in Refs. [13, 15, 19].

The physical xc hole describes how an electron placed at position $\mathbf{r}$ reduces the probability of finding another electron at $\mathbf{r}'$, i.e., the repulsion between the electrons. It has to fulfill the sum rule

$$\int n_{xc}(\mathbf{r}, \mathbf{r}') d\mathbf{r}' = -1 \tag{2.17}$$

indicating that a totally screened electron is present at $\mathbf{r}$.

For the definition of the average xc hole, at first, a modified Hamiltonian H_λ is introduced. It is obtained from the original one by applying the substitutions [13, 19]

$$\frac{1}{|\mathbf{r_i} - \mathbf{r_j}|} \rightarrow \frac{\lambda}{|\mathbf{r_i} - \mathbf{r_j}|} \tag{2.18}$$

and

$$v(\mathbf{r}) \rightarrow v_\lambda(\mathbf{r}). \tag{2.19}$$

Here, $\lambda = 0$ represents the non-interacting Kohn-Sham system, whereas the physical system is related to $\lambda = 1$. The external potential $v_\lambda(\mathbf{r})$ is chosen in a way that for all λ with $0 \leq \lambda \leq 1$ the resulting density equals the density of the real system. The average xc hole is now given by [13, 19]

$$\bar{n}_{xc}(\mathbf{r}, \mathbf{r}') = \int_0^1 d\lambda \; n_{xc}(\mathbf{r}, \mathbf{r}'; \lambda), \tag{2.20}$$

where $n_{xc}(\mathbf{r}, \mathbf{r}'; \lambda)$ denotes the λ-dependent physical xc hole with $\lambda \in [0, 1]$. Using this definition, the xc energy functional can be expressed by

$$E_{xc}[n(\mathbf{r})] = \frac{1}{2} \int \int d\mathbf{r} d\mathbf{r}' \frac{n(\mathbf{r}) \bar{n}_{xc}(\mathbf{r}, \mathbf{r}')}{|\mathbf{r} - \mathbf{r}'|}, \tag{2.21}$$

known as adiabatic connection formula, which was shown independently by Langreth and Perdew [20], Harris and Jones [21], as well as by Gunnarson and Lundquist [22].

2.5 Local-density approximation

From Eq. (2.6) it is obvious that the xc energy functional does not contain the long-range Coulomb term. Moreover, Eq. (2.7) reveals that the kinetic energy of independent electrons has been separated out. Thus, it makes sense to assume a local or quasi-local form for $E_{xc}[n(\mathbf{r})]$. This is also underlined by the findings of Kohn [23]. He proved that local static properties of many-electron systems, like the electron density $n(\mathbf{r})$ or the pair-correlation function $g(\mathbf{r}, \mathbf{r}')$, depend on particles in the neighbourhood of $\mathbf{r}$. In this context, neighbourhood refers to a sphere with a radius approximately equal to the local Fermi wavelength $\lambda_F(\mathbf{r}) = [3\pi^2 n(\mathbf{r})]^{-1/3}$. Changes in the potential stemming from the region outside this sphere have almost no effect on such properties [14, 15, 23].

Among commonly used approximations for E_{xc}, the so-called local-density approximation (LDA) has the simplest form. It is given by [13, 15, 19]

$$E_{xc}^{LDA}[n(\mathbf{r})] = \int n(\mathbf{r}) \epsilon_{xc}[n(\mathbf{r})] d\mathbf{r}, \tag{2.22}$$

where $\epsilon_{xc}[n(\mathbf{r})]$ denotes the xc energy density. Its value equals that of a homogeneous electron gas with electron density $n(\mathbf{r})$. Now, $\epsilon_{xc}[n(\mathbf{r})]$ can be split into an exchange and a correlation part, i.e.,

$$\epsilon_{xc}[n(\mathbf{r})] = \epsilon_x[n(\mathbf{r})] + \epsilon_c[n(\mathbf{r})]. \tag{2.23}$$

For the exchange part, an exact analytic expression is available. Using atomic units, it is given by [13]

$$\epsilon_x[n(\mathbf{r})] = -\frac{0.458}{r_s}. \tag{2.24}$$

Here, r_s is the radius of a sphere defined through $(4\pi/3)r_s^3 = [n(\mathbf{r})]^{-1}$. This sphere contains exactly one electron. In contrast, only estimates are available for the correlation part. A first one, reported by Wigner in 1978, has the form [24]

$$\epsilon_c[n(\mathbf{r})] = -\frac{0.44}{r_s + 7.8}. \tag{2.25}$$

Recent parameterizations reported by Vosko, Wilk, and Nusair [25], Perdew and Zunger [26], as well as Perdew and Wang [27] are based on the Monte Carlo data by Ceperley and Alder [28].

The generalization of LDA for use in spin-polarized systems leads to the local spin-density approximation (LSDA). In this case Eq. (2.22) is substituted by [19]

$$E_{xc}^{LSDA}[n^{\uparrow}(\mathbf{r}), n^{\downarrow}(\mathbf{r})] = \int n(\mathbf{r})\epsilon_{xc}[n^{\uparrow}(\mathbf{r}), n^{\downarrow}(\mathbf{r})]d\mathbf{r}, \tag{2.26}$$

where $n^{\uparrow}(\mathbf{r})$ and $n^{\downarrow}(\mathbf{r})$ denote the spin densities for the two spin orientations.

By construction, LDA is exact for the homogeneous electron gas. Thus, it is assumed to provide reasonable results for systems of slowly varying densities like nearly-free electron metals. It turned out, however, that LDA works well in more cases. As pointed out in Ref. [13], bond lengths are obtained with a maximum devitation of approximately 1%. A detailed overview over the performance of L(S)DA in the description of various systems is given in the review of Jones and Gunnarsson [19].

2.6 Generalized gradient approximations

In order to reduce errors imposed by LDA, one possibility is to include the gradient of the electron density in the description of $E_{xc}[n(\mathbf{r})]$. Expansions of $E_{xc}[n(\mathbf{r})]$ in powers of the gradient in density $\nabla n(\mathbf{r})$ were reported already, for example, by Hohenberg and Kohn [1], as well as by Kohn and Sham [2]. It turned out, however, that this so-called gradient expansion approximation (GEA) in many cases did not improve over LDA and sometimes even lead to worse results. Further development in this field resulted in a large number of generalized gradient approximations (GGAs), which got more and more accurate and are nowadays state-of-the-art [13, 14].

The xc functional in the GGA takes the form

$$E_{xc}^{GGA}[n(\mathbf{r})] = \int \epsilon_{xc}(n(\mathbf{r}), |\nabla n(\mathbf{r})|) n(\mathbf{r}) d\mathbf{r}. \quad (2.27)$$

For the more general spin-polarized case it is given by [14]

$$E_{xc}^{GGA}[n^{\uparrow}(\mathbf{r}), n^{\downarrow}(\mathbf{r})] = \int \epsilon_{xc}(n^{\uparrow}(\mathbf{r}), n^{\downarrow}(\mathbf{r}), |\nabla n^{\uparrow}(\mathbf{r})|, |\nabla n^{\downarrow}(\mathbf{r})|) n(\mathbf{r}) d\mathbf{r}. \quad (2.28)$$

The xc energy density is now a function of the density and its gradient. Various parameterizations of the GGA are available in literature. Since the results presented in the second part of this thesis are based on the GGA reported by Perdew, Burke, and Ernzerhof [29], it will be summarized below following closely the ideas presented in Refs. [14, 29].

The correlation part of the xc functional is given by

$$E_c^{GGA-PBE}[n^{\uparrow}(\mathbf{r}), n^{\downarrow}(\mathbf{r})] = \int d\mathbf{r}\; n(\mathbf{r}) [\epsilon_c^{hom}(r_s, \zeta) + H(r_s, \zeta, t)]. \quad (2.29)$$

Here, $\zeta = (n^{\uparrow} - n^{\downarrow})/n$ represents the relative spin polarization, and $t = |\nabla n|/(2\phi k_s n)$ denotes a dimensionless density gradient. Moreover, the spin-scaling factor ϕ is given by $\phi(\zeta) = [(1+\zeta)^{2/3} + (1-\zeta)^{2/3}]/2$, $k_s = \sqrt{4k_F/\pi a_0}$ is the Thomas-Fermi screening wavevector, and a_0 denotes the Bohr radius. $H(r_s, \zeta, t)$ is defined by

$$H = \frac{e^2 \gamma \phi^3}{a_0} \ln \left\{ 1 + \frac{\beta}{\gamma} t^2 \left[\frac{1 + At^2}{1 + At^2 + A^2 t^4} \right] \right\} \quad (2.30)$$

and

$$A = \frac{\beta}{\gamma} [\exp\{-\epsilon_c^{hom}/(\gamma \phi^3 e^2/a_0)\} - 1]^{-1}, \quad (2.31)$$

with $\beta \approx 0.066725$ and $\gamma \approx 0.031091$.

The exchange part is given by

$$E_x^{GGA-PBE} = \int d\mathbf{r}\; n(\mathbf{r}) \epsilon_x^{hom}(n(\mathbf{r})) F_x(s), \quad (2.32)$$

where the enhancement factor reads as

$$F_x(s) = 1 + \kappa - \kappa/(1 + \mu s^2/\kappa) \quad (2.33)$$

with $\mu \approx 0.21951$ and $\kappa \approx 0.804$.

Improvements over LDA are achieved especially in the description of the total and atomization energies, energy barriers, and structural energy differences. Predictions of bond lengths are improved, but sometimes GGA overcorrects LDA results. For further details see [29] and references therein.

2.7 Interpretation of Kohn-Sham energies

DFT is a theory for the ground state of an electronic system, thus, in principle, only properties related to the ground state are described in an exact way. If interested in optical properties of materials, one needs to account for many-body effects to describe the opto-electronic excitations. Nevertheless, KS eigenvalues ϵ_i and orbitals ψ_i can be considered as a zeroth approximation for the description of excited states. Such procedure turned out to work quite well in many cases like for the optical response of metals. Nevertheless, poor agreement is obtained in the prediction of band-gap energies in semiconductors and insulators, where errors of typically 50% occur. They can be traced back to the fact that there exists no physical justification of describing excited states by KS eigenvalues ϵ_i, since the latter are nothing else than Lagrange multipliers in the KS formalism. The only exception concerns the eigenvalue of the highest occupied state, which is related to $-I$, with I being the ionization energy of the system [14, 19, 30, 31].

Janak proved in 1978 that there exists a relationship between the ground-state energies of the N- and $(N+1)$- particle system and the KS eigenvalues of the form [32]:

$$\epsilon_i = \frac{\partial E}{\partial n_i}. \tag{2.34}$$

Here, the n_i with $i = 1,...,N$ are the occupation numbers of the N-electron system. By introducing n electrons ($0 \leq n \leq 1$) into the lowest unoccupied level and using that the true total energies for the N- and $(N+1)$-electron systems correspond to $n = 0$ and $n = 1$, respectively, one finds that [32]

$$E_{N+1} - E_N = \int_0^1 \epsilon_i(n) dn. \tag{2.35}$$

These two expressions will now be used in the description of the band gap in terms of ground-state properties. The band-gap energy $E_g(N)$ of a N-particle system can be expressed by [19, 30, 31]

$$\begin{aligned} E_g(N) &= I(N) - A(N) \\ &= [E(N-1) - E(N)] - [E(N) - E(N+1)] \end{aligned} \tag{2.36}$$

with the ionization potential $I(N)$ and the electron affinity $A(N)$. The ground-state energy of N particles is denoted by $E(N)$. By using Janak's theorem given in Eq. (2.34), the KS eigenvalues can be linked to the ionization energy and electron affinity [19, 31]

$$\begin{aligned} I(N) &= -\epsilon_N(N - \eta) \\ A(N) &= -\epsilon_{N+1}(N + \eta'), \end{aligned} \tag{2.37}$$

with $0 < \eta, \eta' < 1$. According to Perdew and Levy [31], as well as Sham and Schlüter [30] the energy gap can be expressed by [19]

$$E_g(N) = \epsilon_{N+1}(N + \eta') - \epsilon_N(N - \eta) = \Delta\epsilon + \Delta, \tag{2.38}$$

where

$$\Delta\epsilon = \epsilon_{N+1}(N) - \epsilon_N(N) \tag{2.39}$$

is the band gap obtained from the KS eigenvalues. Eq. (2.38), thus, implies that the real band gap can differ from the value obtained from the DFT results even for the exact xc functional [19]. Still, deviations of the Kohn-Sham gap from the exact gap also arise e.g. from the the self-interaction error of semi-local xc functionals [19,26]. The discussion above indicates that the interpretation of Kohn-Sham eigenvalues as quasi-particle energies is not justified, even if reasonable results can be achieved for a variety of systems.

A proper description of the optical properties of solids involves the investigation of a many-electron system under the influence of a time-dependent external field. A framework for treating such time-dependent many-particle systems is the time-dependent density functional theory (TDDFT). The basic ideas of TDDFT will be presented in the next Chapter.

3 TDDFT

With the formulation of a time-dependent generalization of static DFT, Runge and Gross [3] provided a formalism which is, in principle, exact for neutral excitations. They proved the one-to-one correspondence between the external potential and the now time-dependent density [4]. The new point which comes into play is an additional dependence of the functional on a fixed initial many-particle state Ψ_0. Moreover, Runge and Gross derived a time-dependent version of the Kohn-Sham equations, where again the problem of treating a system of interacting particles is replaced by that of a system of independent particles together with an interacting density. All many-body corrections are, in principle, included in the now time-dependent local xc potential [3, 4, 14]. TDDFT provides a framework to treat systems in the presence of strong external fields where perturbation theory cannot be applied but it is also commonly used within the linear response regime. In the next sections, an overview over the framework of TDDFT is given, following closely the original work of Runge and Gross [3], as well as Refs. [4, 33–36].

3.1 Theorem of Runge and Gross

Within static DFT, the one-to-one correspondence between the density of the interacting electronic system and the external potential is part of the basic lemma of Hohenberg and Kohn [1] (see Section 2.1). The straight-forward generalization to the time-dependent case is not possible, since there exists no minimum principle similar to the Rayleigh-Ritz variational principle.

Therefore, Runge and Gross [3] used as starting point the time-dependent Schrödinger equation

$$i\frac{\partial}{\partial t}\Psi(t) = \hat{H}(t)\Psi(t), \tag{3.1}$$

with the time-dependent Hamiltonian

$$\hat{H}(t) = \hat{T} + \hat{U} + \hat{V}(t). \tag{3.2}$$

It describes the interacting many-electron system containing N electrons and consists of the kinetic energy term [3, 4, 36]

$$\hat{T} = \frac{1}{2} \sum_i \int \hat{\psi}_i^*(\mathbf{r})(-\nabla^2)\hat{\psi}_i(\mathbf{r})d\mathbf{r}, \tag{3.3}$$

the Coulomb repulsion [3, 4, 36]

$$\hat{U} = \frac{1}{2} \sum_{i,j;i\neq j} \int\int \hat{\psi}_i^*(\mathbf{r})\hat{\psi}_j^*(\mathbf{r}')\frac{1}{|\mathbf{r}-\mathbf{r}'|}\hat{\psi}_j(\mathbf{r}')\hat{\psi}_i(\mathbf{r})d\mathbf{r}d\mathbf{r}', \tag{3.4}$$

and the time-dependent external potential [3, 4, 36]

$$\hat{V}(t) = \sum_i \int \hat{\psi}_i^*(\mathbf{r})v(\mathbf{r},t)\hat{\psi}_i(\mathbf{r})d\mathbf{r}. \tag{3.5}$$

The only condition for the single-particle potentials is, that they must be expandable into a Taylor series around a finite initial time t_0 with a radius of convergence greater than zero, i.e.,

$$v(\mathbf{r},t) = \sum_{k=0}^{\infty} \frac{1}{k!} v_k(\mathbf{r})(t-t_0)^k. \tag{3.6}$$

This includes the case of sudden switching, but excludes cases where the perturbation is switched on adiabatically from $t_0 = -\infty$. In addition, only densities $n(\mathbf{r},t)$ evolving from a fixed initial state $\Psi(t_0) = \Psi_0$ are investigated. According to Refs. [4] and [36] it is, furthermore, not necessary, that Ψ_0 is the ground state or any other eigenstate of the initial potential $v(\mathbf{r},t_0) = v_0$. Now, if there exist two potentials $v(\mathbf{r},t)$ and $v'(\mathbf{r},t)$ which differ by more than a time-dependent function and are, in addition, Taylor expandable around t_0, Runge and Gross [3] showed that two densities $n(\mathbf{r},t)$ and $n'(\mathbf{r},t)$ which evolve from a common initial state $\Psi_0 = \Psi(t_0)$ under the influence of $v(\mathbf{r},t)$ and $v'(\mathbf{r},t)$ are different [4, 36].

Due to the one-to-one correspondence between the time-dependent density $n(\mathbf{r},t)$ and the potential $v(\mathbf{r},t)$, the time-dependent wave function can be seen as functional of $n(\mathbf{r},t)$. Another important consequence of the Runge-Gross theorem is that the expectation value of a quantum mechanical operator $\hat{O}(t)$ is a unique functional of the time-dependent density [4]. Moreover, the time-dependent density as well as the current density of the electronic system can be calculated from the following set of equations [3, 4, 36]:

$$\begin{aligned} \frac{\partial}{\partial t} n(\mathbf{r},t) &= -\nabla \mathbf{j}(\mathbf{r},t) \\ \frac{\partial}{\partial t} \mathbf{j}(\mathbf{r},t) &= \mathbf{P}[n](\mathbf{r},t) \end{aligned} \tag{3.7}$$

The first equation is nothing else than the continuity equation. The second one is the equation of motion for the current-density operator, where the density functional $\mathbf{P}[n]$ is of the form [3]

$$\mathbf{P}[n](\mathbf{r},t) = -i\langle\Psi[n](t)|[\hat{\mathbf{j}}(\mathbf{r}),\hat{H}(t)]|\Psi[n](t)\rangle. \tag{3.8}$$

After proving the one-to-one mapping between the time-dependent density and the external potential, the next section will focus on the generalization of the Kohn-Sham equations by including time-dependence.

3.2 Time-dependent Kohn-Sham equations

From the Runge-Gross theorem follows that the quantum mechanical action integral [3, 4, 36]

$$A[n] = \int_{t_0}^{t_1} \langle\Psi[n](t)|i\frac{\partial}{\partial t} - \hat{H}(t)|\Psi[n](t)\rangle dt \tag{3.9}$$

is a functional of the time-dependent density $n(\mathbf{r},t)$. Runge and Gross suggested to rewrite it as [3, 4, 36]

$$A[n] = B[n] - \int_{t_0}^{t_1} dt \int d\mathbf{r}\; n(\mathbf{r},t)v(\mathbf{r},t), \tag{3.10}$$

where the density functional $B[n]$ is defined through

$$B[n] = \int_{t_0}^{t_1} \langle\Psi[n](t)|i\frac{\partial}{\partial t} - \hat{T} - \hat{U}|\Psi[n](t)\rangle dt. \tag{3.11}$$

Since the theorem of Runge and Gross [3] is also valid for $\hat{U} = 0$, the action integral for non-interacting electrons reads as [36]

$$A_s[n] = B_s[n] - \int_{t_0}^{t_1} dt \int d\mathbf{r}\; n(\mathbf{r},t)v(\mathbf{r},t) \tag{3.12}$$

with

$$B_s[n] = \int_{t_0}^{t_1} \langle\Phi[n](t)|i\frac{\partial}{\partial t} - \hat{T}|\Phi[n](t)\rangle dt. \tag{3.13}$$

Here, $\Phi[n](t)$ is a time-dependent Slater determinant and, like in the interacting case, a functional of the time-dependent density.

Now, the response of electrons to a time-dependent external potential is described by the solution of the time-dependent Schrödinger equation for the

initial condition $\Psi(t_0) = \Psi_0$. It is related to a stationary point of the action functional defined in Eq. (3.9) for the correct time-dependent density. Consequently, the exact density is obtained by solving the Euler equation for the action functional [3, 4, 36], i.e.,

$$\frac{\delta A[n]}{\delta n(\mathbf{r},t)} = 0. \tag{3.14}$$

These are the basic ingredients for the derivation of the time-dependent Kohn-Sham equations, which will be presented below following closely the formalism as given in the work of Runge and Gross [3] and in Refs. [4, 36].

Starting with a system of non-interacting electrons moving in an external potential $v_s(\mathbf{r},t)$ one assumes that this potential leads to the same time-dependent density as the interacting system. Consequently, the time-dependent density of the interacting system can be calculated by [4]

$$n(\mathbf{r},t) = \sum_n |\varphi_n(\mathbf{r},t)|^2, \tag{3.15}$$

where $\varphi_n(\mathbf{r},t)$ are the solutions of the time-dependent Kohn-Sham equations

$$i\frac{\partial}{\partial t}\varphi_n(\mathbf{r},t) = \left[-\frac{\nabla^2}{2} + v_s(\mathbf{r},t)\right]\varphi_n(\mathbf{r},t). \tag{3.16}$$

To find an expression for the effective single-particle potential $v_s(\mathbf{r},t)$, the non-interacting and interacting many-particle system are linked. For this purpose, it is favorable to express the action integral defined in Eq. (3.10) by [36]

$$\begin{aligned} A[n] &= B_s[n] - \int_{t_0}^{t_1} dt \int d\mathbf{r}\; n(\mathbf{r},t)v(\mathbf{r},t) \\ &\quad -\frac{1}{2}\int_{t_0}^{t_1} dt \int d\mathbf{r} \int d\mathbf{r}'\; \frac{n(\mathbf{r},t)n(\mathbf{r}',t)}{|\mathbf{r}-\mathbf{r}'|} - A_{xc}[n]. \end{aligned} \tag{3.17}$$

A comparison of Eqs. (3.17) and (3.10) leads to the definition of the xc part of the action integral as

$$A_{xc}[n] = B_s[n] - \frac{1}{2}\int_{t_0}^{t_1} dt \int d\mathbf{r} \int d\mathbf{r}'\; \frac{n(\mathbf{r},t)n(\mathbf{r}',t)}{|\mathbf{r}-\mathbf{r}'|} - B[n]. \tag{3.18}$$

By inserting (3.17) into Eq. (3.14) one obtains [36]

$$\frac{\delta B_s[n]}{\delta n(\mathbf{r},t)} - \left[v(\mathbf{r},t) + \int d\mathbf{r}'\; \frac{n(\mathbf{r}',t)}{|\mathbf{r}-\mathbf{r}'|} + \frac{\delta A_{xc}[n]}{\delta n(\mathbf{r},t)}\right] = 0, \tag{3.19}$$

which is the Euler equation for an independent-particle system under the influence of the effective local and time-dependent single-particle potential

$$v_s(\mathbf{r},t) = v(\mathbf{r},t) + \int d\mathbf{r}' \, \frac{n(\mathbf{r}',t)}{|\mathbf{r}-\mathbf{r}'|} + \frac{\delta A_{xc}[n]}{\delta n(\mathbf{r},t)}. \tag{3.20}$$

It consists of the time-dependent external potential, the Hartree potential and the xc potential expressed as

$$v_{xc}(\mathbf{r},t) = \frac{\delta A_{xc}[n]}{\delta n(\mathbf{r},t)}. \tag{3.21}$$

As in the static case, proper approximations are needed for the xc potential [3, 4, 36].

3.3 Linear density response within TDDFT

When studying optical properties of many-body systems, one is interested in excitation energies. The excitation energies of a system correspond to the poles of the exact density-density response function [14, 33, 35]. If the external perturbation is weak enough, such as in case of light, the response of the system can be treated within perturbation theory. In case of the linear density response, the response of an interacting many-electron system to a time-dependent electric field is investigated to first order in the perturbation. This leads to the time-dependent Kohn-Sham equations for the linear density response. In addition, a relationship between the exact density-density response function and the Kohn-Sham response function of a system of non-interacting electrons can be derived. The underlying formalism is given below, following closely Refs. [4, 33, 36].

The starting point is a many-electron system in its ground state, described by the time-independent external potential $v_0(\mathbf{r})$. Thus, the corresponding initial density $n_0(\mathbf{r})$ can be obtained within static DFT by solving the Kohn-Sham equations given in Eq. (2.14). At t_0, a time-dependent perturbation $v_1(\mathbf{r},t)$ is switched on, resulting in a modified external potential [4, 33, 36]

$$v_{ext}(\mathbf{r},t) = v_0(\mathbf{r}) + v_1(\mathbf{r},t), \tag{3.22}$$

for $t \geq t_0$. Since the initial ground state is a unique functional of the initial ground-state density $n_0(\mathbf{r})$, the time-dependent density can be written as functional of v_{ext} without additional dependence on the initial many-body state, i.e., $n(\mathbf{r},t) = n[v_{ext}](\mathbf{r},t)$. According to the theorem of Runge and Gross [3] it is possible to invert this relationship leading to $v_{ext}(\mathbf{r},t) = v_{ext}[n](\mathbf{r},t)$. The

same arguments hold for the corresponding system of non-interacting particles moving in an effective potential $v_s(\mathbf{r},t)$. Consequently, the relationship $v_s(\mathbf{r},t) = v_s[n](\mathbf{r},t)$ for the single-particle potential v_s, defined by Eqs. (3.20) and (3.21), is obtained by inverting the functional $n(\mathbf{r},t) = n[v_s](\mathbf{r},t)$ [4,33].

If the external perturbation is small enough, the time-dependent density of the many-electron system can be expanded into a Taylor series. The density response $n_1(\mathbf{r},t)$ to first order in $v_1(\mathbf{r},t)$ is then given by [4,33,36]

$$n_1(\mathbf{r},t) = \int dt' \int d\mathbf{r}' \; \chi(\mathbf{r},t;\mathbf{r}',t') v_1(\mathbf{r}',t'), \tag{3.23}$$

with the density-density response function $\chi(\mathbf{r},t;\mathbf{r}',t')$ defined by

$$\chi(\mathbf{r},t;\mathbf{r}',t') = \left.\frac{\delta n[v_{ext}](\mathbf{r},t)}{\delta v_{ext}(\mathbf{r}',t')}\right|_{v_0}. \tag{3.24}$$

Petersilka, Grossmann, and Gross [33] showed, that there exists an alternative way to calculate the linear density response of the system,

$$n_1(\mathbf{r},t) = \int dt' \int d\mathbf{r}' \; \chi_s(\mathbf{r},t;\mathbf{r}',t') v_{s,1}(\mathbf{r}',t'), \tag{3.25}$$

with the help of the Kohn-Sham response function

$$\chi_s(\mathbf{r},t;\mathbf{r}',t') = \left.\frac{\delta n[v_s](\mathbf{r},t)}{\delta v_s(\mathbf{r}',t')}\right|_{v_s[n_0]} \tag{3.26}$$

of the non-interacting system together with some effective perturbation of the form [4,33,36]

$$v_{s,1}(\mathbf{r},t) = v_1(\mathbf{r},t) + \int d\mathbf{r}' \; \frac{n_1(\mathbf{r}',t)}{|\mathbf{r}-\mathbf{r}'|} + \int d\mathbf{r}' \int dt' \; f_{xc}[n_0](\mathbf{r},t;\mathbf{r}',t') n_1(\mathbf{r}',t'). \tag{3.27}$$

Here, f_{xc} denotes the time-dependent xc kernel defined by [4,33,36]

$$f_{xc}[n_0](\mathbf{r},t;\mathbf{r}',t') = \left.\frac{\delta v_{xc}[n](\mathbf{r},t)}{\delta n(\mathbf{r}',t')}\right|_{n_0}, \tag{3.28}$$

which includes all xc effects to first order in the perturbation. Eqs. (3.25) and (3.27) are referred to as time-dependent Kohn-Sham equations for the linear density response [4,33,36].

The density-density response functions for interacting and non-interacting particles can be linked by evaluating the right hand side of Eq. (3.24) and

using (3.26). After some straightforward analysis, one arrives at a Dyson-equation like relationship [4, 33]

$$\chi(\mathbf{r},t;\mathbf{r}',t') = \chi_s(\mathbf{r},t;\mathbf{r}',t') + \int d\mathbf{x} \int d\tau \int d\mathbf{x}' \int d\tau' \; \chi_s(\mathbf{r},t;\mathbf{x},\tau) \times \left[\frac{\delta(\tau-\tau')}{|\mathbf{x}-\mathbf{x}'|} + f_{xc}[n_0](\mathbf{x},\tau;\mathbf{x}',\tau')\right] \chi(\mathbf{x}',\tau';\mathbf{r}',t'). \quad (3.29)$$

A partial Fourier transform with respect to time finally results in [34]

$$\chi(\mathbf{r},\mathbf{r}';\omega) = \chi_s(\mathbf{r},\mathbf{r}';\omega) + \int d\mathbf{x} \int d\mathbf{x}' \; \chi_s(\mathbf{r},\mathbf{x};\omega) \times \left[\frac{1}{|\mathbf{x}-\mathbf{x}'|} + f_{xc}[n_0](\mathbf{x},\mathbf{x}';\omega)\right] \chi(\mathbf{x}',\mathbf{r}';\omega), \quad (3.30)$$

where the Kohn-Sham response function can be calculated with the help of the Kohn-Sham orbitals obtained from static DFT according to [4, 33, 36]

$$\chi_s(\mathbf{r},\mathbf{r}';\omega) = \sum_{ij} (f_j - f_i) \frac{\phi_j^*(\mathbf{r})\phi_i(\mathbf{r})\phi_i^*(\mathbf{r}')\phi_j(\mathbf{r}')}{\omega - (\epsilon_i - \epsilon_j)}. \quad (3.31)$$

Here, f_i and f_j denote the occupation numbers, ω includes a small imaginary part, i.e., $\omega = \omega' + i\delta$, and the sum over occupied and empty states runs over both spin directions. What remains is to find proper approximate expressions for the xc kernel $f_{xc}(\mathbf{r},t;\mathbf{r}',t')$.

3.4 Exchange-correlation kernel f_{xc}

As already pointed out above, the time-dependent xc kernel includes all xc effects of the response to linear order in the perturbation. It is possible to derive an exact expression for f_{xc} with the help of Eqs. (3.23), (3.25), and (3.27), resulting in [4]

$$f_{xc}[n_0](\mathbf{r},t;\mathbf{r}',t') = \chi_s^{-1}[n_0](\mathbf{r},t;\mathbf{r}',t') - \chi^{-1}[n_0](\mathbf{r},t;\mathbf{r}',t') - \frac{\delta(t-t')}{|\mathbf{r}-\mathbf{r}'|}. \quad (3.32)$$

The inverse response operators for the interacting and non-interacting system are denoted by χ^{-1} and χ_s^{-1}, respectively.

Due to the principle of causality, the density-response functions $\chi(\mathbf{r},t;\mathbf{r}',t')$ and $\chi_s(\mathbf{r},t;\mathbf{r}',t')$ as well as the corresponding inverse response operators $\chi^{-1}(\mathbf{r},t;\mathbf{r}',t')$ and $\chi_s^{-1}(\mathbf{r},t;\mathbf{r}',t')$ must vanish if $t' > t$. As a consequence, $f_{xc}(\mathbf{r},t;\mathbf{r}',t')$ must be zero for $t' > t$ which implies that f_{xc} is not symmetric

under the interchange of $(\mathbf{r}, t)$ and $(\mathbf{r}', t')$. By combining Eqs. (3.21) and (3.28) one, in addition, finds that the xc kernel can be obtained as second functional derivative $\delta^2 A_{xc}[n]/[\delta n(\mathbf{r}, t)\delta n(\mathbf{r}', t')]$ of the xc part of the action functional. This expression is, however, symmetric under the exchange of $(\mathbf{r}, t)$ and $(\mathbf{r}', t')$, which is in contradiction with the findings above calling for a causal structure of f_{xc} [4, 34–36].

This paradox was solved by van Leeuwen [35] in 2001 who defined a new action functional adopting the time contour method of Keldysh [37], where the physical time is parameterized by a so-called pseudotime. The response functions are derived as functional derivatives of the modified action functional and are symmetric in the pseudotime. By the back-transformation to physical time they finally become retarded [34, 35].

In general, the task is to find proper approximations for the xc kernel. Expressions for f_{xc} are given, for example, in Refs. [34, 38–44]. In the following, the two simplest forms of the xc kernel are presented. Within the random-phase approximation (RPA), neglecting xc effects completely, the xc kernel is simply set to zero, i.e.,

$$f_{xc}^{RPA} = 0. \tag{3.33}$$

In case of the adiabatic local-density approximation (ALDA), the form of the LDA within static DFT is taken and generalized by adopting a time-dependent density. The xc potential then reads as [4]

$$v_{xc}^{ALDA}[n](\mathbf{r}, t) = v_{xc}^{hom}(n(\mathbf{r}, t)) = \frac{d}{d\rho}\left(\rho\epsilon_{xc}^{hom}(\rho)\right)\Big|_{\rho=n(\mathbf{r},t)}, \tag{3.34}$$

where ϵ_{xc}^{hom} denotes the xc energy per particle of the homogeneous electron gas. From Eqs. (3.34) and (3.28) follows that f_{xc}^{ALDA} is given by [4, 36]

$$f_{xc}^{ALDA}[n_0](\mathbf{r}, t; \mathbf{r}', t') = \delta(t - t')\delta(\mathbf{r} - \mathbf{r}')\frac{d^2}{d\rho^2}\left(\rho\epsilon_{xc}^{hom}(\rho)\right)\Big|_{\rho=n_0(\mathbf{r})}. \tag{3.35}$$

After performing a Fourier transformation it finally reads

$$f_{xc}^{ALDA}[n_0](\mathbf{r}, \mathbf{r}'; \omega) = \delta(\mathbf{r} - \mathbf{r}')\frac{d^2}{d\rho^2}\left(\rho\epsilon_{xc}^{hom}(\rho)\right)\Big|_{\rho=n_0(\mathbf{r})}, \tag{3.36}$$

being completely frequency independent. Gross and Kohn [45] generalized the ALDA kernel including some frequency dependence. They Fourier transformed the xc kernel $f_{xc}^{hom}(n_0(\mathbf{r}), |\mathbf{r} - \mathbf{r}'|; \omega)$ of the homogeneous electron gas and used the $q = 0$ component. The resulting xc kernel is of the form [4, 36, 45]

$$f_{xc}^{LDA,GK}[n_0](\mathbf{r}, \mathbf{r}'; \omega) = \delta(\mathbf{r} - \mathbf{r}')f_{xc}^{hom}(n_0(\mathbf{r}), q = 0; \omega). \tag{3.37}$$

As in the static case, ALDA is expected to work well for systems of slowly varying densities both in time and space. After this short overview dealing with the framework of TDDFT, the next Chapter will focus on the treatment of linear optical response within TDDFT.

4 Linear optical response

In a material, which is exposed to some kind of time-dependent electromagnetic perturbation, forces are acting on the charges inside. Consequently, they rearrange, thereby causing a polarization of the system. The total potential V, measured in experiment, is the sum of the external potential V_{ext} related to the perturbation and the induced potential V_{ind} as a result of the polarization. With the help of the dielectric tensor, it can be linked to the external potential according to [46]

$$V_{ext} = \varepsilon V. \tag{4.1}$$

If the optical properties of the system are studied in the linear regime, the response of the system is considered to first order in the perturbation. Expressions for the complex dielectric function were derived, for example, within many-body perturbation theory by Nozières and Pines [47] or by adopting the self-consistent field method by Ehrenreich and Cohen [48]. It was shown that, in many cases, these two approaches are equivalent within RPA [48]. Adler [49] and Wiser [50] generalized the expressions given by Ehrenreich and Cohen for the longitudional dielectric response introducing local-field effects.

The aim of this Chapter is to present the major steps in the derivation of the longitudinal dielectric constant of a periodic crystal including and neglecting local-field effects as given by Ehrenreich and Cohen [48], Adler [49], and Wiser [50]. Moreover, the expressions for the real and imaginary part of the complex dielectric function in the long-wavelength limit are given. Finally, the treatment of linear optical properties within the framework of TDDFT is discussed. For this purpose, we follow closely the works of Ehrenreich and Cohen [48], Adler [49], Wiser [50], as well as Refs. [51, 52].

4.1 Linearized Liouville equation

The response of any electron of the system to a self-consistent potential is given by the Liouville equation

$$i\frac{\partial \rho}{\partial t} = [H, \rho]\,, \tag{4.2}$$

which describes the time evolution of the single-particle density matrix ρ. In a first step, the single-particle Hamiltonian H is decomposed into two parts,

$$H = H_0 + V(\mathbf{r}, t). \tag{4.3}$$

H_0 is the time-independent Hamiltonian of the unperturbed system consisting of the kinetic energy term and the periodic lattice potential. It fulfills the single-particle Schrödinger equation $H_0|\mathbf{k}, l\rangle = E_{\mathbf{k},l}|\mathbf{k}, l\rangle$, with the Bloch functions $|\mathbf{k}, l\rangle = \frac{1}{\sqrt{\Omega}} e^{i\mathbf{k}\cdot\mathbf{r}} u_{\mathbf{k}l}(\mathbf{r})$ as eigenfunctions. Ω stands for the crystal volume and $u_{\mathbf{k}l}(\mathbf{r})$ is a cell-periodic function. The self-consistent potential $V(\mathbf{r}, t)$, corresponding to the perturbation, can be written as [48, 50, 51]

$$V(\mathbf{r}, t) = V_{ext}(\mathbf{r}, t) + V_{ind}(\mathbf{r}, t). \tag{4.4}$$

Now, a decomposition similar to (4.3) is adopted for the density matrix, i.e.,

$$\rho = \rho_0 + \rho_1, \tag{4.5}$$

with ρ_1 corresponding to the perturbation, and ρ_0 being the unperturbed density matrix. The latter has the property $\rho_0|\mathbf{k}, l\rangle = f_0(E_{\mathbf{k},l})|\mathbf{k}, l\rangle$, where $f_0(E_{\mathbf{k},l})$ is the Fermi-Dirac distribution function.

The linearized form of the Liouville equation is obtained by inserting (4.3) and (4.5) into Eq. (4.2) and neglecting terms of quadratic order in the perturbation. Consequently, it has the form

$$i\frac{\partial \rho_1}{\partial t} = [H_0, \rho_1] + [V, \rho_0]\,. \tag{4.6}$$

Evaluating this expression between the Bloch states $\langle \mathbf{k}, l|$ and $|\mathbf{k}+\mathbf{q}, l'\rangle$ results in [48]

$$\begin{aligned} i\frac{\partial}{\partial t}\langle \mathbf{k}, l|\rho_1|\mathbf{k}+\mathbf{q}, l'\rangle &= (E_{\mathbf{k},l} - E_{\mathbf{k}+\mathbf{q},l'})\,\langle \mathbf{k}, l|\rho_1|\mathbf{k}+\mathbf{q}, l'\rangle \\ &\quad + [f_0\,(E_{\mathbf{k}+\mathbf{q},l'}) - f_0\,(E_{\mathbf{k},l})]\,\langle \mathbf{k}, l|V(\mathbf{r}, t)|\mathbf{k}+\mathbf{q}, l'\rangle. \end{aligned} \tag{4.7}$$

In order to solve Eq. (4.7) it is assumed that the external perturbation, as well as all other quantities, reveal the same time-dependence of $e^{i\omega t}$. Here,

$\omega = \omega' - i\alpha$ with $\alpha \to 0^+$, corresponding to an adiabatic switching on of the perturbation. In addition, a Fourier analysis is performed for the total potential,

$$V(\mathbf{r}) = \sum_{\mathbf{q},\mathbf{G}} V(\mathbf{q},\mathbf{G}) e^{-i(\mathbf{q}+\mathbf{G})\cdot\mathbf{r}}, \tag{4.8}$$

where the wavevector $\mathbf{q}$ is restricted to the first Brillouin zone and $\mathbf{G}$ represents a reciprocal lattice vector. For $\mathbf{G} \neq 0$ it contains terms which are rapidly varying over the unit cell corresponding to so-called local-field effects [49, 50].

Evaluating the potential $V(\mathbf{r})$ given in Eq. (4.8) between the Bloch states $\langle \mathbf{k}, l|$ and $|\mathbf{k}+\mathbf{q}, l'\rangle$ leads to

$$\langle \mathbf{k}, l|V(\mathbf{r})|\mathbf{k}+\mathbf{q}, l'\rangle = \sum_{\mathbf{G}} V(\mathbf{q},\mathbf{G}) M^{\mathbf{G}}_{l,l'}(\mathbf{k},\mathbf{q}), \tag{4.9}$$

with the matrix element $M^{\mathbf{G}}_{l,l'}(\mathbf{k},\mathbf{q})$ defined by

$$M^{\mathbf{G}}_{l,l'}(\mathbf{k},\mathbf{q}) = \langle \mathbf{k}, l|e^{-i(\mathbf{q}+\mathbf{G})\cdot\mathbf{r}}|\mathbf{k}+\mathbf{q}, l'\rangle. \tag{4.10}$$

Now, (4.9) is inserted in Eq. (4.7), and after some straight-forward analysis one arrives at [50]

$$\langle \mathbf{k}, l|\rho_1|\mathbf{k}+\mathbf{q}, l'\rangle = \frac{f_0\left(E_{\mathbf{k}+\mathbf{q},l'}\right) - f_0\left(E_{\mathbf{k},l}\right)}{E_{\mathbf{k}+\mathbf{q},l'} - E_{\mathbf{k},l} - \omega} \sum_{\mathbf{G}} M^{\mathbf{G}}_{l,l'}(\mathbf{k},\mathbf{q}) V(\mathbf{q},\mathbf{G}). \tag{4.11}$$

This relationship is used in the following section to derive an expression for the longitudinal dielectric tensor.

4.2 Longitudinal dielectric response

With the help of the Poisson equation

$$\nabla^2 V_{ind} = -4\pi n(\mathbf{r}) \tag{4.12}$$

the induced electron density $n(\mathbf{r}) = \mathrm{Tr}\left\{\delta(\mathbf{r}-\mathbf{r_e})\cdot\rho_1\right\}$ is linked to the screening potential. Transforming Eq. (4.12) to reciprocal space and using the relation (4.11) leads to [49]

$$\begin{aligned} V_{ind}(\mathbf{q},\mathbf{G}) \;=\; & \frac{4\pi}{|\mathbf{q}+\mathbf{G}|^2\Omega} \sum_{\mathbf{G}'} \sum_{\mathbf{k}ll'} \frac{f_0\left(E_{\mathbf{k}+\mathbf{q},l'}\right) - f_0\left(E_{\mathbf{k},l}\right)}{E_{\mathbf{k}+\mathbf{q},l'} - E_{\mathbf{k},l} - \omega} \\ & \times \left[M^{\mathbf{G}}_{l,l'}(\mathbf{k},\mathbf{q})\right]^* M^{\mathbf{G}'}_{l,l'}(\mathbf{k},\mathbf{q}) V(\mathbf{q},\mathbf{G}'). \end{aligned} \tag{4.13}$$

Combining Eqs. (4.1) and (4.4) results in a relationship for the dielectric tensor. By inserting (4.13), the Fourier components $\varepsilon_{\mathbf{GG'}}(\mathbf{q},\omega)$ of the microscopic longitudinal dielectric tensor can be written as [52]

$$\varepsilon_{\mathbf{GG'}}(\mathbf{q},\omega) = \delta_{\mathbf{GG'}} - v_{\mathbf{G}}(\mathbf{q}) P^0_{\mathbf{GG'}}(\mathbf{q},\omega) \tag{4.14}$$

where

$$v_{\mathbf{G}}(\mathbf{q}) = \frac{4\pi}{|\mathbf{q}+\mathbf{G}|^2} \tag{4.15}$$

is the Coulomb potential and

$$P^0_{\mathbf{GG'}}(\mathbf{q},\omega) = \frac{1}{\Omega}\sum_{\mathbf{k}ll'} \frac{f_0\left(E_{\mathbf{k+q},l'}\right) - f_0\left(E_{\mathbf{k},l}\right)}{E_{\mathbf{k+q},l'} - E_{\mathbf{k},l} - \omega} \left[M^{\mathbf{G}}_{l,l'}(\mathbf{k},\mathbf{q})\right]^* M^{\mathbf{G'}}_{l,l'}(\mathbf{k},\mathbf{q}) \tag{4.16}$$

denotes the irreducible polarizability within RPA.

The quantity that can be obtained from experiment is the macroscopic dielectric function. As pointed out, for example, by Wiser [50], every macroscopic quantity can easily be obtained from the corresponding microscopic quantity by taking the average value over the unit cell. Using this information, it is possible to derive a relationship between the microscopic and macroscopic dielectric function of the form

$$\varepsilon_M(\mathbf{q},\omega) = \frac{1}{\varepsilon^{-1}_{00}(\mathbf{q},\omega)}. \tag{4.17}$$

In practice, this means that it is necessary to calculate the components of the microscopic dielectric tensor, then to determine the inverse of the dielectric tensor before taking the (0,0)-component of the inverse dielectric tensor needed in the calculation of ε_M. This procedure is, however, a time-consuming task. A simplification is achieved by neglecting local-field effects. In this case, the macroscopic dielectric function is just the (0,0)-component of the microscopic dielectric function [52], i.e.,

$$\varepsilon^{NLF}_M(\mathbf{q},\omega) = \varepsilon_{00}(\mathbf{q},\omega) = 1 - v(\mathbf{q}) P^0_{00}(\mathbf{q},\omega) \tag{4.18}$$

or [48, 49]

$$\varepsilon^{NLF}_M(\mathbf{q},\omega) = 1 - \frac{4\pi}{|\mathbf{q}|^2\Omega}\sum_{\mathbf{k}ll'} \frac{f_0\left(E_{\mathbf{k+q},l'}\right) - f_0\left(E_{\mathbf{k},l}\right)}{E_{\mathbf{k+q},l'} - E_{\mathbf{k},l} - \omega} |M^{\mathbf{0}}_{l,l'}(\mathbf{k},\mathbf{q})|^2. \tag{4.19}$$

4.3 The limit q → 0

When studying optical properties, the perturbation of the system one has to deal with, is caused by light. Since the typical wavelength of light is much

longer than that of the electrons in the material, one can restrict oneself to the long-wavelenght limit, or equivalently, $\mathbf{q} \to 0$. Within $\mathbf{k} \cdot \mathbf{p}$ perturbation theory, the matrix element $M^0_{l,l'}(\mathbf{k}, \mathbf{q})$ for small wavevectors $\mathbf{q}$ is given by [52]

$$M^0_{l,l'}(\mathbf{k}, 0) = \delta_{l,l'} + (1 - \delta_{l,l'}) \frac{\hbar}{m} \frac{\mathbf{p}_{l,l',\mathbf{k}}}{E_{\mathbf{k},l'} - E_{\mathbf{k},l}} \cdot \mathbf{q}. \tag{4.20}$$

The expression for the macroscopic dielectric function can be divided into contributions arising from intraband and interband transitions [52]

$$\varepsilon^{NLF}_M(0, \omega) = \varepsilon^{intra}(0, \omega) + \varepsilon^{inter}(0, \omega). \tag{4.21}$$

The intraband part $\varepsilon^{intra}(0, \omega)$ contains only terms with $l = l'$ and has the form

$$\begin{aligned} \varepsilon^{intra}(0, \omega) &= 1 - \lim_{\mathbf{q}\to 0} \frac{4\pi e^2}{|\mathbf{q}|^2 \Omega} \sum_{\mathbf{k}l} \frac{f_0\left(E_{\mathbf{k}+\mathbf{q},l}\right) - f_0\left(E_{\mathbf{k},l}\right)}{E_{\mathbf{k}+\mathbf{q},l} - E_{\mathbf{k},l} - \omega} |M^{\mathbf{0}}_{l,l}(\mathbf{k}, \mathbf{q})|^2 \\ &= 1 - \lim_{\mathbf{q}\to 0} \frac{4\pi\hbar^2 e^2}{\Omega m^2 \omega^2} \sum_{\mathbf{k}l} \left(-\frac{\partial f_0}{\partial E} \right)_{E_{\mathbf{k},l}} \left(\mathbf{p}_{l,l,\mathbf{k}} \cdot \frac{\mathbf{q}}{|\mathbf{q}|} \right)^2 . \end{aligned} \tag{4.22}$$

For the interband contribution only terms with $l \neq l'$ are taken into account, leading to

$$\begin{aligned} \varepsilon^{inter}(0, \omega) &= - \lim_{\mathbf{q}\to 0} \frac{4\pi e^2}{|\mathbf{q}|^2 \Omega} \sum_{\substack{\mathbf{k}ll' \\ l\neq l'}} \frac{f_0\left(E_{\mathbf{k}+\mathbf{q},l'}\right) - f_0\left(E_{\mathbf{k},l}\right)}{E_{\mathbf{k}+\mathbf{q},l'} - E_{\mathbf{k},l} - \omega} |M^{\mathbf{0}}_{l,l'}(\mathbf{k}, \mathbf{q})|^2 \\ &= - \lim_{\mathbf{q}\to 0} \frac{4\pi\hbar^2 e^2}{\Omega m^2} \sum_{\mathbf{k}cv} \frac{(\mathbf{p}_{c,v,\mathbf{k}} \cdot \mathbf{q}/|\mathbf{q}|)^2}{(E_{\mathbf{k},c} - E_{\mathbf{k},v} - \omega)(E_{\mathbf{k},c} - E_{\mathbf{k},v})^2}. \end{aligned} \tag{4.23}$$

Here, c refers to empty and v to occupied states, respectively. Eqs. (4.22) and (4.23) reveal, that the limit for $\mathbf{q} \to 0$ depends on the direction of $\mathbf{q}$. Consequently, the dielectric function in the limit of long wavelengths is represented by a three-dimensional tensor. Depending on the symmetry of the crystal, up to six independent components occur [52].

At this point one can introduce DFT quantities in the calculation of the complex dielectric function. In this case, the momentum matrix elements $p_{i,n',n,\mathbf{k}}$ are evaluated with the help of Kohn-Sham orbitals and Kohn-Sham eigenvalues $\epsilon_{n\mathbf{k}}$ are used. The imaginary part of the interband contribution to the dielectric function is obtained by taking the imaginary part of Eq. (4.23), leading to [52]

$$\mathrm{Im}\, \varepsilon^{inter}_{ij}(\omega) = \frac{\hbar^2 e^2}{\pi m^2 \omega^2} \sum_{nn'} \int d\mathbf{k}\, p_{i,n',n,\mathbf{k}}\, p_{j,n',n,\mathbf{k}} (f_0(\epsilon_{n\mathbf{k}}) - f_0(\epsilon_{n'\mathbf{k}})) \delta(\epsilon_{n'\mathbf{k}} - \epsilon_{n\mathbf{k}} - \omega). \tag{4.24}$$

The real part is obtained by a Kramers-Kronig transformation. For the intra-band part, a Drude-like shape of the form [52]

$$\mathrm{Im}\,\varepsilon_{ij}^{intra}(\omega) = \frac{\Gamma\omega_{pl,ij}^2}{\omega(\omega^2+\Gamma^2)} \tag{4.25}$$

$$\mathrm{Re}\,\varepsilon_{ij}^{intra}(\omega) = 1 - \frac{\omega_{pl,ij}^2}{\omega^2+\Gamma^2} \tag{4.26}$$

is adopted. Here, Γ stands for a lifetime-broadening and $\omega_{pl,ij}$ is the plasma frequency calculated according to

$$\omega_{pl,ij}^2 = \frac{\hbar^2 e^2}{\pi m^2}\sum_n \int d\mathbf{k}\; p_{i,n,n,\mathbf{k}}\; p_{j,n,n,\mathbf{k}}\; \delta(\epsilon_{n\mathbf{k}} - \epsilon_F). \tag{4.27}$$

ϵ_F denotes the Fermi energy. Finally, the electron-energy loss function is calculated from

$$L(\omega) = -\mathrm{Im}\left(\frac{1}{\varepsilon(\omega)}\right), \tag{4.28}$$

and the normal-incidence reflectivity is obtained with the help of

$$R(\omega) = \frac{(n(\omega)-1)^2+\kappa(\omega)^2}{(n(\omega)+1)^2+\kappa(\omega)^2}. \tag{4.29}$$

Here, $n(\omega)$ and $\kappa(\omega)$ represent the refractive index and extinction coefficient, respectively.

4.4 Linear optical response within TDDFT

The calculation of the linear optical response within TDDFT follows the perturbative approach as discussed in Section 3.3. At first, a Fourier transform with respect to space is performed for the Kohn-Sham response function χ^{KS}, given in Eq. (3.31), leading to

$$\chi_{\mathbf{G}\mathbf{G}'}^{KS}(\mathbf{q},\omega) = \frac{1}{\Omega}\sum_{\mathbf{k}ll'} \frac{f_0\left(\epsilon_{\mathbf{k}+\mathbf{q},l'}\right) - f_0\left(\epsilon_{\mathbf{k},l}\right)}{\epsilon_{\mathbf{k}+\mathbf{q},l'} - \epsilon_{\mathbf{k},l} - \omega} \left[M_{l,l'}^{\mathbf{G}}(\mathbf{k},\mathbf{q})\right]^* M_{l,l'}^{\mathbf{G}'}(\mathbf{k},\mathbf{q}). \tag{4.30}$$

In the evaluation of the matrix elements, the Kohn-Sham orbitals as obtained from static DFT are adopted. The next step involves the calculation of the density-density response function χ of the interacting many-particle system from the Kohn-Sham response function χ^{KS} given in Eq. (4.30) with the help

of Eq. (3.30). After performing a Fourier transform with respect to space for the latter, the $(\mathbf{G}, \mathbf{G}')$-Fourier component is given by [53]

$$\begin{aligned}\chi_{\mathbf{G}\mathbf{G}'}(\mathbf{q},\omega) &= \chi^{KS}_{\mathbf{G}\mathbf{G}'}(\mathbf{q},\omega) \\ &\quad + \sum_{\mathbf{G_1},\mathbf{G_2}} \chi^{KS}_{\mathbf{G}\mathbf{G_1}}(\mathbf{q},\omega)\left[v_{\mathbf{G_1}}(\mathbf{q})\delta_{G_1G_2} + f^{xc}_{\mathbf{G_1}\mathbf{G_2}}(\mathbf{q},\omega)\right]\chi_{\mathbf{G_2}\mathbf{G}'}(\mathbf{q},\omega).\end{aligned} \tag{4.31}$$

In this work, the RPA and the ALDA, as defined in Eqs. (3.33) and (3.34), are used for the xc kernel, respectively. The inverse of the dielectric tensor is connected to the density-density response function via [34]

$$\varepsilon^{-1}(\mathbf{r},\mathbf{r}',\omega) = \delta(\mathbf{r}-\mathbf{r}') + \int d\mathbf{r}'' v(\mathbf{r}-\mathbf{r}'')\chi(\mathbf{r}'',\mathbf{r}',\omega). \tag{4.32}$$

Fourier transform with respect to space yields

$$\varepsilon^{-1}_{\mathbf{G}\mathbf{G}'}(\mathbf{q},\omega) = \delta_{\mathbf{G}\mathbf{G}'} + v_{\mathbf{G}}(\mathbf{q})\chi_{\mathbf{G}\mathbf{G}'}(\mathbf{q},\omega). \tag{4.33}$$

This relationship can be used to determine the macroscopic dielectric function including local-field effects from Eq. (4.17), while the macroscopic dielectric function neglecting local-field effects is given by Eq. (4.18). The irreducible polarizability P is related to the density-density response function by [34]

$$P = \chi - Pv\chi. \tag{4.34}$$

Finally, the electron-energy loss function can be calculated using (4.28). For details concerning the implementation of the formalism see Ref. [53].

5 Linearized augmented planewave method

The roots of the linearized augmented planewave (LAPW) method are found in 1937, where Slater [54] came up with a new approach for performing electronic-structure calculations known as augmented planewave (APW) method. Considering the fact that wave functions and potential are strongly varying close to the atomic nuclei, whereas they are smoother in the area in between, he suggested a decomposition of the unit cell into two different regions. These are the non-overlapping muffin-tin spheres centered at the atomic positions and the remaining part of the unit cell outside these spheres referred to as interstitial region. Within these areas, different basis functions were adopted, which match continuously at the sphere boundary [54].

Andersen [55] as well as Koelling and Arbman [56] took up the ideas of Slater and linearized the eigenvalue problem, resulting in the LAPW method. Nowadays, the LAPW method is considered the most accurate method to perform electronic-structure calculations within the framework of DFT.

In the following sections an overview of the LAPW method is given, and the basic concept of the APW+lo method [5] is summarized. Throughout this Chapter, we follow closely the formalism as outlined in the book by Singh [57] and Refs. [5, 55, 56, 58, 59].

5.1 LAPW basis functions

As pointed out above, the potential and the wave functions show a different behavior in the two regions of the unit cell. To account for this, appropriate basis functions are introduced. In the interstital region, wave functions and potential show only moderate variations. Thus, planewaves are used to describe the wave function in this part of the unit cell. They are of the form [56–59]

$$\phi_{\mathbf{k}+\mathbf{G}}(\mathbf{r}) = \frac{1}{\sqrt{\Omega}} e^{i(\mathbf{k}+\mathbf{G})\cdot\mathbf{r}}, \quad \mathbf{r} \in I. \tag{5.1}$$

Here, $\mathbf{G}$ is a reciprocal lattice vector. Close to the atomic nuclei, however, rapid oscillations of the wave functions occur. Consequently, atomic-like basis functions are the best choice inside the muffin-tin spheres. They read as [56–59]

$$\phi_{\mathbf{k}+\mathbf{G}}(\mathbf{S}_\alpha+\mathbf{r}) = \sum_{lm}[A^\alpha_{lm}(\mathbf{k}+\mathbf{G})u^\alpha_l(r,E_l)+B^\alpha_{lm}(\mathbf{k}+\mathbf{G})\dot{u}^\alpha_l(r,E_l)]Y_{lm}(\hat{\mathbf{r}}) \quad (5.2)$$

for $|\mathbf{r}| \leq R_\alpha$, where $\mathbf{S}_\alpha$ stands for the position of the atomic nucleus α, R_α is the radius of the muffin-tin sphere, and $Y_{lm}(\hat{\mathbf{r}})$ are spherical harmonics. The $u^\alpha_l(r,E_l)$ are radial functions fulfilling the radial Schrödinger equation

$$\left\{-\frac{d^2}{dr^2}+\frac{l(l+1)}{r^2}+V^\alpha(r)-E_l\right\}ru^\alpha_l(r,E_l)=0 \quad (5.3)$$

for given linearization energies E_l, with $V^\alpha(r)$ being the spherical part of the potential inside the atomic sphere α. $\dot{u}^\alpha_l(r,E_l)$ denote the corresponding energy derivatives satisfying

$$\left\{-\frac{d^2}{dr^2}+\frac{l(l+1)}{r^2}+V^\alpha(r)-E_l\right\}r\dot{u}^\alpha_l(r,E_l)=ru^\alpha_l(r,E_l). \quad (5.4)$$

The $u^\alpha_l(r,E_l)$ are normalized according to [56,57]

$$\int_0^{R_\alpha}[ru^\alpha_l(r,E_l)]^2dr=1 \quad (5.5)$$

and are orthogonal to $\dot{u}^\alpha_l(r,E_l)$, i.e.,

$$\int_0^{R_\alpha}r^2u^\alpha_l(r,E_l)\dot{u}^\alpha_l(r,E_l)dr=0. \quad (5.6)$$

Finally, the expansion coefficients $A^\alpha_{lm}(\mathbf{k}+\mathbf{G})$ and $B^\alpha_{lm}(\mathbf{k}+\mathbf{G})$ are determined by making the basis functions continuous in value and slope at the sphere boundary [56,57,59].

The wave functions are expanded within this LAPW basis, leading to a representation of $\Psi_{n\mathbf{k}}(\mathbf{r}\,)$ as [56,57,59]

$$\Psi_{n\mathbf{k}}(\mathbf{r}\,)=\sum_{\mathbf{G}}c_{n\mathbf{k}}(\mathbf{G})\phi_{\mathbf{k}+\mathbf{G}}(\mathbf{r}), \quad (5.7)$$

where $c_{n\mathbf{k}}(\mathbf{G})$ denote expansion coefficients. For $\phi_{\mathbf{k}+\mathbf{G}}(\mathbf{r})$ the expressions (5.1) and (5.2) are used in the interstitial region and inside the atomic spheres, respectively.

Different representations are also adopted for the potential and the charge density within the different regions of the unit cell. The valence charge density n_{val} is written as [57, 59]

$$n_{val}(\mathbf{r}) = \sum_{\mathbf{G}} n_{\mathbf{G}} e^{i\mathbf{G}\cdot\mathbf{r}} \qquad \mathbf{r} \in I \tag{5.8}$$

in the interstitial region, while a representation of the form

$$n_{val}(\mathbf{S}_\alpha + \mathbf{r}) = \sum_{lm} n^\alpha_{lm}(r) Y_{lm}(\hat{\mathbf{r}}) \qquad |\mathbf{r}| \leq R_\alpha \tag{5.9}$$

is used within the atomic spheres. In a similar manner, the effective potential V_{eff} is expanded as

$$V_{eff}(\mathbf{r}) = \sum_{\mathbf{G}} V_{\mathbf{G}} e^{i\mathbf{G}\cdot\mathbf{r}} \qquad \mathbf{r} \in I \tag{5.10}$$

and

$$V_{eff}(\mathbf{S}_\alpha + \mathbf{r}) = \sum_{lm} V^\alpha_{lm}(r) Y_{lm}(\hat{\mathbf{r}}) \qquad |\mathbf{r}| \leq R_\alpha. \tag{5.11}$$

After this overview of the major ideas of the LAPW method, the next section deals with an extension of the formalism needed for a proper description of semi-core states.

5.2 Local orbitals

By construction, the LAPW basis set, presented in the previous section, leads to an accurate description of the energy bands if the true band energies have values close to E_l for a given l. It turned out that it is reasonable to choose E_l close to the centre of the band. With this choice it is, however, not possible to achieve a proper description of all band states for a given l at the same time, especially if high-lying semi-core states or bands with an extremely large band width are present [57, 58].

One way out of this problem is the use of so-called local orbitals (LOs) originally proposed by Singh [58]. These are additional basis functions introduced inside the atomic spheres with a form similar to that of the atomic-like functions of the LAPW basis set [58, 59], i.e.,

$$\phi_{LO}(\mathbf{S}_\alpha + \mathbf{r}) = \sum_{lm} [\tilde{A}^\alpha_{lm} u^\alpha_l(r, E_l) + \tilde{B}^\alpha_{lm} \dot{u}^\alpha_l(r, E_l) + \tilde{C}^\alpha_{lm} u^\alpha_l(r, E_{lo})] Y_{lm}(\hat{\mathbf{r}}). \tag{5.12}$$

An additional radial function, denoted by $u_l^\alpha(r, E_{lo})$, is present in the expression for the LO. Here, the linearization energy E_{lo} refers to the semi-core states and the variational parameters $\tilde{A}_{lm}^\alpha$, $\tilde{B}_{lm}^\alpha$ and $\tilde{C}_{lm}^\alpha$ are determined by the conditions that the basis set must be normalized and that the LO must be zero in value and slope at the sphere boundary. Note that this strategy of including LOs for physically relevant states is not restricted to semi-core states. It can also be used to improve the description of conduction bands [57–59].

5.3 APW+lo method

Although the LAPW method has a lot of advantages compared to the original APW method, a larger basis set is required to obtain converged results. Sjöstedt, Nordström, and Singh [5] combined the advantages of both approaches resulting in a new powerful method for electronic-structure calculations known as the APW+lo method. The main idea behind is to increase the flexibility of an energy-independent APW basis by the inclusion of local orbitals inside the atomic spheres [5].

For this purpose, the basis set within the atomic spheres consists of energy-independent APW basis functions given by

$$\phi_{\mathbf{k}+\mathbf{G}}(\mathbf{S}_\alpha + \mathbf{r}) = \sum_{lm} A_{lm}^\alpha(\mathbf{k}+\mathbf{G}) u_l^\alpha(r, E_l) Y_{lm}(\hat{\mathbf{r}}) \tag{5.13}$$

and local orbitals of the form

$$\phi_{lo}(\mathbf{S}_\alpha + \mathbf{r}) = \sum_{lm} [\tilde{A}_{lm}^\alpha u_l^\alpha(r, E_l) + \tilde{B}_{lm}^\alpha \dot{u}_l^\alpha(r, E_l)] Y_{lm}(\hat{\mathbf{r}}), \tag{5.14}$$

with E_l standing for a fixed value of the linearization energy. The local orbitals are included for physically important l-values only and are totally confined within the atomic spheres. The coefficients $\tilde{A}_{lm}$ and $\tilde{B}_{lm}$ in (5.14) are determined by setting $\tilde{A}_{lm} = 1$ and calculating $\tilde{B}_{lm}$ such that the local orbital vanishes at the sphere boundary.

6 Treatment of relativistic effects

Relativistic effects play a central role in the description of the electronic structure and optical properties of heavy elements. Especially in the region close to the nuclei, the inclusion of relativistic corrections turns out to be crucial. In the WIEN2k code [6], which is based on the LAPW method described in Chapter 5, a relativistic treatment is achieved within the atomic spheres and neglected in the interstitial region. Inside the atomic spheres, the inclusion of relativistic effects differs for core and valence states. While for core states the Dirac equation is solved, valence states can be described on a scalar-relativistic level yielding sufficient accuracy if the impact of spin-orbit (SO) coupling is small. If necessary, SO effects are included on top of a scalar-relativistic calculation with the help of a second variational treatment.

The aim of this Chapter is to present the basic equations needed for a fully- and scalar-relativistic calculation, as well as the second variational procedure used to include SO interaction. Throughout this overview, we follow closely the formalism given by Koelling and Harmon [60], and in the book of Kübler [61]. In addition, the work of MacDonald, Pickett, and Koelling [62], as well as the books of Martin [14] and of Singh [57] were used. An informative summary can be found in the work by Novák [63].

6.1 Dirac equation

Within DFT, a fully-relativistic calculation of the electronic structure includes the solution of the Dirac equation, being the relativistic generalization of the Schrödinger equation. The Dirac equation in a Schrödinger-like form reads as

$$i\frac{\partial}{\partial t}\Psi = \hat{H}_{Dirac}\Psi, \tag{6.1}$$

where

$$\hat{H}_{Dirac} = c\boldsymbol{\alpha}\cdot\mathbf{p} + (\beta - 1)mc^2 + V(\mathbf{r}) \tag{6.2}$$

is the Dirac Hamiltonian, if the energies are measured relative to the rest mass energy. Here, $\mathbf{p}$ is the momentum operator, β has the form

$$\beta = \begin{pmatrix} \mathbb{1} & 0 \\ 0 & -\mathbb{1} \end{pmatrix}, \tag{6.3}$$

and the components α_i of the vector operator $\boldsymbol{\alpha}$ can be written according to

$$\alpha_i = \begin{pmatrix} 0 & \sigma_i \\ \sigma_i & 0 \end{pmatrix}, \tag{6.4}$$

with σ_i ($i = x, y, z$) representing the Pauli-spin matrices. The eigenvectors Ψ of the eigenvalue problem

$$\hat{H}_{Dirac}\Psi = \epsilon\Psi \tag{6.5}$$

are four-component functions which can be rewritten as

$$\Psi = \begin{pmatrix} \Phi \\ \chi \end{pmatrix}, \tag{6.6}$$

using the two-component functions Φ and χ. For electrons Φ is known as the large and χ as the small component of the wave function. By inserting the expressions (6.2) and (6.6) into Eq. (6.5), a set of coupled equations for the large and small component is obtained [61, 63]:

$$\begin{aligned} c(\boldsymbol{\sigma}\cdot\mathbf{p})\chi &= (\epsilon - V)\Phi \\ c(\boldsymbol{\sigma}\cdot\mathbf{p})\Phi &= (\epsilon - V + 2mc^2)\chi \end{aligned} \tag{6.7}$$

6.2 Dirac equation in a central field

In the presence of a spherically symmetric potential it is convenient to rewrite the four-component functions as [61]

$$\Psi = \begin{pmatrix} \Phi \\ \chi \end{pmatrix} = \begin{pmatrix} g(r)\,\mathcal{Y}^{j_z}_{j\ell} \\ if(r)\,\mathcal{Y}^{j_z}_{j\ell'} \end{pmatrix}. \tag{6.8}$$

Here, $g(r)$ and $f(r)$ denote radial functions, while the angular-spin functions $\mathcal{Y}^{j_z}_{j\ell}$ are r-independent. The latter are obtained by combining the Pauli spinor with the spherical harmonics and represent eigenfunctions of $\mathbf{J}^2$, J_z, $\mathbf{L}^2$ and $\mathbf{S}^2$.

Using expression (6.8) instead of (6.6) in the evaluation of (6.5) results in a modified set of coupled equations for f and g. They have the form [60]

$$\begin{aligned} \frac{df}{dr} &= \frac{1}{c}(V - \epsilon)g + \frac{\kappa - 1}{r}f \\ \frac{dg}{dr} &= -\frac{\kappa + 1}{r}g + 2Mcf, \end{aligned} \tag{6.9}$$

with κ denoting the relativistic quantum number and M defined by

$$M = m + \frac{\epsilon - V}{2c^2}. \tag{6.10}$$

The equation for the large component g is derived from (6.9) by extracting f from the first equation, substituting it into the second one, and using the identity $\kappa(\kappa+1) = l(l+1)$. After some analysis one arrives at [60]

$$-\frac{1}{2Mr^2}\frac{d}{dr}\left(r^2\frac{dg}{dr}\right) + \left[V + \frac{1}{2M}\frac{l(l+1)}{r^2}\right]g - \frac{1}{4M^2c^2}\frac{dV}{dr}\frac{dg}{dr} - \frac{1}{4M^2c^2}\frac{dV}{dr}\frac{1+\kappa}{r}g = \epsilon g. \tag{6.11}$$

A comparison with the non-relativistic radial Schrödinger equation yields, that the relativistic treatment gives rise to the last two terms on the left-hand side of Eq. (6.11). They correspond to the Darwin and SO corrections, respectively. Moreover, the mass m is replaced by the radially varying mass M, to account for the mass-velocity correction [14, 61, 63].

In order to construct the wave function Ψ, incorporating all relativistic effects, one has to solve Eq. (6.11) for $g(r)$ and calculate $f(r)$ with the help of [61].

$$f = \frac{1}{2Mc}\left(\frac{dg}{dr} + \frac{1+\kappa}{r}g\right). \tag{6.12}$$

6.3 Scalar-relativistic treatment

A simplification of the formalism can be achieved by adopting the so-called scalar-relativistic approximation for cases where the effects of SO coupling turn out to be small. Within this approximation, all terms related to SO interaction, i.e., those depending on κ, are neglected. In Eq. (6.11), this concerns the last term on the left-hand side. Consequently, l and s become good quantum numbers and the modified equation for the large component $\tilde{g}$ in the scalar-relativistic approximation reads as

$$-\frac{1}{2Mr^2}\frac{d}{dr}\left(r^2\frac{d\tilde{g}}{dr}\right) + \left[V + \frac{1}{2M}\frac{l(l+1)}{r^2}\right]\tilde{g} - \frac{1}{4M^2c^2}\frac{dV}{dr}\frac{d\tilde{g}}{dr} = \epsilon\tilde{g}. \tag{6.13}$$

After solving this equation for $\tilde{g}$, the small component is obtained via

$$\tilde{f} = \frac{1}{2Mc}\frac{d\tilde{g}}{dr}, \tag{6.14}$$

with $\tilde{g}$ and $\tilde{f}$ fulfilling the normalization condition

$$\int (\tilde{g}^2 + \tilde{f}^2) r^2 dr = 1. \tag{6.15}$$

Now, the four-component wave function $\tilde{\Psi}$ in the scalar-relativistic approximation can be determined by adopting the relationships

$$\tilde{\phi} = \tilde{g} Y_{lm} \chi_s \tag{6.16}$$

and

$$\tilde{\chi} = i \frac{\boldsymbol{\sigma} \cdot \mathbf{r}}{r} (-\tilde{f} + \frac{\tilde{g}}{2Mcr} \boldsymbol{\sigma} \cdot \mathbf{L}) Y_{lm} \chi_s. \tag{6.17}$$

Note, that these wave functions no longer represent eigenfunctions of the original Dirac Hamiltonian. Nevertheless, they can be used to define the SO Hamiltonian with the help of their deviation from the true eigenfunctions. This leads to a SO Hamiltonian of the form

$$H_{SO} = \frac{1}{(2Mc)^2} \frac{1}{r} \frac{dV}{dr} \begin{pmatrix} \boldsymbol{\sigma} \cdot \mathbf{L} \\ 0 \end{pmatrix} \tag{6.18}$$

which only acts on the large component of the wave function [61, 63].

6.4 Spin-orbit interaction

Sometimes the scalar-relativistic treatment discussed in Section 6.3 is not sufficient for a proper description of e.g. the electronic structure or optical spectra. In such a situation one can, of course, perform a fully-relativistic calculation as described in Section 6.2. Since the size of the corresponding eigenvalue problem doubles, one has to deal with a relatively time-consuming procedure. A faster alternative way is to add SO coupling on top of the scalar-relativistic calculation with the help of a second variational treatment. In a first step, the scalar-relativistic equations (6.13) and (6.14) are solved separately for each spin direction. This is possible since s is a good quantum number in the scalar-relativistic case. As a result, one obtains a set of eigenvalues and eigenfunctions. The eigenfunctions are used as basis set for a new eigenvalue problem of the full Hamiltonian including the SO term with the components $H_{ij} = \epsilon_j \delta_{ij} + H_{ij}^{SO}$, where ϵ_j represent the eigenvalues obtained from the scalar-relativistic Hamiltonian. The corresponding eigenvalue problem is smaller, since the new basis set is better suited for the perturbed problem than the original LAPW basis [57, 62, 63].

Part II

Results

7 Computational details

In this Chapter, the input parameters used in the ground-state calculations and in the determination of the optical properties are listed. Also, the procedure to determine the oscillator strengths as used in the interpretation of spectral features is described, and criteria for the assignment of predominant band characters are given.

7.1 Ground-state calculations

The scalar-relativistic ground-state calculations were carried out with the help of the APW+lo method [5] (see Sec. 5.3) as implemented in the WIEN2k code [6]. For iron, nickel, and cobalt, spin-polarized calculations were performed. In case of gold, platinum, lead, and tungsten, SO interaction was added on top of the scalar-relativistic calculations adopting a second variational scheme as described in Sec. 6.4. Exchange-correlation effects were treated by the GGA in the parameterization of Perdew, Burke, and Ernzerhof [29]. The structural parameters are listed in Tab. 7.1. The unit cell of bismuth contains two atoms at (0.237|0.237|0.237) and (0.763|0.763|0.763) [65]. In the trigonal unit cell of tellurium three atoms are present with atomic positions (u|0|0.$\dot{3}$), (0|u|0.$\dot{6}$), and (1$-u$|1$-u$|1) where u is determined by minimizing the interatomic forces. Its value of 0.2754 is in excellent agreement with $u = 0.276$, obtained by Ghosh and co-workers [67]. Further computational parameters listed in Tab. 7.1 are the **k**-point meshes, the radii of the muffin-tin spheres R_{MT}, and the RK_{max} value, i.e., the product of the smallest muffin-tin radius and the largest wave vector K_{max} in the expansion of the wave functions. Local orbitals included for a proper treatment of semi-core states are also given. Additional local orbitals were taken into account for unoccupied states. For the plane-wave cut-off G_{max} in the Fourier series of the potential and electron density in the interstitial region a value of 24.0 Ry$^{0.5}$ was adopted.

Table 7.1: Crystal structure, lattice parameters (see Refs. [64, 65] and for Te see Ref. [66] and references therein), **k**-point mesh, R_{MT}, RK_{max}, and local orbitals used in the ground-state calculations for the materials under consideration. In case of bismuth, the angles between the lattice vectors are equal to 57.237° [65].

Material	crystal structure	a (in Å)	b (in Å)	c (in Å)	**k** mesh	R_{MT} (in a.u.)	RK_{max}	LO's
Ag	fcc	4.09	4.09	4.09	34×34×34	2.50	11.0	$4s$, $4p$
Al	fcc	4.05	4.05	4.05	34×34×34	2.60	9.0	$2s$, $2p$
Au	fcc	4.08	4.08	4.08	31×31×31	2.50	11.0	$5s$, $5p$, $4f$
Bi	rhombohedral	4.7459	4.7459	4.7459	21×21×21	2.50	11.0	$5d$, $6s$
Co	hcp	2.51	2.51	4.07	29×29×15	2.30	11.0	$3s$, $3p$
Cu	fcc	3.61	3.61	3.61	31×31×31	2.10	10.0	$3p$
Fe	bcc	2.87	2.87	2.87	34×34×34	2.33	10.0	$3s$, $3p$
Mo	bcc	3.15	3.15	3.15	34×34×34	2.50	10.0	$4s$, $4p$
Ni	fcc	3.52	3.52	3.52	34×34×34	2.25	11.0	$3s$, $3p$
Pb	fcc	4.95	4.95	4.95	31×31×31	2.50	11.0	$5p$
Pd	fcc	3.89	3.89	3.89	34×34×34	2.50	11.0	$4p$
Pt	fcc	3.92	3.92	3.92	31×31×31	2.50	11.0	$5s$, $5p$, $4f$
Ta	bcc	3.30	3.30	3.30	31×31×31	2.50	11.0	$4f$, $5s$
Te	trigonal	4.4572	4.4572	5.929	19×19×12	2.50	11.0	—
Ti	hcp	2.95	2.95	4.68	23×23×11	2.60	10.0	$3s$
V	bcc	3.03	3.03	3.03	34×34×34	2.40	10.5	$3s$, $3p$
W	bcc	3.16	3.16	3.16	31×31×31	2.50	11.0	$5s$, $4f$
Zn	hcp	2.66	2.66	4.95	34×34×16	2.40	10.5	$3p$

Table 7.2: **k**-point meshes and theoretical plasma frequencies ω_{pl} calculated from Eq. (4.27) used in the determination of the optical spectra. For gold, platinum, lead, and tungsten, the values were obtained by a relativistic calculation including SO interaction.

Material	**k**-mesh	ω_{pl}^{xx} (in eV)	ω_{pl}^{yy} (in eV)	ω_{pl}^{zz} (in eV)
Ag	58×58×58	9.13	9.13	9.13
Al	58×58×58	12.49	12.49	12.49
Au	58×58×58	8.81	8.81	8.81
Bi	58×58×58	2.46	2.46	1.86
Co	62×62×33	6.08	6.08	6.70
Cu	58×58×58	8.94	8.94	8.94
Fe	58×58×58	6.44	6.44	6.44
Mo	58×58×58	8.61	8.61	8.61
Ni	58×58×58	7.04	7.04	7.04
Pd	58×58×58	7.37	7.37	7.37
Pt	58×58×58	7.54	7.54	7.54
Pb	58×58×58	9.01	9.01	9.01
Ta	53×53×53	8.91	8.91	8.91
Te	40×40×26	0.02	0.02	0.01
Ti	59×59×32	3.72	3.72	3.76
V	58×58×58	7.80	7.80	7.80
W	58×58×58	7.17	7.17	7.17
Zn	70×70×32	8.35	8.35	9.97

7.2 Calculation of optical properties

The formalism used for the calculation of the optical spectra was presented in Sec. 4.3. Since the optical properties are usually very sensitive to the BZ sampling, careful convergence tests were performed with respect to the **k**-point mesh. Table 7.2 lists the resulting **k**-point meshes. In addition, the plasma frequencies ω_{pl} as obtained from Eq. (4.27) are given. They were used in the determination of the free-electron contributions with the help of Eqs. (4.25) and (4.26). For spin-polarized calculations, the total plasma frequency was determined from the values of the two spin orientations according to

$$\omega_{pl} = \sqrt{(\omega_{pl}^{\uparrow})^2 + (\omega_{pl}^{\downarrow})^2}. \tag{7.1}$$

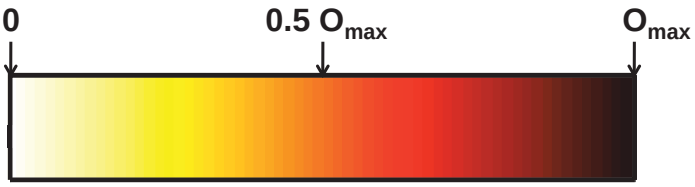

Figure 7.1: Color code used in the visualization of the oscillator strengths. O_{max} refers to a value equal or close to the highest oscillator strengths in a given energy range.

A Lorentzian broadening of 0.1 eV was included for all materials under consideration except for gold, where a smaller value of 0.01 eV was adopted to resolve important details in the spectra. All other input parameters were taken to be the same as in the ground-state calculations (see Tab. 7.1). BZ integrations were carried out by means of the improved tetrahedron method [68].

7.3 Determination of oscillator strengths and assignment of predominant band characters

For palladium, aluminum, gold, lead, and platinum, an analysis in terms of oscillator strength is presented in Chapters 8 - 10, similar to that given in Ref. [69]. The oscillator strength $O_E(\mathbf{k})$ of transitions contributing to a chosen energy range $E_{min} \leq \epsilon_{n',\mathbf{k}} - \epsilon_{n,\mathbf{k}} \leq E_{max}$ for a certain **k** point is given by

$$O_E(\mathbf{k}) = \sum_{n,n'} \int_{E_{min}}^{E_{max}} dE \; p_{n',n,\mathbf{k}} \; p_{n',n,\mathbf{k}} \; \delta\left(\varepsilon_{n',\mathbf{k}} - \varepsilon_{n,\mathbf{k}} - \omega\right). \tag{7.2}$$

The sum runs over all band combinations (n, n') for which the related transition energies lie within the energy range of interest. As a result one obtains information about the oscillator strengths for individual **k** points in the BZ. These **k**-dependent oscillator strengths are then plotted for different planes in the BZ to visualize regions which are highly involved in the creation of a considered peak. The color code used in the visualization is displayed in Fig. 7.1. O_{max} is chosen to be equal or close to the highest oscillator strengths in the selected energy range.

This analysis in terms of oscillator strength is supported by band structure plots including the predominant band characters. They are determined according to the following procedure: The band character, denoted by q ($q = s, p, d, f$),

is assigned if for the chosen **k** point and band the partial charge of type q is greater or equal than 70%, or if it is greater or equal than 50% and all other partial charges contribute with less than 20%. In case of mixed qq' character, the partial charges of q and q' type together must yield a value greater or equal than 65%, and all other partial charges show contributions of less than 20%. For states which do not meet any of the conditions above, no predominant character is defined.

8 Momentum-dependent loss function of Pd

A lot of experimental work on the optical properties of palladium is available in literature [70–75]. Experimental results were obtained from measurements of reflectivity [70, 71], absorptivity [73], or transmission [75], but also combined methods using reflection and transmission data [72] were adopted. Only recently, new experimental data became available from EELS [8] and reflection EELS (REELS) [10]. Early calculations of the electronic structure and optical spectra were reported by Lässer and Smith [76], and Chen and coworkers [77]. More recent theoretical studies include, for instance, the work of Krasovskii and Schattke [78] based on a semi-relativistic **k**·**p** method. Full potential linear muffin tin orbital (FP-LMTO) LDA calculations were performed by Monachesi and co-workers [79]. Fehrenbach [80] investigated the peak structure of the EELS spectrum up to an energy of 30 eV with the help of the spline-augmented planewave method. Concerning momentum-dependent optical properties, Silkin and co-workers [81] studied the evolution of spectral features in the loss function of palladium for energies and momentum-transfer up to 15 eV and 0.7 a.u.$^{-1}$, respectively.

Here, we go beyond the work of Ref. [81] by providing *ab initio* calculations of electron energy-loss spectra of Pd covering an energy range up to 80 eV. We investigate its evolution with increasing momentum transfer along the (100), (110), and (111) directions. These spectra will be used to simulate experimental spectra taken on polycrystalline samples for different q values. Being a prerequisite in the interpretation of momentum-dependent loss functions, the optical spectra of palladium for zero momentum transfer are presented and compared to available experimental and theoretical data. This is supplemented by an analysis in terms of oscillator strengths and origin in **k** space, which to the best of our knowledge was not performed in this way before. The details of the calculations for $q = 0$ are given in Chapter 7. For finite momentum transfer, the ground-state calculation was carried out with the

full-potential APW+lo method as implemented in the **exciting** code [7]. The momentum-dependent electron-energy loss functions and dielectric functions were obtained on top of the ground-state calculation within the framework of TDDFT. SO interaction was neglected. The RPA and the ALDA given in Eqs. (3.33) and (3.36), respectively, were adopted for the xc kernel. The calculations were carried out on an off-symmetry shifted $25\times25\times25$ **k**-point mesh using a RK_{max} value of 8. A cutoff parameter of 3.0 bohr^{-1} for the reciprocal lattice vectors, 50 conduction bands, and a broadening of 0.22 eV were chosen.

8.1 Linear optical properties of Pd

The upper panel of Fig. 8.1 depicts the imaginary part of the complex dielectric function as obtained from a scalar-relativistic calculation (black) in comparison with the experimental spectra derived from reflectance measurements by Vehse, Arakawa, and Williams [71] (green) and from REELS by Werner [10] (blue). As highlighted by the inset, the low-energy part of the spectrum is dominated by strong interband transitions with the first interband peak sitting at approximately 0.4 eV. Therefore, a separation of inter- and intraband contributions in the experimental spectra becomes impossible [71]. As a result, the first interband peak is not visible. In the calculation, the free-electron contribution was taken into account by a Drude-like shape using the calculated plasma frequency of 7.37 eV. At 4.86 eV a little peak is present, followed by a minimum at 7.7 eV, a plateau with several small features in the 8 to 18 eV range, and a multi-peak structure centered at approximately 20.5 eV. In the high-energy region, structures show up around 31.5 and 50 eV. Inclusion of SO interaction especially influences the maximum at 50 eV, splitting it into two peaks at 48.6 and 52.85 eV (not shown here).

The calculated spectrum is in accordance with experiments by Vehse, Arakawa, and Williams [71] (green), but the calculated intensities appear larger. Compared to the REELS data of Werner [10], a blueshift of the calculated spectrum is observed in the energy range below 35 eV, while good overall agreement is found above. The peak heights are, however, greater than the experimentally observed ones for the 20.5, 31.5, and 50 eV structures, while the peak intensity is underestimated for the plateau in the 8 to 18 eV region. Comparison of purely theoretical data reveals that the present result is in excellent agreement with that reported by Krasovskii and Schattke [78], as well as by Monachesi and co-workers [79].

The reflectivity of palladium is displayed in the lower panel of Fig. 8.1. It decreases continuously with only little structure to a value of approximately

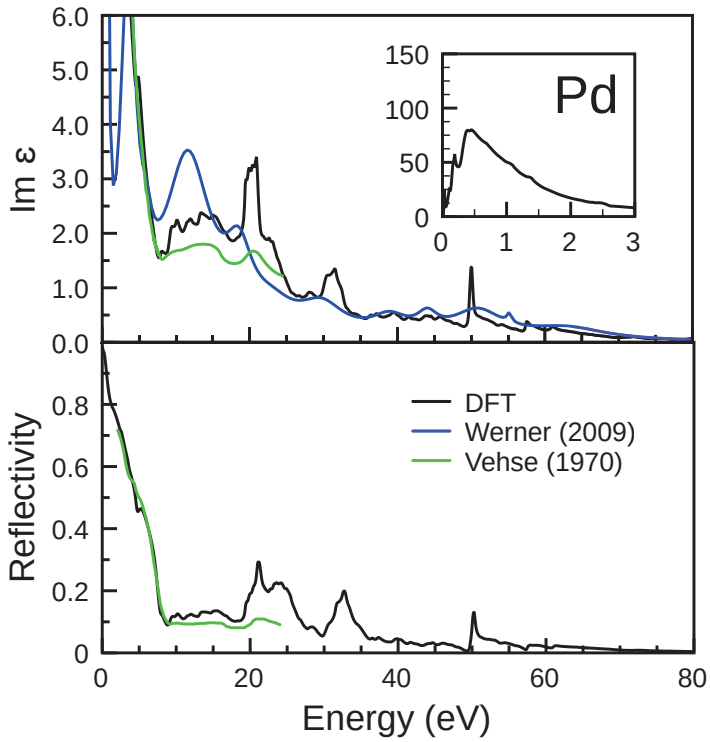

Figure 8.1: Imaginary part of the complex dielectric function (top) and reflectivity (bottom) of palladium (black) in comparison with experimental data reported by Vehse, Arakawa, and Williams [71] (green) and by Werner [10] (blue). The inset zooms into the low-energy region.

8.9% at an energy of 8.8 eV. In the 8 to 19 eV region, the reflectivity varies between 8.9 and 14%. This is followed by a double-peak structure in the 19 to 27 eV range reaching a maximum value of 29.4% at 21.1 eV. The high-energy features centered at 32.7 eV and 50.25 eV show maximum reflectivity values of 20 and 13.4%, respectively. The reflectivity is in excellent agreement with the experimental data of Vehse and co-workers [71]. Only for energies higher than 20 eV, much lower experimental values are observed. In addition, the calculated spectrum is in accordance with that presented by Krasovskii and Schattke [78] up to 30 eV. For the structure at 32.7 eV, a 1.2 eV lower energy and slightly reduced reflectivity is obtained by Ref. [78].

To analyze the origin of spectral features, Fig. 8.2 displays the oscillator strengths for **k** points in the $k_z = 1/34$, 17/34, and 33/34 planes (in units of

$2\pi/a$) for the energy ranges 0.1 - 0.6 eV (b), 8 - 18 eV (c), 19 - 21.5 eV (d), and 30 - 32.5 eV (e), as obtained from the procedure described in Sec. 7.3. The position of the selected planes within the BZ are depicted in Fig. 8.2(a). The full analysis containing oscillator strengths for planes with k_z values increasing from 0 to 1 in steps of $\Delta k_z = 1/34$ is given in Appendix A (see Figs. A.1 - A.4). To provide more information on the origin of spectral features in terms of energy bands, Fig. 8.3 presents the band structure of palladium including the predominant band characters.

Fig. 8.2(b) indicates that the strong interband peak centered at 0.4 eV mainly originates from transitions in an area around the X point for small k_z values up to 0.2 (see first panel). With increasing k_z this region disappears. For k_z values from 0.3 to 0.5 strong contributions are found along lines parallel to Γ - K much closer to the BZ boundary (see middle panel). As k_z approaches 1, **k** points in a ring centered around the k_z axis contribute (see right panel). Note that due to the high symmetry of the fcc BZ the patterns for $0.8 < k_z < 1$ represent oscillator strengths in planes parallel to the (k_y,k_z) plane for $0.8 < k_x < 1$ (see also Fig. A.1). The transitions are predominantly $d \rightarrow p$ like, from d bands sitting at the Fermi level to the first conduction band of mixed pd character.

For the plateau in the 8 to 18 eV range, Fig. 8.2(c) reveals high oscillator strengths for **k** points close to the BZ boundary if k_z is small. The strongest contributions can be located along the sides of a square with the edges lying on the line K - L (see first panel). As k_z increases, these regions concentrate at the edges of the indicated planes, i.e., along the line X - W in k_z direction (see middle panel). For $k_z > 0.5$ they turn into blossom-shaped areas before almost all **k** points in the plane provide high oscillator strengths (see right panel and Fig. A.2). Transitions from a variety of bands contribute to this feature. In the valence band region these are the d bands, whereas conduction bands of mainly sd, pd, pf, and f character are involved.

The multi-peak structure around 20.5 eV is to a large extent created by $d \rightarrow f$ transitions from areas close to the centre of the BZ and symmetric around a line parallel to Γ - K (closer to Γ), as indicated by the first panel of Fig. 8.2(d). The initial bands of d character are present at -2.8 eV at the Γ point, while the conduction band of f character is sitting at 17 eV. With increasing k_z the regions of high oscillator strengths move closer to the BZ boundaries and are centered at **k** points along K - L much closer to L (middle panel). In this case, transitions from initial d bands at the Fermi level and 2.9 eV below to conduction bands of f and mixed pf character (at 16.4 and 21.1 eV at L) take place. For $k_z > 0.8$ the oscillator strengths become negligible (see right panel). The complete analysis is presented in Fig. A.3.

The peak at 31.5 eV is mainly created by $d \rightarrow f$ transitions from a variety of **k** points. For $k_z \approx 0$ the oscillator strengths are, for example, strongest along

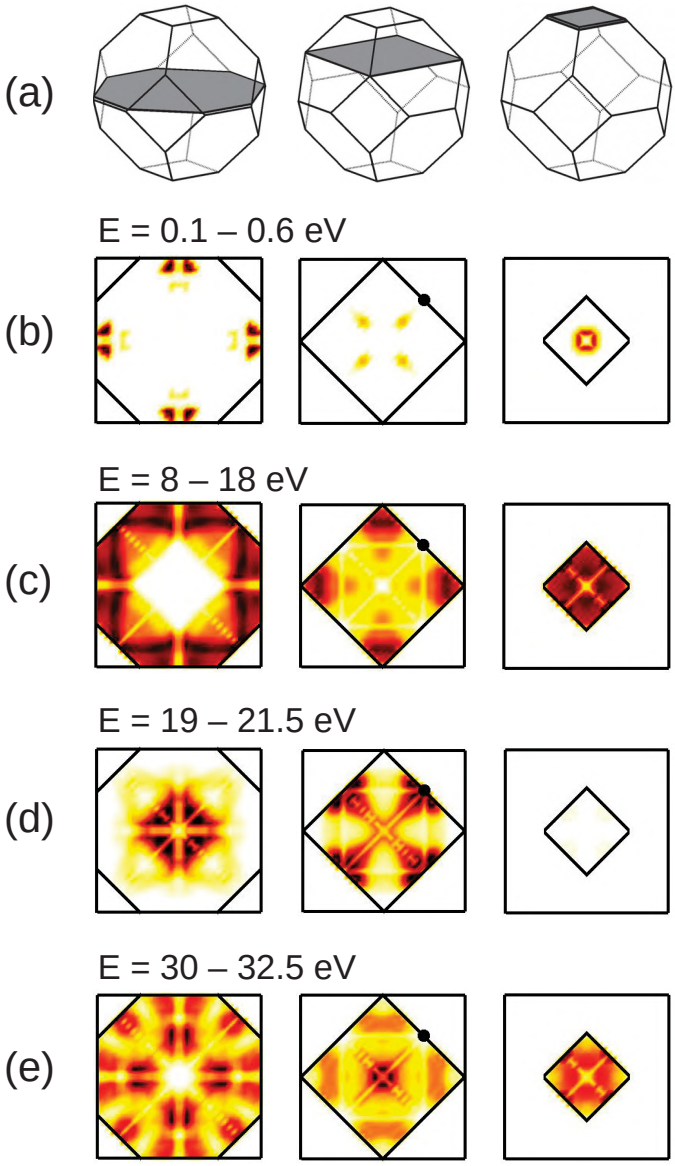

Figure 8.2: (a) fcc BZ with selected planes corresponding to k_z = 1/34, 17/34, and 33/34 (in units of $2\pi/a$) highlighted and oscillator strengths of palladium for the energy ranges 0.1 - 0.6 eV (b), 8 - 18 eV (c), 19 - 21.5 eV (d), and 30 - 32.5 eV (e). Regions with high oscillator strengths are displayed in dark red. The corresponding color bar is shown in Fig. 7.1.

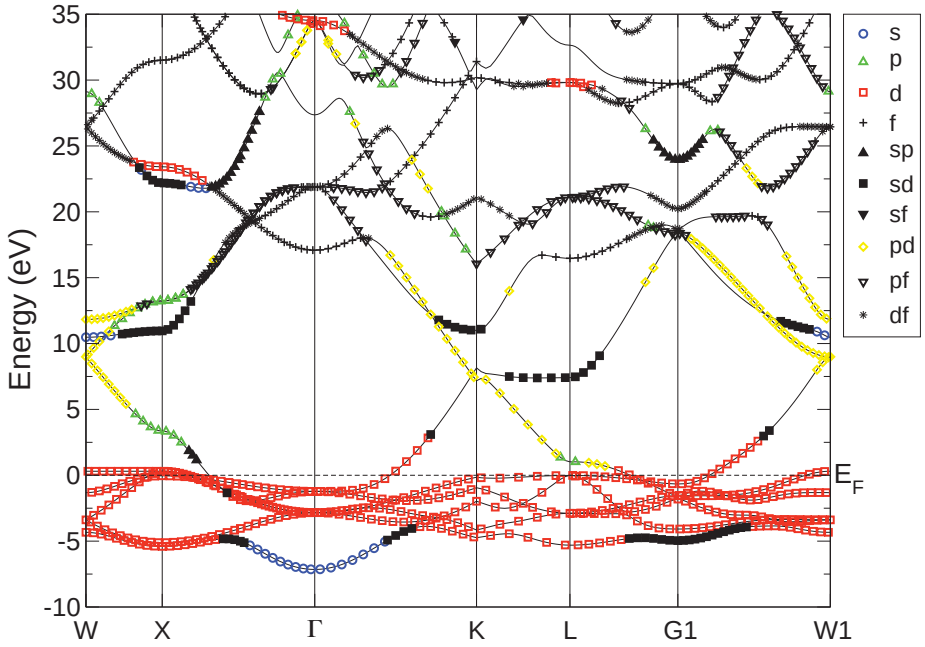

Figure 8.3: Band structure of palladium with predominant band characters highlighted by the colors and symbols given in the legend. G1 and W1 denote the **k** points (0|0|0.5) and (1|0|0.5), respectively.

a line parallel to Γ - X and around the K point (see Fig. 8.2(e), first panel). As k_z increases, at first, **k** points close to the BZ boundary start to contribute. For $0.3 < k_z < 0.6$ transitions in an almost circular area centered at the k_z axis appear together with strong contributions in the region along X - W in k_z direction (see middle panel). For $k_z \approx 1$ the dominating oscillator strengths occur in a ring centered at the k_z axis. For further details see Fig. A.4. Valence bands of d character with energies between -2.8 eV and the Fermi level as well as conduction bands between 27.5 and 32.5 eV, that show predominantly f character, sometimes with admixtures of p type, are involved in the creation of this feature.

Finally, the structure at 50 eV can be traced back to $p \rightarrow d$ transitions from low-lying $4p$ bands located between -50.1 and -49.6 eV to conduction bands at the Fermi level. Thus, this feature corresponds to the $N_{2,3}$ core edge.

In Fig. 8.4, the electron energy-loss function of palladium is depicted. A peak at 7.66 eV is followed by a hump around 17 eV and two maxima at approximately 26.2 and 33.5 eV, respectively. The energy range above 35 eV is characterized by a number of smaller features and three maxima at 50.4,

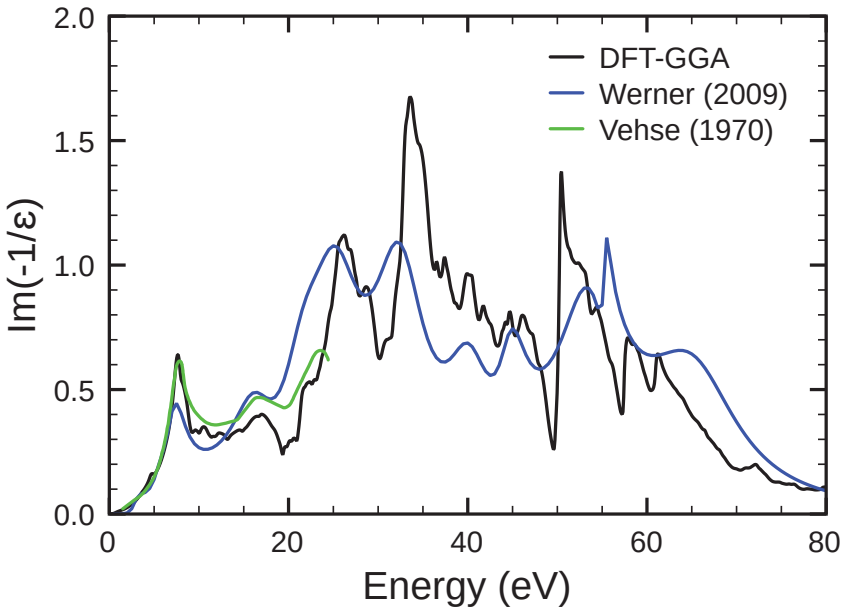

Figure 8.4: Electron energy-loss function of palladium (black) in comparison with experimental data reported by Vehse, Arakawa, and Williams [71] (green) and by Werner [10] (blue).

58.1, and 61.2 eV, respectively. Apart from a reduced peak intensity for energies above 10 eV, excellent agreement with the experimental data of Vehse and co-workers [71] is found. Compared to the experimental spectrum presented by Werner [10], the theoretical features are blueshifted for energies below 40 eV. The experimentally observed humps at 40 and 45 eV can be ascribed to structures predicted at the same energies by the calculation. The double peak with maxima at 53 and 55.5 eV may be related to the feature found at 50.4 eV in the theoretical spectrum while the subsequent shoulder may correspond to the maxima at 58.1 and 61.2 eV. Except for a redshift of the maxima at 26.2 and 33.5 eV and slightly lower intensities for energies greater than 10 eV, the present result is in excellent overall agreement with the theoretical curve reported by Krasovskii and Schattke [78], while it is slightly blueshifted and higher in intensity than the spectrum obtained from a FP-LMTO calculation by Monachesi and co-workers [79]. Agreement with the calculation of Fehrenbach [80] is found for the position of the hump, while the intensity is roughly 50% higher compared to the present calculation. In addition, Fehrenbach predicts the low-energy feature at a higher energy of approximately 8.2 eV and

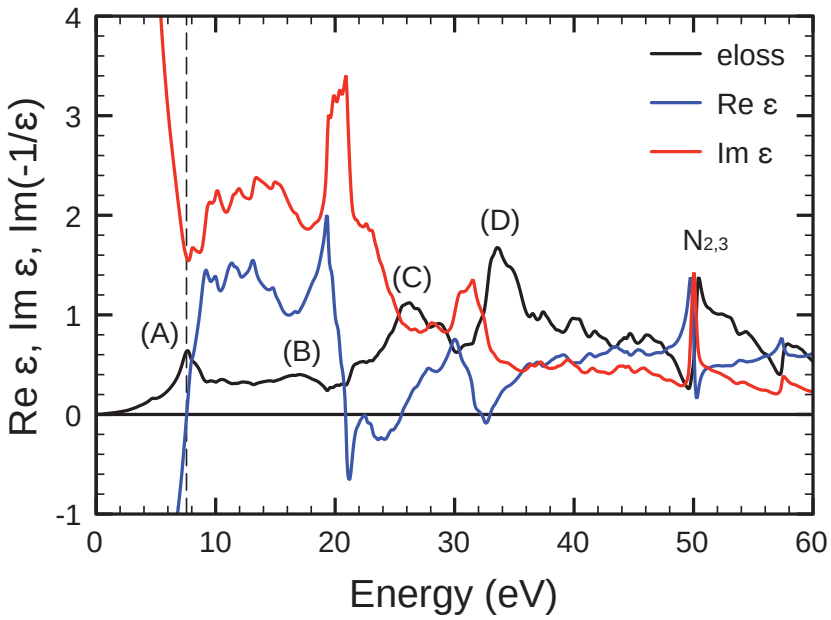

Figure 8.5: Electron energy-loss function (black), real (blue) and imaginary (red) part of the complex dielectric function of palladium for energies up to 40 eV.

the peak at 26.2 eV is redshifted and shows only half the intensity.

To investigate the origin of the spectral features in the electron energy-loss function, Fig. 8.5 depicts the real and imaginary part of the complex dielectric function together with the electron energy-loss function for energies up to 60 eV. The real part of the complex dielectric function crosses the zero line at about 7.56 eV (marked by the dashed line) while the imaginary part is small and has a minimum at this position. This implies that the peak at 7.66 eV (A) is a low-energy plasmon resonance, in line with the findings of Yu and Spicer [70] and Vehse et. al. [71], reporting plasmon resonances at 7.5 and 7.6 eV, respectively. In contrast, the structures at 17 (B), 26.2 (C), and 33.5 eV (D) are related to features at slightly lower energies in the imaginary part of the complex dielectric function, i.e., the plateau centered at 13 eV, the multi-peak structure at 20.5 eV, and the maximum at 31.5 eV, respectively. As pointed out in Ref. [82], each peak in Imε arising from interband transitions can be associated with a feature in the electron energy-loss function at a slightly higher energy, with the energy difference between them decreasing with increasing transition energy. Thus, features (B) - (D) arise from interband transitions. The analysis performed for the corresponding features in the imaginary

part of the complex dielectric function reveals that, to a large extent, excitations from d bands to conduction bands of p and f character are involved in their creation. The peak at 50.4 eV can be ascribed to the 50 eV peak in Imε and, therefore, corresponds to the $N_{2,3}$ edge.

8.2 Momentum-dependent loss function

The behavior of selected spectral features with increasing momentum transfer will be investigated in the following. To study the evolution of peaks (A) - (D), Fig. 8.6 depicts the q-dependent electron energy-loss functions up to 80 eV for momentum transfer increasing from 0.097 to 1.615 Å^{-1} in (100) direction, from 0.091 to 1.626 Å^{-1} in (110) direction, and from 0.084 to 1.622 Å^{-1} in (111) direction in equidistant steps. The spectra were obtained by TDDFT calculations adopting the RPA, i.e., including local-field effects. At first, the focus lies on the dispersion of the low-energy plasmon (A). Fig. 8.7 displays the mean peak positions for increasing momentum transfer up to 0.8 Å^{-1} for the three main directions. It reveals that for $q \leq$ 0.4 Å^{-1} the upward shift in peak position is almost isotropic. Above 0.4 Å^{-1} the further increase in plasmon energy with increasing q differs for the three directions. It is most pronounced in (111) direction. The increase in plasmon energy is accompanied by a decrease in peak height and an increase in its width. The general trend in the evolution of the plasmon energy, including the anisotropic behavior at higher momentum transfer, agrees well with findings presented by Silkin and co-workers [81].

Position and height of the shoulder (B) remain almost unaffected for momentum transfer up to 0.355 Å^{-1}, while the minimum at approximately 19.7 eV decreases in depth and, for $\mathbf{q}$ parallel to (110) and (111), shifts to 20 eV. A slight reduction in height together with an upward shift in energy is observed at higher q. For $q =$ 0.646 Å^{-1} in (100) direction, the feature is found at approximately 17.8 eV. It continues moving upwards in energy, thereby decreasing in width before it finally gets integrated into the background for $q \approx$ 1.13 Å^{-1}. A slightly different behavior occurs for momentum transfer in (110) and (111) direction. For $q \approx$ 0.7 Å^{-1}, the hump and the minimum disappear and a plateau shows up instead. For even higher momentum transfer, a little peak emerges out of this plateau at an energy of 20 eV, showing higher intensity in (111) direction. In addition, it slightly shifts to lower energy and its height grows, reaching its maximum value for $q =$ 1.063 Å^{-1}. Then, the height starts decreasing, the feature moves to higher energies and gets part of a plateau for momentum transfer in (111) direction, while it emerges again out of the plateau for the (110) direction.

Maximum (C) remains almost constant in position and height up to $q \approx$

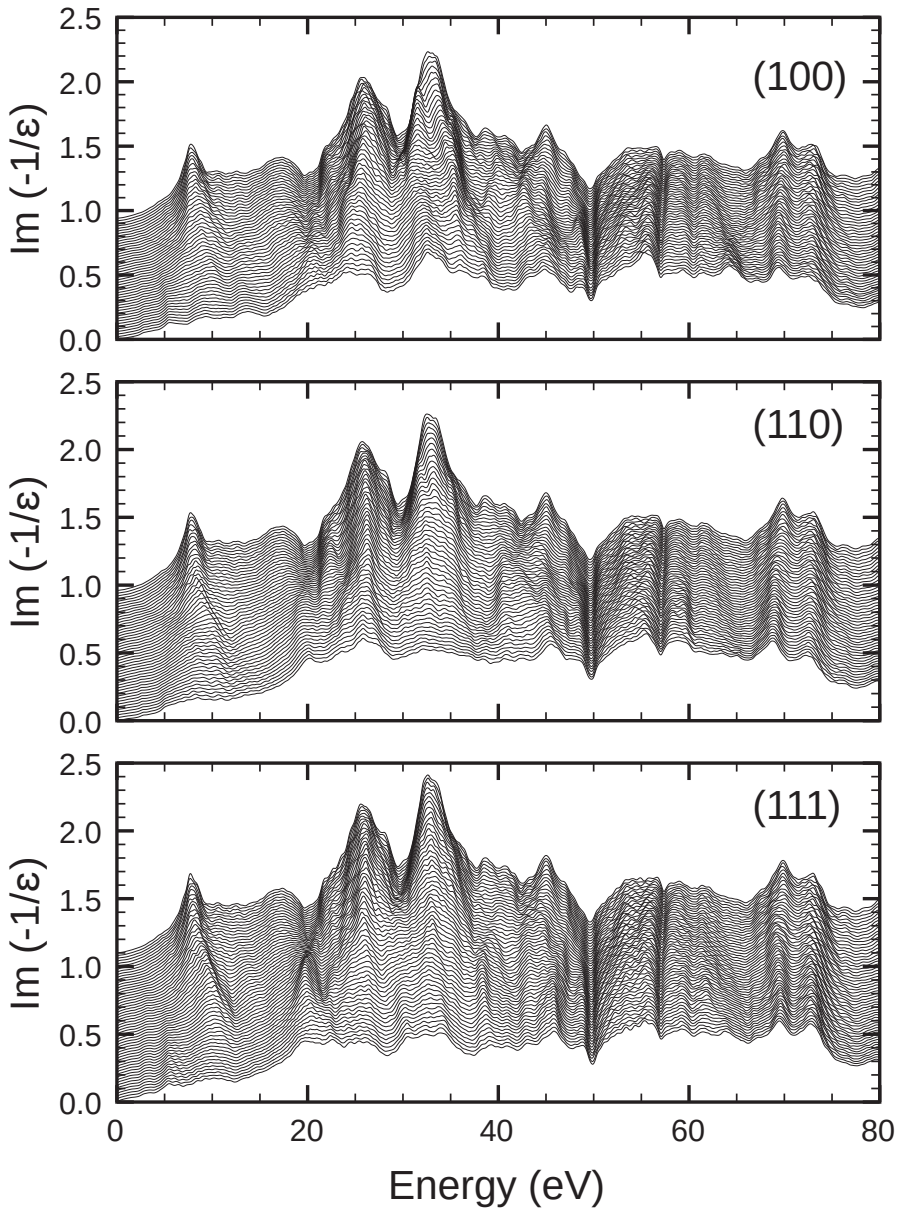

Figure 8.6: Evolution of the electron energy-loss function of palladium for momentum transfer from $q = 0.097$ to 1.615 Å^{-1} in (100), from 0.091 to 1.626 Å^{-1} in (110), and from 0.084 to 1.622 Å^{-1} in (111) direction (from top to bottom). The momentum transfer increases in equidistant steps. The highest spectrum always corresponds to the case of lowest momentum transfer and the spectra are offset for clarity.

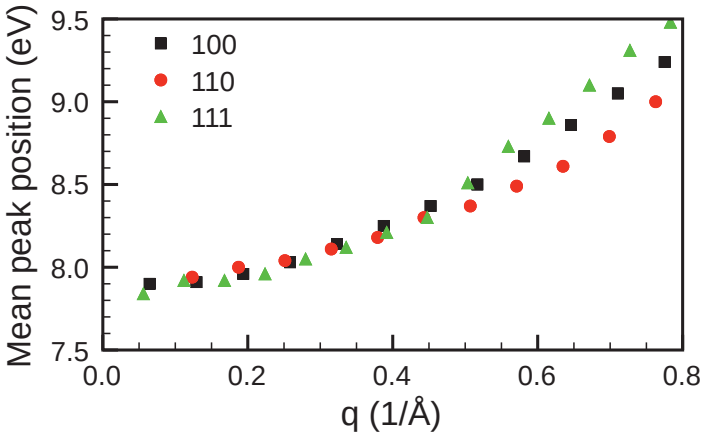

Figure 8.7: Evolution of the low-energy plasmon peak for momentum transfer up to 0.8 Å^{-1} in (100), (110), and (111) direction.

0.258 Å^{-1} in (100) direction, before a reduction in peak intensity occurs. This is followed by a downward shift in peak position by approximately 1.1 eV together with a slight increase in width, starting at $q \approx 0.646$ Å^{-1}. A mean peak position of 25 eV is reached for $q \approx 1.163$ Å^{-1}. For even higher q, the structure gradually turns into a plateau. In (110) direction, a peak position of 26.3 eV is reached for $q \approx 0.959$ Å^{-1}. The subsequent downward shift by roughly 0.3 eV for q increasing to 1.279 Å^{-1} is, however, much smaller than in (100) direction. The position of the maximum, now centered at 26 eV, is almost stable, while its intensity decreases. The behavior for momentum transfer in (111) direction is quite similar. While the mean position stays approximately the same, the peak height starts decreasing at $q \approx 0.392$ Å^{-1} and for q values above 1.007 Å^{-1} it gradually gets part of the background.

Maximum (D) splits into a shoulder and a peak at 31.6 and 33.1 Å^{-1}, respectively, for $q \approx 0.161$ Å^{-1} in (100) direction. The peak evolving out of the shoulder for increasing momentum transfer stays almost constant in position before it disappears for $q \approx 0.71$. It shows up again at an energy of roughly 32 eV for $q \approx 1.0$ Å^{-1}. As it then moves to higher energies it gets more prominent and is clearly visible for $q = 1.615$ Å^{-1} around 32.8 eV. The maximum itself shifts to higher energies and gradually gets weaker in intensity. It is situated at an energy of 36 eV before it integrates into the background for $q \approx 1.615$ Å^{-1}. In (110) direction, a shoulder emerges around 31.8 eV out of the maximum centered at 33 eV for $q = 0.274$ Å^{-1}. The shoulder merges with the main peak for $q \approx 0.594$ Å^{-1} to form a broad feature centered at approximately 33 eV. For even higher q, the intensity decreases and the feature

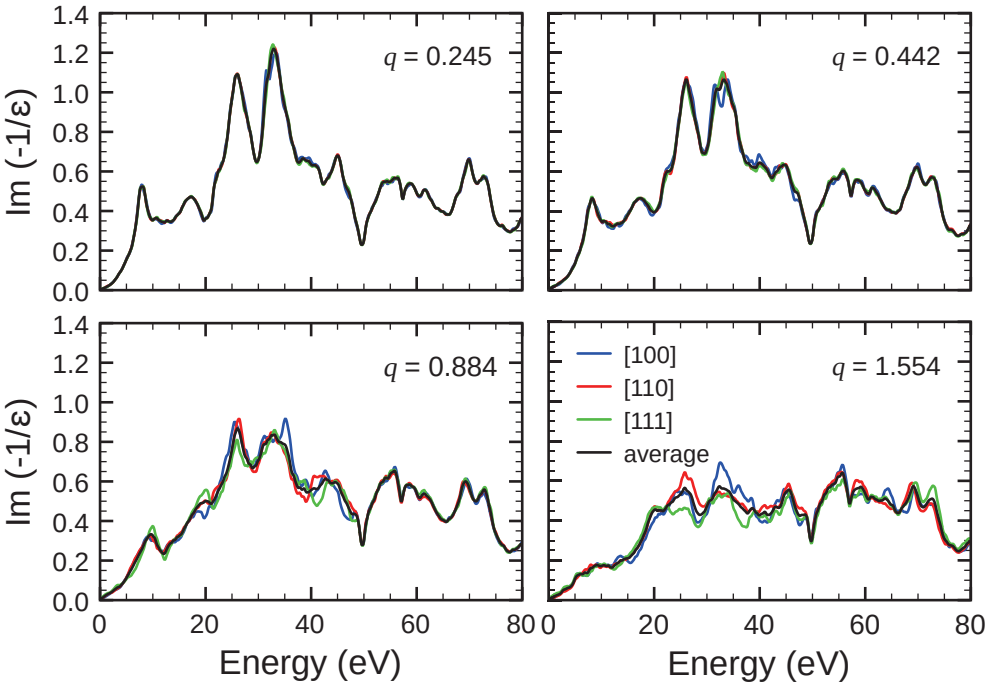

Figure 8.8: Electron-loss spectra for momentum transfer in Å^{-1} in (100), (110), and (111) direction in comparison with their weighted sum.

flattens before it gets part of the background. Increasing momentum transfer in (111) direction leaves the mean peak position of 33 eV almost unchanged, while a reduction in intensity occurs. For momentum transfer above 1.063 Å^{-1}, the peak gradually turns into a plateau centered at a lower energy of roughly 32.5 eV.

Experimental data obtained from measurements on polycrystalline probes contain contributions for momentum transfer in various directions. To account for this, the q-dependent electron energy-loss spectra are averaged over spectra corresponding to momentum transfer along the (100), (110), and (111) direction adopting weights of $\frac{3}{13}$, $\frac{6}{13}$, and $\frac{4}{13}$, respectively. The so-obtained spectra are displayed for different q values in Fig. 8.8 together with the individual components. The upper row reveals that almost no anisotropy is present for small momentum transfer. The second row indicates that the anisotropy between the spectra for momentum transfer in different directions grows with growing q but stays moderate for all q values and energies. As visible from the lower left panel, the energy range below 50 eV is affected first. For $q =$ 0.884 Å^{-1}, the shape of structure (B) is quite similar to that obtained for q in

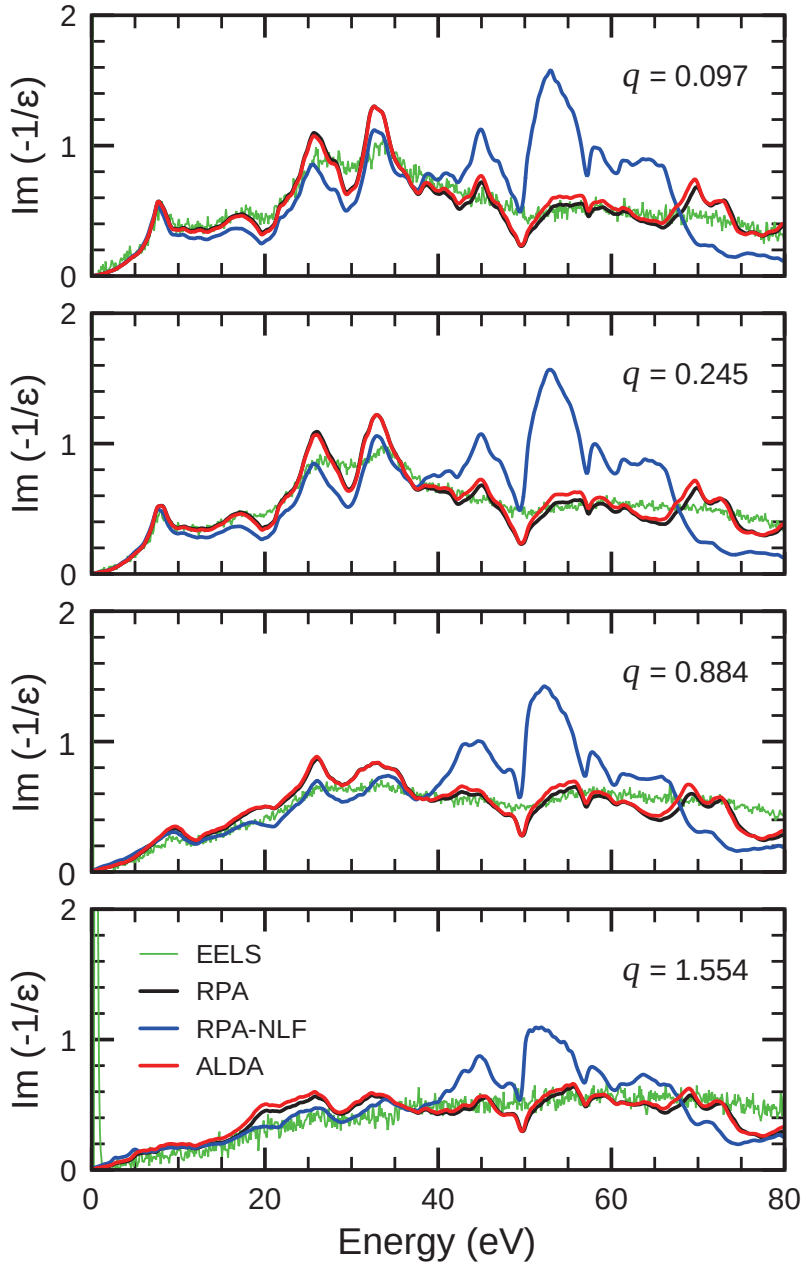

Figure 8.9: Momentum-dependent electron energy-loss functions of palladium for momentum transfer q increasing from 0.097 to 1.554 Å^{-1} in comparison with experimental EELS data of Hébert [8] (green). The theoretical curves are as follows: RPA including (black) and neglecting (blue) local-field effects, ALDA including local-field effects (red).

(110) direction, since the minimum occurring for q in (100) direction to a large extent cancels out the maximum present for q in (111) direction. The sharp peak of feature (D) for q along (100) is smoothened by the average with the other components. The lower right panel reveals that for $q = 1.554$ Å^{-1}, the total spectrum around peak (C) is similar to the contribution for q in (100), while for peak (D) it exhibits the form of that for q in (110) direction. To conclude, the dominating contributions to the total spectrum differ for different spectral features and q values. Thus, care must be taken when comparing theoretical results for higher q in only one specific direction with measurements performed on polycrystalline probes.

To judge the quality of the present results, they are compared to most recent experimental EELS data of Hébert [8] (green) in Fig. 8.9 for energies up to 80 eV. The momentum transfer q is varied from 0.097 to 1.554 Å^{-1}. The theoretical curves correspond to TDDFT calculations adopting the ALDA (red) and the RPA including (black) as well as excluding (blue) local-field effects. Fig. 8.9 reveals that the use of the ALDA kernel instead of RPA has hardly any effect on the electron energy-loss spectra. They are almost identical below 40 eV and show only slight differences above. A different situation occurs for the inclusion of local-field effects. At low energies, the impact of local-field effects on the spectra is small. Their inclusion in the theoretical description of the electron-energy loss function, however, turns out to be crucial for energies greater than 40 eV. Between 40 and 60 eV a reduction in spectral weight of up to 70% takes place, leading to an excellent overall agreement with experiment in this energy range. Alkauskas and co-workers [82] reported similar effects in the spectra of noble metals by inclusion of local-field effects. The importance of local-field effects for excitations from semicore states had been pointed out already by Vast and co-workers [83]. It was shown above, that excitations from d bands dominate the energy region up to 40 eV and around 50 eV transitions from the $4p$ semicore states set in. Both, the d states and the $4p$ semicore states are quite localized, which makes the inclusion of local-field effects necessary to meet experimental data, especially at higher energies

Finally, we see that the evolution of features (A) - (D) with increasing momentum transfer obtained from the calculations including local-field effects agrees well with experiment for energies up to 40 eV. The features are, however, more prominent than the related experimental ones. At higher energies, the calculation predicts a peak at roughly 45 eV, a minimum at 50 eV, and a double-peak structure in the 65 to 75 eV range which remain stable in position for increasing q. New measurements with better resolution are going to be performed soon, which are expected to confirm the existence of these three features, not having a visible counterpart in the experimental data sets yet.

9 Optical properties of aluminum and thin aluminum films

A lot of experimental and theoretical studies on the optical properties of bulk aluminum are available in literature [52, 84–94]. From the experimental side, Ehrenreich and co-workers [84] provided a compilation of reflectivity data up to 22 eV including measurements by Hass and Waylonis [85], Bennett and co-workers [86], as well as Madden and co-workers [87]. Pressure-dependent reflecitivity measurements were done by Tups and Syassen [91] on an aluminum-diamond interface. More recently, pseudopotential calculations were performed by Lee and Chang [92] and full-potential LAPW calculations were reported by Ambrosch-Draxl and Sofo [52] as well as by Youn and co-workers [93]. A theoretical study of the pressure-dependent optical properties was presented by Dandrea and Ashcroft [94]. In contrast to bulk Al, theoretical work on thin aluminum (001) films is quite rare. Caruthers and co-workers [95] performed energy-band calculations for the (001) surface based on a model potential. Heinrichsmeier and co-workers [96] adopted a pseudopotential approach to study surface states on the three low-index surfaces of aluminum. The thickness dependence of the optical spectra was studied in the infrared region by Kurbatsky and co-workers [97].

This Chapter focusses on the optical spectra of thin Al(001) films up to 5 eV as a function of film thickness. The evolution of spectral features with increasing film thickness will be traced back to changes in the band structure, and the impact of the presence of a surface on the spectra will be investigated. Being, however, a prerequisite in the interpretation of the thin-film spectra, the optical properties of bulk Al and their pressure dependence are discussed too. This includes a detailed analysis of the origin of the two low-energy interband peaks, which, to the best of our knowledge, has not been presented in this way before. The computational details are summarized in Chapter 7.

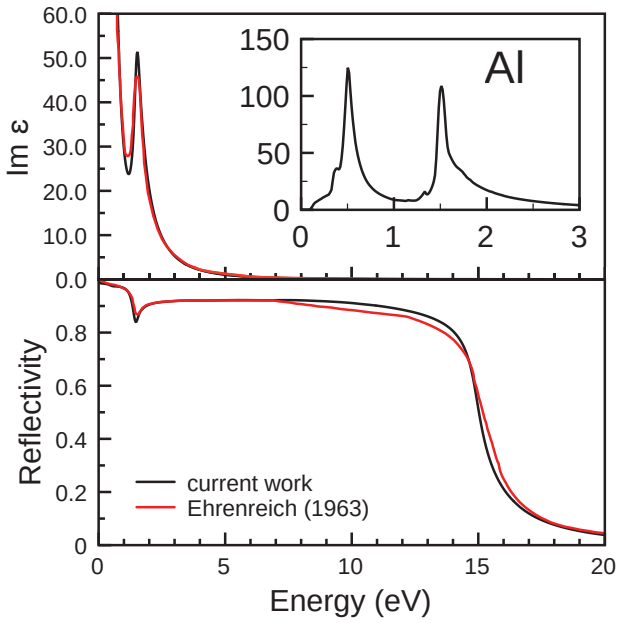

Figure 9.1: Imaginary part of the complex dielectric function (top) and reflectivity (bottom) of aluminum from a scalar-relativistic DFT-GGA calculation in comparison with experimental data presented by Ehrenreich, Philipp, and Segall [84]. A Lorentzian broadening of 0.1 eV was adopted. The inset shows the interband contribution only (without broadening).

9.1 Optical properties of bulk aluminum

As shown in Ref. [52], the optical properties of aluminum are highly dependent on the **k**-point sampling. Therefore, a $58\times58\times58$ **k**-point mesh corresponding to 4735 **k** points in the IBZ was used. The top panel of Fig. 9.1 depicts the imaginary part of the complex dielectric function up to 20 eV. It reveals excellent agreement with the spectrum derived from experimental data by Ehrenreich, Philipp, and Segall [84]. As can be seen in the inset, the low energy region up to 3 eV is dominated by strong interband transitions, with peaks appearing at 0.5 and 1.5 eV, respectively. Their positions compare well with the results of Lee and Chang [92] but the intensity of the first interband peak is found to be approximately 20% smaller in our calculation. The free-electron contribution is described by a plasma frequency of 12.49 eV, which is in excellent agreement

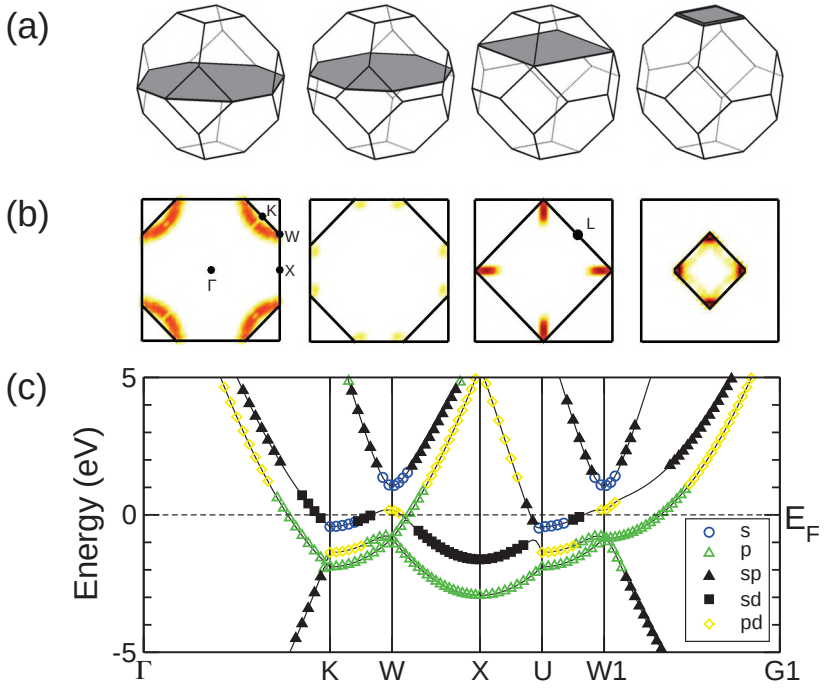

Figure 9.2: (a) fcc BZ indicating selected planes with $k_z = 0$, 5/34, 17/34, 33/34 (in units of $2\pi/a$). (b) Oscillator strengths for the energy range 0.1 to 2.1 eV. (c) Band structure of aluminum highlighting the predominant band characters as shown in the legend. G1 and W1 denote the **k** points (0|0|0.5) and (1|0|0.5), respectively.

with theoretical values of 12.56 eV and 12.6 eV reported in Refs. [92] and [52], respectively, and an estimate of 12.5 $\pm$ 0.3 eV extracted from results of Shiles and co-workers [88] by Smith and Segall [90]. It is, however, 0.21 eV lower than the value extracted from a compilation of experimental data by Ehrenreich, Philipp, and Segall [84]. The first interband peak is totally masked by the corresponding intraband contribution, thus, only the second peak centered at 1.5 eV shows up in the total spectrum. It gives rise to an absorption edge, with the reflectivity dropping to roughly 84% as shown in the bottom panel of Fig. 9.1. It then rises to approximately 92% and stays almost constant up to 9 eV before it starts to decrease continuously reaching values below 1% at roughly 25.5 eV. Again, excellent agreement is achieved with the compilation of reflectance data reported by Ehrenreich and co-workers [84].

To analyze the origin of the two interband peaks, the procedure described in Sec. 7.3 is applied. Figure 9.2(b) shows the oscillator strengths of aluminum in the energy range 0.1 to 2.1 eV for selected planes in the BZ (see Fig. 9.2(a)). A more detailed analysis is given in Appendix B (see Fig. B.1). It reveals that a fine **k** grid is necessary to correctly reproduce the spectrum, since the **k** points contributing to the features are extremely localized within the BZ, as already pointed out in Ref. [93]. The strongest contributions for $k_z \approx 0$ are found in a half-moon shaped area centered at the K point and reaching the W point (see Figure 9.2(b), first panel). With increasing k_z, these regions concentrate along W - U (second panel) until they merge around $k_z = 0.5$ and form important areas on a line parallel to Γ - X (third panel) for even larger values of k_z. As k_z approaches 1, major contributions are found at the edges of the indicated square together with weaker ones near its sides (outermost right panel). These findings are in agreement with results of Youn and co-worker [93] obtained from a study of the Fermi surfaces.

To facilitate further analysis, the band structure along the line Γ - K - W - X - U - W1 - G1 with W1 = (1|0|0.5) and G1 = (0|0|0.5) is depicted in Fig. 9.2(c) including the predominant band characters. It implies that transitions between the highest valence band of sd character and the first p-like conduction band crossing the Fermi level along W - X in the vicinity of W determine the interband onset energy and are responsible for the first maximum centered at 0.5 eV. In addition, $p \rightarrow d$ transitions from the uppermost valence band to the first conduction band around the W point contribute to this feature. The second interband peak is also dominated by transitions between the same two bands along Γ - K (closer to K), from initial states being predominantly p-like to final states of sd character. They are approximately parallel in the region of interest, leading to a high joint density of states. Moreover, there are small contributions from $p \rightarrow d$ and $p \rightarrow s$ transitions along W1 - G1 as well as $sd \rightarrow p$ transitions along W - X and $p \rightarrow s$ transitions around the W point. This assignment of the interband peaks to excitations along high-symmetry lines compares well with results of Lee and Chang [92] and of Ehrenreich, Philipp, and Segall [84].

9.2 Optical properties of aluminum under pressure

From the experimental side, pressure-dependent reflecitivity measurements were performed by Tups and Syassen [91] on an aluminum-diamond interface. A theoretical study for pressures up to 31 GPa was presented by Dandrea and Ashcroft [94]. In this work, the evolution of the complex dielectric

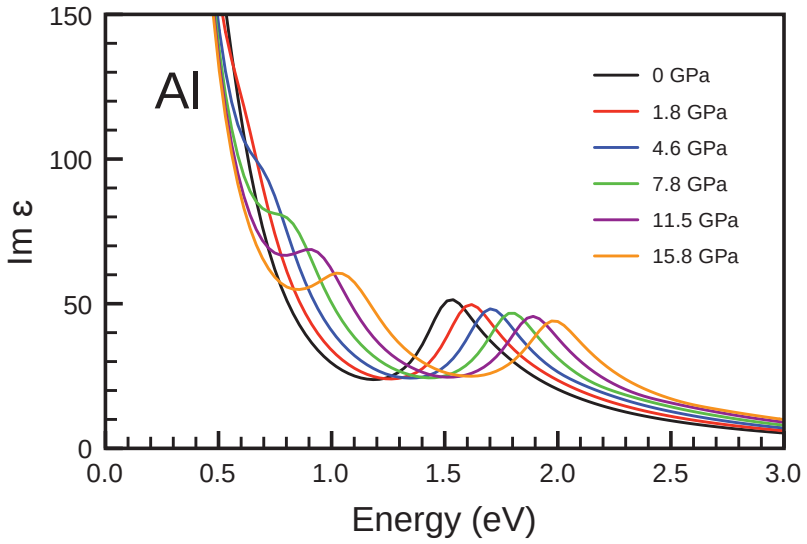

Figure 9.3: Imaginary part of the complex dielectric function of aluminum for increasing pressure up to 15.8 GPa.

function and reflectivity for increasing pressure up to 15.8 GPa will be investigated, including an analysis in terms of oscillator strengths.

Figure 9.3 depicts the imaginary part of the complex dielectric function for different pressure values. An increase in pressure, in general, leads to a blueshift of the whole spectrum. As a consequence, the first interband peak, normally masked by the free-electron contribution to the complex dielectric function, starts to emerge at approximately 4.6 GPa. As pressure increases further, it moves to higher energies accompanied by a reduction in height. Similarly to the first interband peak, the peak at 1.5 eV shifts upwards in energy. Its reduction in intensity is, however, smaller than that of the first peak. This can be traced back to the $1/\omega^2$ dependence of the imaginary part of the complex dielectric function which strengthens features at low energies, while it has a diminishing effect at higher energies. In fact, the multiplication of $\mathrm{Im}\,\epsilon(\omega)$ with ω^2 reveals an average increase per GPa, which is greater for the second interband peak. At 15.8 GPa, peak positions of 1.02 and 1.97 eV are found, respectively, corresponding to a total shift of roughly 0.5 eV.

The pressure dependence of the reflectivity is visualized in Fig. 9.4. As already discussed in the previous section, it is characterized by an absorption edge with a reflectivity of 84% at 1.47 eV. With increasing pressure, it gradually moves to higher energies. At a pressure of 15.8 GPa it is found at 1.9 eV with a lower reflectivity value of 78%. The reduction in reflectivity with

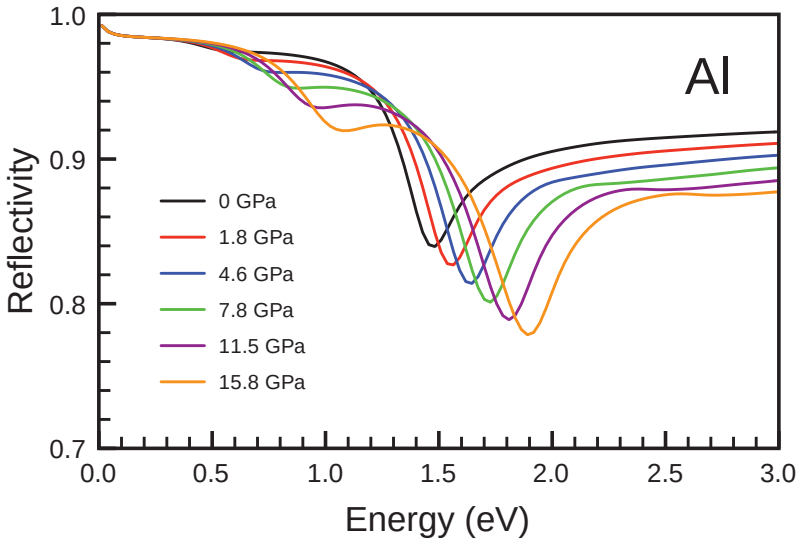

Figure 9.4: Reflectivity of aluminum for increasing pressure up to 15.8 GPa.

increasing pressure is observed almost for the whole energy range of interest. Only for very small energies up to approximately 0.4 eV no differences between the spectra are visible. In addition, applying pressure gives rise to a second minimum in the 0.5 to 1.3 eV range, developing out of a shoulder present at low pressure. At 15.8 GPa the minimum is found at 1.1 eV corresponding to a reflectivity of 92%. These results are in line with the findings of Dandrea and Ashcroft [94] and compare well with experimental data of Tups and Syassen [91] in terms of position. The features appear, however, less enhanced in the present calculation. This was traced back [94] to the fact that measurements and calculations were done for an aluminum-diamond interface instead of an aluminum-vacuum interface.

To allow for further analysis concerning the development of the two low-energy interband peaks, Fig. 9.5 shows the oscillator strengths for the $k_z = 0$, 5/34, 17/34, 33/34 (in units of $2\pi/a$) planes and transitions in the energy range from 0.1 to 2.1 eV. The positions of the planes within the fcc BZ are depicted in (a). In (b) - (d), the oscillator strengths for increasing pressure are visualized (see Sec. 7.3). The full analysis in terms of oscillator strengths for k_z increasing from 0 to 1 is given in Appendix B including cases not shown in Fig. 9.5 for applied pressures of 1.8, 4.6, and 11.5 GPa (see Figs. B.1 - B.6). In general, no change in the overall shape and position of the regions contributing to the two low-energy features are observed. Only the areas with the highest oscillator strengths move slightly, when pressure is applied. A closer look at the

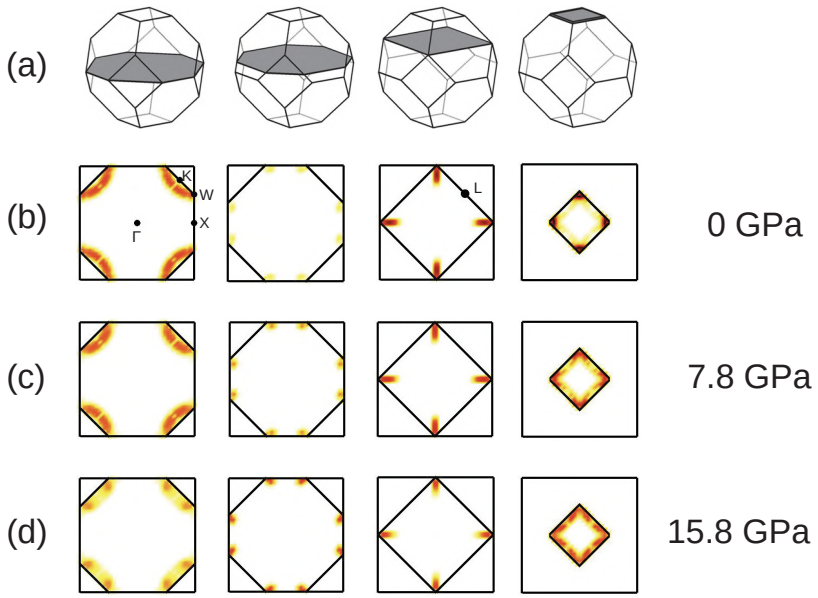

Figure 9.5: Oscillator strengths of aluminum under pressure for transitions in the energy range 0.1 to 2.1 eV. (a) fcc BZ with the selected plane highlighted. (b) - (d) Oscillator strengths for 0, 7.8, and 15.8 GPa, respectively. From left to right: $k_z = 0$, 5/34, 17/34, 33/34 (in units of $2\pi/a$). Regions with high oscillator strengths appear in dark red. The corresponding color bar is shown in Fig. 7.1.

first column of Fig. 9.5 reveals that for $k_z \approx 0$ predominant contributions stem from **k** points in an arc centered at the K point and reaching the W point. As pressure grows, the highest contributions are found around the W point. For greater k_z values, increasing oscillator strength along W - U (second column) are found for increasing pressure and around $k_z = 0.5$ (third column), the areas related to strong contributions move also closer to the W point. The case of k_z approaching 1 is shown in the fourth column. Without applied pressure, major oscillator strengths appear at the edges of the indicated square, while for a pressure of 15.8 GPa **k** points from the whole border of the BZ contribute.

To gain deeper insight, the band structures corresponding to pressures of 0, 7.8, and 15.8 GPa (from top to bottom) are given in Fig. 9.6. Comparison between them shows the changes in the band position. For the two valence bands sitting at -1.36 and -1.89 eV at K at zero pressure, a downwards shift is observed. At 15.8 GPa they are found 1.68 and 2.18 eV below E_F, respectively. In addition, the band character of the higher lying one changes

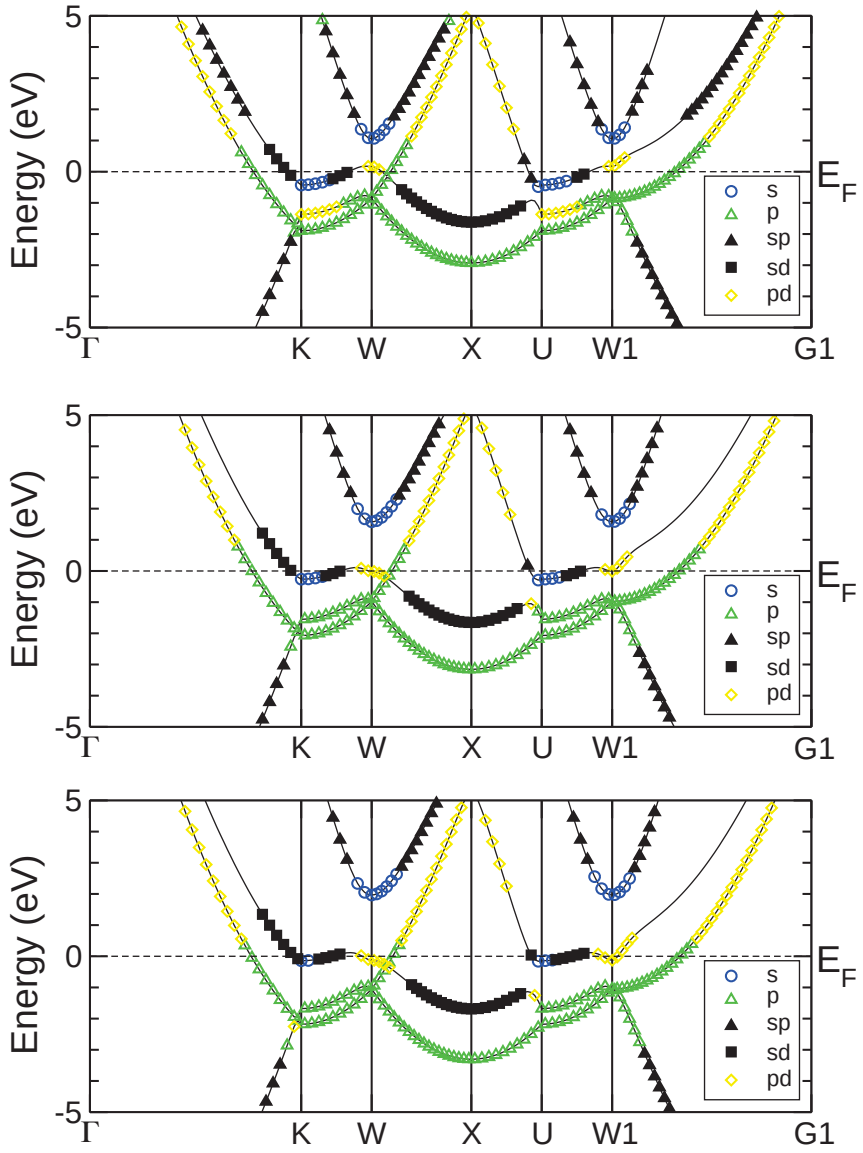

Figure 9.6: Band structure of aluminum for zero pressure (top) and for an applied pressure of 7.8 (middle) and 15.8 GPa (bottom).

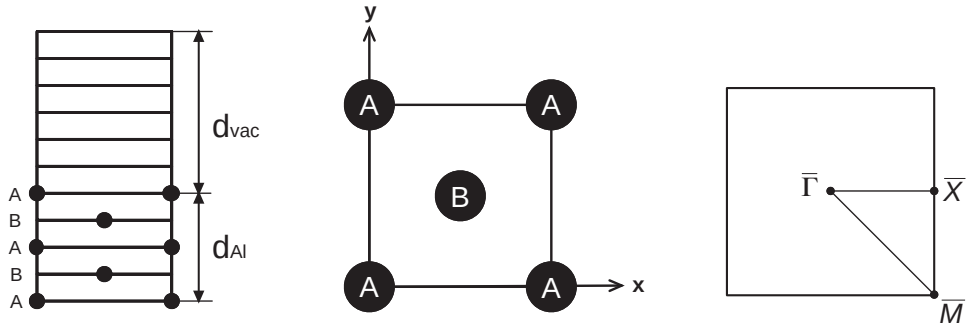

Figure 9.7: Left: Aluminum supercell consisting of a 5 MLs aluminum slab with thickness d_{Al} followed by a vacuum region of thickness d_{vac} corresponding to 6 MLs. The atomic positions are indicated by full circles. Middle: Top view onto the supercell. Right: Surface BZ with high-symmetry points marked by full circles.

from predominantly pd to p like along K - W and U - W1. The band at the Fermi level flattens and the parabolic conduction band of s and mixed sp character found at 1.06 eV above E_F at W shifts to a higher energy of 1.97 eV for a pressure of 15.8 GPa. As a consequence, the interband peaks gradually move to higher energies.

9.3 Thin Al(001) films

In this Section, the behavior of the complex dielectric function of thin Al(001) films is investigated for increasing slab thickness. To simulate thin films, a supercell approach is used, considering the experimental bulk lattice constant of 4.05 Å [64, 65]. As visible from the left panel of Fig. 9.7, the supercell consists of several monolayers (MLs) Al, where two subsequent MLs are shifted relative to each other by (0.5|0.5) in the xy plane (right panel). The supercell is built by adding Al MLs in z direction, until the Al slab reaches the desired thickness d_{Al}. A vacuum region of thickness d_{vac} is introduced to separate surfaces of subsequent slabs. The lattice constants of the Al(001) supercell are given by

$$a_x = a_y = \frac{1}{\sqrt{2}} a_{Al} = \frac{1}{\sqrt{2}} \cdot 4.05 \text{ Å} \approx 2.86 \text{ Å} \tag{9.1}$$

in x and y direction, whereas the lattice constant in z direction is determined by $a_z = d_{Al} + d_{vac}$. Within this supercell, the inequivalent atoms of the Al slab

are sitting at

$$\text{A}\left(0.0|0.0|\frac{(k-1)\cdot a_{Al}}{2\cdot a_z}\right) \quad \text{for } 1\leq k\leq n \text{ and } k \text{ odd} \tag{9.2}$$

and

$$\text{B}\left(0.5|0.5|\frac{(k-1)\cdot a_{Al}}{2\cdot a_z}\right) \quad \text{for } 1\leq k\leq n \text{ and } k \text{ even}, \tag{9.3}$$

where n denotes the number of Al MLs.

The ground-state calculations were performed for a 67×67×1 **k**-point mesh adopting a RK_{max} value of 8 and including local orbitals for the $2s$ and $2p$ semi-core states. 150×150×1 **k**-point meshes were used for the optical spectra. To find an appropriate thickness of the vacuum region, careful convergence tests were performed for a 5 MLs Al slab. d_{vac} was varied from 8.1 to 20.25 Å. The resulting spectra are depicted in the upper panel of Fig. 9.8. A decrease of Im $\varepsilon(\omega)$ for increasing vacuum thickness is observed. This behavior is related to the use of the supercell approach to simulate the thin films. We have to consider that the complex dielectric function of the supercell not only contains the contribution of the Al slab but also from the vacuum region, i.e., the imaginary part of the dielectric function is given by

$$\text{Im } \varepsilon(\omega) = \text{Im } \varepsilon_{slab}(\omega) + \text{Im } \varepsilon_{vac}(\omega), \tag{9.4}$$

where the latter is zero. Since ε is dimensionless, the integration over unit cells of different sizes (see Eq. (4.24)) introduces an artificial volume dependence, which makes a renormalization of the spectra necessary. For correcting the spectra, one has to rescale them by

$$\frac{\Omega_{sc}}{\Omega_{slab}} = \frac{a_z}{d_{Al}}, \tag{9.5}$$

where Ω_{sc} and Ω_{slab} denote the volumes of the whole supercell and the Al slab, respectively. The result is displayed in the lower panel of Fig. 9.8. The artificial decrease of Im $\varepsilon(\omega)$ for increasing thickness of the vacuum region has disappeared and except for the spectrum corresponding to $d_{vac} = 8.10$ Å, all spectra now lie on top of each other. This indicates that interactions across the vacuum region between the top layer of one slab and the bottom layer of the subsequent one are still present for a 8.10 Å thick vacuum region. A vacuum region of 12.15 Å thickness is then already sufficient to prevent these interactions (at least) in the energy range considered here. To be on the save side, supercells with $d_{vac} = 16.2$ Å (i.e. 8 empty MLs) were finally used in the calculations.

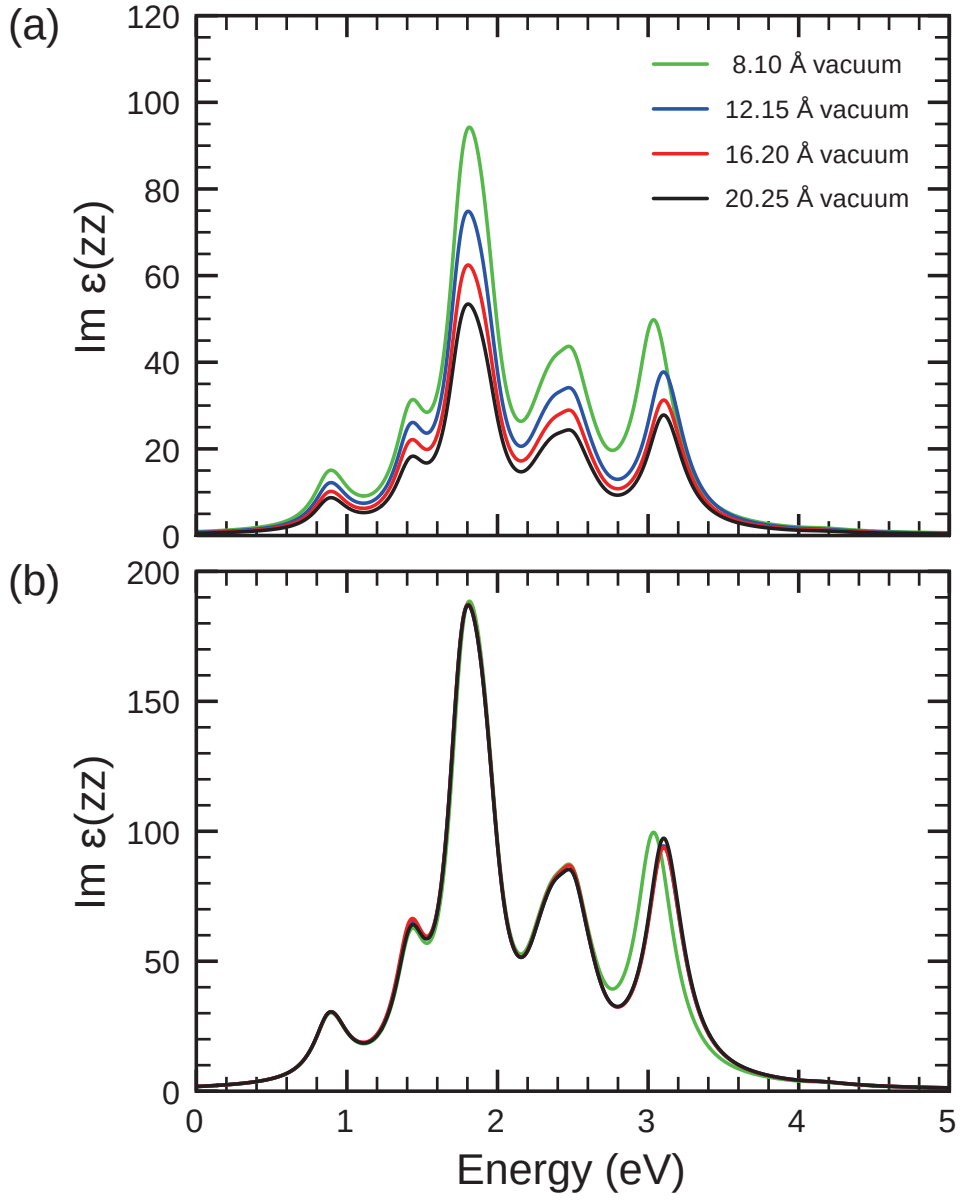

Figure 9.8: Evolution of the zz component of Im $\varepsilon(\omega)$ with increasing thickness of the vacuum region for a 5 MLs Al(001) slab. (a) Raw data; (b) renormalized spectra. The spectra for 12.15, 16.20, and 20.25 Å vacuum lie on top of each other. A Lorentzian broadening of 0.1 eV was included.

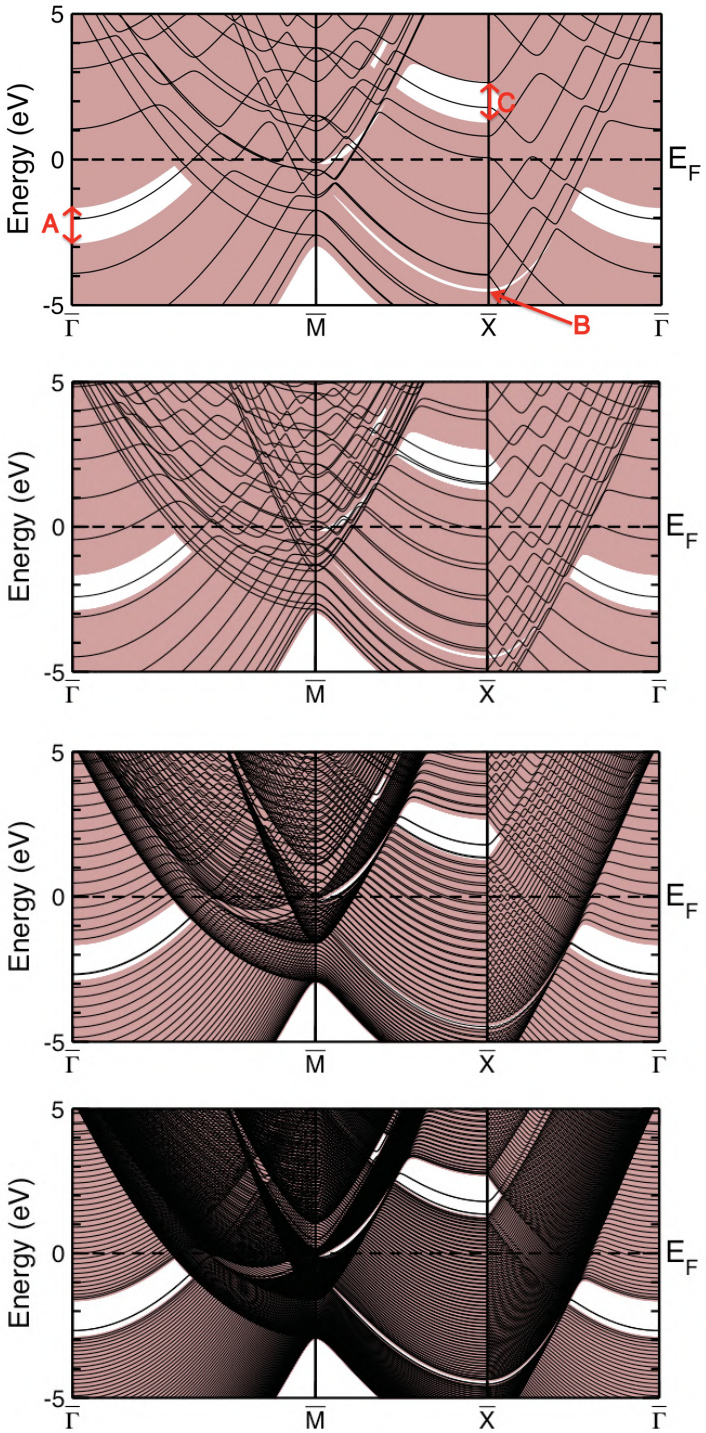

Figure 9.9: Band structure of Al slabs of different thickness together with the two-dimensional projection of the Al bulk bands onto the (001) surface. From top to bottom: 5 MLs, 11 MLs, 41 MLs, and 101 MLs Al.

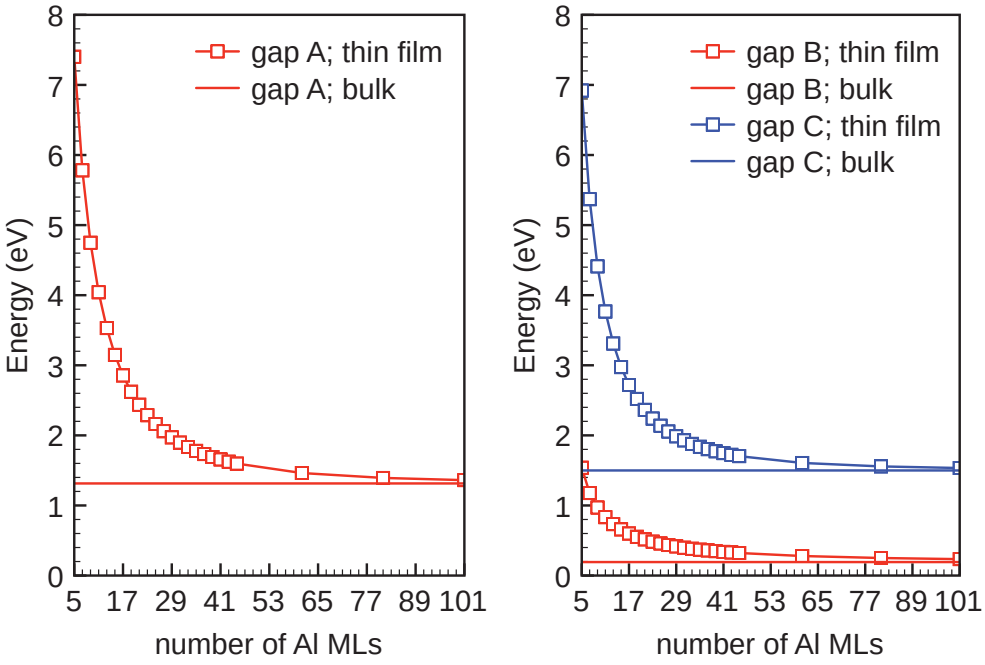

Figure 9.10: Evolution of the energy gaps at $\overline{\Gamma}$ (left panel) and $\overline{\mathrm{X}}$ (right panel) as a function of Al MLs.

Before we turn to the optical excitations, the evolution of the energy band structure with increasing slab thickness is investigated. Figure 9.9 depicts the energy bands for different Al slabs (black). In addition, the projection of the three-dimensional band structure of bulk Al onto the two-dimensional Al(001) surface is displayed in brown. Thereby, the procedure described in Ref. [95] was followed, considering 320 equidistant k_z values. It will be used to distinguish between bulk-like bands and additional bands due to the presence of the surface, that are located in the gaps of the bulk projection. The uppermost panel of Fig. 9.9 shows the existence of several gaps in the two-dimensional bulk BS. A broad one starts at $\overline{\Gamma}$ and ends at approximately half the distance $\overline{\Gamma}$ - $\overline{\mathrm{M}}$ in the valence-band region. Three gaps are visible along $\overline{\mathrm{M}}$ - $\overline{\mathrm{X}}$. The very narrow first one is situated in the valence-band region. The second one starts approximately at the Fermi level. It is extremely narrow at the beginning but turns into a broad gap at roughly half the distance $\overline{\mathrm{M}}$ - $\overline{\mathrm{X}}$. The third one is found at a higher energy in the second quarter of the path $\overline{\mathrm{M}}$ - $\overline{\mathrm{X}}$. Along $\overline{\mathrm{X}}$ - $\overline{\Gamma}$ one gap is present in the valence region and another one occurs above E_F around $\overline{\mathrm{X}}$. These observations are in line with the findings of Caruthers and

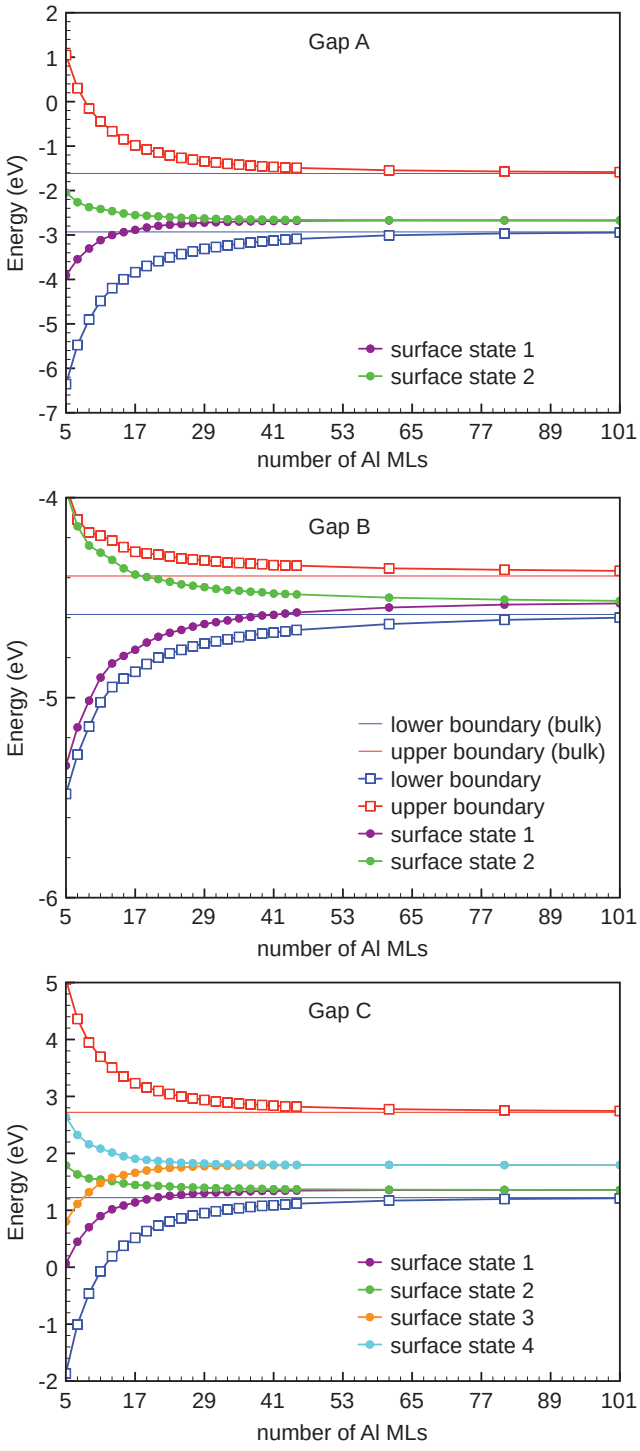

Figure 9.11: Behavior of surface states at $\overline{\Gamma}$ and $\overline{X}$ as a function of Al MLs.

co-workers [95], except for the third gap along $\overline{\mathrm{M}}$ - $\overline{\mathrm{X}}$, which is not present in their results. Fig. 9.9 also reveals that the energy bands for very thin Al slabs already reproduce the overall structure of the projected bulk BS. Due to the finite thickness of the slabs, well separated bands are present, which move closer together as the slab thickness grows. As a consequence, gap A at $\overline{\Gamma}$ as well as gaps B and C at $\overline{\mathrm{X}}$ decrease in size (see Fig. 9.10). Gap A is roughly 0.2 and 0.8 eV smaller than obtained by Caruthers and co-workers [95] for a 13 and 39 MLs slab, respectively, which is most likely a consequence of the higher accuracy reached in the present *ab initio* calculation of the electronic structure. For the 101 MLs thin film, gaps of 1.36 eV (A) at $\overline{\Gamma}$, 0.23 (B) and 1.53 eV (C) at $\overline{\mathrm{X}}$ are obtained by the calculations, which are already quite close to values of 1.31, 0.19, and 1.50 eV found for bulk Al, respectively.

Surface bands are formed within these gaps. The knowledge about the behavior of surface states is extremely important for the interpretation of the optical spectra given below. Thus, the evolution of the energies of surface states as well as of energy states defining the gaps at $\overline{\Gamma}$ and $\overline{\mathrm{X}}$ are displayed in Fig. 9.11. Two surface states are present in gap A (see upper panel). As the film thickness increases, the lower one moves upwards in energy, while the upper one shifts downwards. As a consequence, the energy difference between them decreases. For 101 MLs they are degenerate at an energy of -2.673 eV. The energies of the two surface states within gap B are -4.529 eV and -4.516 eV, respectively (see middle panel). Gap C contains four well separated surface states for a 5 MLs thin film (see bottom panel). With increase in film thickness always two of them converge to the same energy. For 101 MLs these pairs degenerate at energies of 1.356 and 1.793 eV, respectively. The results show the same general trend as found in Ref. [95], i.e., a decrease in the surface-state splittings at $\overline{\Gamma}$ and $\overline{\mathrm{X}}$ with growing slab thickness. Due to the higher accuracy reached in the present calculation, the obtained energy differences are, in general, smaller. Caruthers and co-workers [95] ascribed these splittings to interactions between surface states of the top and bottom surface, which have not decayed to zero in the middle of the film. Excellent agreement with Heinrichsmeier and co-workers [96] is achieved for the surface-state splittings and the average energies of different pairs of surface states (deviations of less than 0.03 eV for the 25 MLs slab). Only the energy gap at $\overline{\Gamma}$ is 0.76 eV bigger in the present calculation.

Figure 9.12 depicts the imaginary part of the xx and zz component of the dielectric tensor for Al slabs increasing from 5 (uppermost right panel) to 101 MLs (lowest right panel). Due to the symmetry of the unit cell in x and y direction, the xx and yy components of the dielectric tensor are identical. For comparison, the bulk dielectric function of Al is displayed. By increasing the slab thickness, the shape of the xx component (red) approaches that of the

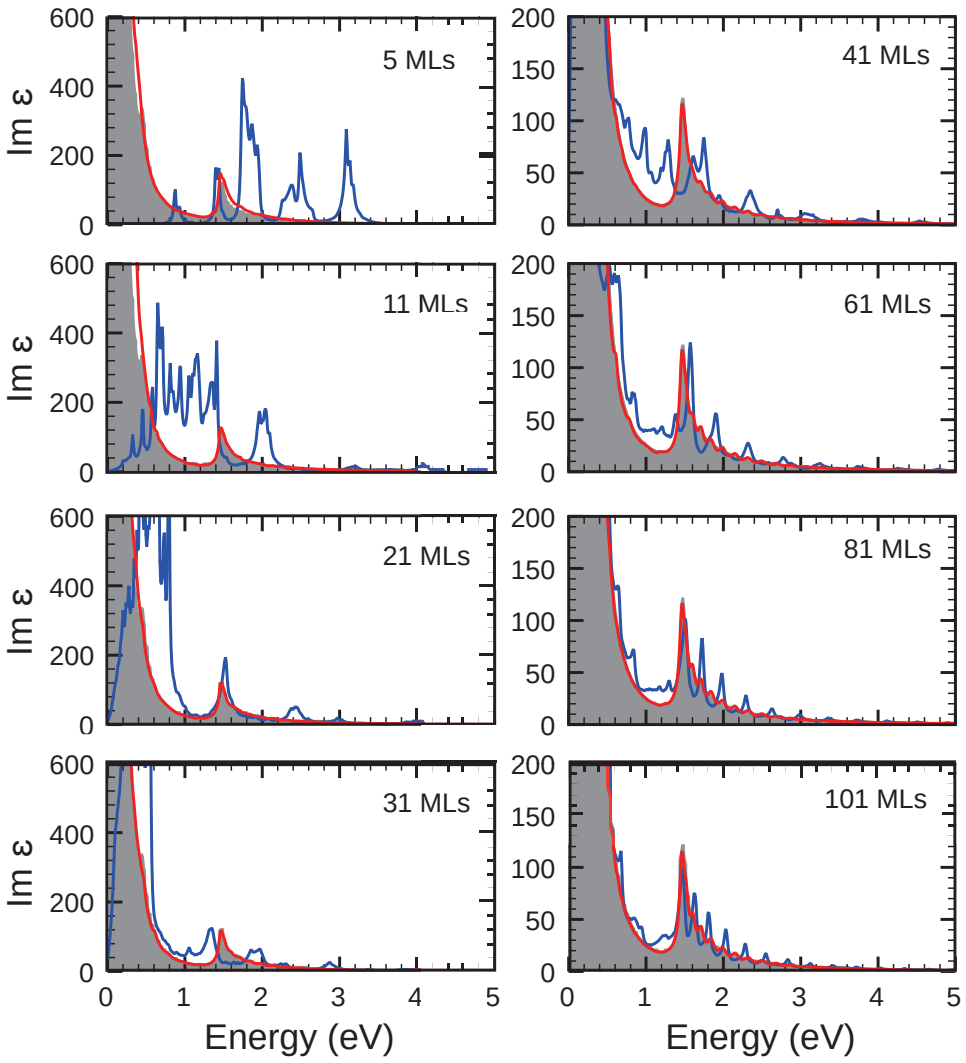

Figure 9.12: Imaginary part of the xx (red) and zz (blue) component of the complex dielectric tensor of a thin Al(001) film for increasing thickness of the Al slab in comparison with the bulk dielectric function (grey-shaded area). A Lorentzian broadening of 0.01 eV was adopted.

Figure 9.13: Oscillator strengths of a 5 MLs Al slab for the energy ranges 0.7 - 1.2 eV (a), 1.2 - 1.5 eV (b), 1.5 - 2.1 eV (c), 2.1 - 2.7 eV (d), and 2.7 - 3.4 eV (e). Regions with high oscillator strengths are displayed in dark red. The corresponding color bar is shown in Fig. 7.1.

bulk dielectric function (grey-shaded area). 11 MLs Al are enough to reproduce the main spectral features of bulk Al. As the number of Al MLs increases, only slight deviations remain.

A different situation occurs for the zz component (blue). For 5 MLs the spectrum consists of five well-separated interband peaks, but no intraband transitions are present, characteristic for an insulator or semiconductor. The origin of these five features will be investigated in the following using the oscillator strengths determined by the procedure described in Sec. 7.3. The double-peak at roughly 0.9 eV originates from excitations between bands around the Fermi level. Fig. 9.13(a) reveals that the highest contributions stem from **k** points at and close to the $\overline{\mathrm{M}}$ point (along $\overline{\mathrm{M}}$ - $\overline{\Gamma}$) as well as on slightly bent lines starting at half the distance $\overline{\Gamma}\,\overline{\mathrm{X}}$ and ending at half the distance $\overline{\Gamma}\,\overline{\mathrm{M}}$. Transitions in thin arc-shaped regions starting and ending at the $\overline{\mathrm{M}}$ points give rise to the feature centered at 1.4 eV. The arcs intersect the line $\overline{\Gamma}$ - $\overline{\mathrm{X}}$ between 50 and 60% of the distance $\overline{\Gamma}\,\overline{\mathrm{X}}$ (see Fig. 9.13(b)). The multi-peak structure around 1.8 eV arises from excitations at **k** points in similar arc-shaped areas slightly closer to the BZ boundary as well as in a ring touching the BZ boundary at $\overline{\mathrm{X}}$. As visible from Fig. 9.13(c), the highest contributions are located in areas where these regions overlap. A different situation occurs for the subsequent structure centered at 2.4 eV. Fig. 9.13(d) shows that it arises from boomerang-shaped regions centered along $\overline{\Gamma}$ - $\overline{\mathrm{M}}$ at roughly 40, 65, and 80% of the distance from the centre of the BZ. Weaker contributions stem from lines parallel to the BZ boundary at 1/3 and 1/2 $\overline{\Gamma}\,\overline{\mathrm{X}}$, respectively. With the help of Fig. 9.13(e), the peak at 3.1 eV can be ascribed to transitions in a circular area with a radius of approximately 70% $\overline{\Gamma}\,\overline{\mathrm{X}}$, except of a small region around $\overline{\Gamma}$.

As the number of Al MLs grows, a low-energy multi-peak feature forms in the energy range up to 1.6 eV (see second row, left panel). It shifts to lower

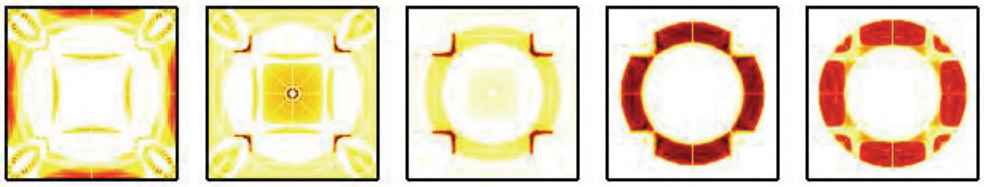

Figure 9.14: Oscillator strengths of a 101 MLs Al slab for the energy ranges 0.63 - 0.69 eV (a), 0.75 - 0.96 eV (b), 1.15 - 1.29 eV (c), 1.36 - 1.54 eV (d), and 1.75 - 1.86 eV (e). Regions with high oscillator strengths are displayed in dark red. The corresponding color bar is shown in Fig. 7.1.

energies, thereby decreasing in width and increasing in magnitude, in line with findings presented by Kurbatsky and co-workers [97]. From the band structures given in Fig. 9.9 it is visible, that the number of bands around the Fermi level increases and the distance between them decreases as the slab thickness grows. As a consequence, the single peaks shift to lower energies and start to overlap, as they get closer together. The second column of Fig. 9.12 shows that the overall shape of the spectrum below approximately 1.3 eV gets more and more bulk-like.

For the thickest film studied in this work, the spectral weight in the 0.5 to 1.3 eV range is still roughly 20% higher than for bulk Al, which is related to the existence of three additional features in the 101 Al MLs thin-film spectrum. Fig. 9.14(a) indicates, that the spike at 0.67 eV mainly arises from transitions between discrete thin-film bands at **k** points close to the $\overline{\mathrm{X}}$ point as well as along $\overline{\mathrm{X}}$ - $\overline{\mathrm{M}}$. In the 0.75 to 0.96 eV range, high oscillator strenghts are present close to the centre of the BZ and in boomerang-shaped areas located between 48 and 52% of the distance $\overline{\Gamma}\,\overline{\mathrm{M}}$ measured from $\overline{\Gamma}$ (see Fig. 9.14(b)). The transitions predominantly take place between discrete thin-film bands. To some extent, excitations at **k** points in the boomerang-shaped areas also involve energy states, which lie on the continuation of the surface band into the region of densely-packed descending thin-film bands along $\overline{\Gamma}$-$\overline{\mathrm{M}}$. Fig. 9.14(c) reveals that in the 1.15 to 1.29 eV range, highest oscillator strengths occur again in boomerang-shaped regions between 44 and 48% of the distance $\overline{\Gamma}\,\overline{\mathrm{M}}$ measured from $\overline{\Gamma}$. In addition, **k** points in a ring-shaped area contribute. Excitations from energy states along the continuation of the surface bands into the region of densely-packed bands along $\overline{\Gamma}$ - $\overline{\mathrm{X}}$ and $\overline{\Gamma}$ - $\overline{\mathrm{M}}$ are predominantly involved in its creation. In the boomerang-shaped region, in addition, transitions be-

tween the discrete thin-film bands occur. Since the origin of this feature can be attributed to the presence of surface bands, we expect it to remain in the spectrum at roughly the same position, if the film thickness is further increased.

The peak at 1.47 eV in the spectrum of the 101 MLs slab is related to the bulk interband peak, but still has a slightly lower magnitude. Fig. 9.14(d) shows high oscillator strengths in a ring shaped region between 53 and 84% of the distance $\overline{\Gamma}\,\overline{\mathrm{X}}$ (measured from $\overline{\Gamma}$), except of small triangular areas along $\overline{\Gamma}$ - $\overline{\mathrm{M}}$. The corresponding transitions occur predominantly between the discrete thin-film bands. Energy states lying on the continuation of the two bands defining the gaps along $\overline{\Gamma}$ - $\overline{\mathrm{X}}$ and $\overline{\Gamma}$ - $\overline{\mathrm{M}}$ and crossing the region of descending bands, are mainly involved in its creation. Since the bands are further apart for thinner Al slabs, this peak shifts to higher energies, when decreasing the slab thickness. At least 61 Al MLs have to be considered in the thin-film calculation to obtain a peak position, which is in reasonable agreement with the position of the bulk interband peak.

The sharp spikes above 1.5 eV do not have a counterpart in the bulk Al spectrum. Their presence leads to a roughly 15% higher spectral weight and the magnitudes at the peak positions are between 65 and 125% bigger than for bulk Al. For slabs thinner than 61 Al MLs, they are visible as multi-peak features. Their origin can be traced back to the finite size of the thin-film and the presence of the two surfaces, which result in discrete energy bands and additional surface bands. Fig. 9.14(e) depicts the oscillator strengths for one of these spikes centered at 1.8 eV. It predominantly arises from excitations at **k** points in a similar region as for the bulk-like feature before. The width of the peaks and the spacing between them slightly grow with growing energy. The changes in magnitude when increasing the number of Al MLs from 81 to 101 indicate, that their magnitudes will diminish further. We expect that an increase in film thickness by, at least, 40 to 60 MLs is necessary to bring the magnitudes of these peaks close to those obtained for the wells in the xx component.

The investigations above revealed that the finite thickness of the Al films and the presence of the surfaces alter the band structure, thereby giving rise to additional spectral features compared to bulk Al. The effects are strongest for thin Al slabs, where Imε_{zz} is characterized by various multi-peak structures. Starting with roughly 61 Al MLs slabs, the overall shape of the spectrum can be seen as bulk-like. Transitions between discrete thin-film bands mainly influence the energy range above the bulk interband peak, where additional features in form of almost equally-shaped spikes are present. These spikes have the tendency to move closer together and to diminish with increasing slab thickness. Thus, they will most likely vanish completely. Excitations involving surface bands have the greatest impact on the 1 to 1.5 eV range, giving rise to a feature which we expect to remain visible in the spectra of much thicker slabs.

10 Relativistic effects in the optical spectra of selected metals

In this Chapter, the influence of SO coupling on the optical spectra of gold, platinum, lead, and tungsten is studied. Calculations including and neglecting SO coupling were performed to underline the importance of a relativistic treatment. Comparison with experimental data also highlight for which material and energy range SO interaction is indeed relevant. Furthermore, an analysis of the most important features in terms of oscillator strengths and origin within the BZ is given. The theoretical spectra together with the discussion and analysis of the most important relativistic effects have already been published in Ref. [98]. For details concerning the calculations and the analysis in terms of oscillator strengths see Chapter 7.

10.1 Gold

Because of its high atomic mass, gold is one of the best candidates for studying relativistic effects in the description of the electronic structure and optical properties. The golden color, for example, is only predicted correctly if a relativistic treatment is adopted [99–103]. Thus, numerous theoretical studies dealing with relativistic effects are available in literature [99, 103–111]. Most of them focus on the band structure, like the early pioneering work by Christensen and Seraphin [104–107] carried out by means of the relativistic APW method, adopting a potential constructed to achieve best possible agreement with experiment. The model band structure presented by Smith [112] was obtained by a fitting procedure to non-relativistic and relativistic APW data including SO effects through an additional parameter. More recently, Dal Corso,

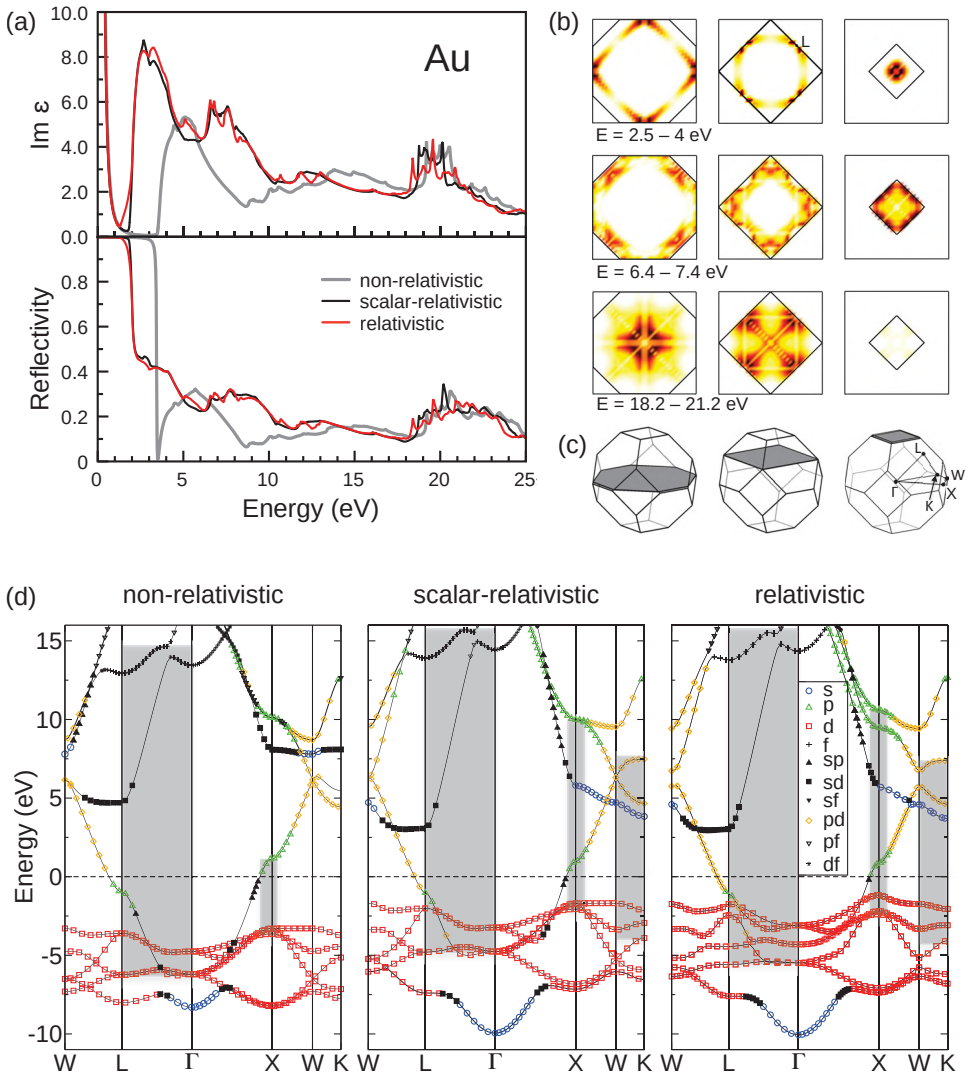

Figure 10.1: (a) Imaginary part of the complex dielectric function (top) and reflectivity (bottom) of gold from a non-relativistic (gray), a scalar-relativistic (black) and a relativistic calculation (red). (b) Oscillator strengths for selected energy ranges and planes inside the BZ. From top to bottom: $E = 2.5$ - 4 eV, $E = 6.4$ - 7.4 eV, and $E = 18.2$ - 21.2 eV; from left to right: $k_z = 1/34$, 17/34, and 33/34 (in units of $2\pi/a$). Regions with high oscillator strengths appear in dark red. (c) fcc BZ with the selected planes highlighted. (d) Band structures of gold for the non-relativistic (left panel), scalar-relativistic (middle panel) and relativistic (right panel) calculation. The predominant band characters are shown by the symbols and colors depicted in the legend. Important regions for the creation of the different optical features are marked by gray boxes.

and Mosca Conte [108] presented results obtained with fully-relativistic ultrasoft pseudopotentials. Theileis and Bross [110] used the relativistic modified APW method in their electronic-structure calculations. Calculations of the optical spectra including relativistic effects were performed by Antonov and co-workers [111] within the relativistic LMTO method, adopting the atomic-sphere approximation. More recent *ab initio* results of Romaniello and co-workers [103] are based on the ZORA approximation to include scalar-relativistic effects, whereas SO coupling was introduced in the electronic-structure calculation only. Its effect on the dielectric function was only estimated. In both cases, no analysis of relativistic effects on the spectra was given.

In this Section, a detailed discussion on the impact of scalar-relativistic effects and SO coupling on the optical spectra is presented for energies up to 25 eV. For this purpose, a non-relativistic, a scalar-relativistic, as well as a relativistic calculation including SO coupling were performed. The most prominent features are compared and analyzed in terms of oscillator strength, thereby locating their origin in **k** space.

In Fig. 10.1(a) the results for the non-relativistic (gray), scalar-relativistic (black), and relativistic calculation including SO interaction (red) are displayed. For the imaginary part of the complex dielectric function (upper panel), the inclusion of scalar-relativistic terms, i.e., the mass-velocity and Darwin corrections, has the greatest effect. The interband onset is lowered by 1.65 eV from 3.5 to 1.85 eV. Inclusion of SO coupling leads to an additional decrease in transition energy by 0.5 eV. Similarly to the interband onset, the first maximum is shifted downwards in energy by roughly 2 eV, even getting more prominent compared to its non-relativistic counterpart. Around 7 eV, scalar-relativistic effects give rise to a double-peak structure which is completely missing in the non-relativistic spectrum. At higher energies, a difference in position of 0.5 eV between the non- and scalar-relativistic spectrum is observed for the multi-peak structure around 20 eV. Comparing our results with the calculations of Romaniello and de Boeij [103] reveals reasonable agreement for energies up to 10 eV. Overall agreement with the results of Antonov and co-workers [111] is observed for the energy range up to 20 eV, whereas in the 20 - 25 eV range, the peak positions deviate from ours by a few eV, thereby failing to reproduce recent measurements [10].

The impact of the interband onset is visible in the reflectivity depicted in the lower panel of Fig. 10.1(a). A sharp absorption edge is observed at 3.5 eV in the non-relativistic case, with the reflectivity dropping to almost 0%. Since the reflectivity is 100% up to this energy and photons related to the visible range of the electromagnetic spectrum carry energies between 1.7 and 3.4 eV, gold would reflect the whole spectrum of visible light, thus appearing white in contrast to reality. As the absorption edge is lowered in energy when relativ-

ity is accounted for, the red component of incoming light is reflected almost perfectly. The reflectivity of the remaining colors, corresponding to energies greater than 1.9 eV, reduces to roughly 40%. This, in principle, explains the formation of the characteristic golden color. Still, the yellow contribution is diminished due to the underestimated interband onset energy, which can be traced back to an improper d-band position.

The relativistic treatment also influences the plasma frequency describing the free-electron contributions. It gets reduced from 9.44 to 8.96 eV when scalar-relativistic terms are taken into account. Inclusion of SO interaction leads to a further decrease to 8.81 eV, being in excellent agreement with a value of 8.83 eV extracted from experimental data by Cooper, Ehrenreich, and Philipp [99]. Moreover, it compares well with the theoretical value of 8.78 eV reported by Antonov and co-workers [111].

In the following, the differences between the optical spectra of the three calculations are analyzed in terms of oscillator strengths and assigned to regions in **k** space. For this purpose, the oscillator strengths corresponding to the relativistic case including SO interaction were determined according to Eq. (7.2). The results are depicted in Fig. 10.1(b) for the energy ranges 2.5 - 4 eV, 6.4 - 7.4 eV, and 18.2 - 21.2 eV together with the selected planes shown in Fig. 10.1(c). It should be noted at this point, that relativistic effects mainly influence the joint density of states rather than the matrix elements. As already pointed out by Benbow and Smith [113], SO interaction leads to a redistribution of matrix elements with the sum over the squared matrix elements almost staying constant.

To support the analysis of the most important spectral features, the band structures are displayed in Fig. 10.1(d). Therein, the predominant band characters are marked by the colors and symbols given in the legend, which allows for an interpretation of the momentum matrix elements in terms of atomic-like selection rules. A comparison of the band structure with recent results by Dal Corso and Mosca Conte [108] and by Theileis and Bross [110] reveals reasonable agreement. The deviations of the energy eigenvalues at high-symmetry points are smaller than 0.2 and 0.3 eV, respectively. In case of an earlier calculation of Christensen and Seraphin [105], however, maximum deviations of 1.25 eV occur.

In the valence-band region, a scalar-relativistic treatment shifts the highest d bands closer to E_F by roughly 1.6 eV. In addition, the band width of the low-lying parabolic s band increases, with the minimum at Γ appearing at -10 eV, compared to -8.3 eV in the non-relativistic case. For the conduction bands, the major effects are an upward shift of the f bands situated between 12.9 and 14.6 eV along L - Γ by approximately 1 eV (left and middle panel of Fig. 10.1(d)) and a downward shift of the lowest sd bands around 5 eV along

W - L and around 8 eV along X - W - K. The former one is then found at 3 eV above E_F and stays almost horizontal. For the latter, an increase in bandwidth is observed, accompanied by a change of its predominant character to s-like. In the scalar-relativistic case the corresponding s states are sitting at 5.8 eV (at X), 4.7 eV (at W), and 3.8 eV (at K). Inclusion of SO coupling results in only minor changes, mainly in form of band splittings around high-symmetry points (see right panel of Fig. 10.1(d)).

Combining the analysis of oscillator strengths with the bandstructure reveals that the interband threshold energy is determined by $d \rightarrow p$ excitations from the uppermost valence band to the Fermi level. The corresponding **k** points are located in a V-shaped region around the X point (see upper left panel of Fig. 10.1(b)). The subsequent interband peak at 5 eV can be ascribed to transitions in regions around the X and L points. Moreover, **k** points in a ring-shaped area close to the BZ boundaries contribute.

The double-peak structure around 7 eV, which shows up in the relativistic case only, arises due to $d \rightarrow s$ and $d \rightarrow p$ transitions along W - K. The d-like valence bands are situated close to the Fermi level. The conduction bands involved in its creation show predominant s and pd character. In addition, **k** points from the BZ boundaries contribute (see middle row of Fig. 10.1(b)).

The small hump around 12 eV in the scalar-relativistic spectrum arises from $d \rightarrow p$ transitions in a region around the X point. The excitations occur between a d band 2.1 eV below E_F and a p-like conduction band at 10 eV above the Fermi level. The SO splitting of the p band, with the two branches appearing at 9.5 and 10.6 eV, leads to the observed double-peak structure (see Figs. 10.1(a) and (d)).

Finally, $d \rightarrow f$ transitions give rise to the features observed around 20 eV. As shown in the bottom row of Fig. 10.1(b), **k** points located close to the center of the BZ, as well as in an area around L are involved. In addition, excitations at **k** points along Γ - L and K - L (closer to L) contribute. The reduction in transition energy by roughly 0.5 eV due to the inclusion of scalar-relativistic terms mainly results from changes in the band structure. The flat d-like valence bands around -6.2 eV along Γ - L move closer to the Fermi level by approximately 1.5 eV. This is accompanied by an upward shift of the f bands at 12.9 eV at L and 13.5 eV at Γ (left panel of Fig. 10.1(d)) by roughly 1 eV (middle panel of Fig. 10.1(d)). SO interaction splits the d band around -4.8 eV into branches around -4.4 and -5.6 eV at L, and -4.3 and -5.5 eV at Γ. The f bands remain almost unaffected. Only a moderate downward shift of 0.1 eV occurs (see right panel of Fig. 10.1(d)). The results presented in this Section are published in Refs. [10] and [98]. For the full analysis in terms of oscillator strengths including 35 planes in the BZ see Appendix C (Figs. C.1 - C.3).

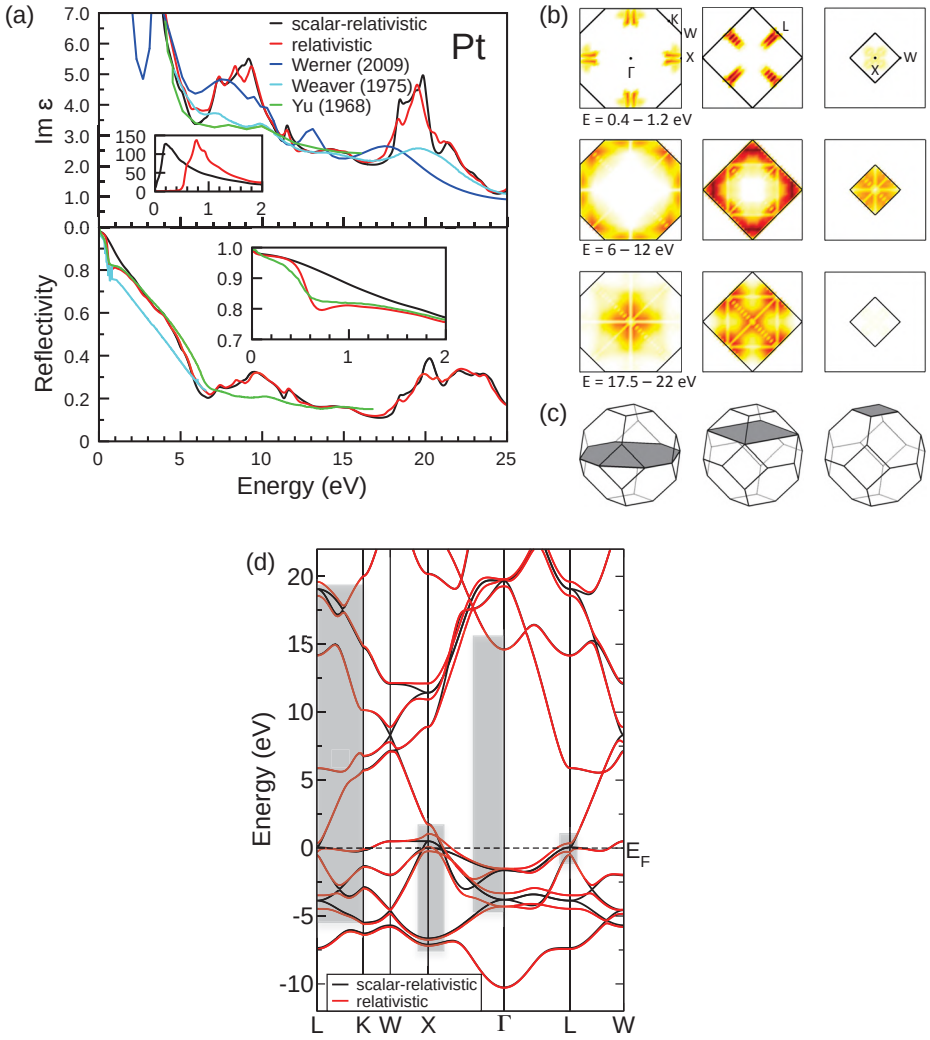

Figure 10.2: (a) Imaginary part of the complex dielectric function (upper panel) and reflectivity (lower panel) of platinum for the scalar-relativistic (black) and relativistic calculation including SO coupling (red). Experimental data are taken from Werner [10] (dark blue), Weaver [74] (light blue) and Yu [114] (green). (b) Analysis of oscillator strengths of platinum for selected energy ranges and planes inside the Brillouin zone. From top to bottom: $E = 0.4$ - 1.2 eV, $E = 6$ - 12 eV, and $E = 17.5$ - 22 eV; from left to right $k_z = 0$, 0.5, and 1.0 (in units of $2\pi/a$). (c) fcc BZ with the selected planes highlighted. (d) Band structure of platinum along high-symmetry lines. The bands including SO interaction are given in red, whereas black indicates the scalar-relativistic result. The gray boxes highlight the most active regions for the creation of different optical features.

10.2 Platinum

The imaginary part of the complex dielectric function is given in the upper panel of Fig. 10.2(a) for energies up to 25 eV together with the experimental data of Werner [10], Weaver [74], and Yu [114]. A Comparison of the present results with an earlier calculation of Krasovskii and Schattke [78] yields reasonable overall agreement. The findings presented below are, however, in contradiction with their observation that SO coupling has no tangible effect on the optical spectra up to 40 eV. Concerning the calculations of Antonov and coworkers [111], good agreement is obtained except for the first interband peak which is roughly twice as high in the present calculation. The relativistic band structure, displayed in Fig. 10.2(d) (red curve) and used in the interpretation of the spectra, is similar to the results of Dal Corso and Mosca Conte [108] and of Theileis and Bross [110]. Deviations at high-symmetry points are lower than 0.3 and 0.4 eV, respectively.

A plasma frequency of 7.54 eV, which is 0.12 eV smaller than the value given by Antonov and co-workers [111], is obtained and further used for the description of the free-electron contributions. Neglecting SO interaction leads to a considerably larger plasma frequency of 8.82 eV. Strong interband transitions occur in the low-energy part of the spectrum (see inset in the upper panel of Fig. 10.2(a)). SO effects have the greatest impact on this part of the spectrum. The inclusion of SO interaction results in an upward shift of the first interband peak by roughly 0.6 eV. Although this absorption feature, now present around 0.8 eV in Imε, is masked by the free-electron contribution, a reduction in the reflectivity by approximately 12% occurs. This is crucial to achieve good agreement with experimental data in this energy range (see insets of Fig. 10.2(a)). From an analysis in terms of oscillator strengths follows that major contributions in this low-energy range stem from small pockets around the high-symmetry points X and L (see top row of Fig. 10.2(b)). The main peak is created by excitations at **k** points along Γ - X, distinctly closer to X. The corresponding transitions are predominantly $d \rightarrow p$ like. Although the momentum matrix elements are moderate, the $1/\omega^2$ behavior of Imε leads to significant contributions to the optical response. The inclusion of SO interaction causes band splittings at the Fermi level around the high-symmetry points X and L (see Fig. 10.2(d)), which are responsible for the opening of a gap between the highest valence and lowest conduction band, resulting in a higher interband-transition energy (see Fig. 10.2(a)).

The triple-peak structure in the 6 - 12 eV range is created by transitions between d-like valence bands with slight admixtures of s- and p-type and conduction bands of sd and pd character. As visible in the second row of Fig. 10.2(b), the corresponding **k** points are located at the BZ boundary. Further analysis

reveals, that the first subpeak is created by transitions in an area around the L point. Moreover, **k** points in the $k_z = 11/34$ plane at half the distance from the k_z axis and the $k_x = 1$ plane contribute. The bands involved are almost unaffected by SO interaction. The double peak in the 8 - 9 eV range emerges from an area close to X and along K - L close to K as well as at about half the distance from K. While in the latter case the conduction band at 5.6 eV above E_F remains almost unchanged by SO interaction, two nearly degenerate valence bands at 3 eV below E_F split. They are then sitting at 2.7 and 3.4 eV below E_F, respectively (Fig. 10.2(d), along K - L).

The absorption feature around 20 eV is dominated by $d \rightarrow f$ transitions with small admixtures of $d \rightarrow p$ excitations. It can be ascribed to regions around Γ and L (Fig. 10.2(b), bottom row). The higher peak at 19.5 eV originates from **k** points along K - L and in an arc-shaped area centered at this line. The lower peak at 18.35 eV can also be traced back to excitations along K - L (closer to L). In the scalar-relativistic calculation it is present at a higher energy of 18.44 eV and is enhanced compared to its relativistic counterpart. The relative peak height is influenced by the oscillator strengths, being lower in the relativistic case. The omission of SO coupling results in a degeneracy of two valence bands at 3.9 eV below E_F at L. The higher-lying one is then almost parallel to the conduction band involved along K - L (closer to L), leading to a high joint density of states. In Appendix C, the full analysis in terms of oscillator strength for 35 planes in the BZ is given (see Figs. C.4 - C.6). The results presented above are published in Refs. [10] and [98].

10.3 Lead

To investigate the influence of SO interaction on the low-energy spectra of lead, Fig. 10.3 displays the imaginary part of the complex dielectric function (upper panel) and the reflectivity (lower panel) up to 10 eV. The calculated spectra are compared with experimental data of Lemonnier and coworkers [115]. The relativistic spectrum is characterized by an approximately 0.5 eV broad dip centered at 1.3 eV, a double-peak structure with maxima at 2.0 and 2.7 eV, respectively, and a shoulder around 3.8 eV. As highlighted by the inset of Fig. 10.3, a relativistic treatement including SO coupling is crucial to achieve excellent agreement with experiment. The improvement over the scalar-relativistic results is also visible in the reflectivity (lower panel). It is compared with two experimental curves determined by Lemonnier et al. [115]. The data taken under ultra-high vacuum (UHV) conditions show higher reflectivity values in the measured energy range, which implies that smaller magnitudes often observed for experimental data in comparison with calculated ones may

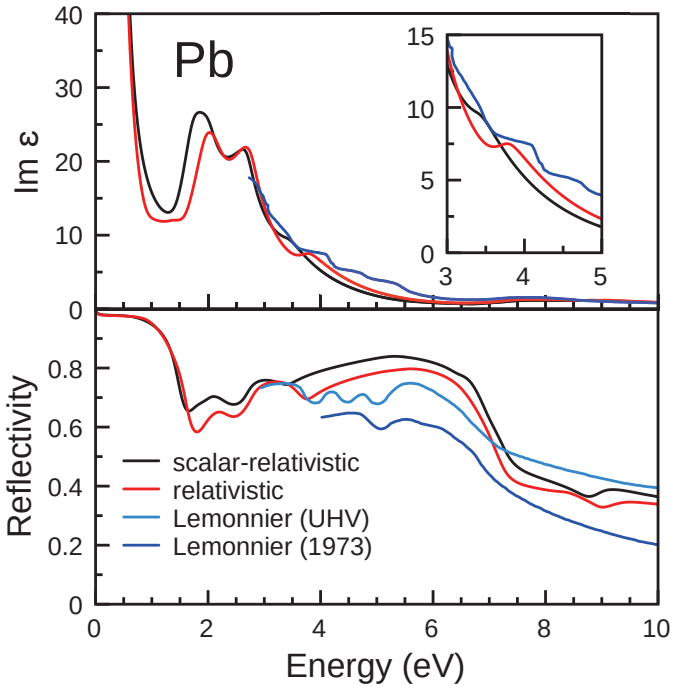

Figure 10.3: Imaginary part of the complex dielectric function (upper panel) and reflectivity (lower panel) of lead for a scalar-relativistic (black) and a relativistic calculation (red). Experimental data are taken from Lemonnier et al. [115] (dark blue), including measurements under UHV conditions (light blue).

be the result of surface contamination.

SO interaction shifts a shoulder from 1.3 to 1.5 eV, thereby increasing in magnitude. In addition, the plasma frequency gets reduced from 9.4 to 9.0 eV. Since the free-electron and the interband contributions overlap in this energy range, the dip at 1.3 eV gets wider when SO effects are taken into account.

In the double-peak structure, SO coupling has only an impact on the first maximum at 1.85 eV. It moves to a higher energy of 2.0 eV and decreases in magnitude by roughly 10%. The analysis of momentum matrix elements and oscillator strengths reveals, that for $k_z \approx 0$ **k** points along a line parallel to W - K at about half the distance Γ - K, and for $0.3 < k_z < 0.7$ along a line parallel to the k_x axis contribute (see Appendix C, Figs. C.7 and C.8). The downward

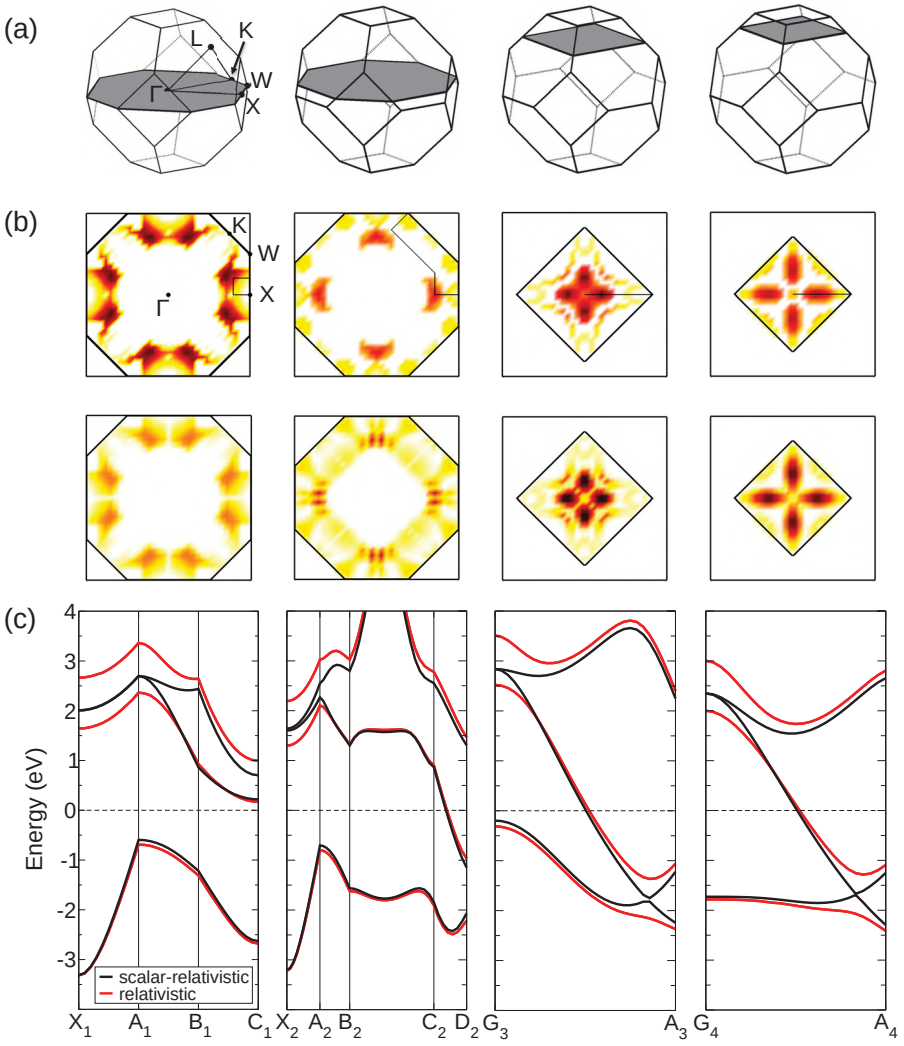

Figure 10.4: (a) fcc BZ with the selected planes highlighted, i.e., $k_z = 0$, 4/34, 23/34, and 27/34 (from left to right). (b) Analysis of optical transitions in lead including SO coupling for the energy range 3.5 - 4.5 eV. Top: transition matrix elements only. Bottom: oscillator strengths according to Eq. (7.2) with strong contributions appearing in dark red. (c) Band structure along the following lines: X_1(1,0) - A_1(27/34,0) - B_1(27/34,7/34) - C_1(1,7/34) in the $k_z = 0$ plane, X_2(1,0) - A_2(24/34,0) - B_2(24/34,4/34) - C_2(6/34,27/34) - D_2(13/34,1) in the $k_z = 4/34$ plane, G_3(0,0) - A_3(28/34,0) in the $k_z = 23/34$ plane, and G_4(0,0) - A_4(24/34,0) in the $k_z = 27/34$ plane (all coordinates are given in units of $2\pi/a$).

shift of the sp-like valence bands in combination with an upward shift of the p-like conduction bands results in the observed higher transition energy when SO coupling is taken into account.

The most important SO effect in the spectrum of lead concerns the shoulder at 3.4 eV in the scalar-relativistic case. As visible in the inset of Fig. 10.3, it shifts to a higher energy of 3.8 eV, thereby getting more prominent. Similarly to the double-peak structure at 2 eV, it emerges from $s \rightarrow p$ transitions from initial states of mixed sp to final states of p character. To allow for further analysis, the bare transition matrix elements (top) and the oscillator strengths (bottom) are displayed in Fig. 10.4(b) for the 3.5 to 4.5 eV range, the selected planes are highlighted in Fig. 10.4(a), and the band structures for important lines are given in Fig. 10.4(c).

These figures indicate that major contributions stem from excitations in areas around the X and W points. For k_z almost equal to zero, dominating matrix elements and oscillator strengths occur at **k** points along a line parallel to X - W close to the BZ boundary (first column). With increasing k_z, this region moves closer to a line parallel to Γ - X (second column). Between $k_z = 0.3$ and $k_z = 0.6$ the oscillator strengths gradually decrease (see Appendix C, Fig. C.8), while for even larger k_z new strong contributions can be localized around the k_z axis and along a line parallel to Γ - X (third and fourth column). Note that due to the high symmetry of the fcc BZ, patterns produced for $0.6 < k_z < 0.9$ represent oscillator strengths in planes parallel to the (k_y, k_z) plane for k_x values between 0.6 and 0.9.

In the $k_z = 4/34$ plane (second column of Fig. 10.4(b)), the strongest matrix elements are present in the vicinity of the W and X points, especially in a half-moon-shaped area close to the X point (top). Due to the influence of the band structure, an additional ring shows up, which is almost parallel to the BZ boundary in this plane (bottom). Its existence can be explained by the high joint density of states between the almost parallel valence and conduction bands along B_2 - C_2.

A completely different situation occurs for the $k_z = 23/34$ plane (third column). Major contributions are now located in a star-shaped region, with the patterns produced by the bare matrix elements and oscillator strength being roughly of the same shape. The differences arise from phase-space effects leading to a reduction in oscillator strengths close to the k_z (k_x) axis. When SO interaction is neglected, only the edges of the star contribute (see Appendix C). The band structure along G_3 - A_3 (see Fig. 10.4(c), third image) reveals that SO interaction causes a splitting of the two lowest conduction bands at G_3. This results in an increase in excitation energy for transitions to the second conduction band.

Finally, the last column of Fig. 10.4(b) depicts the matrix elements and

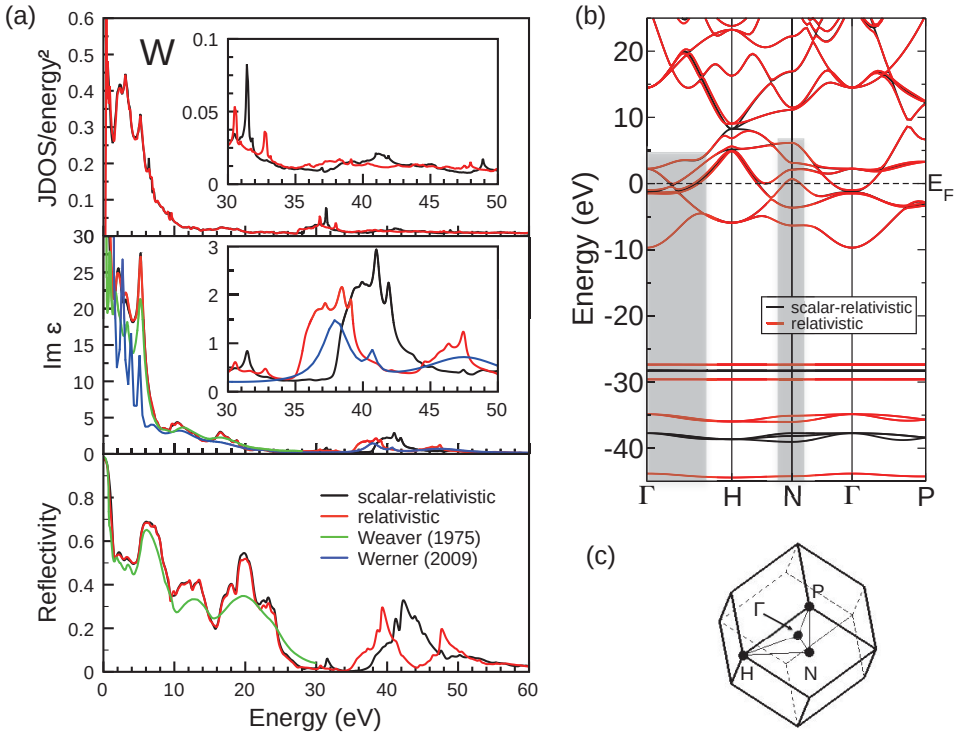

Figure 10.5: (a) Joint density of states per energy squared (top), imaginary part of the complex dielectric function (middle), and reflectivity (bottom) of tungsten for a scalar-relativistic (black) and a relativistic (red) calculation in comparison with experimental data of Weaver et al. [116] (green) and Werner et al. [10] (blue). (b) Band structure of tungsten along high-symmetry lines as indicated in the bcc BZ (c). The bands including SO interaction are given in red, whereas black indicates the scalar-relativistic results. The gray boxes highlight most active regions for the creation of the different optical features.

oscillator strengths for the $k_z = 27/34$ plane. Here, major contributions stem from **k** points in a blossom-shaped region around the k_z axis close to the diagonals of the indicated square, i.e., along a line parallel to Γ - X. As in the previous case, the higher transition energy has its origin in the SO splitting of the lowest p-like conduction bands (see Fig. 10.4(c), outermost right image). The full analysis in terms of momentum matrix elements and oscillator strengths is given in Appendix C (see Figs. C.7 and C.8). The spectra and the corresponding analysis presented above are published in Refs. [10] and [98].

10.4 Tungsten

Fig. 10.5(a) depicts the joint density of states (top), the imaginary part of the complex dielectric function (middle), and the reflectivity (bottom) of the 5d transition metal tungsten for energies up to 60 eV together with the experimental data of Weaver and co-workers [116] and Werner et al. [10]. From the theoretical side, Romaniello and co-workers [117] reported optical spectra obtained within time-dependent current-density functional theory adopting the ZORA to account for scalar-relativistic effects. They, however, did not include SO interaction explicitly in their optical calculations. Antonov and co-workers [111] performed relativistic LMTO calculations relying on the atomic-sphere approximation. Previous work by Christensen and Feuerbacher [118] was based on the relativistic APW method, but using a constructed potential to achieve agreement with experiment. In the following, the influences of SO interaction on the optical spectra will be studied, thereby focussing on the energy range above 30 eV. Therefore, Fig. 10.5(a) includes the spectra obtained from a scalar-relativistic (black) and a relativistic calculation including SO coupling (red).

The joint density of states (Fig. 10.5(a), top) shows great similarities with the imaginary part of the complex dielectric function (middle) in terms of peak positions. The peak heights are, however, influenced by the momentum matrix elements, which give rise to two wells at 11 and 17 eV and strengthen the features centered at 38 and 47 eV, respectively. On the other hand, the matrix elements suppress peaks at 30.5 and 32.8 eV. As a result, excellent agreement with experiment is achieved (see inset in the middle panel of Fig. 10.5(a)). The only tangible effect of SO coupling in the energy region up to 30 eV is a decrease of the plasma frequency from 7.65 to 7.17 eV. The latter compares well with the theoretically obtained value of 7.06 eV given in Ref. [111].

The spectra above 30 eV are much more interesting for investigations concerning SO coupling, since its omission leads to significant deviation from experiment. In the scalar-relativistic spectrum, for example, only one triple-peak structure is present around 41 eV. Moreover, the splitting of a peak around

31.4 eV into peaks at 30.5 and 32.8 eV disappears. The spectra presented here show reasonable agreement with previous calculations [111, 117] for the energy range up to 30 eV. For the 30 - 40 eV range, where the influences of SO coupling are important to meet experimental data, no optical data are available from Ref. [111]. In Ref. [117], however, no prominent structures are visible, in contrast to experiment.

The reflectivity displayed in the bottom panel of Fig. 10.5(a) is in excellent agreement with the experimental data of Weaver and co-workers [116]. It shows a rapid drop reaching the first minimum at 1.65 eV. Then, it stays almost constant up to approximately 5 eV, with the reflectivity values varying between 50 and 55%. Due to this reduction in reflectivity throughout the visible region, tungsten appears grey. For energies greater than 5 eV, the reflectivity shows structures centered at roughly 6.5, 12, and 20 eV. The impact of SO interaction on the reflectivity spectrum is strongest for the multi-peak structure in the 37 to 48 eV range, dividing it into two features with maxima at 39.3 and 47.7 eV, respectively.

For further investigations concerning peak positions and peak splittings, the band structure of tungsten is depicted in Fig. 10.5(b). Here, the scalar-relativistic energy bands appear in black, while red indicates the relativistic results. The relativistic band structure (red) shows deviations of up to 0.8 eV at high-symmetry points when compared with the early results of Christensen and Feuerbacher [118]. Accounting for SO interaction does not lead to major changes of the conduction bands up to 40 eV. Only some small band splittings appear at the high-symmetry points Γ and N. The same is found for the highest valence bands of d character with small admixtures of s and p type.

The greatest effect of SO coupling is obtained for the lower-lying valence bands of f and p character sitting at -28.2 and -37.6 eV at Γ, respectively. The band structure indicates that the small peak at 31.4 eV originates from $f \rightarrow d$ excitations along Γ - H and around N. The SO-related band splitting of the f-like valence band at -28.2 eV into two bands around -27.3 and -30.9 eV, with the d-like conduction bands staying in their position, creates the observed structure. The triple-peak structure, with peaks situated at roughly 40, 41, and 42 eV, can be ascribed to $p \rightarrow d$ transitions in an area around the N point. In this case, SO-splitting of the p bands at -37.6 eV (at Γ) takes place. One is lowered in energy by approximately 7 eV, the other appears higher in energy by roughly 2 eV. Again, the final states of d character stay in their position, i.e, 0.5, 2.0, and 3.2 eV at N. Consequently, the multi-peak structure is divided into two features centered at 38 and 47 eV. Moreover, additional contributions arise from **k** points along Γ - H and Γ - P. The findings presented above are published in Refs. [10] and [98].

11 Optical properties of selected elemental metals

The aim of this Chapter is to provide a compilation of optical data sets for a variety of elemental metals adopting the independent-particle approximation (IPA). Using experimental spectra available in literature, predominantly most recent REELS data of Werner et al. [10], the performance of the IPA based on the Kohn-Sham band structure will be studied. With the help of an extensive analysis, the origin of spectral features is investigated to identify sources of discrepancies between theory and experiment. This should highlight to which extent features are described reasonably well within the IPA and where drawbacks of the formalism lie.

In the following, silver, copper, nickel, iron, molybdenum, tantalum, vanadium, cobalt, titanium, zinc, tellurium, and bismuth are discussed. The major part of the optical spectra has been published in Refs. [9, 10]. For comparison with experiment, the spectra of cobalt, titanium, zinc, tellurium, and bismuth represent an average over the xx, yy, and zz components of the dielectric tensor. In case of nickel, iron, and cobalt, the sum over the two spin orientations is displayed. All sections are self-contained and have the same structure. Computational details are summarized in Chapter 7.

As will be seen, the spectra agree well with experimental results, especially with most recent REELS data for energies above 10 eV. In the low-energy range, the REELS data exhibit large error bars, while other available data are quite old. This makes conclusions more difficult, to which extent the interpretation in terms of the IPA based on Kohn-Sham bands is justified. It turned out that discrepancies occur predominantly for features where d bands are involved in the excitations. This is a well-known drawback of DFT, which does not provide the quasi-particle band structure. To achieve an improvement in the description of the optical properties it would be necessary to go beyond DFT, for example, by adopting the *GW* method.

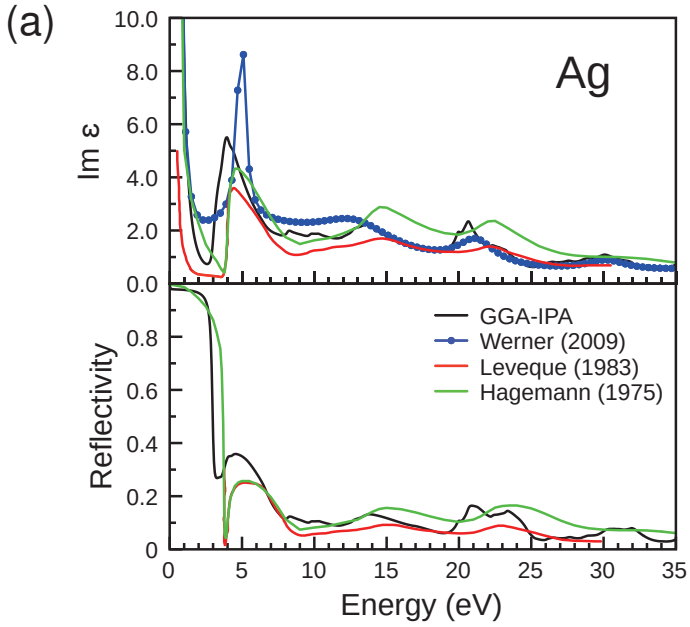

Figure 11.1: (a) Imaginary part of the complex dielectric function (top) and reflectivity (bottom) of silver in the independent-particle approximation in comparison with the experimental data of Werner (blue) [10], Leveque (red) [119], and Hagemann (green) [120]. (b) Kohn-Sham band structure of silver from a scalar-relativistic DFT-GGA calculation. The predominant band character is highlighted by symbols and colors given in the legend.

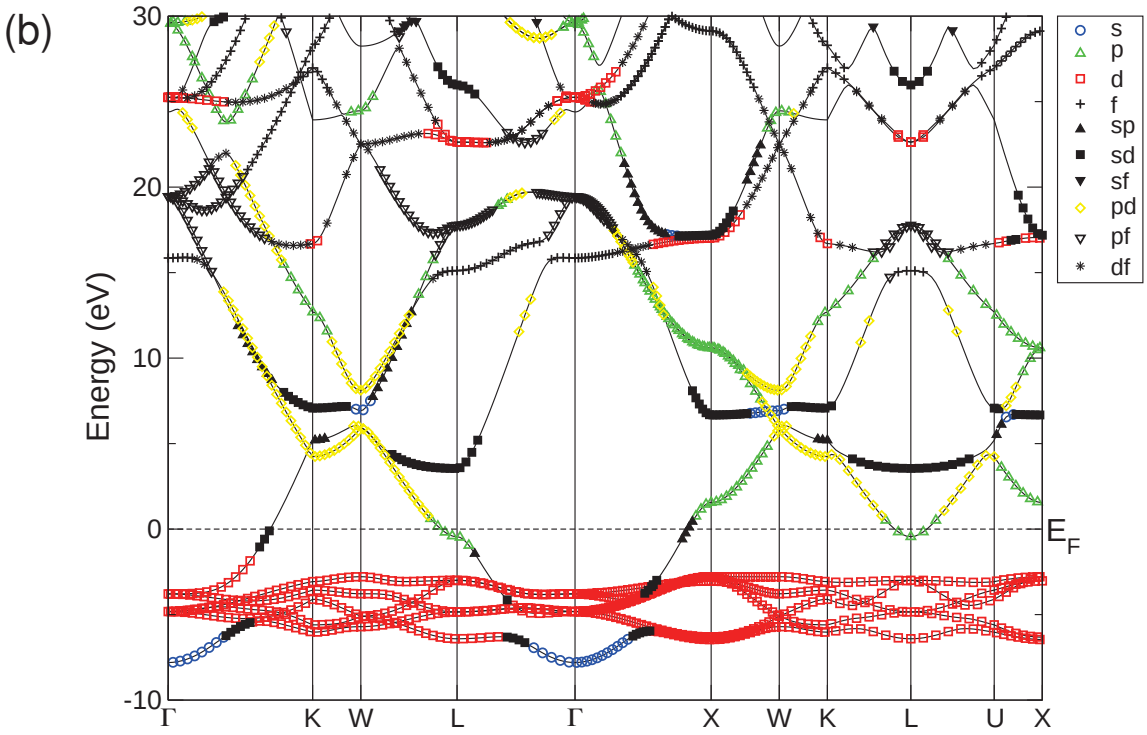

11.1 Silver

The optical spectra of the noble metal silver are displayed in Fig. 11.1(a) for energies up to 35 eV and include inter- as well as intraband contributions. The imaginary part of the complex dielectric function is shown in the upper panel. Intraband contributions are described by a Drude-like shape, adopting the calculated plasma frequency of 9.13 eV, which is in excellent agreement with a value of 9.2 eV reported by Ehrenreich and Philipp [121], but is 0.35 eV smaller than that given in Ref. [122]. Interband transitions set in at 2.94 eV, which is almost 1 eV lower than the experimentally observed onset energy of 3.9 eV [121]. From the band structure given in Fig. 11.1(b) it is visible that the interband onset energy is determined by $d \rightarrow p$ transitions from the highest valence band to the Fermi level in the vicinity of the X and L points. The discrepancy between theory and experiment can be ascribed to the position of the uppermost d-like valence bands, appearing too high in energy. This improper position of the d bands, furthermore, results in a reduction of the transition energy for all excitations involving these bands, leading to a redshift of the related spectral features compared to experiment.

Several attempts to improve the agreement with experiment are reported in literature. Semi-empirical approaches were presented by Stahrenberg and co-workers [123], as well as by Zhukov and co-workers [124]. Marini, del Sole, and Onida [122] introduced many-body corrections adopting the *GW* method. Major contributions to the first interband peak at 3.95 eV stem from $d \rightarrow p$ transitions between the uppermost valence bands and the first conduction band in the area around X and L. Moreover, $p \rightarrow sd$ transitions at L (from a valence band 0.45 eV below the Fermi level to the first conduction band 3.55 eV above) contribute. The three humps at approximately 8.3, 10, and 13.5 eV originate from transitions between a variety of bands. In the valence-band region these are the d bands, while conduction bands of s and p character with admixtures of d type from the energy range between 3 and 11 eV above the Fermi level are involved. For the broad feature at roughly 20.5 eV major contributions are located in an area close to the centre of the BZ and along the line K - L, closer to L. The transitions take place between d-like valence bands and conduction bands of f and pf character. The little peak at approximately 20 eV is mainly produced by transitions from a valence band sitting at -4.84 eV at L to a conduction band 15.11 eV above the Fermi level and to some extent by $d \rightarrow pf$ transitions along Γ - K. The major peak centered at 20.7 eV arises from $d \rightarrow f$ transitions from a valence band 4.82 eV below E_F to the first conduction band around Γ and along Γ - X. Moreover, excitations from the two uppermost valence bands to a pf-like conduction band (17.77 eV above E_F at L) contribute along K - L. For higher energies, a multi-

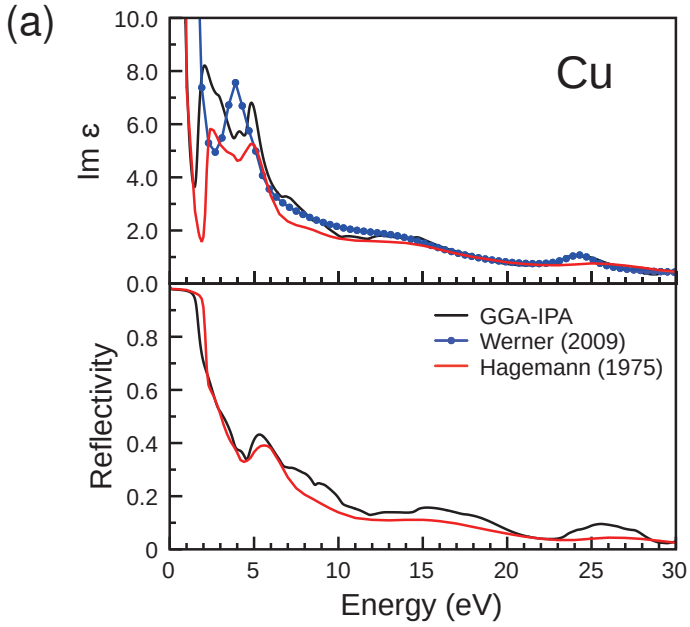

Figure 11.2: (a) Imaginary part of the complex dielectric function (top) and reflectivity (bottom) of copper in the independent-particle approximation in comparison with the experimental data of Werner (blue) [10] and Hagemann (red) [120]. (b) Kohn-Sham band structure of copper from a scalar-relativistic DFT-GGA calculation. The predominant band character is highlighted by symbols and colors given in the legend.

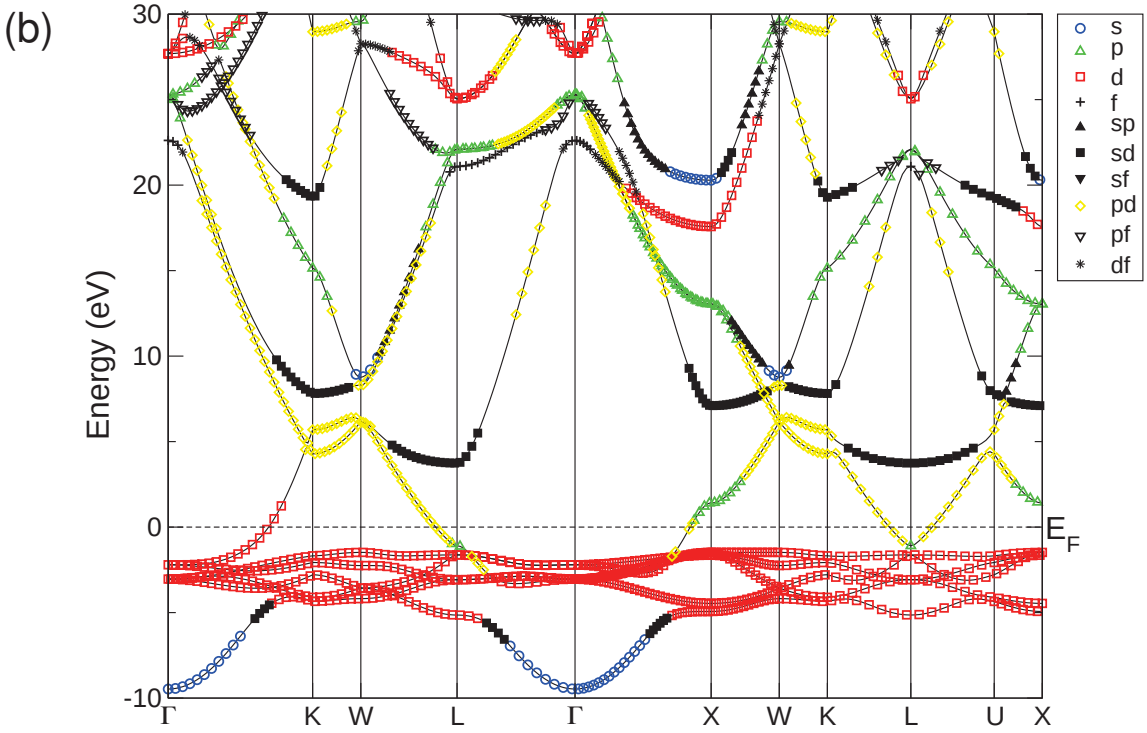

peak structure shows up around 30 eV. It mainly originates from $d \rightarrow p$ and $d \rightarrow f$ transitions from d-like valence bands to conduction bands in the 22 to 30 eV range. The excitations predominantly occur in regions around Γ and L, along K - L (closer to L) as well as along Γ - K and Γ - X (closer to Γ). Apart from the discrepancy found for the interband onset, which also influences the first interband peak and is a well-known drawback of the formalism, excellent overall agreement with experimental data of Werner et al. (blue) [10] is achieved. A comparison with the experimental curves of Leveque, Olson, and Lynch (red) [119], and of Hagemann, Gudat, and Kunz (green) [120] reveals, that the spectrum is in reasonable agreement concerning its shape, but appears redshifted. The reflectivity depicted in the lower panel of Fig. 11.1(a) shows a sharp absorption edge at a lower energy of 3 eV compared to the experimental value of 3.85 eV [119, 120], which is again a consequence of the underestimated interband-onset energy.

11.2 Copper

For copper, the theoretically obtained plasma frequency of 8.94 eV is slightly smaller than the value of 9.3 eV extracted from experimental data by Ehrenreich and Philipp [121]. The optical spectra including inter- and intraband contributions are displayed in Fig. 11.2(a) for energies up to 30 eV. The imaginary part of the complex dielectric function is depicted in the upper panel. Interband transitions set in at approximately 1.6 eV. Thus, the calculation underestimates the experimental value of 2.1 eV for the onset energy of interband transitions reported by Ehrenreich and Philipp [121]. Above the interband onset, a double-peak structure with maxima at 2.1 and 4.8 eV is present. The energy bands depicted in Fig. 11.2(b) reveal that the interband onset and the first interband peak are, similarly to silver, determined by $d \rightarrow p$ transitions from the uppermost valence band to the first conduction band around the X and L points. Since the involved bands again appear closer to the Fermi level, both, the onset energy for interband transitions and the transition energy for the first peak are smaller than found in experiment. In the theoretical spectra presented in Refs. [123] and [124], improvements were achieved by adopting semi-empirical approaches. Marini, Onida, and del Sole [126] showed that the introduction of many-body corrections using the *GW* method lowers the position of the d-like valence bands, thereby bringing them into good agreement with experimental data. The peak at 4.8 eV arises due to excitations from the p- and pd-like valence band to a conduction band of sd character in the region around L. In addition, $d \rightarrow p$ transitions from the lowest d band shown in Fig. 11.2(b) at L and X to the Fermi level contribute along W - L, K - L -

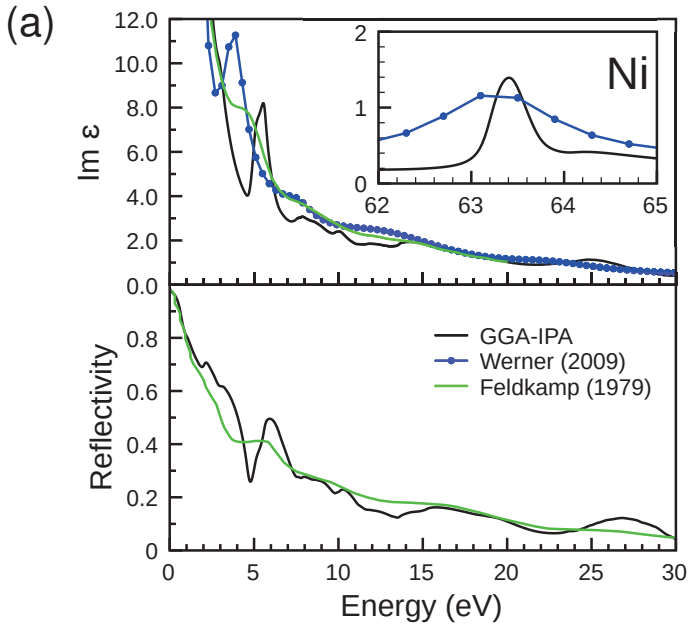

Figure 11.3: (a) Imaginary part of the complex dielectric function (top) and reflectivity (bottom) of nickel in the independent-particle approximation in comparison with the experimental data of Feldkamp [125] (green) and Werner [10] (blue). (b) Kohn-Sham band structure of nickel including bands of both spin orientations from a spin-polarized scalar-relativistic DFT-GGA calculation. The predominant band character is highlighted by symbols and colors given in the legend.

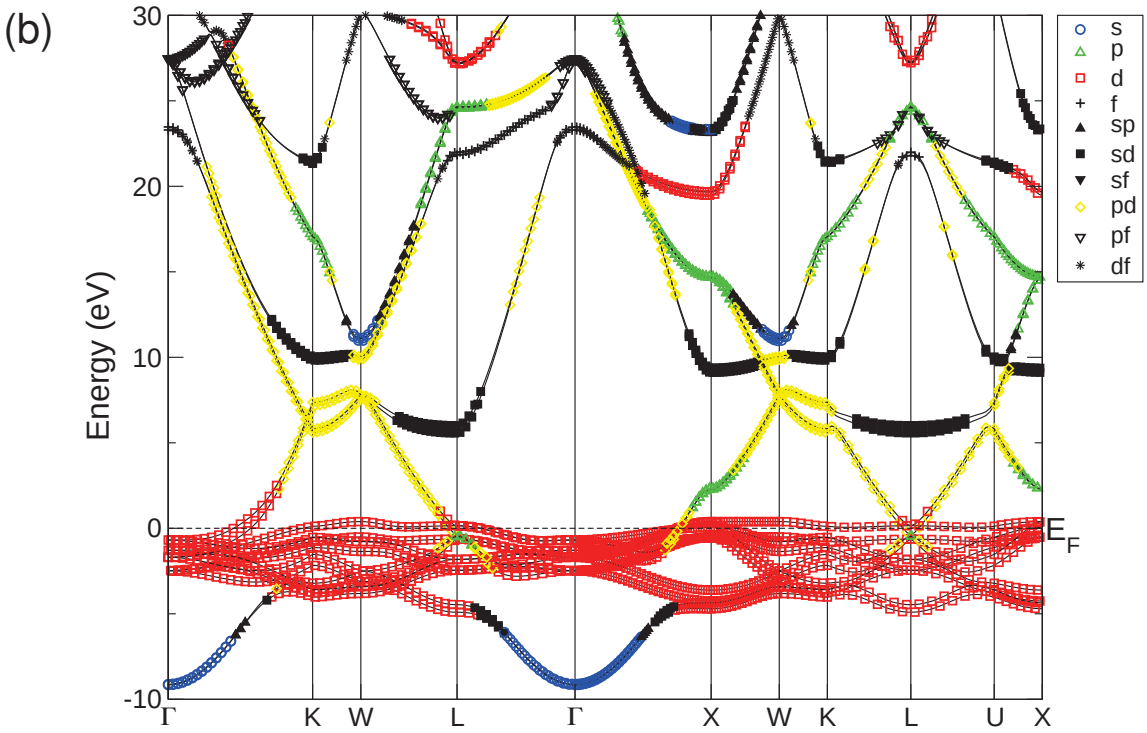

U, and Γ - X. Between 10 and 15 eV a plateau is created by $d \rightarrow p$ transitions in areas around the W point, along X - W - K and along U - X. The initial bands are the d-like valence bands, while the final states between 5 and 13 eV above E_F show p, pd, and sp character as well as sd character with slight admixtures of p type. The plateau is followed by a broader peak centered at 24 eV. It can be ascribed to $d \rightarrow p$ and $d \rightarrow f$ transitions around L and along Γ - X. The comparison with REELS data of Werner et al. (blue) [10] reveals excellent agreement in the energy region above 10 eV. Reasonable agreement is also achieved with experimental data of Hagemann, Gudat, and Kunz (red) [120]. Below this energy, the theoretical spectrum appears slightly redshifted and predicts a higher peak intensity as found in the experimental data of Hagemann, Gudat, and Kunz [120]. In contrast, only one peak at 3.9 eV is present in the spectrum reported by Werner [10]. The reflectivity is shown in the lower panel of Fig. 11.2(a). It stays almost equal to 100% for energies up to 1.5 eV before it starts to drop. The first minimum at 4.55 eV corresponds to a reflectivity of 34%. It then rises to 43%, reached for an energy of 5.3 eV. Around 15 and 25.5 eV two more humps are observed with maximum reflectivity values of 15 and 10%, respectively. Apart from a redshift of the low-energy absorption edge, the theoretical curve compares well with reflection measurements of Hagemann, Gudat, and Kunz [120].

11.3 Nickel

The optical spectra of ferromagnetic nickel are depicted in Fig. 11.3(a) for energies up to 30 eV. They represent the sum over the two spin orientations and include inter- as well as intraband contributions. Fig. 11.3(b) displays the energy bands for both spin orientations. The imaginary part of the complex dielectric function (see upper panel of Fig. 11.3(a)) shows a sharp peak at 5.5 eV. It can be ascribed to transitions from the two lowest d-like valence bands shown in Fig. 11.3(b) to conduction bands of p- and pd-like character close to the Fermi level in the area around the L points and along Γ - X, closer to X. The structure at 8 eV mainly arises from transitions along W - L and K - L - U between an initial d band sitting -1.13 eV below E_F and an almost flat sd-like band with slight admixtures of p type at 7.17 eV at K. Further contributions stem from $d \rightarrow p$ excitations from d-like valence bands to the lowest conduction bands of pd-like character along W - K - L - U. $d \rightarrow p$ transitions predominantly occuring in areas at or close to the BZ boundary are responsible for the creation of structures around 10 and 15 eV. For the 10 eV feature highest oscillator strengths are located along X - W and in arc-shaped regions centered at **k** points along K - L, while for the 15 eV feature transitions at **k**

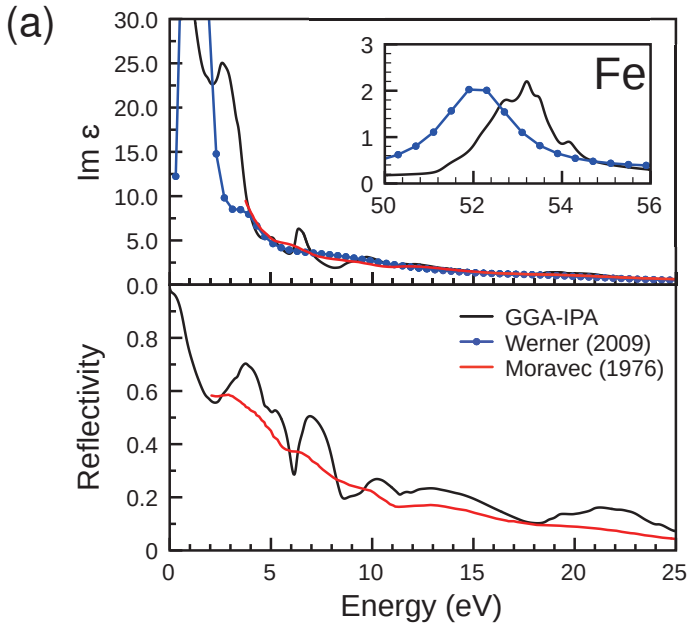

Figure 11.4: (a) Imaginary part of the complex dielectric function (top) and reflectivity (bottom) of ferromagnetic iron in the independent-particle approximation in comparison with the experimental data of Moravec (red) [127] and Werner (blue) [10]. (b) Kohn-Sham band structure of iron including bands of both spin orientations from a spin-polarized scalar-relativistic DFT-GGA calculation. The predominant band character is highlighted by symbols and colors given in the legend.

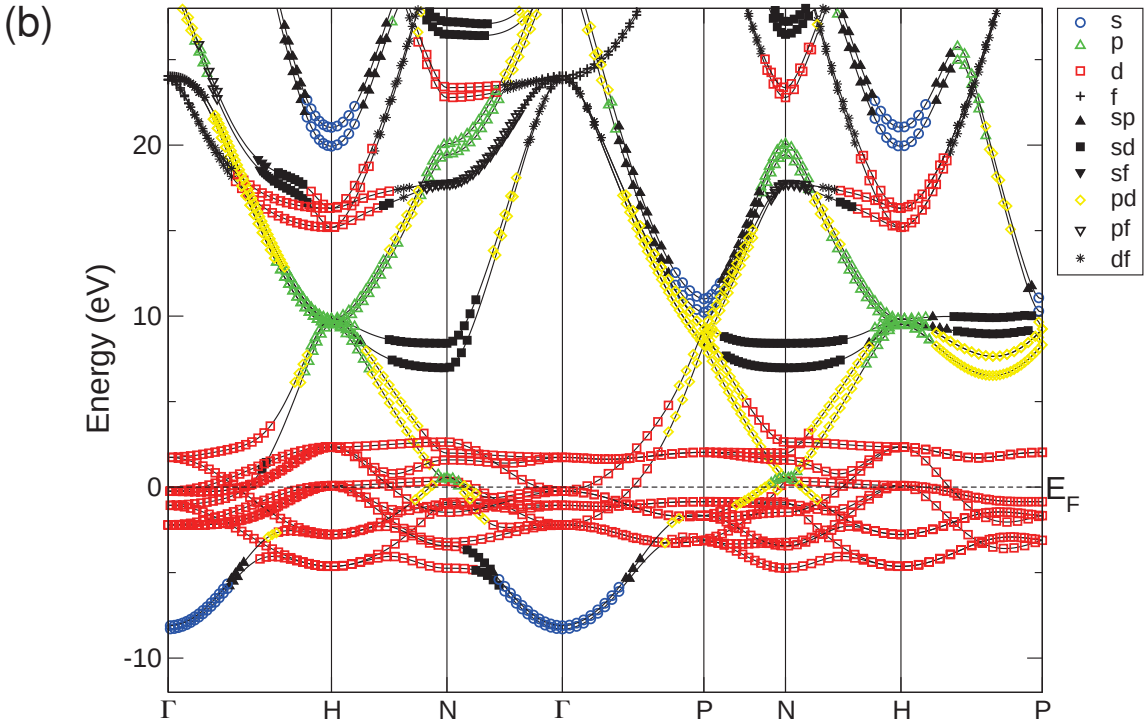

points around the X and W points as well as along X - W contribute. $d \rightarrow f$ and $d \rightarrow p$ excitations between valence bands of d character and conduction bands in the 20 to 25 eV range give rise to the feature centered at 25 eV. The corresponding **k** points are located especially around L, close to the centre of the BZ, along Γ - X, Γ - L, and K - L. The only prominent structure for higher energies is a little peak at 63.4 eV. It arises from $p \rightarrow d$ transitions from low-lying p-like bands (not shown in the figure) sitting between 63 and 63.5 eV below E_F to the Fermi level. A comparison with experimental curves of Feldkamp and co-workers (green) [125] and of Werner et al. (blue) [10, 128] reveals good overall agreement for energies greater than 10 eV. For low energies, the structure at 5.5 eV can be related to the maximum at 3.9 eV in the experimental spectrum of Werner [10] and to a shoulder visible in the data of Feldkamp [125] around the same energy. Aryasetiawan [129] obtained an upwards shift of the d-like valence bands and a decrease in band width by adopting the *GW* method. Since an upwards shift of the d-like valence bands will lead to a reduction in transition energy for structures involving these bands we expect an improvement in the theoretical description of experimental features by the inclusion of many-body corrections via the *GW* method. The reflectance spectrum given in the bottom panel of Fig. 11.3(a) shows a continuous drop in reflectivity to 26% at 4.8 eV. It then rises to 50%, reached at 6 eV, before it decreases again showing features at 16 and 27 eV. The theoretical spectrum again compares well with the experimental result of Feldkamp [125]. The greatest discrepancies are observed in the 4 to 8 eV range where a shoulder is visible in the experimental data, while a minimum followed by a peak at 6 eV shows up in the calculated spectrum. In addition, the structure centered at 27 eV is not seen in experiment.

11.4 Iron

The optical spectra of ferromagnetic iron are displayed in Fig. 11.4(a) for energies up to 25 eV. They include inter- as well as intraband contributions and represent the sum over the two spin orientations. The energy bands for both spin orientations are given in Fig. 11.4(b). As visible from the upper panel of Fig. 11.4(a), a little peak is present in the imaginary part of the complex dielectric function at 2.6 eV. It can be ascribed to $p \rightarrow d$ transitions in areas close to the N point. Major contributions stem from excitations between a pd-like valence band crossing the Fermi level in the vicinity of N and d-like conduction bands in the 1.5 to 2.7 eV range above E_F. The shoulder at 5 eV and the peak at 6.4 eV are mainly created by excitations along Γ - H and Γ - P. For the shoulder, the bands in question are the lowest valence band shown in Fig. 11.4(b)

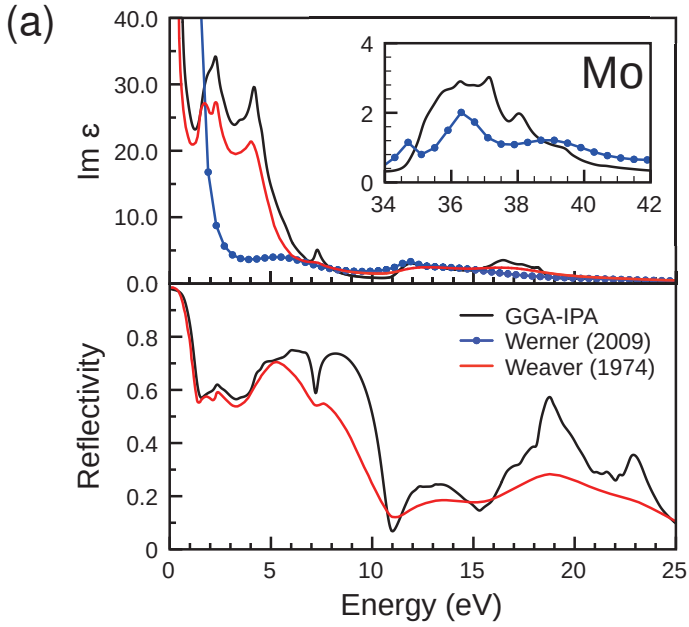

Figure 11.5: (a) Imaginary part of the complex dielectric function (top) and reflectivity (bottom) of molybdenum in the independent-particle approximation in comparison with the experimental data of Weaver, Lynch, and Olson (red) [130] and Werner (blue) [10]. (b) Kohn-Sham band structure of molybdenum from a scalar-relativistic DFT-GGA calculation. The predominant band character is highlighted by symbols and colors given in the legend.

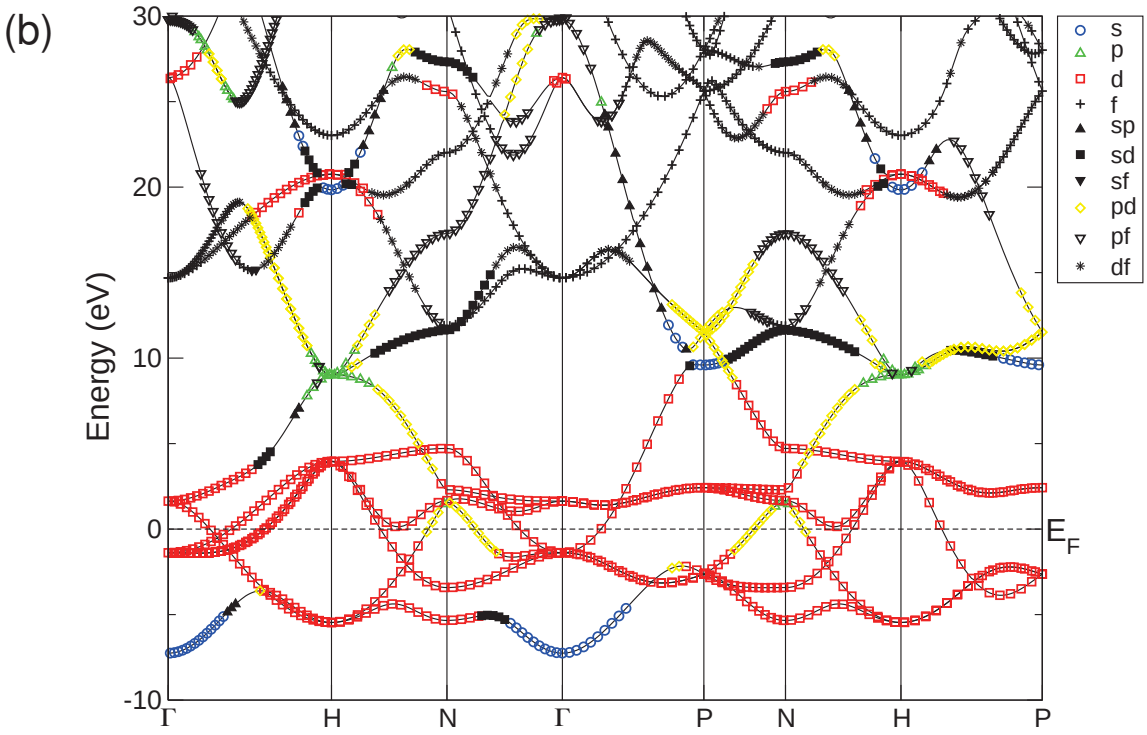

and a conduction band of d character crossing the Fermi level. The peak at 6.4 eV can be ascribed to transitions from a valence band sitting at -8.11 eV at Γ to a conduction band showing predominant d and pd character in the 2.6 to 4.6 eV range above the Fermi level. Excitations around the N points and along the lines N - P and N - H contribute to the structure around 10 eV. The valence bands are predominantly d and pd like. The conduction bands located at 6.98 eV and 8.41 eV at N show sd character and are almost horizontal along N - P and N - H. The only appreciable structure for higher energies is a feature centered at 53.2 eV. It is mainly created by $p \rightarrow d$ transitions between low-lying p bands (not shown here) present between -51.8 and -51 eV as well as in the energy region from -54.3 to -53.7 eV and d-like conduction bands sitting just above the Fermi level. A comparison with experimental data by Moravec, Rife, and Dexter (red) [127] and by Werner et al. (blue) [10,128] reveals excellent agreement in the energy region above 10 eV, except for the structure at 53.2 eV, which is blueshifted by approximately 1 eV in the calculated spectrum (see inset). The shoulder at 5 eV is present at an approximately 1 eV higher energy compared to that in the experimental spectrum of Werner [10], while it is roughly 1 eV lower in energy as reported by Moravec [127]. Finally, the little peak at 6.4 eV is completely missing in both experimental data sets. The reflectance curve of iron, depicted in the lower panel of Fig. 11.4(a), shows minima at 2.2, 6.1, and 8.6 eV. Maxima with reflectivity values of 70% and 50% appear at 3.7 and 6.9 eV, respectively. For higher energies, additional features show up around 10.3, 13, and 21.5 eV. Compared to the reflectivity measurements of Moravec, Rife, and Dexter [127], the features are more prominent, but arise almost at the same position than wells and shoulders seen in experiment. Moreover, the general trend of reduction in reflectivity is well reproduced by the calculation.

11.5 Molybdenum

Intraband contributions to the optical spectra of the $4d$ transition metal molybdenum were taken into account by a theoretical plasma frequency of 8.61 eV, which agrees well with a value of 8.66 eV reported by Romaniello and coworkers [117]. The spectra including inter- and intraband contributions are presented in Fig. 11.5(a) for energies up to 25 eV. The imaginary part of the complex dielectric function is displayed in the upper panel and shows a double-peak structure with maxima at 2.25 and 4.15 eV. Using Fig. 11.5(b), its origin can be ascribed to regions along Γ - N and H - N, which is in accordance with Ref. [130], as well as along P - N. The transitions occur between the pd-like band crossing the Fermi level and conduction bands of d character, sitting

1.67 eV and 2.3 eV above E_F at N. In addition, excitations between two d-like bands with slight admixtures of p type contribute along Γ - P, Γ - H, and P - H. These assignments are consistent with those reported by Romaniello et al. [117]. For the narrow peak at 7.3 eV highest oscillator strengths are found in an area at roughly half the distance Γ - H, in line with Ref. [130]. The transitions take place between the lowest band displayed in Fig. 11.5(b) and a conduction band sitting at 1.64 and 9.01 eV at Γ and H, respectively. The initial states show s character with slight admixtures of p type and sp character, while the final states are d like. Regions along Γ - P and around N, which according to Weaver, Lynch, and Olson [130] may also contribute to this feature, only play a minor role. The maximum at approximately 12 eV is predominantly created by $d \rightarrow p$ excitations at **k** points along H - P and N - P, in both cases closer to P and at the P point. The initial bands are the two highest d-like valence bands, while the final states in the 9 to 12 eV range above E_F show pd character. The structure at 16.5 eV arises due to $d \rightarrow f$ transitions between the three highest d-like valence bands and the two lowest f-like conduction bands at and close to the centre of the BZ. Finally, $p \rightarrow d$ excitations from low-lying p bands (between 34.5 and 36 eV below E_F) to d-like conduction bands sitting slightly above the Fermi level give rise to the multi-peak structure centered at 37 eV (see inset). Besides a higher peak intensity obtained by the calculation, the theoretical spectrum is in excellent agreement with experimental data of Weaver, Lynch, and Olson (red) [130]. It also compares well with experimental data of Werner et al. (blue) [10], except for the low-energy double-peak structure and the broad well around 16.5 eV. While the former can be ascribed to a hump centered at approximately 5.1 eV, the latter is completely missing in the experimental data. From the theoretical side, the spectrum is in reasonable overall agreement with calculations by Romaniello and co-workers [117] performed within time-dependent current-density functional theory. The reflectivity depicted in the lower panel of Fig. 11.5(a) shows a sharp absorption edge around 1 eV. It then varies between 59 and 75% before it drops rapidly to a value of 7% reached at 11 eV. For higher energies, features are present at 13, 18.75, and 23 eV, corresponding to maximum reflectivity values of 25, 57, and 35%, respectively. Excellent agreement with measurements of Weaver, Lynch, and Olson [130] is obtained for energies up to 5 eV. Above this energy the calculation in principle yields all features seen in experiment. Nevertheless, the experimental reflectivity is, in general, lower and does not show the detailed fine structure of the theoretical features.

11.6 Tantalum

The calculated plasma frequency of 8.91 eV for the 5d transition metal tantalum is 0.23 eV higher than the value reported by Antonov and co-workers [111], but in excellent agreement with a value of 8.88 eV given in Ref. [117]. Figure 11.6(a) shows the optical spectra including inter- and intraband contributions up to 25 eV. The imaginary part of the complex dielectric function is displayed in the upper panel. A double-peak structure is present at low energies. The band structure in Fig. 11.6(b) indicates that the first maximum at 3.2 eV mainly originates from transitions in areas along H - N - Γ between the two uppermost valence bands of pd and d character with slight admixtures of p type and a d-like conduction band located 3.9 eV above the Fermi level at N. The second maximum at 5.3 eV is predominantly created by transitions from the p- and pd-like band crossing the Fermi level along N - P to a conduction band sitting at 4.94 eV at N. In addition, excitations from the two lowest valence bands shown in Fig. 11.6(b) to a conduction band 3.9 eV above E_F (at N) contribute. The bands involved show d character with admixtures of s and p type. Strong contributions stem from areas along and close to the high-symmetry lines P - N, P - H, and P - Γ as well as from regions involved in the creation of the first peak. The feature at 9 eV mainly arises due to transitions from all valence bands plotted in Fig. 11.6(b) to conduction bands in the 5 to 8 eV range especially along Γ - H and to some extent along H - N. $d \rightarrow f$ and $d \rightarrow p$ excitations in regions around the N point and along N - Γ - P - N give rise to the well around 15 eV. The transitions mainly occur between the highest d-like valence band (at N) and the lowest conduction bands of pf, df, f, and pd character. The little peak at 23.7 eV arises from $f \rightarrow d$ excitations at **k** points in the NHP plane and neighboring areas as well as along N - Γ (closer to N). The f bands are sitting in the 18.6 to 19 eV range below the Fermi level while the d-like conduction band is located at 4.94 eV at N. In the 33 to 40 eV range, a multi-peak structure with maxima at 33.6, 38, and 38.9 eV shows up. It marks the onset of transitions from low-lying p bands present between -34.3 and -32.9 eV to the lowest d-like conduction bands. In general, good overall agreement with the experimental data of Werner et al. (blue) [10] is achieved. The low-energy double-peak structure can be ascribed to a shoulder seen in experiment at this energy. Excellent agreement in terms of peak position is found for the same structure, when compared with experimental results of Weaver (red) [130]. The peak intensities are, however, lower in the experimental data. For the multi-peak feature in the 33 to 40 eV range (see inset) slight deviations from the experimental data of Werner [10] are visible. Instead of the second experimentally observed maximum, a shoulder is present in the theoretical spectrum. Finally, the theoretical result compares

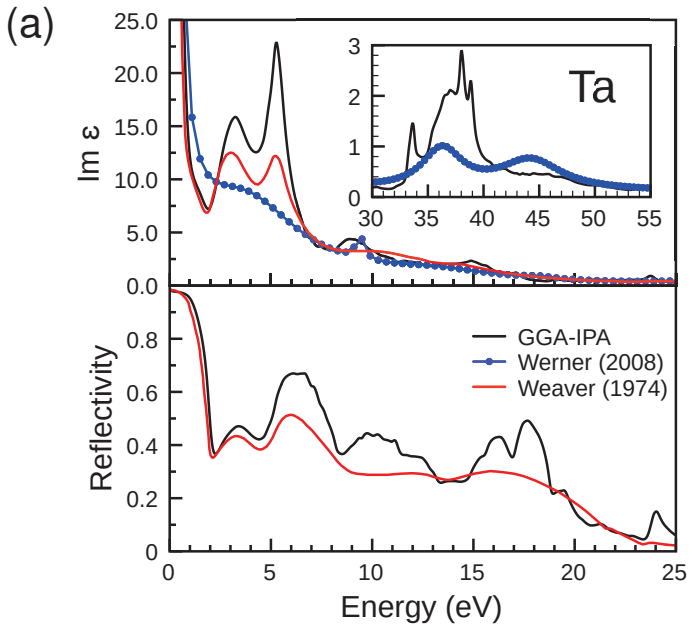

Figure 11.6: (a) Imaginary part of the complex dielectric function (top) and reflectivity (bottom) of tantalum in the independent-particle approximation in comparison with experimental data of Werner (blue) [10] and Weaver (red) [130]. (b) Kohn-Sham band structure of tantalum from a scalar-relativistic DFT-GGA calculation. The predominant band character is highlighted by symbols and colors given in the legend.

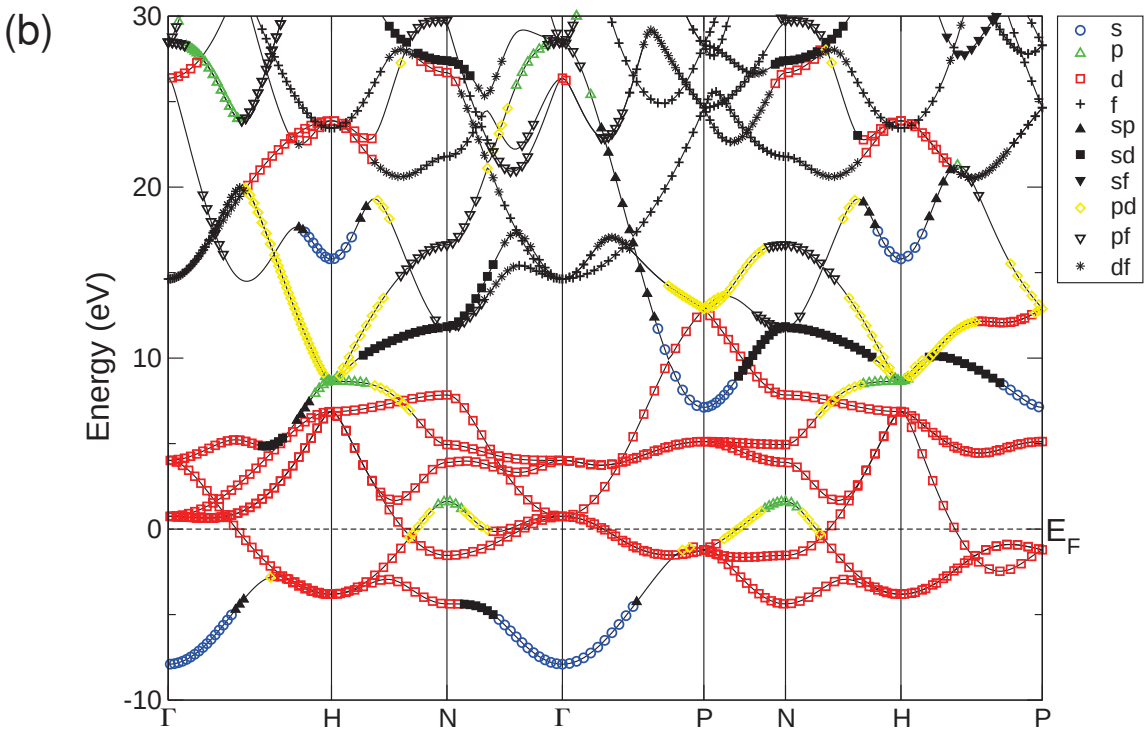

well with calculations performed by Romaniello et al. [117] and by Antonov and co-workers [111] including the discussion of the origin of certain contributions to selected spectral features. The reflectivity is shown in the lower panel of Fig. 11.6(a). The visible region is characterized by a sharp drop to 36% reached at an energy of 2.25 eV followed by an increase to 47% observed at 3.4 eV. For higher energies, four additional features show up around 6.5, 10, 17, and 24 eV. The theoretical reflectance spectrum is consistent with the experimental data reported by Weaver [130] except for the intensity. Above 5 eV, the measured reflectivity is significantly lower as predicted. Apart from a faster decrease in reflectivity for energies greater than 18 eV, the present calculation agrees reasonably well with that of Ref. [111].

11.7 Vanadium

For the $3d$ transition metal vanadium, intraband contributions were included by a Drude-like shape adopting a theoretical plasma frequency of 7.80 eV, which is 0.26 eV smaller than the value given in Ref. [117]. The optical spectra including inter- and intraband contributions are presented in Fig. 11.7(a) for energies up to 25 eV. The upper panel shows the imaginary part of the complex dielectric function. A double-peak structure with maxima at 2.1 and 3.2 eV is present at low energies. From the band structure depicted in Fig. 11.7(b) it is visible that it mainly arises from $p \rightarrow d$ transitions between the uppermost d-like valence band with admixtures of p type and two d-like valence bands (2.34 and 2.69 eV above the Fermi level) at N. The first peak at 2.1 eV can be ascribed to regions along H - N - Γ where a pd-like band crosses the Fermi level. Areas along the same line but closer to N are responsible for the second maximum at 3.2 eV. Additional contributions stem from excitations between d bands around the Fermi level which become allowed due to slight admixtures of p type. These findings are in line with assignments reported by Romaniello and co-workers [117]. Transitions occurring predominantly in regions along Γ - H and Γ - P are involved in the creation of the peak centered at 6.4 eV. They take place between the lowest valence band displayed in Fig. 11.7(b) and a conduction band sitting 3.96 and 2.35 eV above the Fermi level at N and Γ, respectively. The initial states show sp and pd character while the final states are d-like. For higher energies, a multi-peak structure shows up around 39 eV. It can be related to $p \rightarrow d$ transitions from low-lying valence bands present between 37 and 38 eV below E_F to the lowest conduction bands. Finally, the well at 47.6 eV originates from transitions between a p-like valence band and an almost horizontal conduction band of sd character along P - N - H - P. The band positions at N are -37.89 and 9.8 eV, respectively. In general, good overall

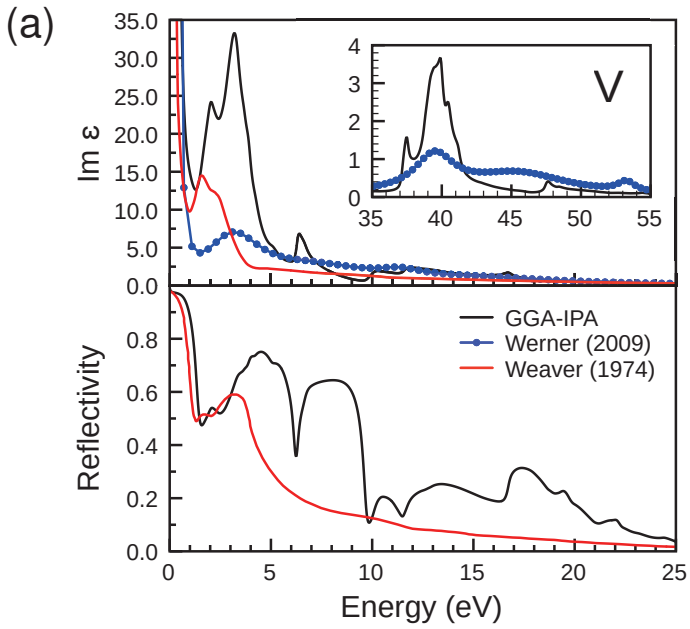

Figure 11.7: (a) Imaginary part of the complex dielectric function (top) and reflectivity (bottom) of vanadium in the independent-particle approximation in comparison with experimental data of Weaver, Lynch, and Olson (red) [130] and Werner (blue) [10]. (b) Kohn-Sham band structure of vanadium from a scalar-relativistic DFT-GGA calculation. The predominant band character is highlighted by symbols and colors given in the legend.

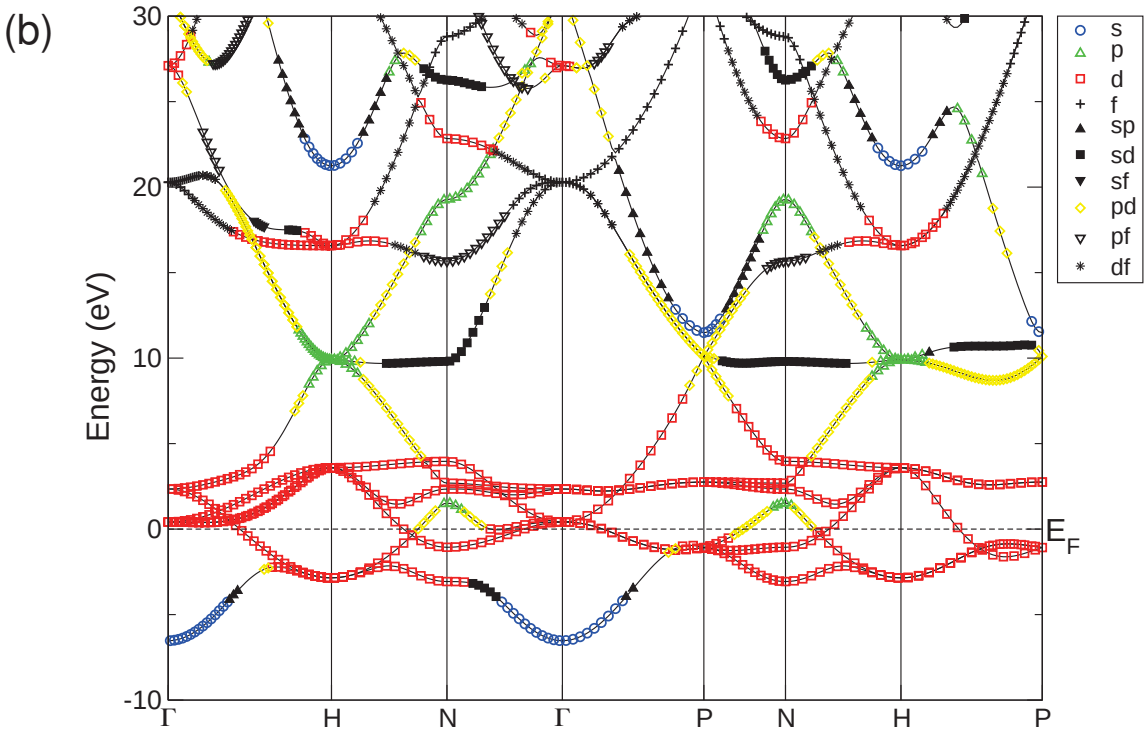

agreement with experimental data of Werner et al. (blue) [10] is observed. The low-energy double-peak structure and the multi-peak structure centered at 39 eV are visible as wells in the experimental data. Discrepancies occur for the peaks at 6.4 and 47.6 eV. While for the former no comparable structure is seen in experiment, the latter can be related to the experimental feature at 53 eV. Poor agreement with the data of Weaver, Lynch, and Olson (red) [130] is found for energies above 3 eV. We ascribe this disagreement to problems concerning an oxide layer on the vanadium sample as reported by Weaver, Lynch, and Olson (red) [130]. Apart from a small redshift, the present calculation agrees reasonably well with that of Romaniello and co-workers [117] carried out within time-dependent current-density functional theory. The reflectivity depicted in the lower panel of Fig. 11.7 is characterized by a series of sharp drops at 1.5, 6.2, and 9.8 eV, followed by several maxima in the energy region up to 30 eV. While excellent agreement with the experimental reflectance curve of Weaver, Lynch, and Olson [130] is found up to 3 eV, significant discrepancies occur for higher energies. The calculation yields several features in this energy region, while the experimental curve shows an almost structureless steady decrease.

11.8 Cobalt

The optical spectra of the ferromagnetic $3d$ transition metal cobalt including inter- and intraband contributions are shown in Fig. 11.8(a) for energies up to 30 eV. For comparison with experiment, the contributions of the two spin orientations were added and the mean value of the xx, yy, and zz contribution to the complex dielectric tensor was calculated. The band structure given in Fig. 11.8(b) shows bands of both spin orientations. In the imaginary part of the complex dielectric function, depicted in the upper panel of Fig. 11.8(a), the first interband peak shows up at 1.2 eV, followed by two shoulders at 1.7 and 3.2 eV. It is mainly created by $d \rightarrow p$ transitions between the uppermost d-like valence bands and conduction bands of p and pd character along M - L as well as in regions where these bands cross the Fermi level. Moreover, excitations between pd- and d-like bands occur. To some extent also transitions between d bands contribute due to slight admixtures of s and p type. The little peak at 5.1 eV is predominantly created by $d \rightarrow p$ excitations. The **k** points are located along Γ - M, L - A, and parallel lines as well as along L - M, in regions where mainly p- and pd-like bands cross the Fermi level. In the neighborhood of M, along Γ - K (closer to K), along H - A and parallel lines transitions from the lowest sd-like band shown in Fig. 11.8(b) to d states with s and p admixtures occur. The feature at 6.2 eV arises from transitions along Γ - K and Γ

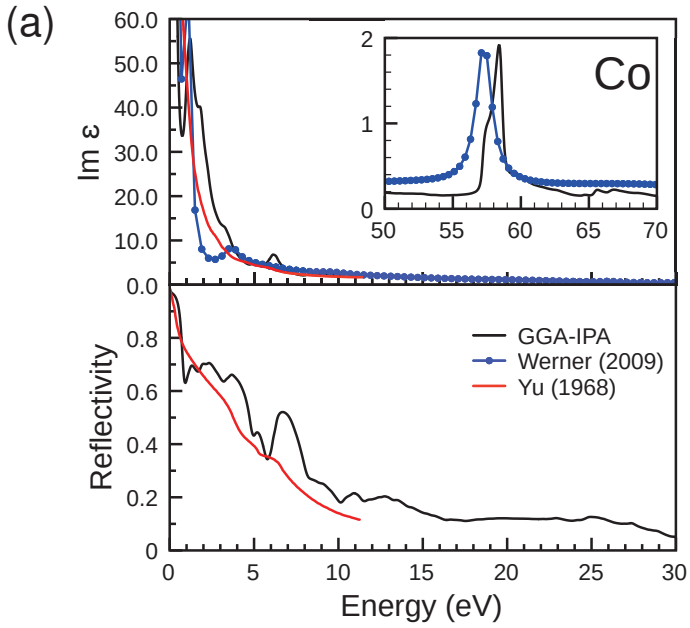

Figure 11.8: (a) Imaginary part of the complex dielectric function (top) and reflectivity (bottom) of cobalt in the independent-particle approximation in comparison with experimental data of Yu, Donovan, and Spicer (red) [131], and of Werner [10] (blue). (b) Kohn-Sham band structure of cobalt including bands of both spin orientations from a spin-polarized scalar-relativistic DFT-GGA calculation. The predominant band character is highlighted by symbols and colors given in the legend.

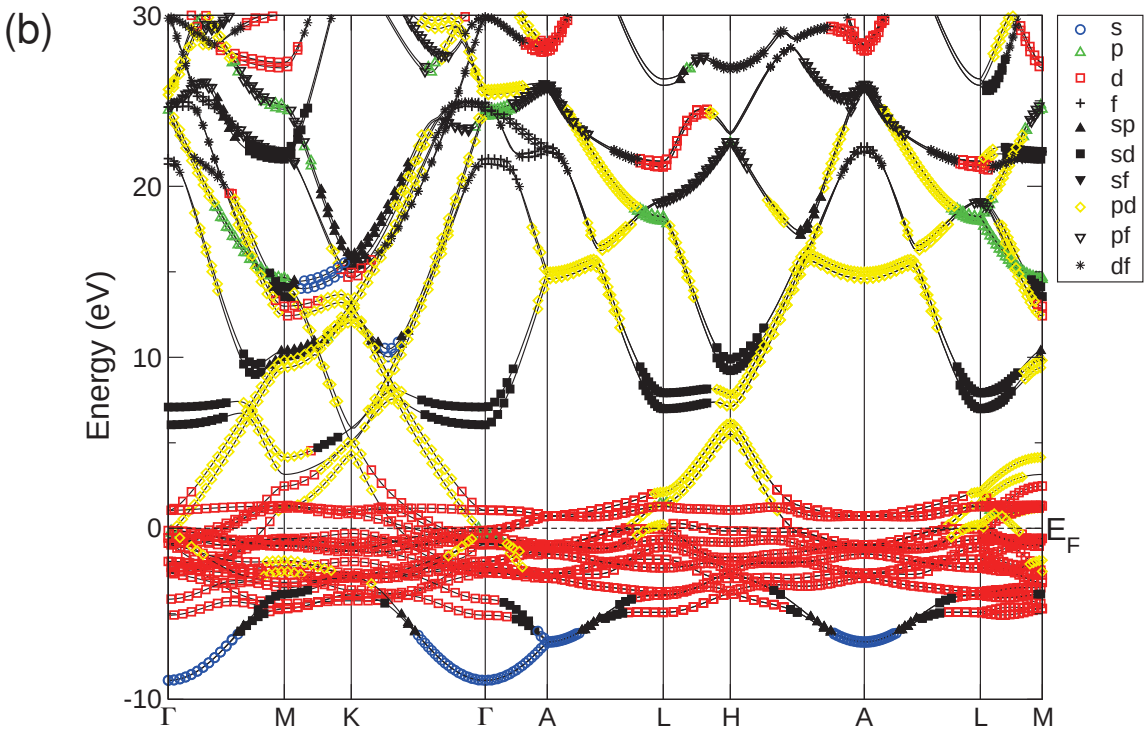

- M as well as parallel lines for higher k_z values, including A - H and A - L for $k_z = 0.5$. The initial states show sd, sp, and d character while the final states have d character with p admixtures and pd character. Finally, the high-energy structure centered at 58.4 eV can be ascribed to $p \rightarrow d$ transitions from low-lying p bands present in the 57 to 57.5 eV range below E_F to d- and pd-like conduction bands at the Fermi level. The theoretical result compares well with recent experimental data of Werner et al. (blue) [10], especially for energies above 10 eV. Small deviations occur for the maxima at 1.2 and 58.4 eV, which are seen in experiment at slightly lower energies. The shoulder at 3.2 eV can be related to the well present in the experimental data at approximately 3.5 eV. For the features at 5.1 and 6.2 eV, however, no experimental counterparts are found in the spectrum of Werner [10], while Yu, Donovan, and Spicer (red) [131] report a structure near 5.5 eV. In the reflectance spectrum of cobalt, depicted in the lower panel of Fig. 11.8(a), a sharp absorption edge, where the reflectivity drops to a value of 63%, is observed at 0.9 eV. It is followed by a plateau with three maxima and reflectivity values varying between 64 and 70%. At approximately 7 eV, a broad feature with a maximum reflectivity of 52% is present. The minima at 3.2, 5.0, and 5.8 eV can be related to shoulders found at 3.5, 5.0, and 6.0 eV in the experimental data of Yu, Donovan, and Spicer [131]. Instead of the sharp absorption edge, a more moderate decrease is observed in experiment.

11.9 Titanium

The optical spectra of the $3d$ transition metal titanium including inter- and intraband contributions are given in Fig. 11.9(a) for energies up to 25 eV. To allow for comparison with experiment, the mean value of the xx, yy, and zz contribution to the complex dielectric tensor is depicted. The imaginary part of the complex dielectric function is displayed in the upper panel. A small feature is visible at 0.6 eV. It originates from transitions between d-like bands at the Fermi level due to admixtures of p type. The **k** points are located in star-shaped regions parallel to the $k_z = 0$ plane starting at $k_z \approx 0.25$ (in units of $2\pi/a$). The points of the polygons forming the stars lie on lines parallel to Γ - M and Γ - K. In the band structure given in Fig. 11.9(b), which includes only high-symmetry lines, contributions are located at about half the distance along A - L and A - H. Features at higher energies, in general, arise from transitions at **k** points in star-shaped areas parallel to the $k_z = 0$ plane. In the $k_z = 0$ plane the points of the polygon are the M points and points at approximately 2/3 of the distance Γ - K (starting at Γ). The peak at 1.5 eV is predominantly created by transitions between the highest valence and the second conduction band

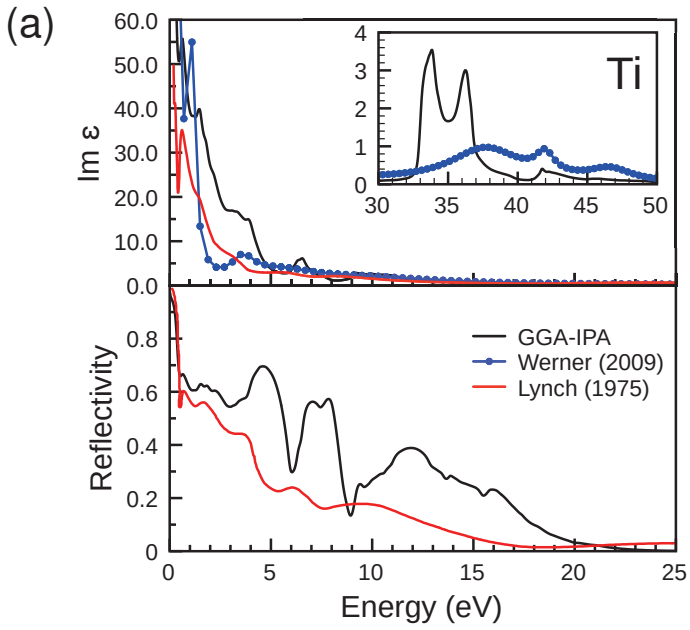

Figure 11.9: (a) Imaginary part of the complex dielectric function (top) and reflectivity (bottom) of titanium in the independent-particle approximation in comparison with the experimental data of Lynch (red) [132] and Werner (blue) [10]. (b) Kohn-Sham band structure of titanium from a scalar-relativistic DFT-GGA calculation. The predominant band character is highlighted by symbols and colors given in the legend.

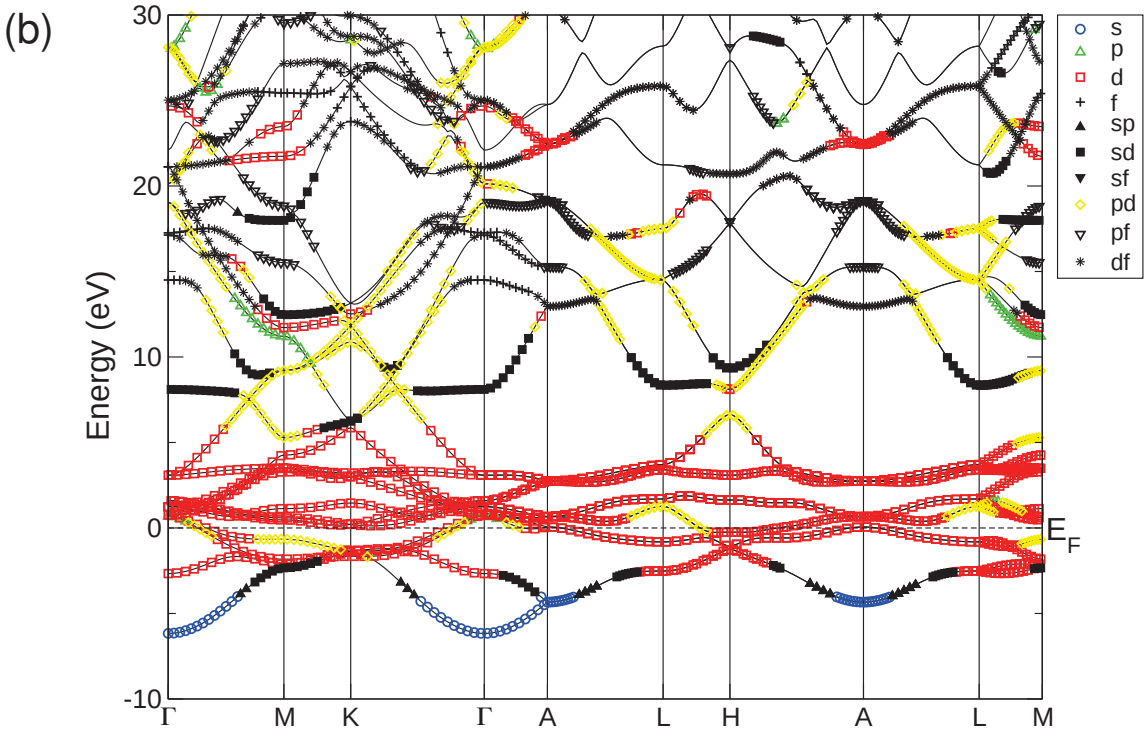

which both show d and pd character. Especially **k** points along the edges of the star-shaped regions, i.e., in areas along Γ - M (close to M) and lines parallel to it as well as along M - L, contribute. Transitions between all valence bands and mainly d-like conduction bands up to 4 eV give rise to two shoulders at 3 and 4 eV. The highest contributions occur for $k_z > 0.25$ in ring-shaped areas located between 1/3 and 2/3 of the distance ΓM. The 6.5 eV peak mainly arises due to transitions at **k** points along the edges of the star-shaped regions for small k_z values. With growing k_z excitations which are highly relevant for the creation of this feature can be located in areas parallel to the lines H - A - L between roughly 1/3 and 1/2 of the distance from the k_z axis to the BZ boundary. In the band structure these regions are partly visible along M - Γ - K, M - L, and H - A - L. The initial states are predominantly sp- and sd-like, while the final states around 3 eV show d character with admixtures of p type. The origin of the broad feature centered at 10 eV can be traced back to transitions from the uppermost valence bands of d and mixed pd character to sd- and pd-like conduction bands in the 7 to 11 eV range above the Fermi level. For higher energies, a double-peak structure is visible at 35 eV. It is created by $p \rightarrow d$ transitions from low-lying p bands sitting in the 32.7 to 33.4 eV range below E_F to d-like conduction bands above the Fermi level. Moreover, a well shows up at roughly 41.8 eV, which can be ascribed to transitions from the low-lying p bands to pd- and sd-like conduction bands present between 7 and 10 eV above the Fermi level. For energies below 15 eV, the theoretical spectrum is, besides a higher peak intensity, in better agreement with the experimental data of Lynch, Olson, and Weaver (red) [132]. The features at 6.5 and 10 eV are visible in the experimental curve as wells at lower energies. A comparison of the high-energy spectrum with experimental data of Werner et al. (blue) [10] indicates, that the double-peak structure around 35 eV may correspond to the well present in the experimental spectrum at 37.7 eV. The subsequent experimental peak at 41.9 eV is roughly twice as high compared to the calculated one and for the well at approximately 46.3 eV, no theoretical feature is visible.

The reflectivity is depicted in the lower panel of Fig. 11.9(a) and shows an absorption edge at 0.5 eV, where the reflectivity drops to 66%. This is followed by a plateau and two features centered at approximately 4.6 and 7.5 eV. In between, two minima with reflectivity values of 29.7 and 13.4%, are present at 6.05 and 8.95 eV, respectively. Moreover, a broad structure shows up in the 9 to 18 eV range, reaching its maximum reflectivity of 38.8% at 11.9 eV. The spectrum compares well with the experimental reflectivity determined by Lynch and co-workers [132] in the energy region below 3 eV. For higher energies, the experimental data show lower reflectivity values and the wells appear redshifted compared to the more prominent theoretical features.

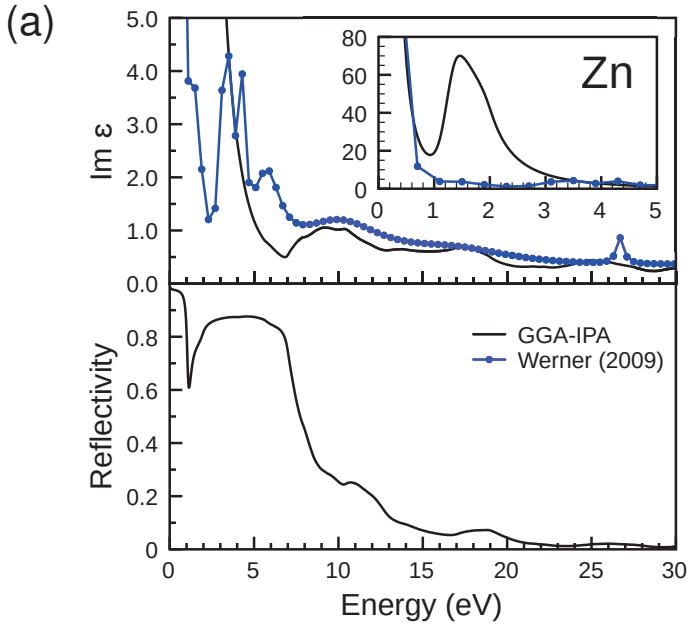

Figure 11.10: (a) Imaginary part of the complex dielectric function together with the experimental REELS data of Werner [10] (top) and reflectivity (bottom) of zinc in the independent-particle approximation. (b) Kohn-Sham band structure of zinc from a scalar-relativistic DFT-GGA calculation. The predominant band character is highlighted by symbols and colors given in the legend.

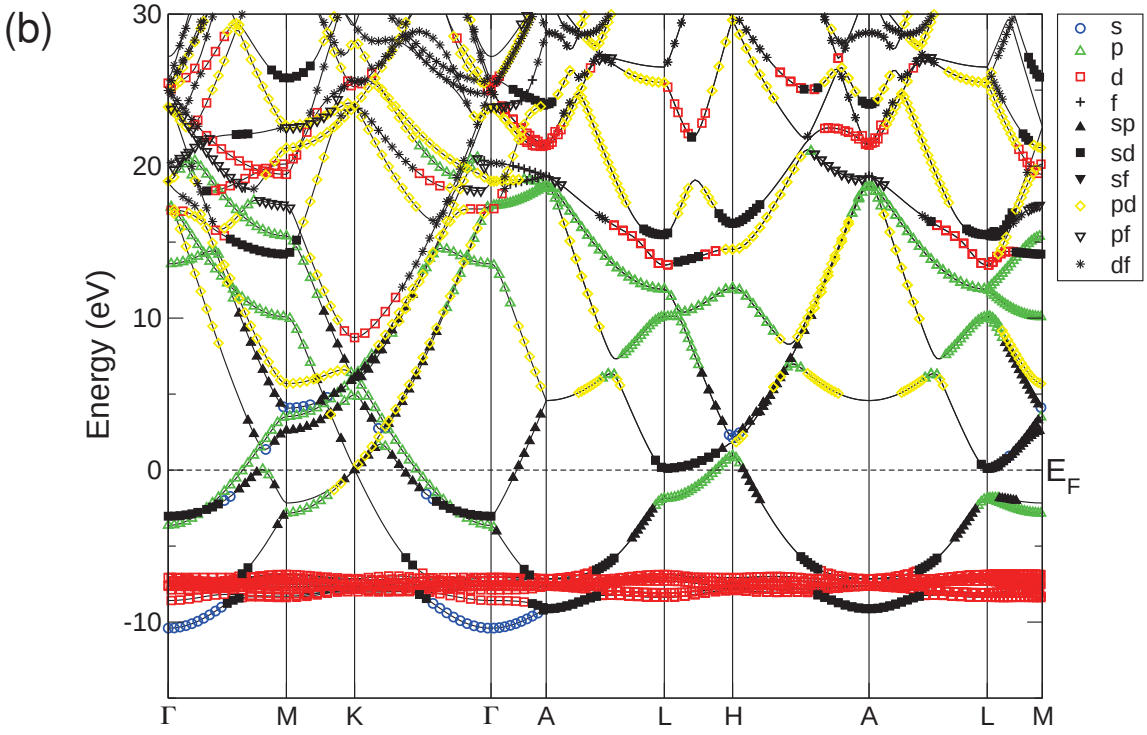

11.10 Zinc

Intraband contributions to the optical spectra of the $3d$ transition metal zinc were taken into account by a Drude-like shape. A plasma frequency of 8.92 eV was used. It is smaller than values of 10.1 eV and 9.8 eV given in Refs. [133] and [134], respectively. The optical spectra including inter- and intraband contributions are shown in Fig. 11.10(a) for energies up to 30 eV. To allow for comparison with experiment, they represent the mean value of the xx, yy, and zz contribution to the complex dielectric tensor. The low-energy region of the imaginary part of the complex dielectric function (see upper panel) up to 2 eV is dominated by strong interband transitions with a maximum at approximately 1.45 eV (see inset). For small k_z values the corresponding **k** points are located along a line parallel to the BZ boundary at approximately 1/3 of the distance ΓM as well as along a star-shaped polygon formed by connecting points along Γ - M (closer to M) with points at 1/3 ΓK (measured from Γ). As k_z grows the points making up the star-shaped polygons shift closer to the BZ boundary. The band structure displayed in Fig. 11.10(b) indicates that transitions along Γ - M and Γ - K occur between sp- and p-like states while excitations from p- and sp-like states to sd-like states contribute around L and along M - L. For higher energies, three broad wells centered at 10, 17.5, and 25 eV are visible. The corresponding transitions occur at **k** points in a star-shaped area defined by a polygon connecting the M points with points at roughly 2/3 ΓK (measured from Γ) for $k_z = 0$ and parallel areas of the same shape for greater k_z values. The majority of the initial bands involved in the creation of the three wells belong to the d-band complex present in the energy range from approximately 6.85 to 8.6 eV below the Fermi level. The feature at 10 eV is predominantly created by $d \rightarrow p$ transitions to the lowest conduction bands up to approximately 5 eV. To some extent transitions between states of sd and sp character along Γ - A contribute. The hump at 17 eV also arises from $d \rightarrow p$ excitations with final states present in the 7.9 to 11.9 eV range above the Fermi level. Finally, $d \rightarrow p$ and $d \rightarrow f$ transitions to conduction bands between 14.2 and 21.2 eV above E_F are mainly involved in the creation of the feature at 25 eV. A comparison with REELS data of Werner et al. (blue) [10] reveals excellent overall agreement for energies above 7 eV, except for the spike seen in the experimental data at 26.7 eV, which is missing in the theoretical spectrum. Instead of the strong low-energy interband peak obtained by the calculation, the experimental data show, however, a double-peak structure followed by a smaller peak.

In the reflectance curve of zinc, depicted in the lower panel of Fig. 11.10(a), an absorption edge with the reflectivity dropping to 60% is present at 1.1 eV. It is followed by a broad maximum with values between 81 and 88% in the en-

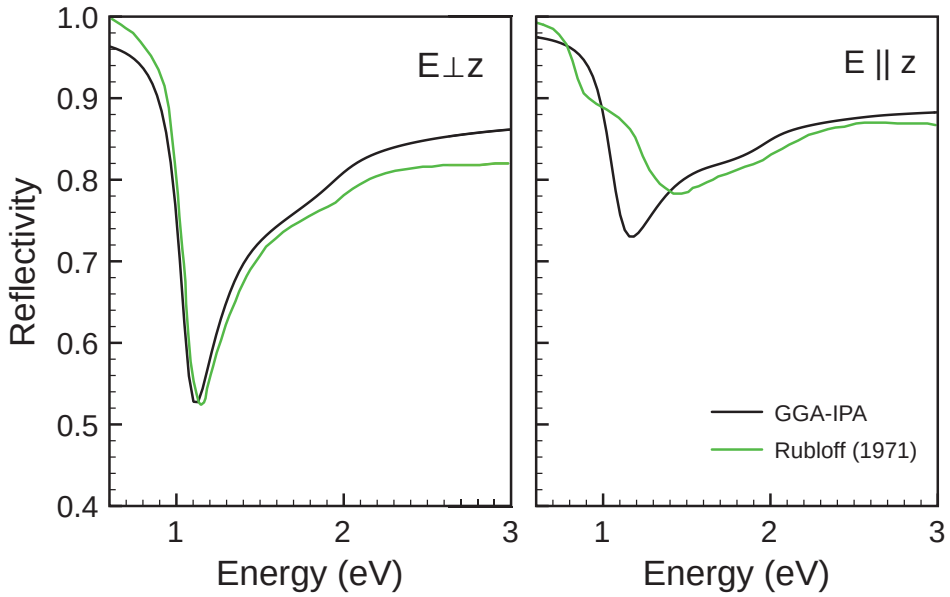

Figure 11.11: Reflectivity of zinc for the polarization directions $\vec{E} \perp \vec{z}$ (left panel) and $\vec{E} \parallel \vec{z}$ (right panel) in comparison with measurements of Rubloff [135] (green) performed at 300K.

ergy range from 2 to 6.2 eV. Then, the reflectivity decreases showing features at 11 and 18.5 eV. In Fig. 11.11 the theoretical curves for two different polarization directions are compared with reflectance data obtained at 300 K by Rubloff (green) [135]. For $\vec{E} \perp \vec{z}$, position and depth of the absorption edge are in excellent agreement with experiment. At lower (higher) energies, the calculated reflectivity values are up to 4% lower (higher). Rubloff [135] attributed the decrease in reflectivity with increasing energy to the presence of an oxide layer on the sample surface, which results in the observed discrepancies between theory and experiment at higher energies. A different situation occurs for $\vec{E} \parallel \vec{z}$. While the calculation predicts an absorption edge at a slightly higher energy of approximately 1.2 eV, which is broader and less deep as in the case before, experimental data show a shoulder around 1 eV followed by a minimum at 1.4 eV.

11.11 Tellurium

The optical spectra of tellurium are depicted in Fig. 11.12(a) for energies up to 30 eV. To allow for comparison with experiment, the mean value of the xx, yy, and zz contribution to the complex dielectric tensor is displayed. It includes inter- as well as intraband contributions. The upper panel shows the imaginary part of the complex dielectric function. A strong interband peak is present at 1.45 eV. The band structure given in Fig. 11.12(b) indicates that it arises from transitions between the two uppermost valence and the two lowest conduction bands of p character due to slight admixtures of s and d type. The first interband peak is followed by a little shoulder at 4.1 eV and a minimum at 5.75 eV. The sharp feature at 6.87 eV is mainly created by $p \rightarrow d$ excitations from the p-like valence bands to conduction bands of d and mixed pd character located in the energy range up to approximately 9 eV above the Fermi level. Transitions between the three s-like valence bands displayed in Fig. 11.12(b) and the three lowest conduction bands of p character give rise to a kink around 14 eV. The peak at 38.7 eV (see inset) can be ascribed to $d \rightarrow p$ transitions from low-lying d bands present in the energy range between 37.1 and 37.4 eV below E_F to the first three p-like conduction bands. Finally, $d \rightarrow f$ and to some extent $d \rightarrow p$ excitations between the low-lying d bands and conduction bands above 10 eV are involved in the creation of a multi-peak structure around 64 eV. Excellent agreement with experimental data of Werner et al. (blue) [10] is observed for the 10 to 30 eV range. In the low energy range, however, the first interband peak is missing in the experimental spectrum and the second one is found at a lower energy of 6.3 eV. In the energy range above 30 eV, the experimental peaks at 39.9 and 58.7 eV can be ascribed to features at slightly lower energies in the theoretical spectrum, but for the 49.1, 71.1, and 83.9 eV structure no theoretical counterparts exist. The reflectance curve is depicted in the lower panel of Fig. 11.12(a). A maximum corresponding to a reflectivity of 76.9% is present at 2.3 eV. Then, the reflectivity drops to a value of 17.8% reached at 5.95 eV. A broad well is observed in the 6 to 13.5 eV range and a peak is present at 14.88 eV. Fig. 11.13 shows a decomposition of the imaginary part of the complex dielectric function into contributions stemming from the two polarization directions $\vec{E} \perp \vec{z}$ and $\vec{E} \parallel \vec{z}$. The calculation yields a shoulder at approximately 1 eV followed by an interband peak at 1.48 eV for $\vec{E} \perp \vec{z}$, while for $\vec{E} \parallel \vec{z}$ a double-peak structure with a little peak at 0.97 eV and a more prominent one at 1.43 eV occurs. Reasonable overall agreement with experimental data reported by Bammer and co-workers (green) [137] is found for $\vec{E} \parallel \vec{z}$, while for $\vec{E} \perp \vec{z}$ the theoretical features appear at lower energies. Compared to the data of Tutihasi and co-workers (red) [136], the calculated spectra are redshifted in both cases. The peak height of the main peak is,

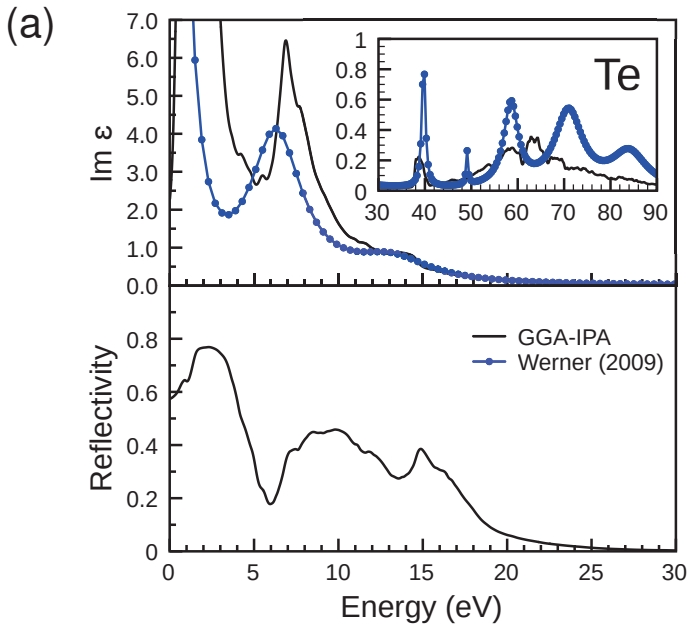

Figure 11.12: (a) Imaginary part of the complex dielectric function (top) and reflectivity (bottom) of tellurium in the independent-particle approximation in comparison with the experimental data of Werner (blue) [10] (b) Kohn-Sham band structure of tellurium from a scalar-relativistic DFT-GGA calculation. The predominant band character is highlighted by symbols and colors given in the legend.

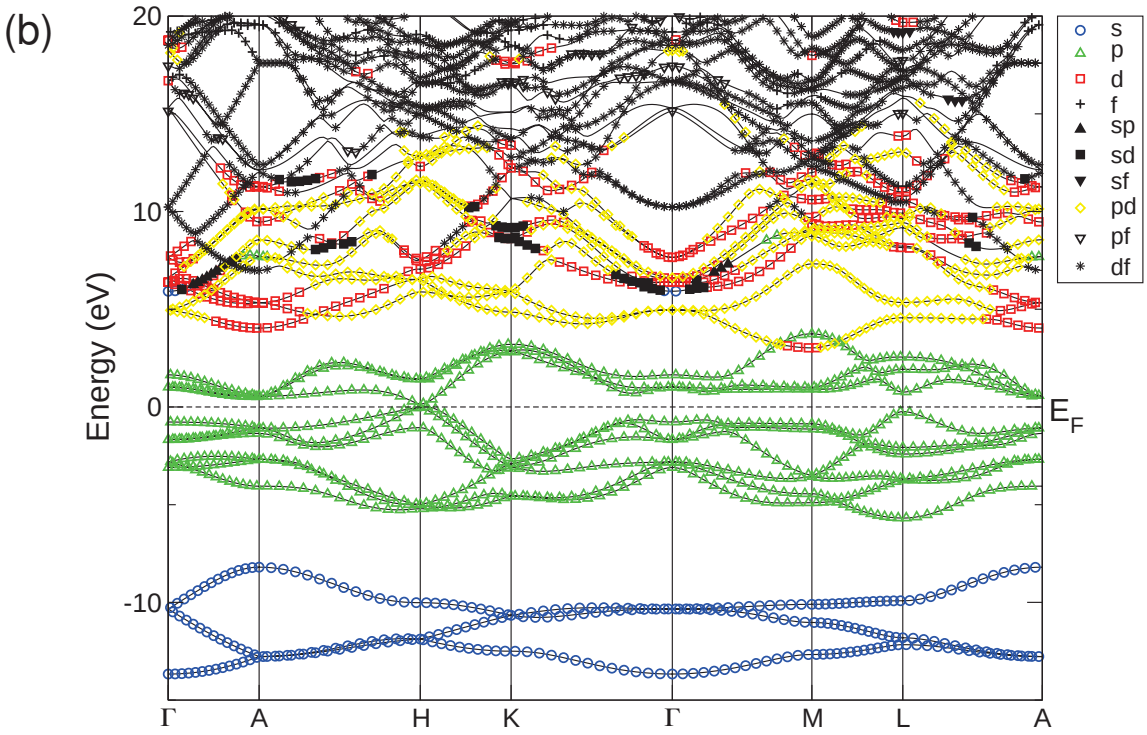

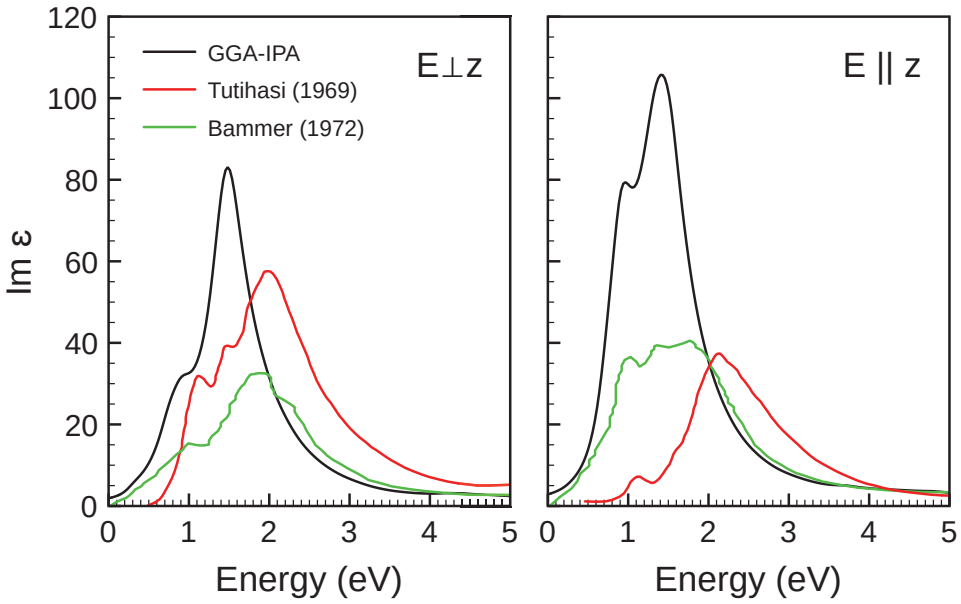

Figure 11.13: Imaginary part of the complex dielectric function of tellurium for the polarization directions $\vec{E} \perp \vec{z}$ (left panel) and $\vec{E} \parallel \vec{z}$ (right panel) in comparison with experimental data of Tutihasi et. al. [136] (red), and Bammer et. al. [137] (green).

however, always overestimated. From the theoretical side, the spectra agree reasonably well with recent theoretical results by Ghosh and co-workers [67], based on optimized pseudopotentials, especially for the $\vec{E} \parallel \vec{z}$ component. In case of the $\vec{E} \perp \vec{z}$ component they report spectral features with lower intensity at slightly lower energies as well as additional features like a peak at 0.61 eV and three wells at roughly 2.1, 2.5 and 2.9 eV, respectively. Fig. 11.14 displays the reflectivity for the polarization directions $\vec{E} \perp \vec{z}$ and $\vec{E} \parallel \vec{z}$. The first maximum shows up at almost the same energy for both polarization directions, but the $\vec{E} \parallel \vec{z}$ component exhibits higher reflectivity values. The following minimum appears at 5.78 eV for $\vec{E} \perp \vec{z}$ and at a higher energy of 6.27 eV for $\vec{E} \parallel \vec{z}$, with reflectivity values of approximately 15% and 29.5%, respectively. A broad structure centered at roughly 10 eV is present for $\vec{E} \perp \vec{z}$. It is split into three separate features for $\vec{E} \parallel \vec{z}$ with the broad maximum centered at 9.4 eV, accompanied by two peaks at 7.09 and 11.93 eV, respectively. Finally, the peak at 14.82 eV for $\vec{E} \perp \vec{z}$ appears at a slightly higher energy with a lower reflectivity for $\vec{E} \parallel \vec{z}$. The calculated spectra compare well with experimental data

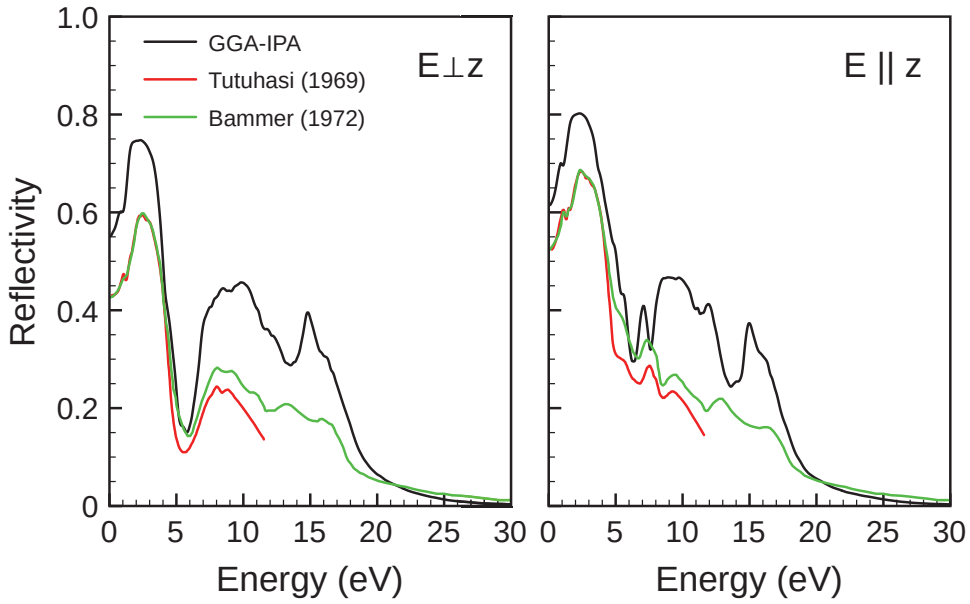

Figure 11.14: Reflectivity of tellurium for the polarization directions $\vec{E} \perp \vec{z}$ (left panel) and $\vec{E} \,||\, \vec{z}$ (right panel) in comparison with experimental data of Tutihasi et. al. [136] (red), and Bammer et. al. [137] (green).

of Tutihasi and co-workers [136] and of Bammer et al. [137], who observed features almost at the same energy, which are, however, not that prominent, and show, in general, lower reflectivity values than the calculated ones.

11.12 Bismuth

The optical spectra of bismuth are displayed in Fig. 11.15(a) for energies up to 30 eV. To allow for comparison with experiment, the mean value of the xx, yy, and zz contribution to the complex dielectric tensor including inter- and intraband contributions is depicted. A double-peak structure with peaks at 5.35 and 6.52 eV is present in the imaginary part of the complex dielectric function (see upper panel). The band structure given in Fig. 11.15(b) indicates, that it is created by transitions from the uppermost p- and sp-like valence bands to the lowest conduction bands of pd and d character. $s \rightarrow p$ transitions from s bands sitting around -10 eV to the lowest p-like conduction bands are involved in the creation of a shoulder at roughly 11.5 eV and a kink at 15.85 eV. At

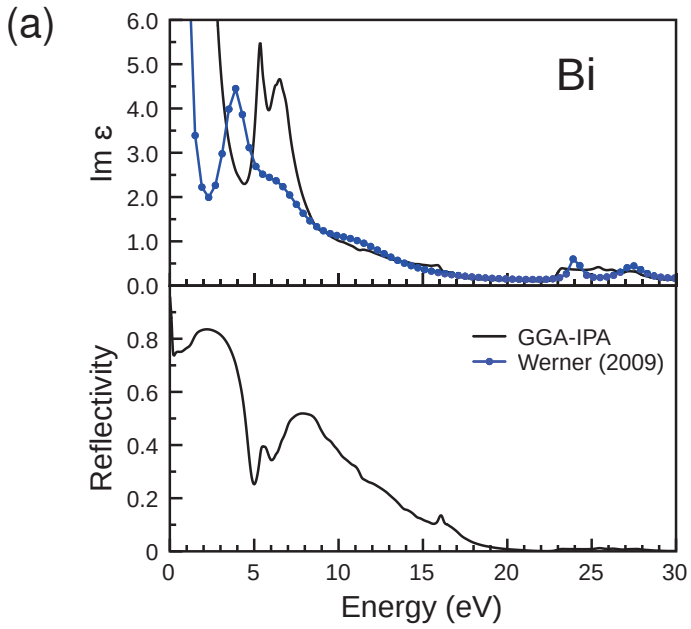

Figure 11.15: (a) Imaginary part of the complex dielectric function (top) and reflectivity (bottom) of bismuth in the independent-particle approximation in comparison with the experimental data of Werner (blue) [10]. (b) Kohn-Sham band structure of bismuth from a scalar-relativistic DFT-GGA calculation. The predominant band character is highlighted by symbols and colors given in the legend.

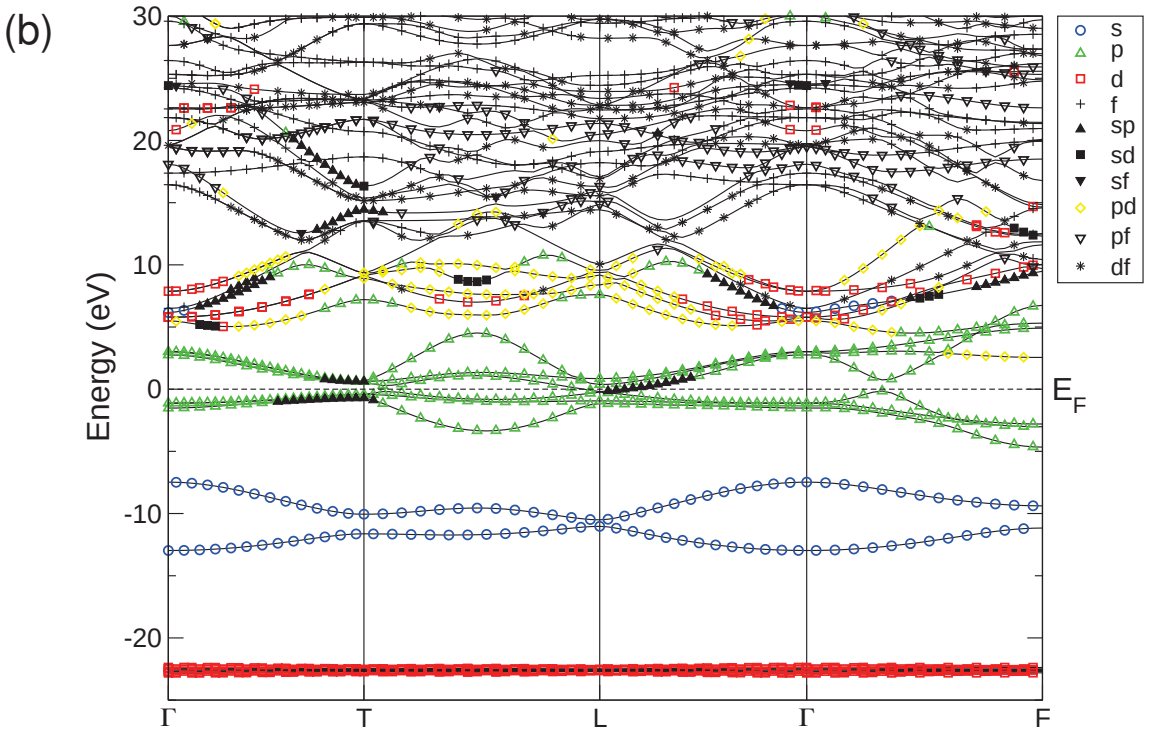

higher energies, features are observed in the 22 to 30 eV range. They occur due to $d \rightarrow p$ excitations from low-lying d bands sitting in the energy range from 22.3 to 22.9 eV below E_f to the lowest conduction bands. The present calculation agrees reasonably well with experimental data of Werner et al. (blue) [10] in the energy range above 10 eV, while discrepancies occur for the low-energy double-peak structure. The first peak is visible at a lower energy of 3.9 eV and instead of the second peak, a shoulder shows up in the experimental data around 6.3 eV. The reflectivity of bismuth is depicted in the lower panel of Fig. 11.15(a). A sharp drop to 73.6% occurs at a very low energy of 0.23 eV. Then, the reflectivity rises, reaching a maximum value of 83.55% around 2.2 eV. The subsequent minimum, representing a reflectivity of 25.24%, is found at 4.99 eV. For higher energies the calculation yields maxima at 5.51 as well as around 8 eV and a little spike at 16.07 eV. Around 22 eV the reflectivity finally reaches values close to zero.

12 Summary and conclusions

In this work, the optical spectra of a variety of metals were investigated. A detailed analysis of the origin of the spectral features was given in all cases. Since the independent-particle approximation (IPA) is regarded to be a reasonable framework for metals, it was adopted for the majority of the materials under investigation. To judge the performance of this approach, highly-accurate calculations were carried out, in order to prevent inaccuracies introduced by the solution of the Kohn-Sham equations. In addition, many different aspects related to optical properties were discussed. For palladium, the origin of optical excitations was studied in detail for zero momentum transfer. Thereafter, the momentum-dependence of the electron-loss spectra was examined for increasing momentum transfer in (100), (110), and (111) direction. The optical properties of bulk aluminum were explored at ambient conditions and for increasing pressure. In case of Al(001) thin films, the impact of growing film thickness and of corresponding surface bands on the imaginary part of the complex dielectric function was investigated. The influence of spin-orbit coupling on the optical spectra was discussed for gold, platinum, lead, and tungsten. For gold, the spectra obtained from a non-relativistic and a scalar-relativistic treatment were calculated for comparison. The complex dielectric function and the reflectivity were studied for silver, copper, nickel, iron, molybdenum, tantalum, vanadium, cobalt, titanium, zinc, bismuth, and tellurium, representing benchmark data for the IPA based on the Kohn-Sham band structure.

The ground-state calculations were carried out within density functional theory adopting the APW+lo method. The resulting Kohn-Sham orbitals and eigenvalues were subsequently used in the determination of the optical spectra within the IPA, or, in some cases, the random-phase approximation (RPA) and the adiabatic local-density approximation (ALDA). A detailed analysis of the origin of spectral features was performed. For this purpose, I have developed a procedure for tracing back the origin of spectral features to regions within the Brillouin zone. In a first step, the oscillator strength of transitions contributing to a chosen energy range are determined for the individual **k** points

within the Brillouin zone (BZ). These **k**-dependent oscillator strengths are visualized for different planes within the BZ to highlight regions that are involved in the creation of a selected spectral feature. The interpretation of the results is supported by band-structure plots including the predominant band characters.

For palladium, the momentum-dependent electron-loss spectra were studied for energies up to 80 eV and momentum transfer along the three main crystallographic directions. A detailed analysis of the origin of spectral features in terms of oscillator strengths was performed for zero momentum transfer. It turned out that anisotropic behavior is almost absent at low momentum transfer and even for higher q values it stays moderate for the whole energy range and q values under investigation. The inclusion of local-field effects has the greatest impact on the 40 to 60 eV range, leading to a reduction in spectral weight by up to 70%. This is crucial to reproduce the experimental spectra. In this energy range, transitions involving localized d states and $4p$ semicore states dominate. The spectra are almost insensitive to a change of the exchange-correlation kernel from RPA to ALDA. Increasing momentum transfer causes an upward shift of the low-energy plasmon peak thereby reducing its height. Its evolution is isotropic for $q \leq 0.4$ Å^{-1}, while for higher q, plasmon energy and peak height are greatest for momentum transfer in (111) direction. The present results compare well with experimental electron energy-loss spectroscopy (EELS) data for energies up to 40 eV. We expect measurements with higher resolution to confirm features that are predicted by the calculation at energies above 40 eV, but do not have a visible counterpart in the experimental data sets currently available.

For aluminum, the pressure dependence of the imaginary part of the complex dielectric function up to 5 eV was investigated. It revealed that applying pressure causes a blueshift of the whole spectrum. Its origin was traced back to changes in the band structure with the help of a detailed analysis in terms of oscillator strengths. The first interband peak, normally masked by the free-electron contribution at ambient pressure, becomes visible at roughly 4.6 GPa. At 15.8 GPa, the two low-energy interband peaks show up at a roughly 0.5 eV higher energy compared to their position in the zero-pressure spectrum (at 0.5 and 1.5 eV, respectively).

The evolution of the optical spectra as a function of film thickness was studied for thin Al(001) films for energies up to 5 eV. The number of Al monolayers (MLs) was varied from 5 to 101. Changes in the band structure with growing number of layers have the greatest impact on the out-of-plane component of the complex dielectric function. For the 5 MLs Al film, the spectrum contains well-separated interband peaks but no intraband contribution. With growing film thickness transitions between discrete thin-film bands around the Fermi level give rise to a low-energy multi-peak feature. The spectra for Al

slabs with 61 Al MLs or more can already be regarded as bulk-like for the considered energy range. Features present at energies above roughly 1.5 eV also arise from transitions between discrete thin-film bands and have the tendency to move closer together and to diminish when going to thicker slabs up to 101 Al MLs. This behavior results from a growing number of thin-film bands in the considered energy range for increasing slab thickness. Surface effects have the greatest impact on the energy range below 1.5 eV, while they are of minor importance at higher energies.

The inclusion of relativistic effects is important for a proper description of the electronic structure and optical properties especially for heavy elements. The impact of a scalar-relativistic treatment as well as of spin-orbit (SO) coupling on the optical spectra was studied for gold, platinum, lead, and tungsten. A scalar-relativistic treatment of gold shifts the uppermost d bands closer to the Fermi level, which is crucial for a correct prediction of its color. The threshold energy for interband transitions is lowered from 3.5 to 1.85 eV, leading to a drop in reflectivity from 100% to approximately 40% for energies above 1.9 eV, while it remains 100% up to 3.5 eV in the non-relativistic case. Slight discrepancies in the position of the absorption edge with respect to experiment remain as a consequence of the underestimated interband onset. Compared to scalar-relativistic effects, the impact of SO interaction is found to be small.

For platinum, SO-related band splittings around the X and L points give rise to a dip in the reflectivity at 0.7 eV, resulting in excellent agreement with experiment.

In case of lead, band splittings of the two lowest p-like conduction bands caused by the inclusion of SO interaction result in an upwards shift of a shoulder from 3.4 to 3.8 eV, thereby improving the agreement with experiment significantly.

SO effects in the spectrum of tungsten occur especially for energies above 30 eV. The greatest impact of SO coupling concerns band splittings of the low-lying f-like and p-like valence bands sitting around -28.2 eV and -37.6 eV at the Γ point, respectively.

Calculated optical spectra of silver, copper, nickel, iron, molybdenum, tantalum, vanadium, cobalt, titanium, zinc, bismuth, and tellurium represent a highly accurate data set that has been found in overall excellent agreement with most recent reflection EELS (REELS) data.

To conclude, the optical properties obtained within the IPA based on the Kohn-Sham band structure are in reasonable overall agreement with experiments in all cases studied in this work, especially when compared to the most recent REELS data in the energy range above 10 eV. Since the REELS data exhibit large error bars for energies below 10 eV and other available experimental data are quite old, there is a need for new experiments with a better

resolution in the low-energy range. Remaining discrepancies between experiment and theory in terms of peak positions and heights occur especially for features where d bands are involved in the transitions. The improper description of the d-band positions is, however, a well-known drawback of DFT. Since DFT does not provide the quasi-particle band structure, an improvement in the theoretical description of spectral features is expected only when going beyond DFT, for example, by introducing many-body effects adopting the *GW* method.

A Oscillator strengths of palladium

In the following, the oscillator strengths of palladium are depicted. They were determined according to Eq. (7.2) for the energy ranges 0.1 - 0.6 eV, 8 - 18 eV, 19 - 21.5 eV and 30 - 32.5 eV. The results are shown for 35 different planes in the BZ starting with oscillator strenghts for **k** points within the $k_z = 0$ plane in the top left corner and ending with oscillator strengths for **k** points in the $k_z = 1$ plane in the bottom right corner. The distance between two subsequent planes is $\Delta k_z = 1/34$ (in units of $2\pi/a$). Regions with high oscillator strengths appear in dark red.

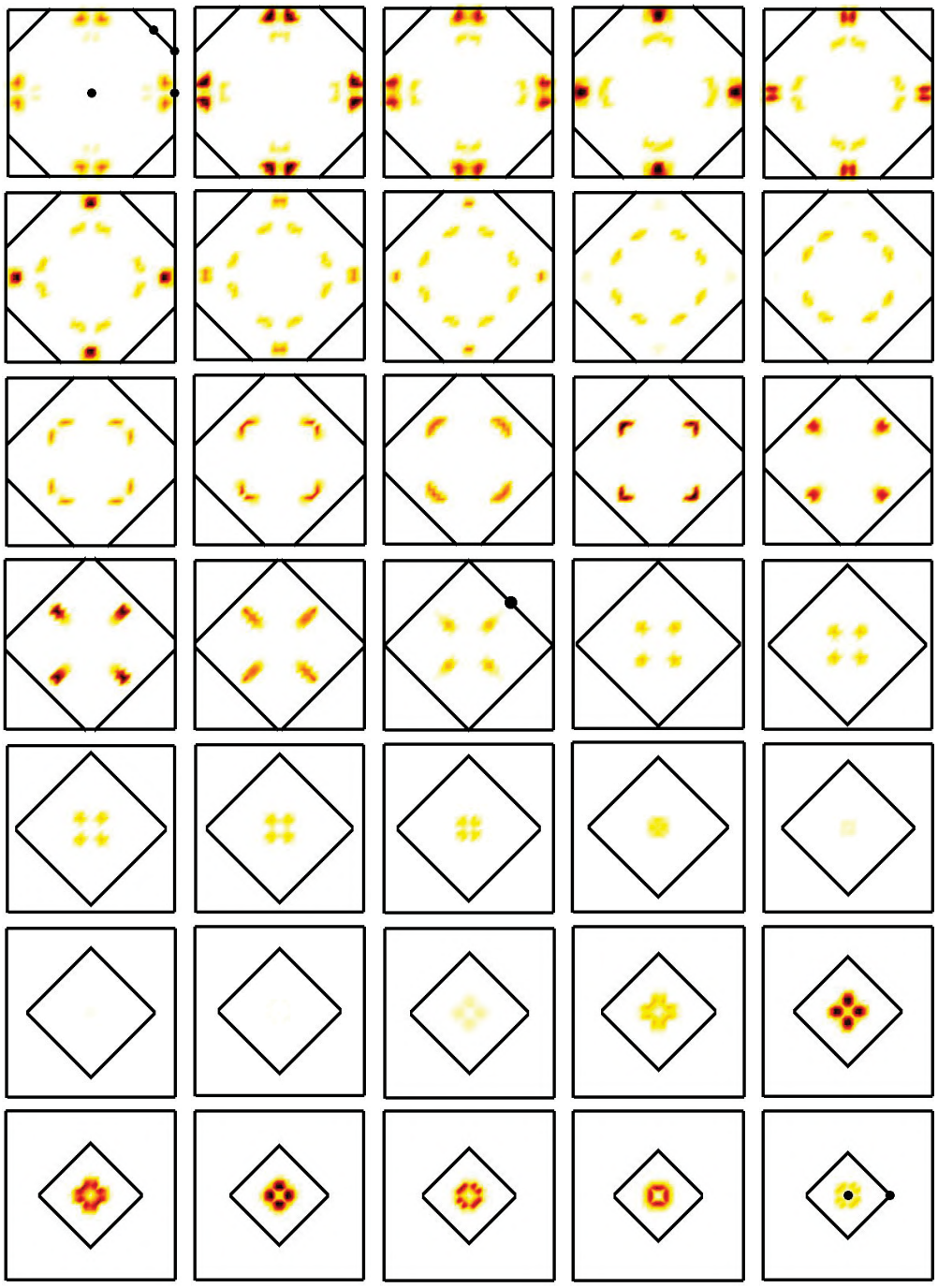

Figure A.1: Oscillator strengths of palladium for transitions in the 0.1 to 0.6 eV range.

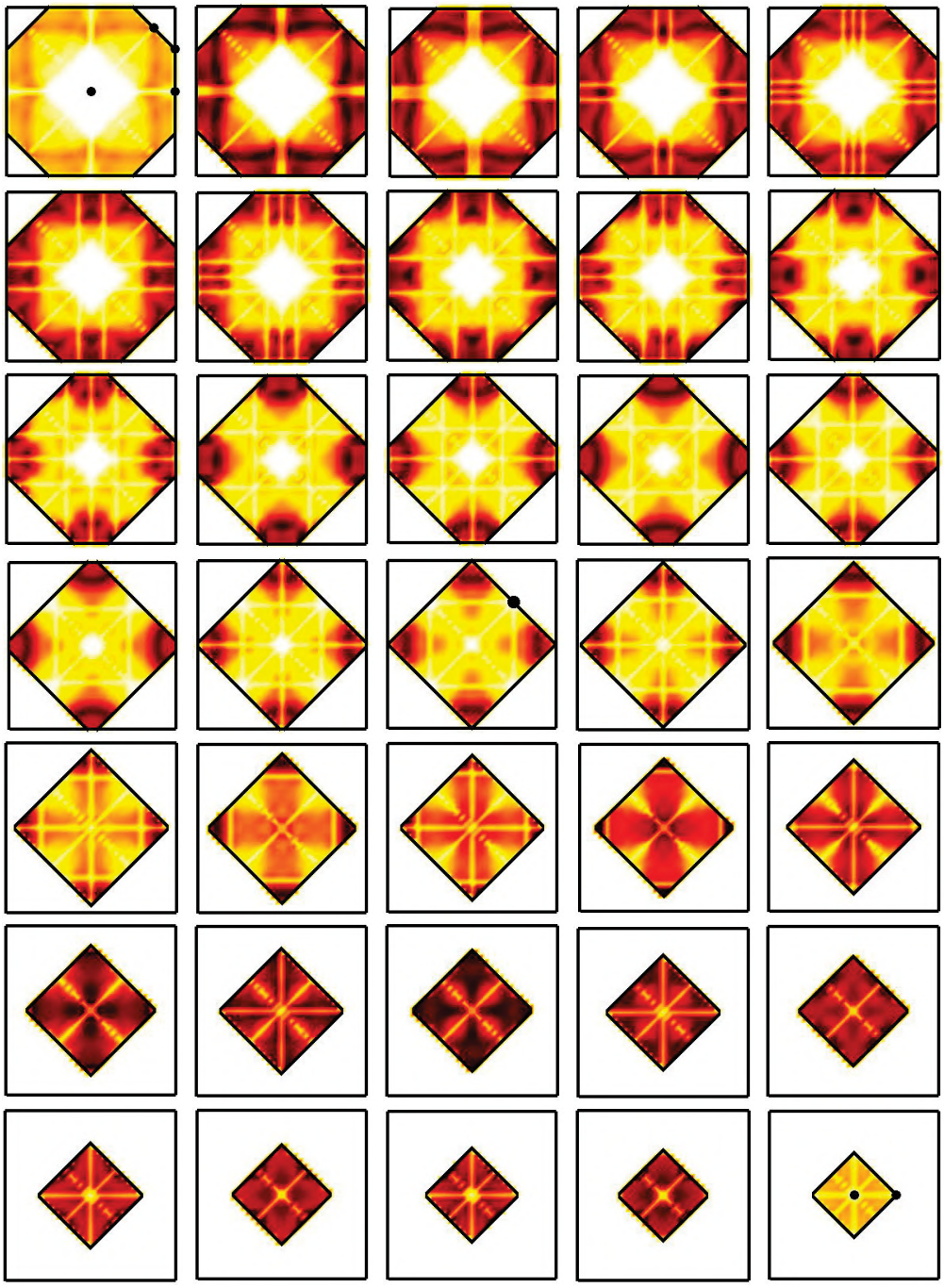

Figure A.2: Oscillator strengths of palladium for transitions in the 8 to 18 eV range.

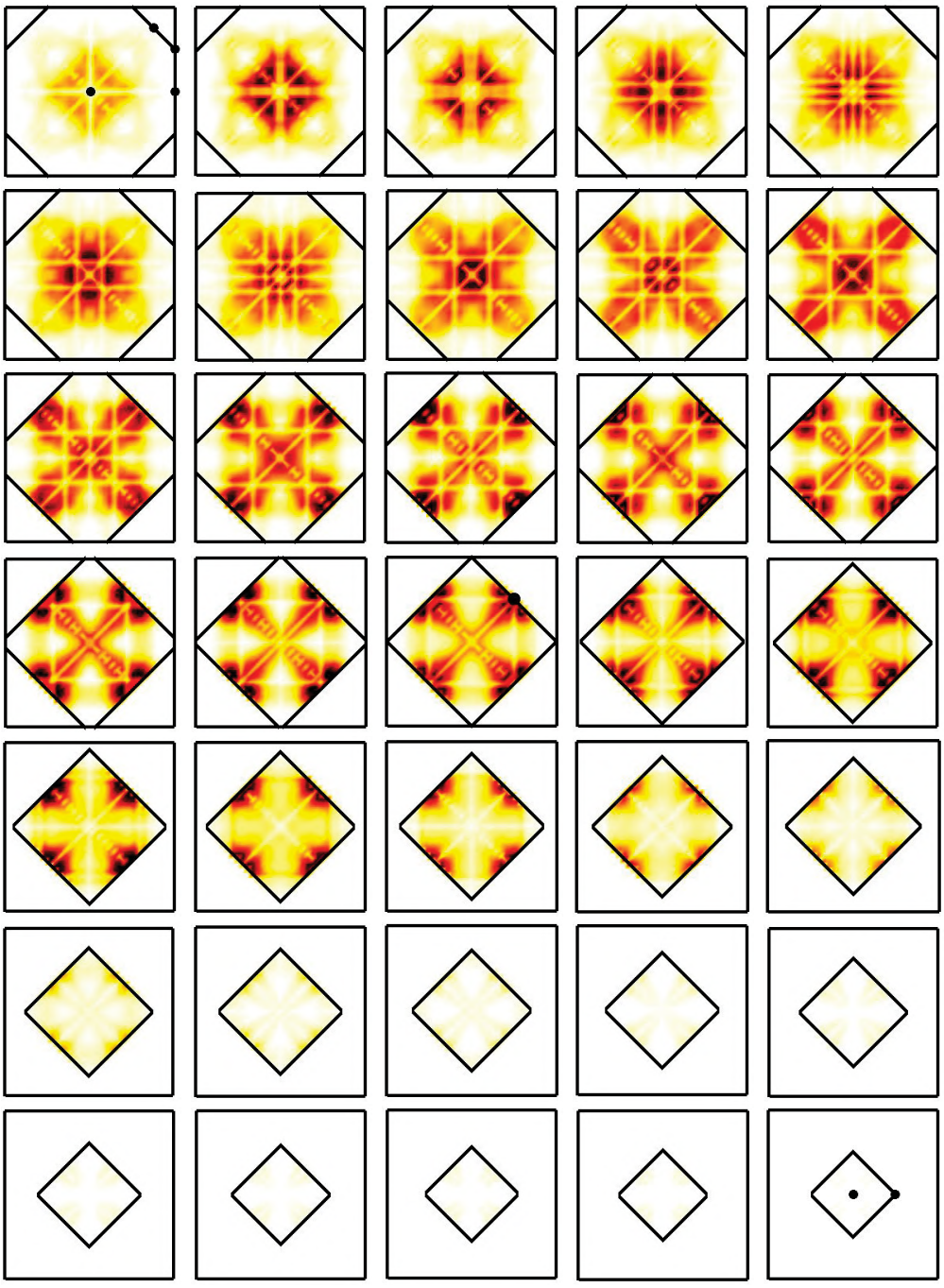

Figure A.3: Oscillator strengths of palladium for transitions in the 19 to 21.5 eV range.

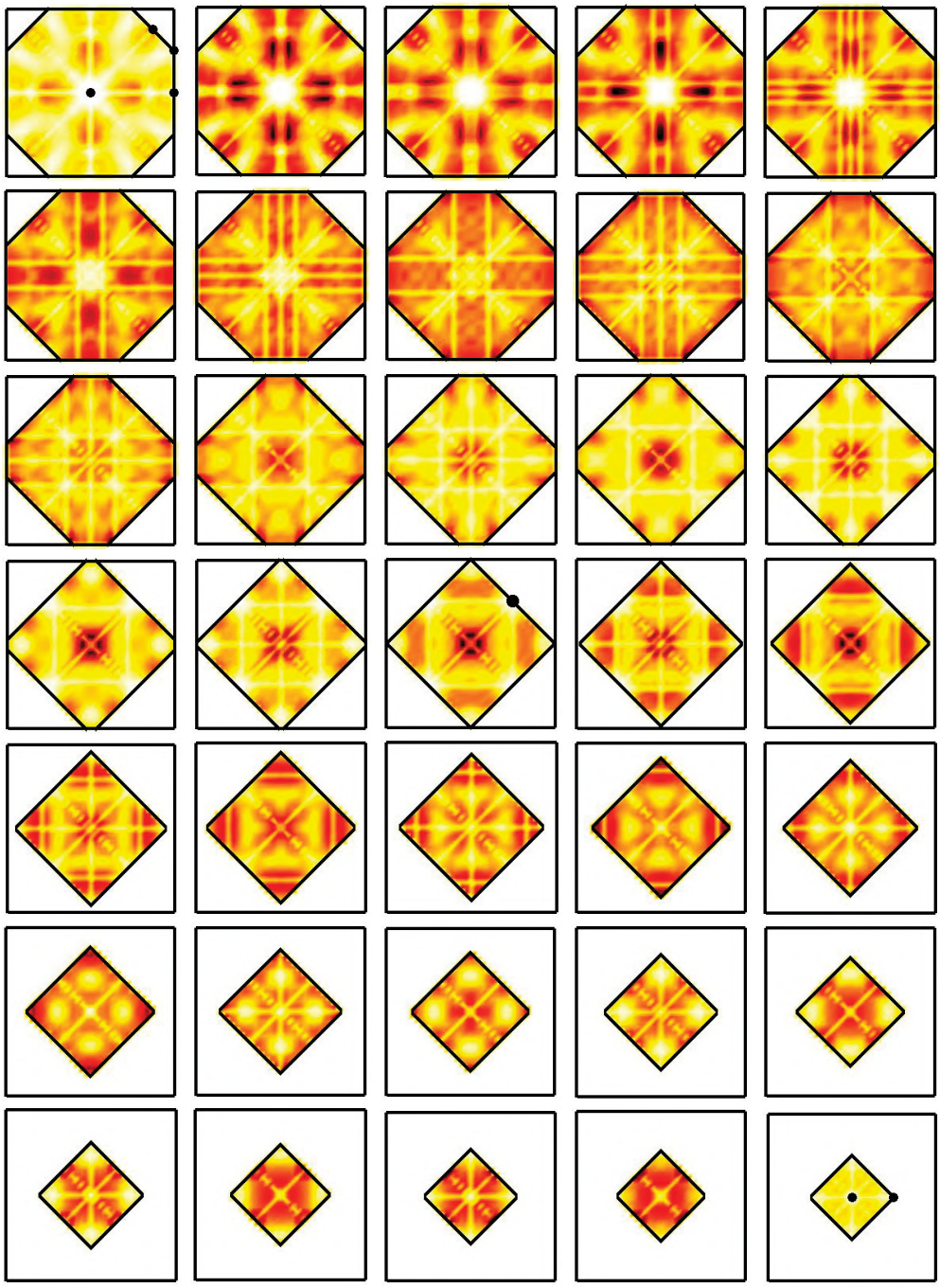

Figure A.4: Oscillator strengths of palladium for transitions in the 30 to 32.5 eV range.

B Oscillator strengths of aluminum

In the following, the oscillator strengths of aluminum are depicted. They were determined according to Eq. (7.2) for the 0.1 to 2.1 eV range and pressures up to 15.8 GPa. For the lattice constants values of 7.6534, 7.5769, 7.5003, 7.4238, 7.3473, and 7.2707 a.u. were adopted corresponding to an applied pressure of 0, 1.8, 4.6, 7.8, 11.5, and 15.8 GPa, respectively. The results are shown for 35 different planes in the BZ starting with oscillator strenghts for **k** points within the $k_z = 0$ plane in the top left corner and ending with oscillator strengths for **k** points in the $k_z = 1$ plane in the bottom right corner. The distance between two subsequent planes is $\Delta k_z = 1/34$ (in units of $2\pi/a$). Regions with high oscillator strengths appear in dark red.

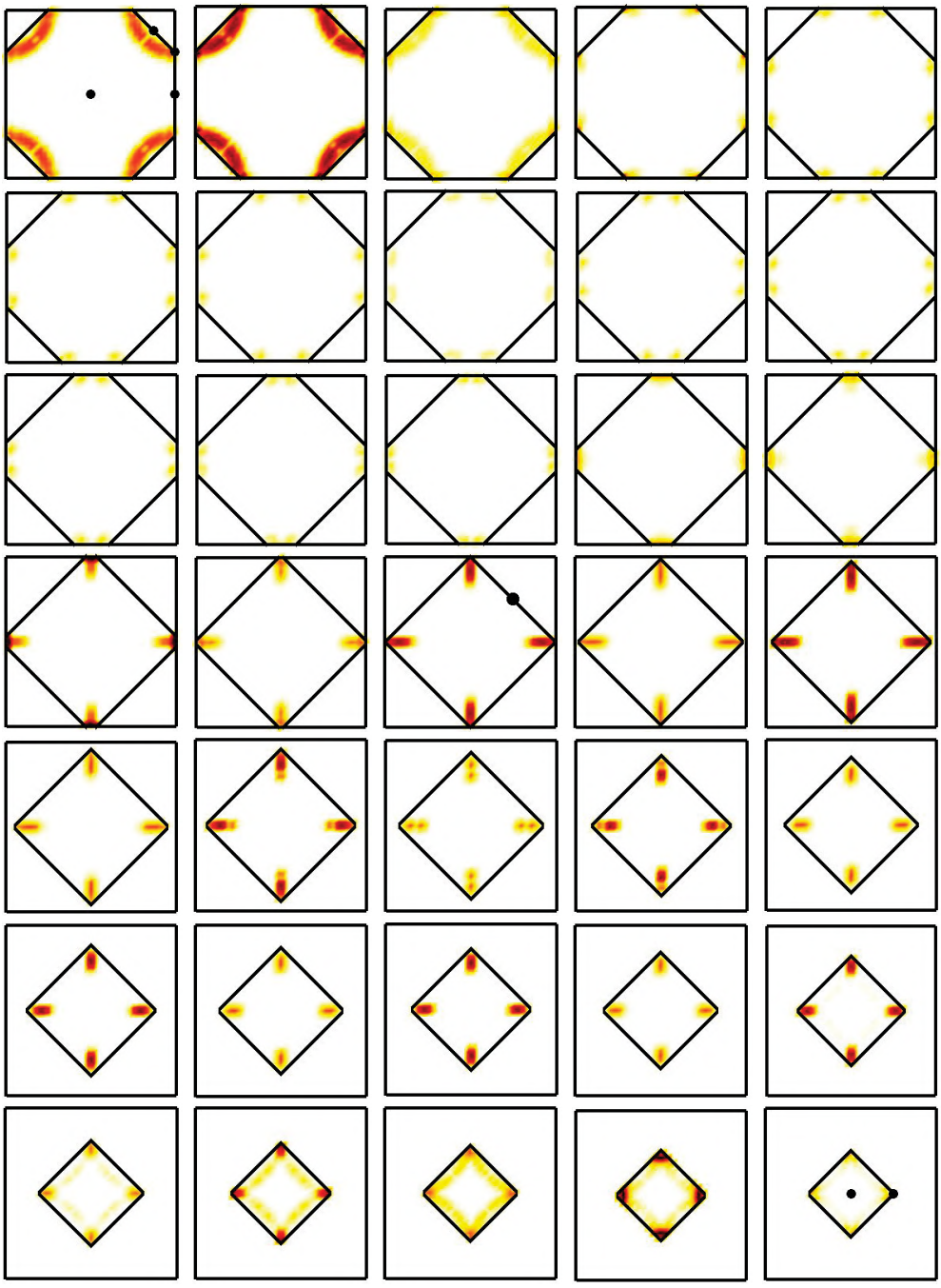

Figure B.1: Oscillator strengths of aluminum for transitions in the 0.1 to 2.1 eV range.

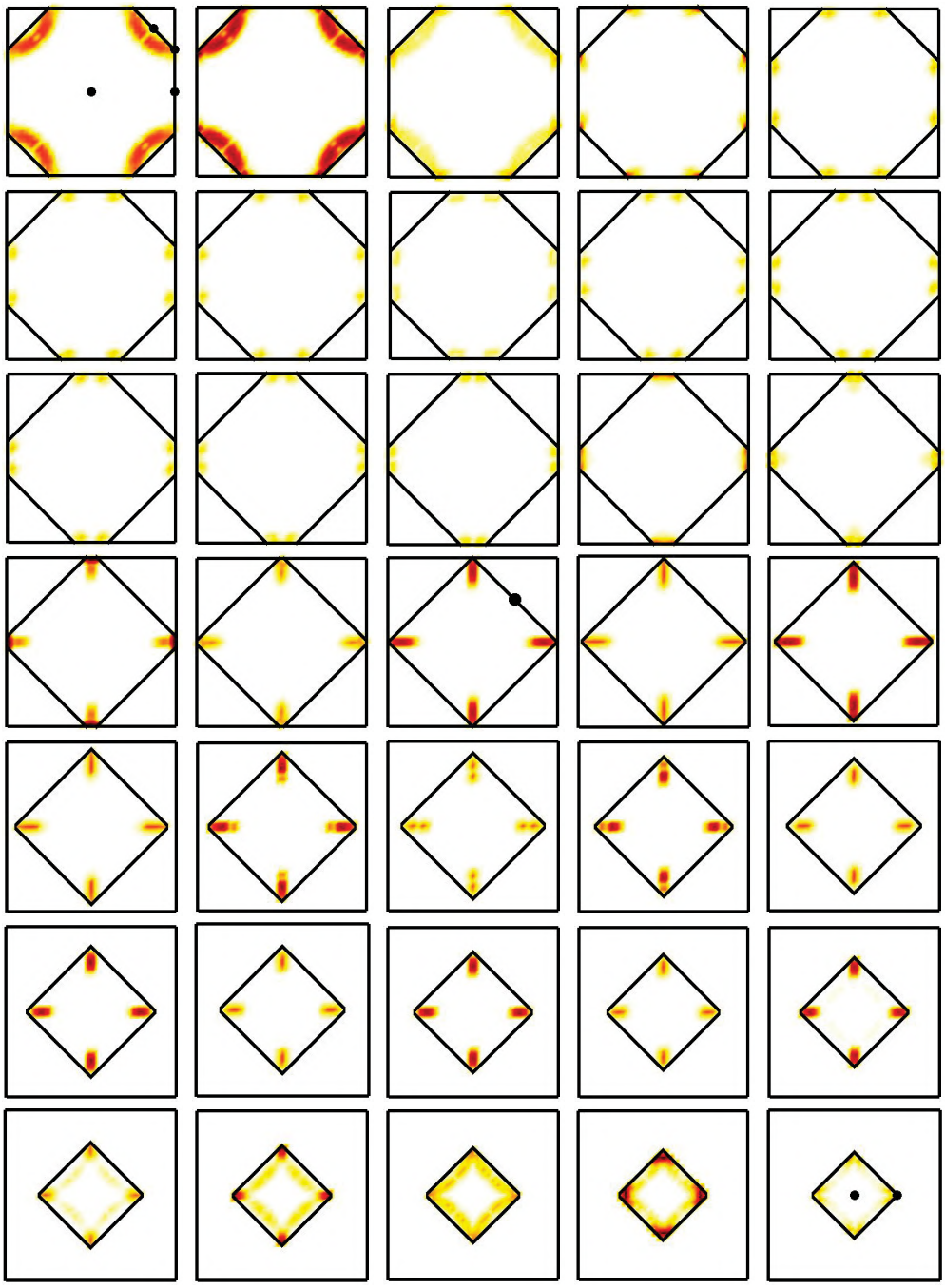

Figure B.2: Oscillator strengths of aluminum for transitions in the 0.1 to 2.1 eV range and an applied pressure of 1.8 GPa.

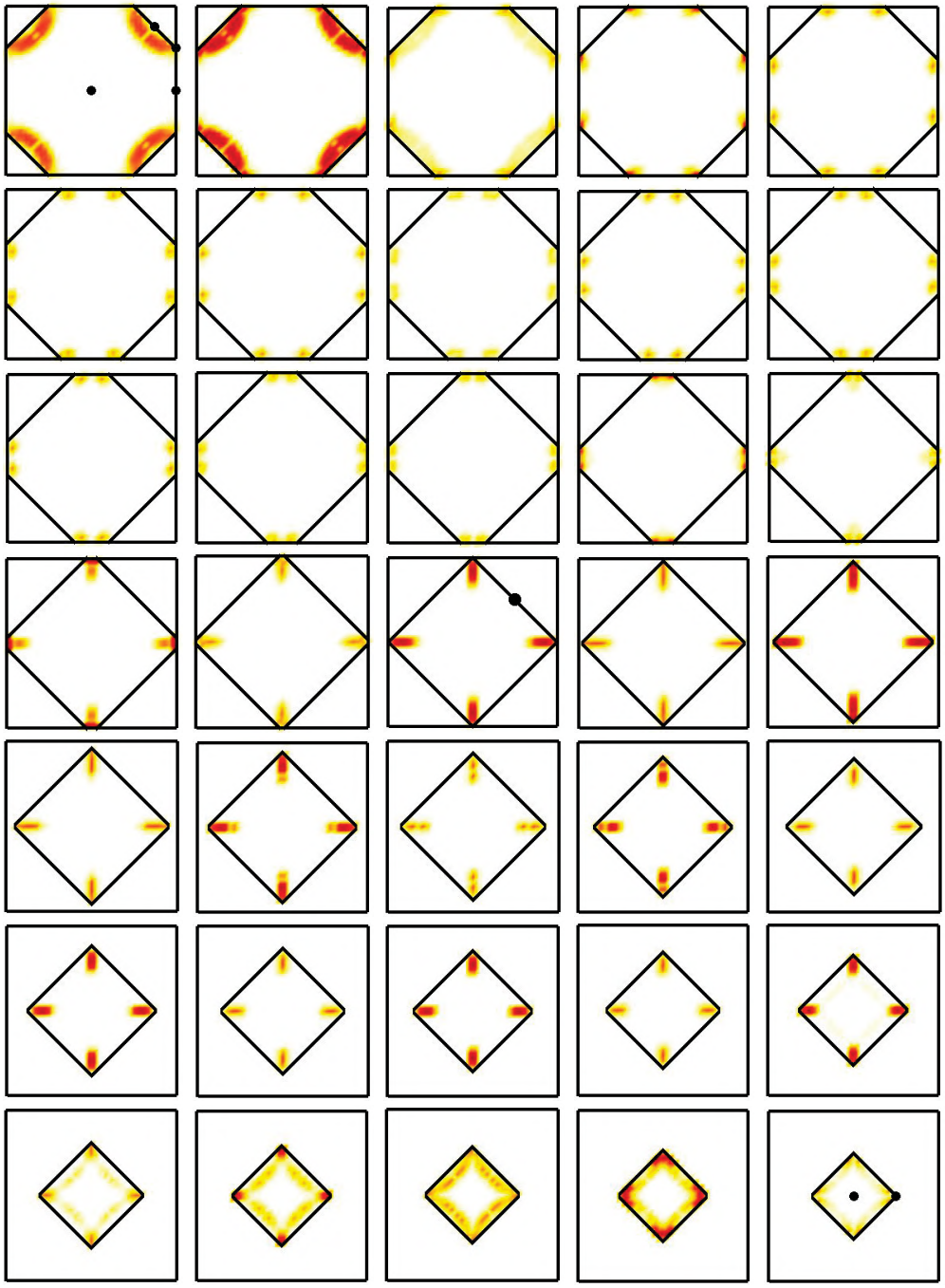

Figure B.3: Oscillator strengths of aluminum for transitions in the 0.1 to 2.1 eV range and an applied pressure of 4.6 GPa.

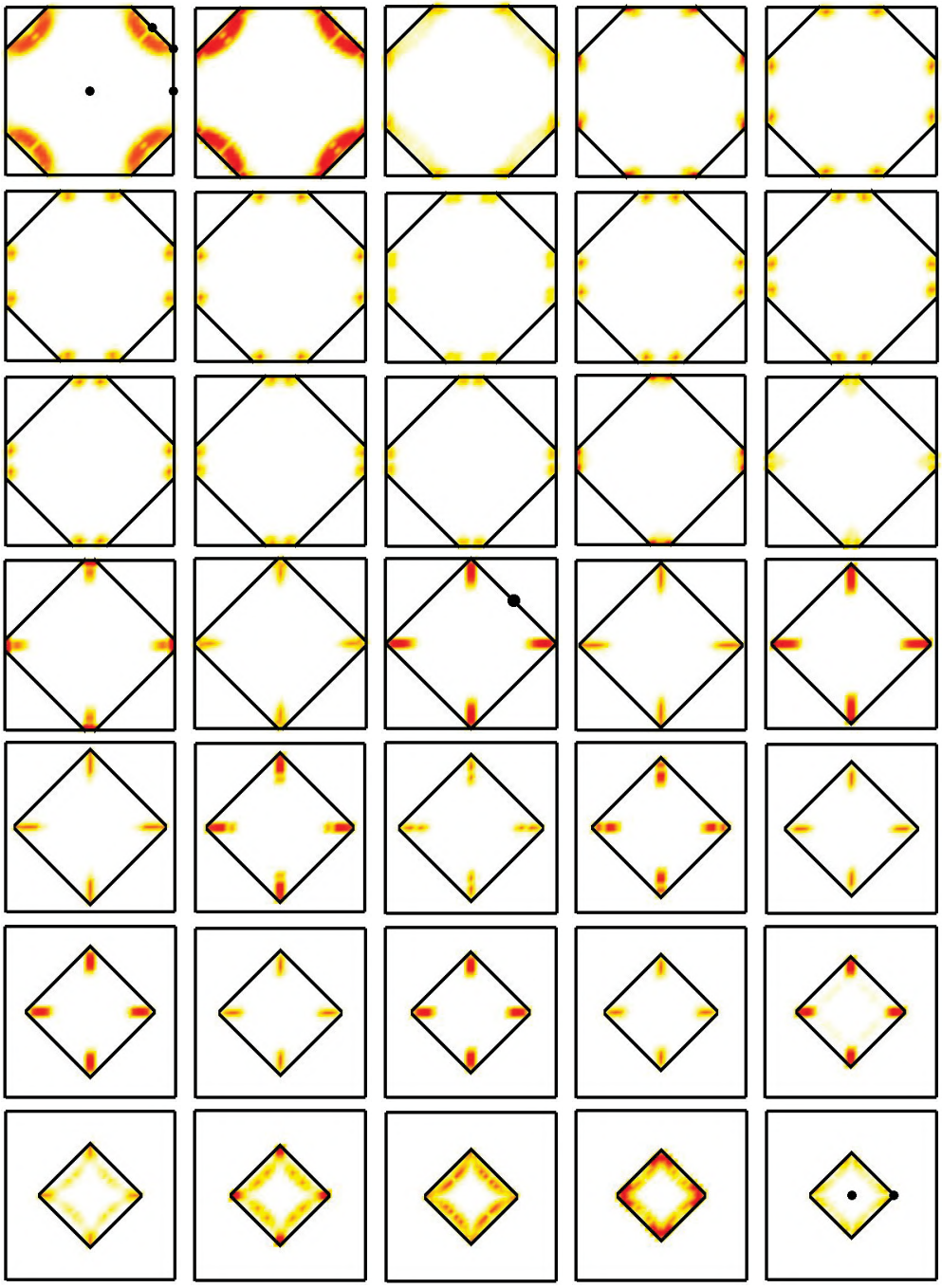

Figure B.4: Oscillator strengths of aluminum for transitions in the 0.1 to 2.1 eV range and an applied pressure of 7.8 GPa.

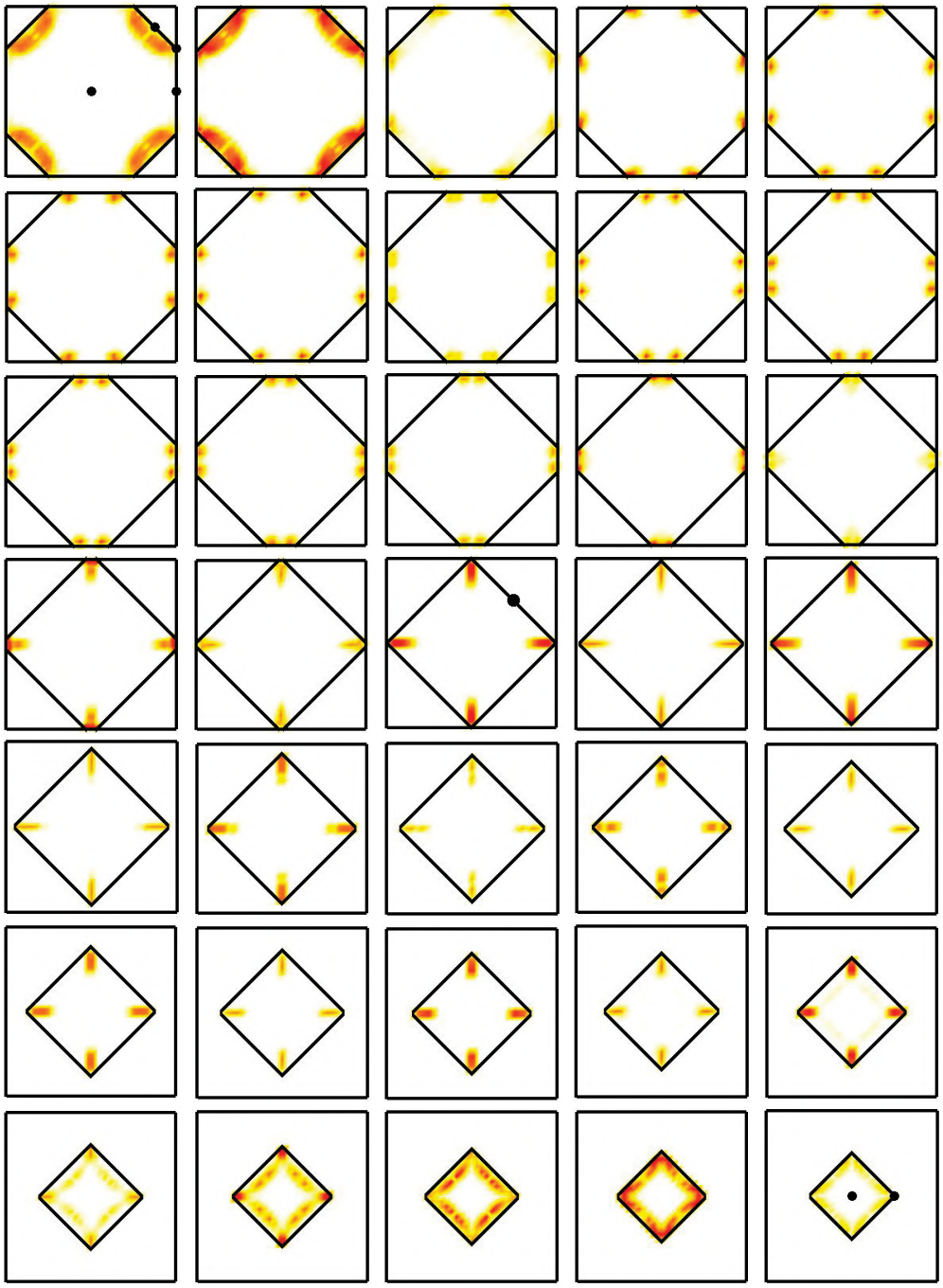

Figure B.5: Oscillator strengths of aluminum for transitions in the 0.1 to 2.1 eV range and an applied pressure of 11.5 GPa.

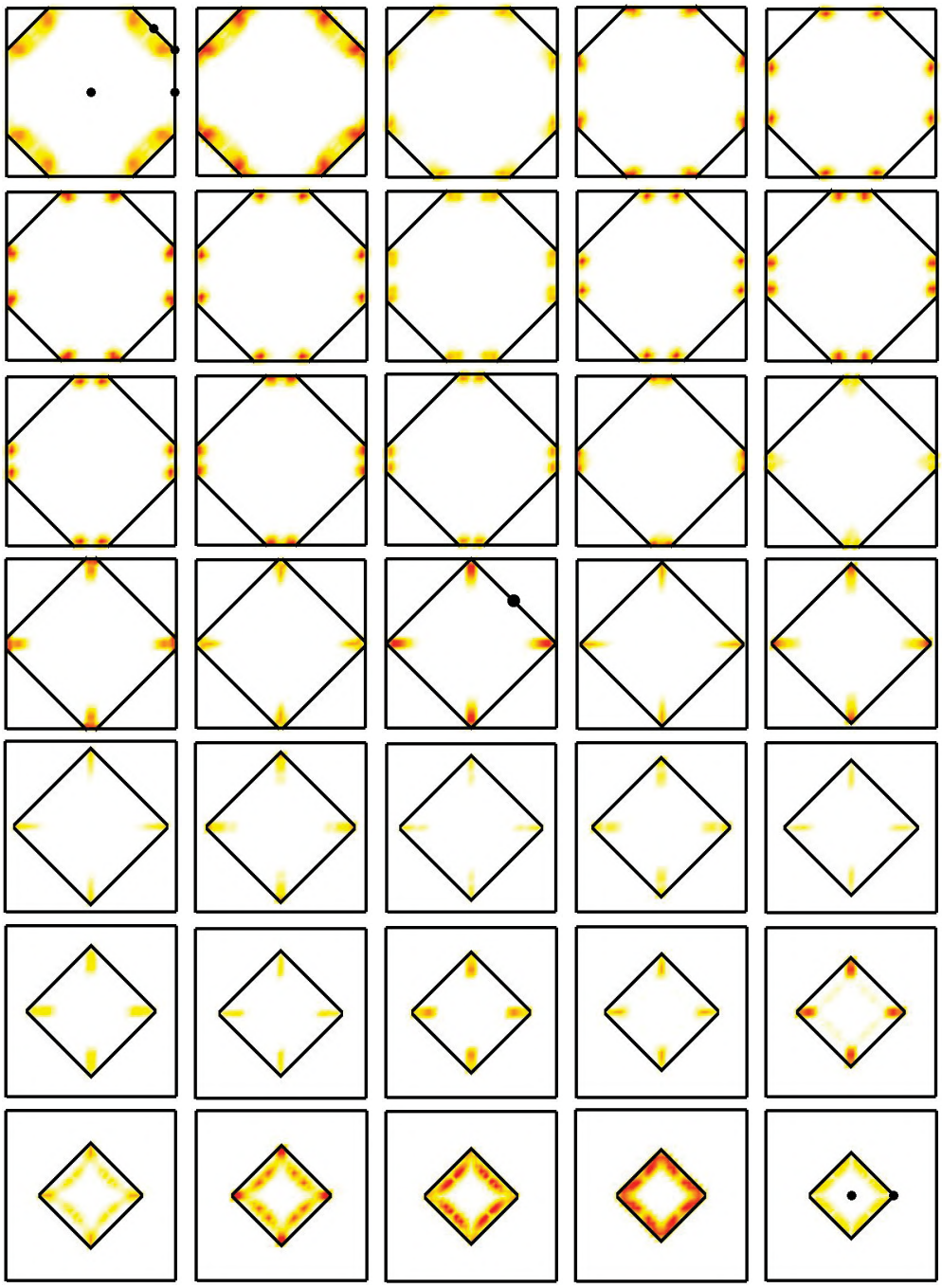

Figure B.6: Oscillator strengths of aluminum for transitions in the 0.1 to 2.1 eV range and an applied pressure of 15.8 GPa.

C Oscillator strengths and momentum matrix elements of gold, platinum, and lead

In the following, the oscillator strengths of the fcc metals gold, platinum, and lead, as well as the momentum matrix elements of lead are depicted. The oscillator strengths were calculated according to Eq. (7.2) for the 2.5 - 4 eV, 6.4 - 7.4 eV, and 18.2 - 21.2 eV range for gold, the 0.4 - 1.2 eV, 6 - 12 eV, and 17.5 - 22 eV range for platinum, and the 3.5 - 4.5 eV range for lead. The results are shown for 35 different planes in the BZ starting with oscillator strenghts for **k** points within the $k_z = 0$ plane in the top left corner and ending with oscillator strenghts for **k** points within the $k_z = 1$ plane in the bottom right corner. The distance between two subsequent planes is $\Delta k_z = 1/34$ (in units of $2\pi/a$). Regions with high oscillator strengths appear in dark red.

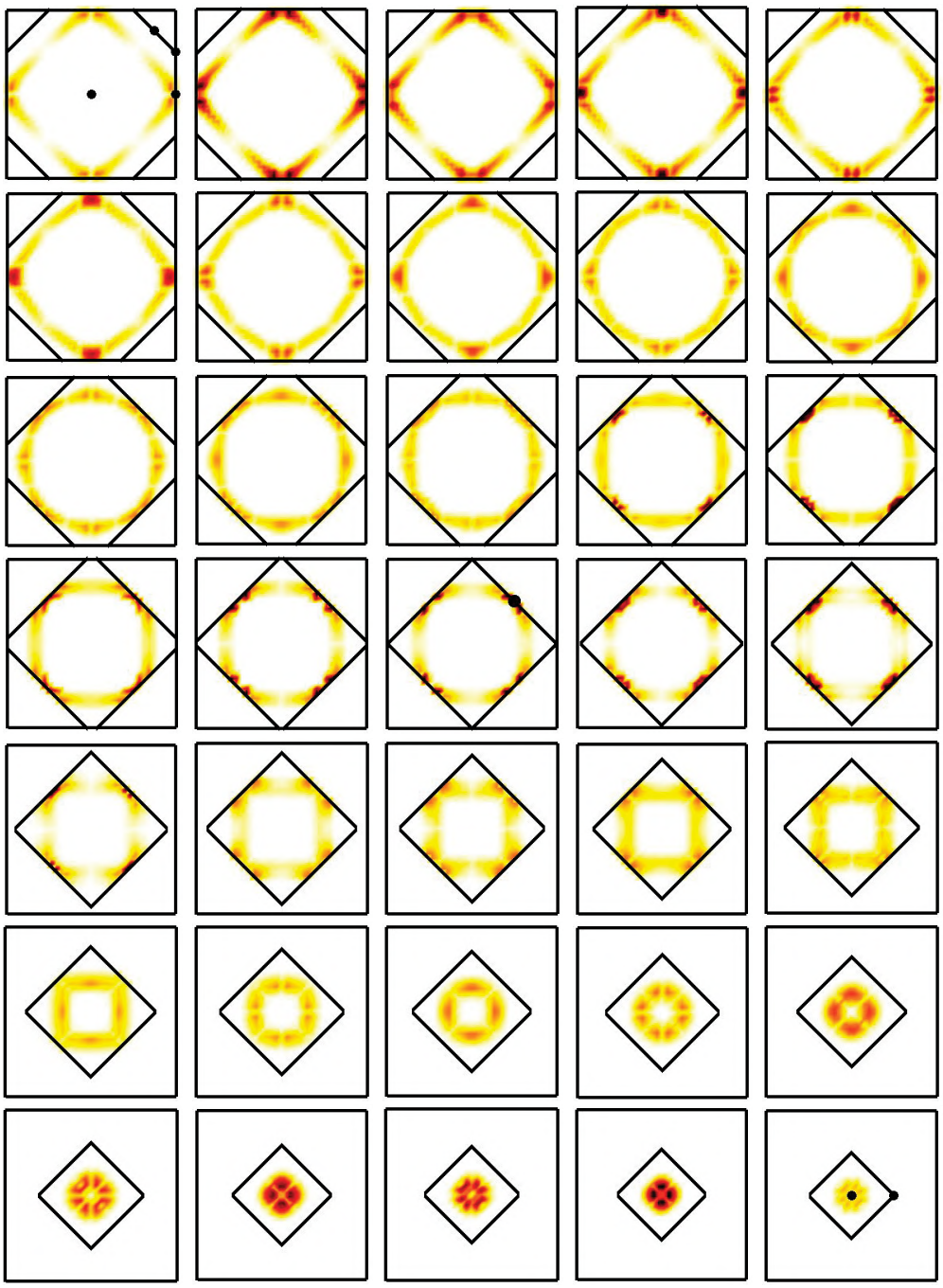

Figure C.1: Oscillator strengths of gold for transitions in the 2.5 to 4 eV range including spin-orbit interaction.

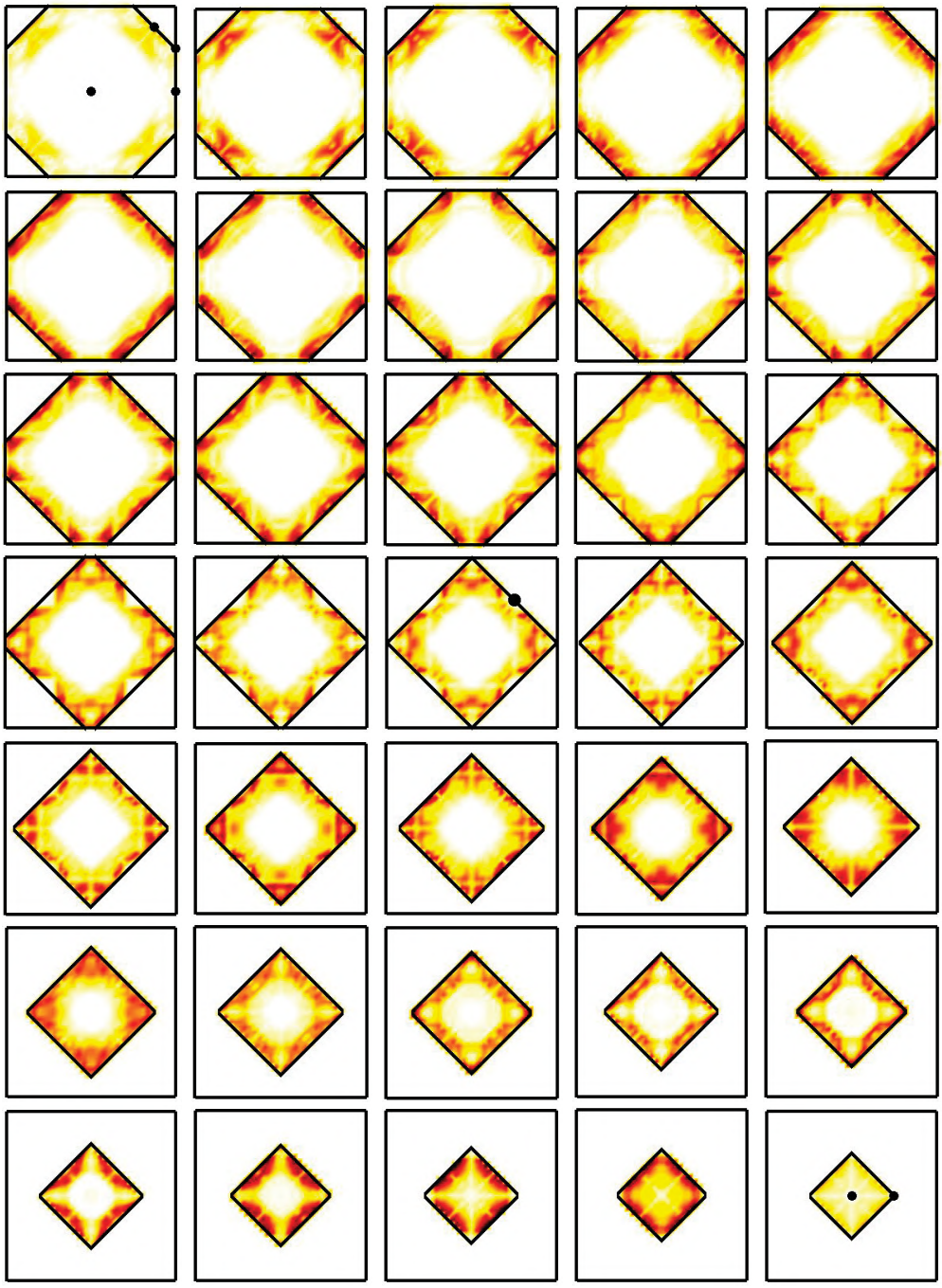

Figure C.2: Oscillator strengths of gold for transitions in the 6.4 to 7.4 eV range including spin-orbit interaction.

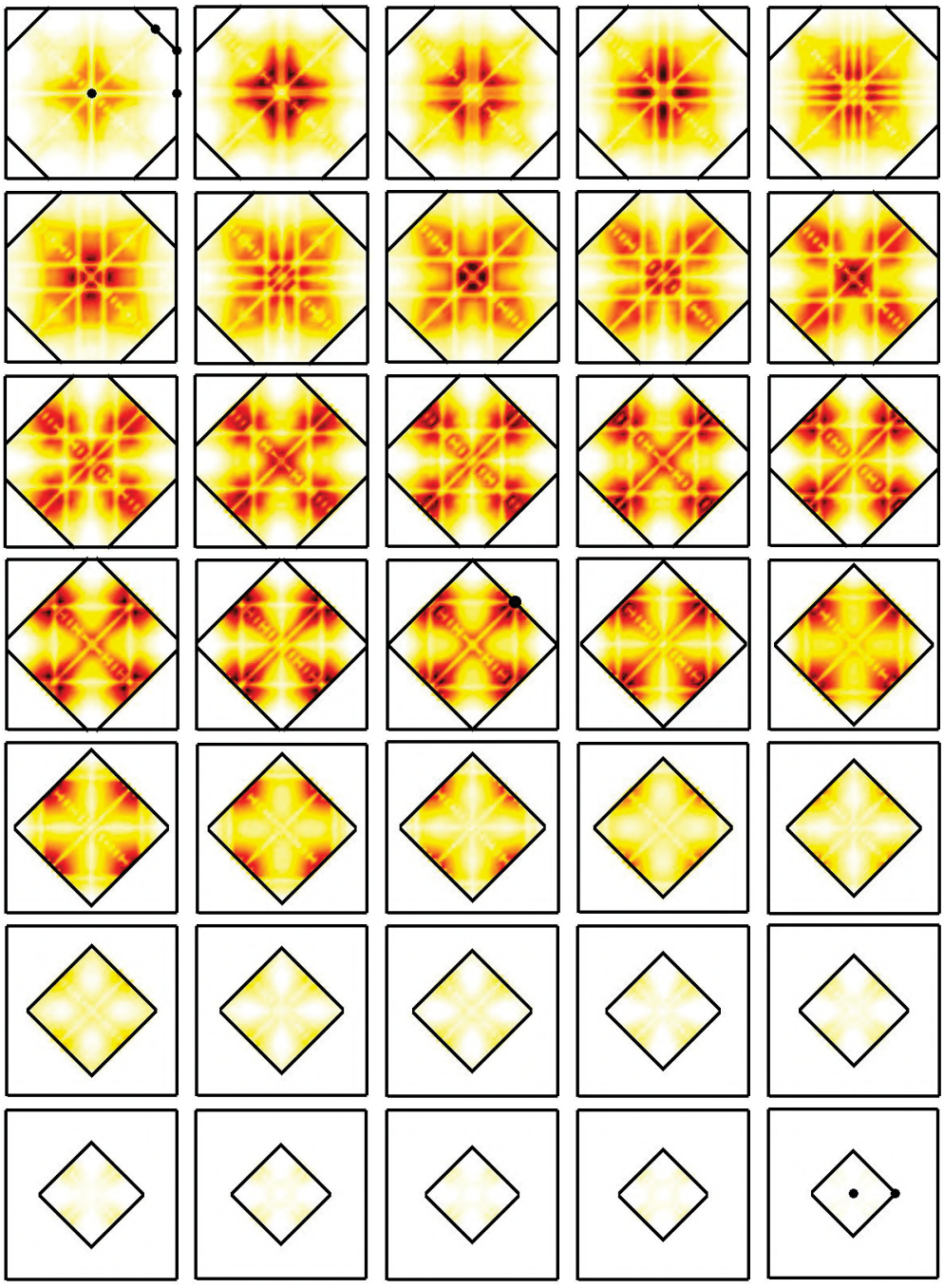

Figure C.3: Oscillator strengths of gold for transitions in the 18.2 to 21.2 eV range including spin-orbit interaction.

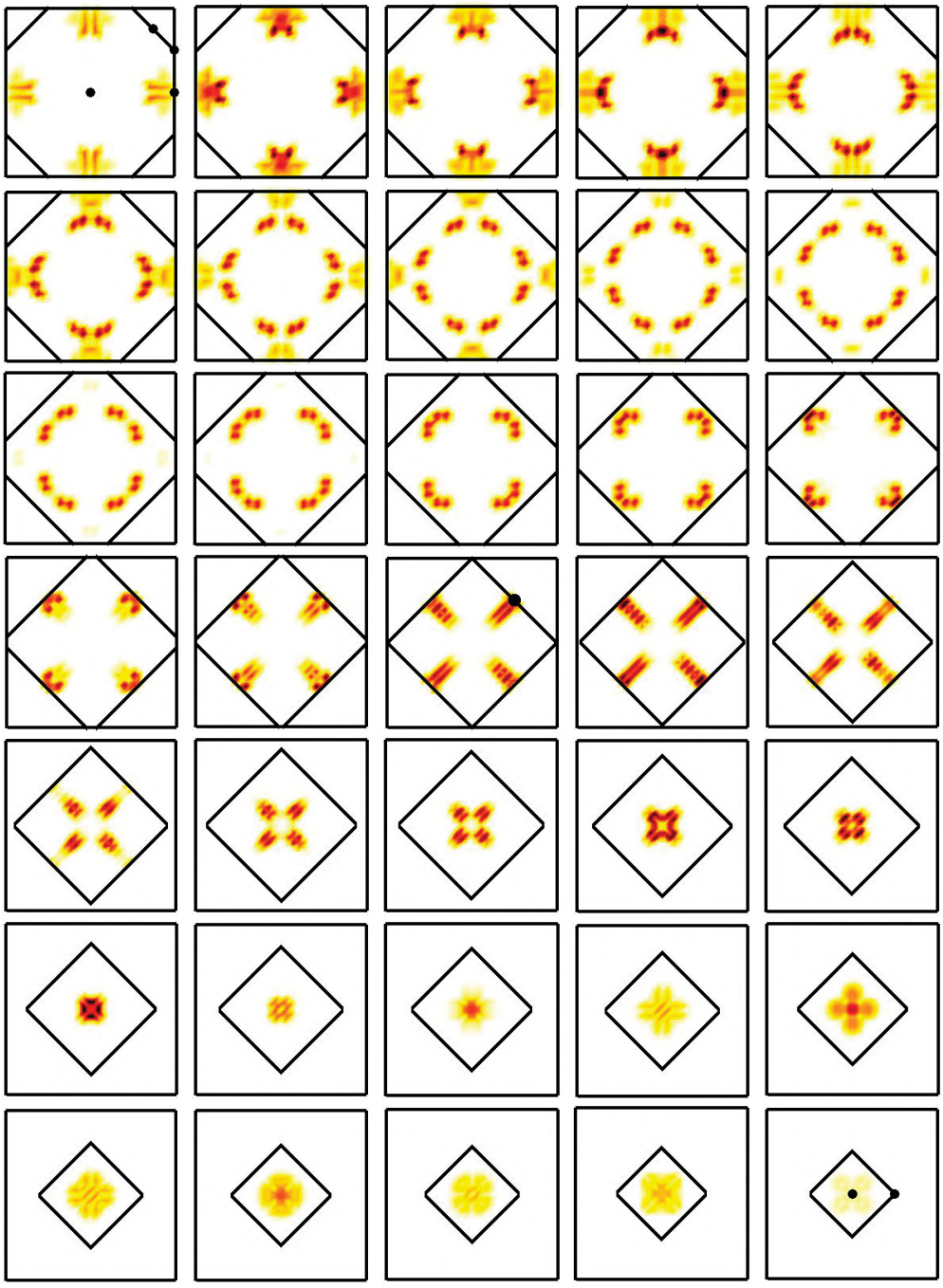

Figure C.4: Oscillator strengths of platinum for transitions in the 0.4 to 1.2 eV range including spin-orbit interaction.

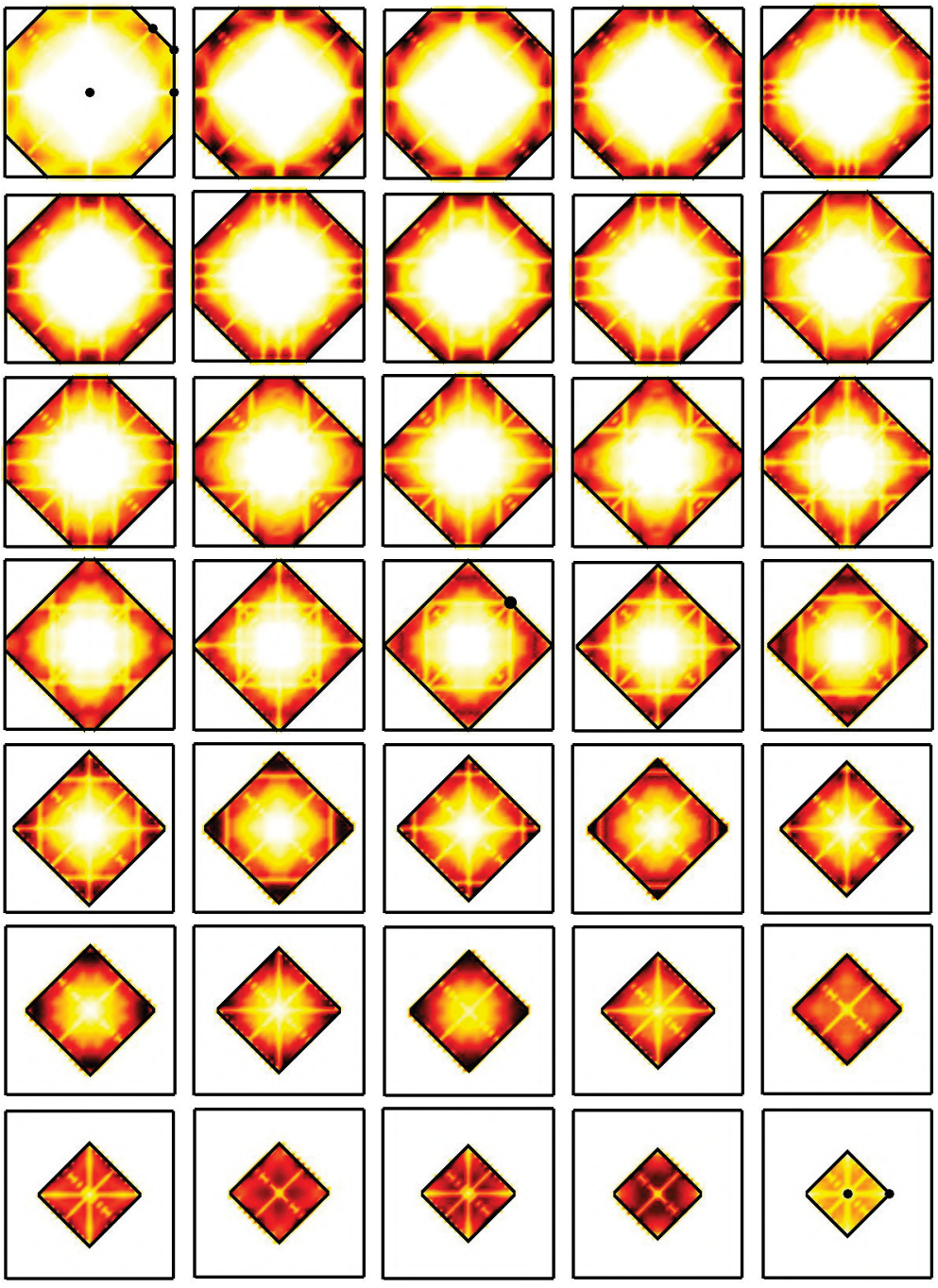

Figure C.5: Oscillator strengths of platinum for transitions in the 6 to 12 eV range including spin-orbit interaction.

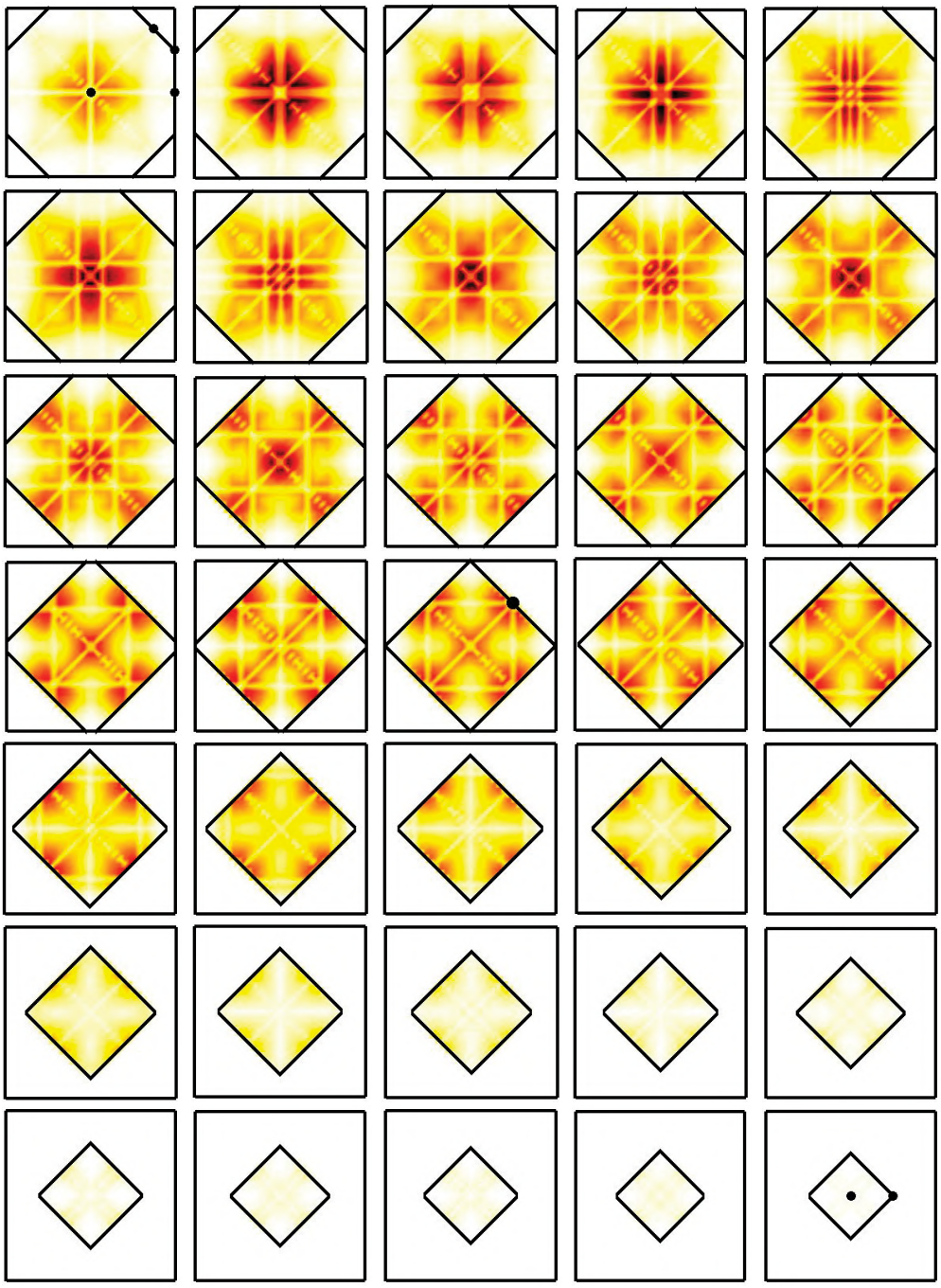

Figure C.6: Oscillator strengths of platinum for transitions in the 17.5 to 22 eV range including spin-orbit interaction.

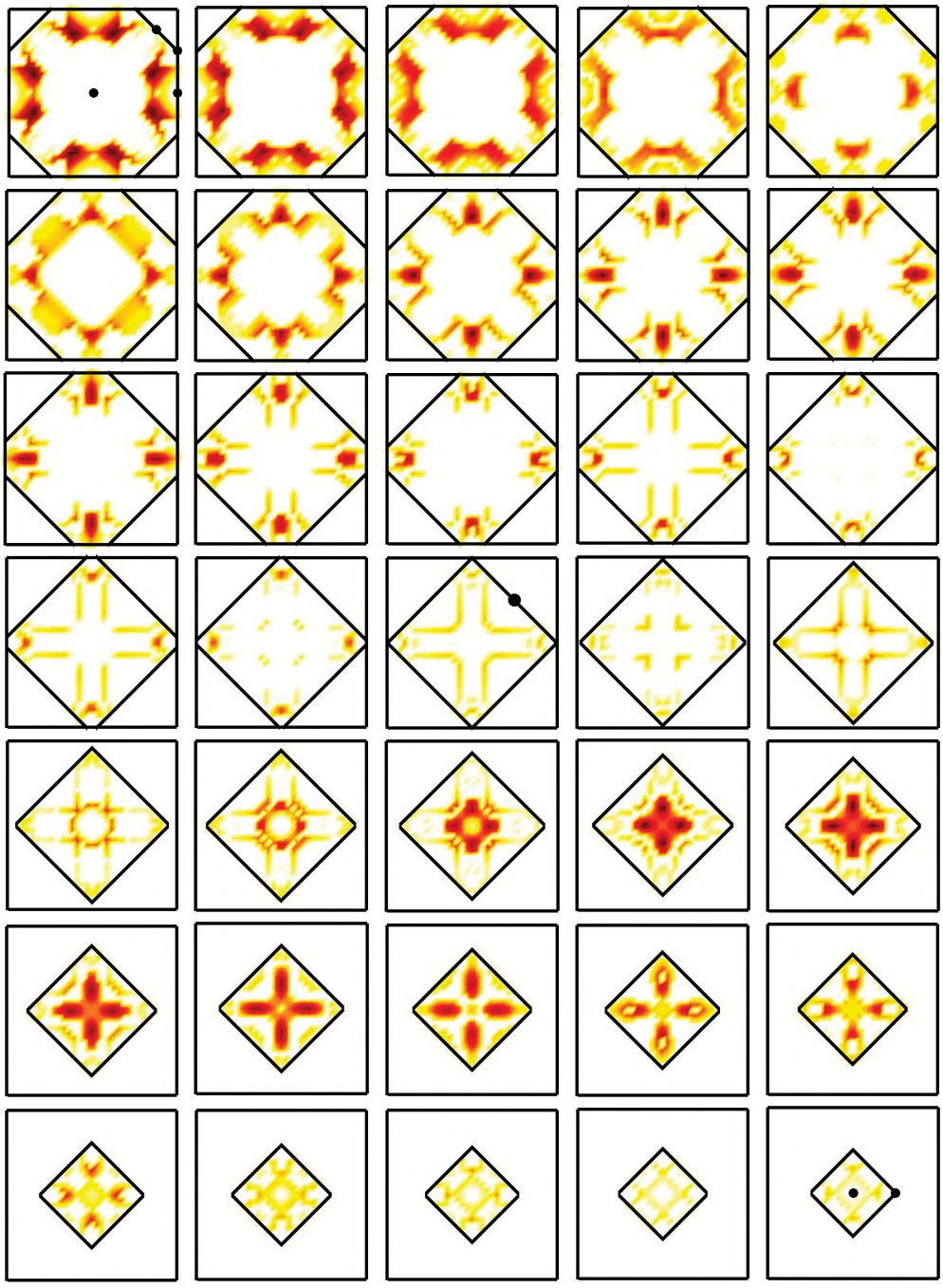

Figure C.7: Momentum matrix elements of lead for transitions in the 3.5 to 4.5 eV range including spin-orbit interaction.

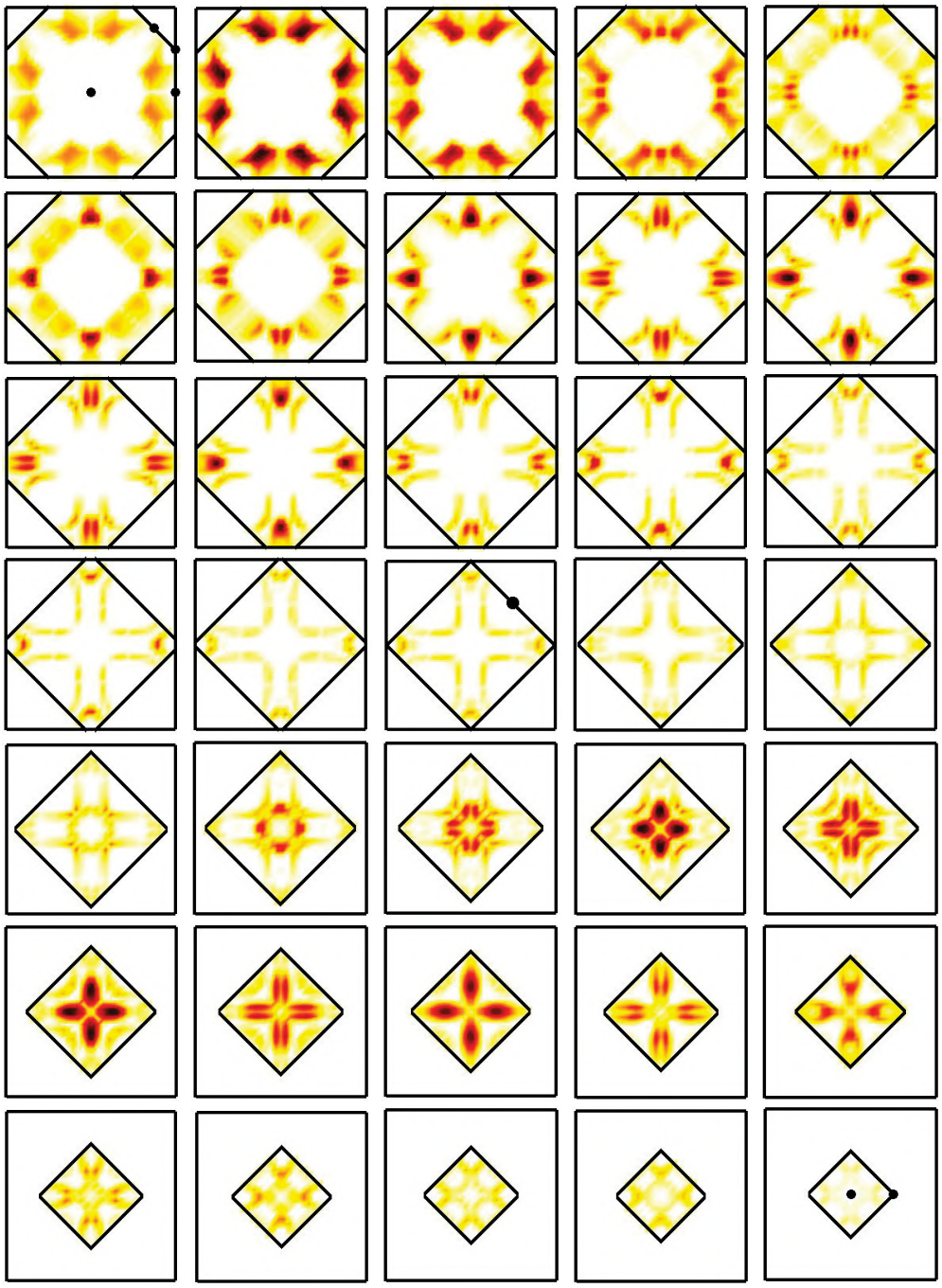

Figure C.8: Oscillator strengths of lead for transitions in 3.5 to 4.5 eV range including spin-orbit interaction.

Acknowledgments

I particularly want to thank Claudia Draxl for supervising this PhD thesis with immense patience during the last years. I am grateful for her support, for her advices and remarks, for numerous interesting discussions, and for many tips on how to improve my scientific writing, which helped me a lot throughout my work on this PhD thesis. I am also thankful for her thorough proofreading of this work.

I want to thank Ulrich Hohenester for being the second reviewer of this work.

I wish to extend special thanks to Cécile Hébert and Wolfgang Werner for providing me with experimental data sets.

Many thanks go to the group members of the research group of Claudia Draxl in Berlin, as well as to the former group members in Leoben and Graz, for fruitful discussions, for showing me how to use WIEN2k and the **`exciting`** code, for help in terms of grafics tools, as well as for the enjoyable working atmosphere I experienced during my visits.

Last but not least I want to express gratitude to my family. Their steady support and encouragement during the last years made it possible to find enough time to work on this PhD thesis in parallel to my full-time job.

List of Figures

List of Tables

Bibliography

[1] P. HOHENBERG and W. KOHN, *Phys. Rev.* **136**, B864 (1964).

[2] W. KOHN and L. J. SHAM, *Phys. Rev.* **140**, A1133 (1965).

[3] E. RUNGE and E. K. U. GROSS, *Phys. Rev. Lett.* **52**, 997 (1984).

[4] E. K. U. GROSS, J. F. DOBSON, and M. PETERSILKA, Density functional theory of time-dependent phenomena, in *Density Functional Theory*, edited by R. F. NALEWAJSKI, volume 181 of *Topics in Current Chemistry*, p. 81, Springer-Verlag Berlin Heidelberg, 1996.

[5] E. SJÖSTEDT, L. NORDSTRÖM, and D. J. SINGH, *Solid State Commun.* **114**, 15 (2000).

[6] P. BLAHA, K. SCHWARZ, G. K. H. MADSEN, D. KVASNICKA, and J. LUITZ, *Wien2k, An Augmented Plane Wave + Local Orbitals Program for Calculating Crystal Properties*, Karlheinz Schwarz, Technische Universität Wien, Austria, 2001.

[7] **`exciting`** code, http://exciting-code.org.

[8] C. HÉBERT, private communication.

[9] W. S. M. WERNER, M. R. WENT, M. VOS, K. GLANTSCHNIG, and C. AMBROSCH-DRAXL, *Phys. Rev. B* **77**, 161404(R) (2008).

[10] W. S. M. WERNER, K. GLANTSCHNIG, and C. AMBROSCH-DRAXL, *J. Phys. Chem. Ref. Data* **38**, 1013 (2009).

[11] L. H. THOMAS, *Proc. Cambridge Phil. Soc.* **23**, 542 (1927).

[12] E. FERMI, *Rend. Accad. Naz. Lincei* **6**, 602 (1927).

[13] W. KOHN, *Rev. Mod. Phys.* **71**, 1253 (1999).

[14] R. M. MARTIN, *Electronic structure: basic theory and practical methods*, Cambridge University Press, 2004.

[15] F. DUAN and J. GUOJUN, *Introduction to condensed matter physics*, volume 1, World Scientific, 2005.

[16] W. KOHN, *Proceedings of the International School of Physics, "Enrico Fermi"* **Course LXXXIX**, 4 (1985).

[17] M. LEVY, *Phys. Rev. A* **26**, 1200 (1982).

[18] E. H. LIEB, *Int. J. Quant. Chem.* **24**, 243 (1983).

[19] R. O. JONES and O. GUNNARSSON, *Rev. Mod. Phys.* **61**, 689 (1989).

[20] D. C. LANGRETH and J. P. PERDEW, *Solid State Commun.* **17**, 1425 (1975).

[21] J. HARRIS and R. O. JONES, *J. Phys. F* **4**, 1170 (1974).

[22] O. GUNNARSSON and B. I. LUNDQVIST, *Phys. Rev. B* **13**, 4274 (1976).

[23] W. KOHN, *Phys. Rev. Lett.* **76**, 3168 (1996).

[24] E. P. WIGNER, *Trans. Faraday Soc.* **34**, 678 (1938).

[25] S. H. VOSKO, L. WILK, and M. NUSAIR, *Can. J. Phys.* **58**, 1200 (1980).

[26] J. P. PERDEW and A. ZUNGER, *Phys. Rev. B* **23**, 5048 (1981).

[27] J. P. PERDEW and Y. WANG, *Phys. Rev. B* **45**, 13244 (1992).

[28] D. M. CEPERLEY and B. J. ALDER, *Phys. Rev. Lett.* **45**, 566 (1980).

[29] J. P. PERDEW, K. BURKE, and M. ERNZERHOF, *Phys. Rev. Lett.* **77**, 3865 (1996).

[30] L. J. SHAM and M.SCHLÜTER, *Phys. Rev. Lett.* **51**, 1888 (1983).

[31] J. P. PERDEW and M. LEVY, *Phys. Rev. Lett.* **51**, 1884 (1983).

[32] J. F. JANAK, *Phys. Rev. B* **18**, 7165 (1978).

[33] M. PETERSILKA, U. J. GOSSMANN, and E. K. U. GROSS, *Phys. Rev. Lett.* **76**, 1212 (1996).

[34] G. ONIDA, L. REINING, and A. RUBIO, *Rev. Mod. Phys.* **74**, 601 (2002).

[35] R. VAN LEEUWEN, *Int. J. Mod. Phys. B* **15**, 1969 (2001).

[36] E. K. U. GROSS and W. KOHN, *Adv. Quant. Chem.* **21**, 255 (1990).

[37] L. V. KELDYSH, *Sov. Phys. JETP* **20**, 1018 (1965).

[38] S. BOTTI, F. SOTTILE, N. VAST, V. OLEVANO, L. REINING, H.-C. WEISSKER, A. RUBIO, G. ONIDA, R. DEL SOLE, and R. W. GODBY, *Phys. Rev. B* **69**, 155112 (2004).

[39] L. REINING, V. OLEVANO, A. RUBIO, and G. ONIDA, *Phys. Rev. Lett.* **88**, 066404 (2002).

[40] S. BOTTI, A. FOURREAU, F. NGUYEN, Y.-O. RENAULT, F. SOTTILE, and L. REINING, *Phys. Rev. B* **72**, 125203 (2005).

[41] G. ADRAGNA, R. DEL SOLE, and A. MARINI, *Phys. Rev. B* **68**, 165108 (2003).

[42] A. MARINI, R. DEL SOLE, and A. RUBIO, *Phys. Rev. Lett.* **91**, 256402 (2003).

[43] R. DEL SOLE, G. ADRAGNA, V. OLEVANO, and L. REINING, *Phys. Rev. B* **67**, 045207 (2003).

[44] F. SOTTILE, V. OLEVANO, and L. REINING, *Phys. Rev. Lett.* **91**, 056402 (2003).

[45] E. K. U. GROSS and W. KOHN, *Phys. Rev. Lett.* **55**, 2850 (1985).

[46] H. BRUUS and K. FLENSBERG, *Many-body quantum theory in condensed matter physics - an introduction*, Oxford University Press, 2004.

[47] P. NOZIÈRES and D. PINES, *Phys. Rev.* **109**, 762 (1958).

[48] H. EHRENREICH and M. H. COHEN, *Phys. Rev.* **115**, 786 (1959).

[49] S. L. ADLER, *Phys. Rev.* **126**, 413 (1962).

[50] N. WISER, *Phys. Rev.* **129**, 62 (1963).

[51] M. DRESSEL and G. GRÜNER, *Electrodynamics of solids: optical properties of electrons in matter*, Cambridge University Press, Cambridge, 2002.

[52] C. AMBROSCH-DRAXL and J. O. SOFO, *Comp. Phys. Commun.* **175**, 1 (2006).

[53] S. SAGMEISTER, *Excitonic Effects in Solids: Time-Dependent Density Functional Theory versus the Bethe-Salpeter Equation*, PhD thesis, University of Graz, 2009.

[54] J. C. SLATER, *Phys. Rev.* **51**, 846 (1937).

[55] O. K. ANDERSEN, *Phys. Rev. B* **12**, 3060 (1975).

[56] D. D. KOELLING and G. O. ARBMAN, *J. Phys. F* **5**, 2041 (1975).

[57] D. J. SINGH, *Planewaves, Pseudopotentials and the LAPW method*, Kluwer Academic Publishers, Dodrecht, 1994.

[58] D. SINGH, *Phys. Rev. B* **43**, 6388 (1991).

[59] C. AMBROSCH-DRAXL, *Phys. Scr.* **T109**, 48 (2004).

[60] D. D. KOELLING and B. N. HARMON, *J. Phys. C* **10**, 3107 (1977).

[61] J. KÜBLER, *Theory of itinerant electron magnetism*, Oxford University Press, New York, 2000.

[62] A. H. MACDONALD, W. E. PICKETT, and D. D. KOELLING, *J. Phys. C* **13**, 2675 (1980).

[63] P. NOVÁK, http://www.wien2k.at/reg_user/textbooks/novak_lecture_on_spinorbit.ps.

[64] C. KITTEL, *Introduction to solid state physics*, John Wiley & Sons, Inc., 7th edition, 1996.

[65] R. W. G. WYCKOFF, *Crystal Structures*, volume 1, Interscience Publishers, New York, 2nd edition, 1963.

[66] P. CHERIN and P. UNGER, *Acta Cryst.* **23**, 670 (1967).

[67] P. GHOSH, M. U. KAHALY, and U. V. WAGHMARE, *Phys. Rev. B* **75**, 245437 (2007).

[68] P. E. BLÖCHL, O. JEPSEN, and O. K. ANDERSEN, *Phys. Rev. B* **49**, 16223 (1994).

[69] J. H. SEXTON, D. W. LYNCH, R. L. BENBOW, and N. V. SMITH, *Phys. Rev. B* **37**, 2879 (1988).

[70] A. Y.-C. YU and W. E. SPICER, *Phys. Rev.* **169**, 497 (1968).

[71] R. C. VEHSE, E. T. ARAKAWA, and M. W. WILLIAMS, *Phys. Rev. B* **1**, 517 (1970).

[72] P. B. JOHNSON and R. W. CHRISTY, *Phys. Rev. B* **9**, 5056 (1974).

[73] J. H. WEAVER and R. L. BENBOW, *Phys. Rev. B* **12**, 3509 (1975).

[74] J. H. WEAVER, *Phys. Rev. B* **11**, 1416 (1975).

[75] J. H. WEAVER and C. G. OLSON, *Phys. Rev. B* **14**, 3251 (1976).

[76] R. LÄSSER and N. V. SMITH, *Phys. Rev. B* **25**, 806 (1982).

[77] H. CHEN, N. E. BRENER, and J. CALLAWAY, *Phys. Rev. B* **40**, 1443 (1989).

[78] E. E. KRASOVSKII and W. SCHATTKE, *Phys. Rev. B* **63**, 235112 (2001).

[79] P. MONACHESI, R. CAPELLI, and R. DEL SOLE, *Eur. Phys. J. B* **26**, 159 (2002).

[80] G.-M. FEHRENBACH, *Phys. Rev. B* **59**, 15085 (1999).

[81] V. M. SILKIN, I. P. CHERNOV, P. M. ECHENIQUE, Y. M. KOROTEEV, and E. V. CHULKOV, *Phys. Rev. B* **76**, 245105 (2007).

[82] A. ALKAUSKAS, S. D. SCHNEIDER, C. HÉBERT, S. SAGMEISTER, and C. DRAXL, *Phys. Rev. B* **88**, 195124 (2013).

[83] N. VAST, L. REINING, V. OLEVANO, P. SCHATTSCHNEIDER, and B. JOUFFREY, *Phys. Rev. Lett.* **88**, 037601 (2002).

[84] H. EHRENREICH, H. R. PHILIPP, and B. SEGALL, *Phys. Rev.* **132**, 1918 (1963).

[85] G. HASS and J. E. WAYLONIS, *J. Opt. Soc. Am.* **51**, 719 (1961).

[86] H. E. BENNETT, M. SILVER, and E. J. ASHLEY, *J. Opt. Soc. Am.* **53**, 1089 (1963).

[87] R. P. MADDEN, L. R. CANFIELD, and G. HASS, *J. Opt. Soc. Am.* **53**, 620 (1963).

[88] E. SHILES, T. SASAKI, M. INOKUTI, and D. Y. SMITH, *Phys. Rev. B* **22**, 1612 (1980).

[89] F. SZMULOWICZ and B. SEGALL, *Phys. Rev. B* **24**, 892 (1981).

[90] D. Y. SMITH and B. SEGALL, *Phys. Rev. B* **34**, 5191 (1986).

[91] H. TUPS and K.SYASSEN, *J. Phys. F* **14**, 2753 (1984).

[92] K.-H. LEE and K. J. CHANG, *Phys. Rev. B* **49**, 2362 (1994).

[93] S. J. YOUN, B. I. MIN, T. H. RHO, and K. S. KIM, *Phys. Rev. B* **69**, 033101 (2004).

[94] R. G. DANDREA and N. W. ASHCROFT, *Phys. Rev. B* **32**, 6936 (1985).

[95] E. CARUTHERS, L. KLEINMAN, and G. P. ALLDREDGE, *Phys. Rev. B* **8**, 4570 (1973).

[96] M. HEINRICHSMEIER, A. FLESZAR, and A. G. EGUILUZ, *Surf. Sci.* **285**, 129 (1993).

[97] V. P. KURBATSKY, A. V. KOROTUN, V. V. POGOSOV, and E. V. VASYUTIN, *Phys. Sol. State* **50**, 949 (2008).

[98] K. GLANTSCHNIG and C. AMBROSCH-DRAXL, *New J. Phys.* **12**, 103048 (2010).

[99] B. R. COOPER, H. EHRENREICH, and H. R. PHILIPP, *Phys. Rev.* **138**, A494 (1965).

[100] P. PYYKKÖ and J.-P. DESCLAUX, *Acc. Chem. Res.* **12**, 276 (1979).

[101] P. PYYKKÖ, *Angew. Chem. Int. Ed.* **41**, 3573 (2002).

[102] P. PYYKKÖ, *Angew. Chem. Int. Ed.* **43**, 4412 (2004).

[103] P. ROMANIELLO and P. L. DE BOEIJ, *J. Chem. Phys.* **122**, 164303 (2005).

[104] N. E. CHRISTENSEN and B. O. SERAPHIN, *Solid State Commun.* **8**, 1221 (1970).

[105] N. E. CHRISTENSEN and B. O. SERAPHIN, *Phys. Rev. B* **4**, 3321 (1971).

[106] N. E. CHRISTENSEN, *Phys. Rev. B* **13**, 2698 (1976).

[107] N. E. CHRISTENSEN, *Int. J. Quant. Chem.* **25**, 233 (1984).

[108] A. DAL CORSO and A. MOSCA CONTE, *Phys. Rev. B* **71**, 115106 (2005).

[109] R. LÄSSER, N. V. SMITH, and R. L. BENBOW, *Phys. Rev. B* **24**, 1895 (1981).

[110] V. THEILEIS and H. BROSS, *Phys. Rev. B* **62**, 13338 (2000).

[111] V. N. ANTONOV, A. I. BAGLJUK, A. YA. PERLOV, V. V. NEMOSHKALENKO, VL. N. ANTONOV, O. K. ANDERSEN, and O. JEPSEN, *Low Temp. Phys.* **19**, 494 (1993).

[112] N. V. SMITH, *Phys. Rev. B* **9**, 1365 (1974).

[113] R. L. BENBOW and N. V. SMITH, *Phys. Rev. B* **27**, 3144 (1983).

[114] A. Y.-C. YU, W. E. SPICER, and G. HASS, *Phys. Rev.* **171**, 834 (1968).

[115] J. C. LEMONNIER, M. PRIOL, and S. ROBIN, *Phys. Rev. B* **8**, 5452 (1973).

[116] J. H. WEAVER, C. G. OLSON, and D. W. LYNCH, *Phys. Rev. B* **12**, 1293 (1975).

[117] P. ROMANIELLO, P. L. DE BOEIJ, F. CARBONE, and D. VAN DER MAREL, *Phys. Rev. B* **73**, 075115 (2006).

[118] N. E. CHRISTENSEN and B. FEUERBACHER, *Phys. Rev. B* **10**, 2349 (1974).

[119] G. LEVEQUE, C. G. OLSON, and D. W. LYNCH, *Phys. Rev. B* **27**, 4654 (1983).

[120] H. J. HAGEMANN, W. GUDAT, and C. KUNZ, *J. Opt. Soc. Am.* **65**, 742 (1975).

[121] H. EHRENREICH and H. R. PHILIPP, *Phys. Rev.* **128**, 1622 (1962).

[122] A. MARINI, R. DEL SOLE, and G. ONIDA, *Phys. Rev. B* **66**, 115101 (2002).

[123] K. STAHRENBERG, TH. HERRMANN, K. WILMERS, N. ESSER, W. RICHTER, and M. J. G. LEE, *Phys. Rev. B* **64**, 115111 (2001).

[124] V. P. ZHUKOV, F. ARYASETIAWAN, E. V. CHULKOV, I. G. DE GURTUBAY, and P. M. ECHENIQUE, *Phys. Rev. B* **64**, 195122 (2001).

[125] L. A. FELDKAMP, M. B. STEARNS, and S. S. SHINOZAKI, *Phys. Rev. B* **20**, 1310 (1979).

[126] A. MARINI, G. ONIDA, and R. DEL SOLE, *Phys. Rev. Lett.* **88**, 016403 (2001).

[127] T. J. MORAVEC, J. C. RIFE, and R. N. DEXTER, *Phys. Rev. B* **13**, 3297 (1976).

[128] W. S. M. WERNER, *Surf. Sci.* **601**, 2125 (2007).

[129] F. ARYASETIAWAN, *Phys. Rev. B* **46**, 13051 (1992).

[130] J. H. WEAVER, D. W. LYNCH, and C. G. OLSON, *Phys. Rev. B* **10**, 501 (1974).

[131] A. Y.-C. YU, T. M. DONOVAN, and W. E. SPICER, *Phys. Rev.* **167**, 670 (1968).

[132] D. W. LYNCH, C. G. OLSON, and J. H. WEAVER, *Phys. Rev. B* **11**, 3617 (1975).

[133] L. P. MOSTELLER JR and F. WOOTEN, *Phys. Rev.* **171**, 743 (1968).

[134] E. T. ARAKAWA, R. N. HAMM, W. F. HANSON, and T. M. JELINEK, in *Optical Properties and Electronic Structure of Metals and Alloys*, edited by F. ABELÈS, North Holland Publishing Co., 1966.

[135] G. W. RUBLOFF, *Phys. Rev. B* **3**, 285 (1971).

[136] S. TUTIHASI, G. G. ROBERTS, R. C. KEEZER, and R. E. DREWS, *Phys. Rev.* **177**, 1143 (1969).

[137] P. BAMMES, R. KLUCKER, E. E. KOCH, and T. TUOMI, *Phys. Status Solidi B* **49**, 561 (1972).

List of publications

In the following, publications written during the development of this thesis are listed:

[P-1] W. S. M. WERNER, M. R. WENT, M. VOS, K. GLANTSCHNIG, and C. AMBROSCH-DRAXL, *Phys. Rev. B* **77**, 161404(R) (2008).

[P-2] W. S. M. WERNER, K. GLANTSCHNIG, and C. AMBROSCH-DRAXL, *J. Phys. Chem. Ref. Data* **38**, 1013 (2009).

[P-3] K. GLANTSCHNIG and C. AMBROSCH-DRAXL, *New J. Phys.* **12**, 103048 (2010).